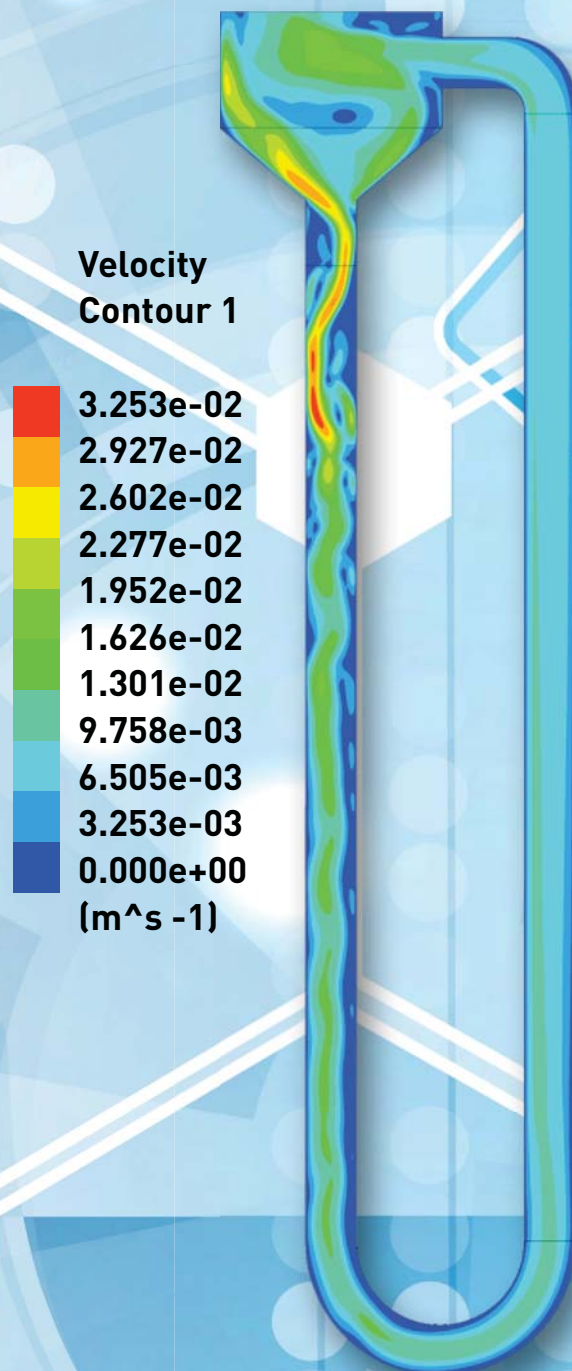


# THE DEVELOPMENT AND EVALUATION OF A NOVEL PHOTOBIOREACTOR FOR PHOTOFERMENTATIVE HYDROGEN PRODUCTION

*RWM Pott, JP du Toit, AC Bovinille, PR Uys, B Ross, L Mabutya, E Buhrmann and MA van Niekerk*



**WATER  
RESEARCH  
COMMISSION**

TT 851/21



# **The Development and Evaluation of a Novel Photobioreactor for Photofermentative Hydrogen Production**

Report to the  
**WATER RESEARCH COMMISSION**

by

**RWM Pott, JP du Toit, AC Bovinille, PR Uys, B Ross  
L Mabutyana, E Buhrmann and MA van Niekerk**  
Department of Process Engineering  
University of Stellenbosch

**WRC Report No. TT 851/21**

**ISBN 978-0-6392-0256-3**



**July 2021**

**Obtainable from**

Water Research Commission

Private Bag X03

GEZINA, 0031

[orders@wrc.org.za](mailto:orders@wrc.org.za) or download from [www.wrc.org.za](http://www.wrc.org.za)

**DISCLAIMER**

This report has been reviewed by the Water Research Commission (WRC) and approved for publication. Approval does not signify that the contents necessarily reflect the views and policies of the WRC, nor does mention of trade names or commercial products constitute endorsement or recommendation for use

## EXECUTIVE SUMMARY

Industrial and municipal wastewaters often contain significant concentrations of organic compounds, which require treatment or removal before the water can be safely reused or disposed of in natural waterways. There is a growing need to develop water treatment technologies which can purify wastewaters, to allow for their reuse. In addition to the imperative to increase water recycling, through treatment, there has been a global shift in paradigm away from simply treating wastewaters to within required emission levels, and rather there is a recognition that the contaminants in wastewaters can be used to produce valuable products additionally. Hydrogen has been proposed as a valuable commodity chemical, and as an energy carrier. While there are significant limitations to the current use of hydrogen-based technologies, there is still an interest and potential applications internationally. There is a need to develop processes which produce hydrogen from renewable resources. The bacterium *Rhodospseudomonas palustris* displays a great metabolic repertoire, being able to metabolise a huge array of organic compounds; many of which other organisms find toxic. In addition, this organism has been shown to efficiently convert organic substrates into high purity hydrogen gas, as part of its normal photofermentative metabolic functioning.

Phototrophic organisms require cultivation in specialised photobioreactors, however the vast majority of work in photobioreactor design and operation has focused on the optimal cultivation of microalgae or cyanobacteria. Very little work to date has been done on designing a photobioreactor optimised for PNS bacterial cultivation. This work has adapted a phenomenon utilised in solar powered water heaters, the thermosiphon effect to passively circulate fluid within a novel thermosiphon photobioreactor (TPBR). This novel photobioreactor was designed, constructed, tested, and to more fully understand the operation modelled. This bioreactor utilises heat generated by light absorption to cause passive circulation, and thus requires no additional power addition for flow.

In order to more fully understand the bioreactor diameter limitations with regards light intensity, and whether this organism suffers from light inhibition, experiments were set up examining growth rate over time, under various light intensities, in a thin tube reactor (to minimise mutual shading). From these experiments it can be seen that *R. palustris* is able to grow well up to a light intensity of around 500-600  $\text{w/m}^2$ , which is significantly higher than, for instance, many microalgae. While at light intensities lower than 70  $\text{w/m}^2$  showed light limitation. In comparison to insolation values, for example in Stellenbosch, these numbers indicate that for the majority of the day the organism will be operating within a light intensity where it does not experience either light limitation or photo-inhibition. On the basis of this information, and using light

attenuation modelling to understand how light diminishes in intensity as it travels through the culture, the optimal diameter of outdoor reactors can be calculated.

A prototype reactor was built at laboratory scale (2 litre working volume) and assessed for suitability for bacterial cultivation. Hydrogen productivity, and glycerol consumption (as a proxy for metabolism) in the novel bioreactor is comparable to that seen in the test bioreactors, with  $H_2$  production rates of approximately  $15 \text{ ml } H_2/g_{DCW}/h$ . As an initial test these productivities are encouraging, since the operation of the prototype reactor was not yet optimised.

A mathematical model used Matlab as a tool to calculate the expected velocity of light absorbing fluid under the assumption of laminar flow, and based on expected heat generation by light absorbed by the bacteria. This model anticipated fluid velocities of  $0.01 \text{ m/s}$ , which was verified using experimentation on the prototype reactor. However, the predictive power of this model is limited, due to its limited parameterisation. Therefore, a more complex, but more powerful, CFD model was developed. The CFD model included an energy dissipation term linked to the Beer-Lambert approximation of light dissipation in a fluid. This builds significantly on the previous thermosiphon CFD literature (which has been performed only with respect to thermosiphon heat transfer equipment – not a light absorbing photobioreactor). The CFD model successfully predicted both heat and velocity characteristics of the prototype reactor, indicating the fluid flow characteristics. The system was shown to be suitable for use with photosynthetic bacteria, as the flow profiles are sufficient to keep the vast majority of the biomass in suspension, a result borne out by experimentation with the prototype reactor.

Having developed a novel photobioreactor, the project looked towards what wastewaters might be suitable for treatment. Detailed information, and effluent samples, were gathered from various industrial partners (in terms of samples, specifically from tannery effluent, anaerobic digester effluent, fish processing factory effluent, tannery effluent, olive mill effluent, winery effluent). From these data, a conceptual map of what industries are producing significant volumes of organic containing wastewaters was developed. This data was captured to indicate i) the types of compounds generally found in each effluent, ii) the volume, periodicity, concentration and variability of each stream, iii) current treatment methodologies (if treatment is carried out), iv) whether photosynthetic bacteria have been shown to metabolise each component, or each waste stream, and from this information then to indicate the viability of: 1. The treatment of each wastewater by PNS bacteria and 2. The potential for simultaneous biohydrogen production.

Some wastewaters showed promise with regards both treatment and hydrogen production potential. In particular, food-system wastewaters were shown to be particularly amenable to photofermentative treatment. For instance, winery wastewaters, olive mill wastewaters and anaerobic digestate effluent have all been shown to decrease in both COD and nitrate concentration during photofermentation, although most require dilution as an initial step. However, many wastewaters have high nitrogenous compound concentrations – these compounds inhibit the production of hydrogen by *R. palustris* by inducing the organism's posttranslational modification system, which shuts down the nitrogen fixing enzymes (and therefore hydrogen production).

In conclusion the objective of this project has been met: a novel photobioreactor has been designed and fabricated at bench scale, following metabolic and fluid mechanic modelling and experimentation. This purpose of this reactor is to allow for integration of photofermentative treatment of wastewater, with simultaneous hydrogen production.

## ACKNOWLEDGEMENTS

The authors would like to thank the Reference Group of the WRC Project 2758 for the assistance and the constructive discussions during the duration of the project:

Dr J Burgess	Water Research Commission
Dr JN Zvimba	Water Research Commission
Prof Daramola	University of Witwatersrand
Prof G Wolfaardt	Stellenbosch University
Prof O Aoyi	Botswana International University of Science & Technology
Prof L Pillay	Stellenbosch University
Prof S Harrison	University of Cape Town
Dr R van Hille	The Moss Group
Dr R Huddy	University of Cape Town

# TABLE OF CONTENTS

<b>EXECUTIVE SUMMARY</b> .....	<b>III</b>
<b>ACKNOWLEDGEMENTS</b> .....	<b>VI</b>
<b>TABLE OF CONTENTS</b> .....	<b>VII</b>
<b>LIST OF FIGURES</b> .....	<b>IX</b>
<b>LIST OF TABLES</b> .....	<b>XIV</b>
<b>LIST OF ABBREVIATIONS</b> .....	<b>XV</b>
<b>1 CHAPTER 1: INTRODUCTION AND OBJECTIVES</b> .....	<b>1</b>
1.1 BACKGROUND.....	1
1.2 RATIONALE .....	1
1.3 AIMS AND OBJECTIVES .....	2
<b>2 CHAPTER 2: LITERATURE REVIEW</b> .....	<b>4</b>
2.1 HYDROGEN.....	4
2.1.1 Hydrogen production by photofermentation .....	5
2.1.2 <i>Rhodospseudomonas palustris</i> .....	5
2.1.3 Industrial applications of <i>R. palustris</i> .....	13
2.1.4 Substrates for hydrogen production by <i>R. palustris</i> .....	13
2.2 WASTEWATERS FOR TREATMENT IN A SOUTH AFRICAN CONTEXT .....	15
2.2.1 Wastewater characteristics .....	15
2.2.2 Wastewater sources .....	17
2.3 PHOTOBIOREACTORS .....	17
2.3.1 Introduction.....	17
2.3.2 Current designs in industry .....	21
2.3.3 Tubular photobioreactors .....	22
2.3.4 Typical circulation methods.....	22
2.3.5 Specific anaerobic circulation.....	23
2.3.6 Thermosiphons.....	23
<b>3 CHAPTER 3: RESULTS, TREATMENT OF RESULTS AND DISCUSSION</b> .....	<b>28</b>
3.1 TREATMENT OF WASTEWATERS BY <i>R. PALUSTRIS</i> .....	28
3.1.1 Materials and methods.....	28
3.1.2 Reactor operating conditions .....	31
3.1.3 Growth curves.....	36
3.1.4 Maximum specific growth rates .....	40
3.1.5 Identification of wastewaters for treatment.....	47
3.1.6 Growth of <i>R. palustris</i> on wastewaters .....	58
3.1.7 H <sub>2</sub> production from wastewaters .....	60

3.2	THERMOSIPHON REACTOR DEVELOPMENT AND FABRICATION .....	61
3.2.1	Thermosiphon reactor development.....	61
3.2.2	Prototype photobioreactor operation .....	64
3.2.3	Thermosiphon PBR geometry .....	67
3.2.4	Pilot-scale TPBR set-up.....	68
3.2.5	Bacteria growth and substrate consumption within the TPBR. ....	69
3.2.6	Biomass growth and biohydrogen production within the TPBR. ....	71
3.2.7	Limitations of bacterial free suspension within the TPBR.....	72
3.3	PHOTOBIOREACTOR MODELLING .....	73
3.3.1	Mathematical modelling .....	73
3.3.2	Fluent modelling .....	92
3.3.3	CFD simulation results.....	99
3.3.4	Flow visualization.....	107
3.3.5	Validation of CFD by comparison with physical experiments.....	110
3.3.6	Effect of light absorption on heating rate.....	113
3.3.7	Effect of light absorption on thermosiphoning cells .....	115
3.4	WASTE SURVEY .....	115
3.4.1	Waste survey approach .....	115
3.4.2	Summary of waste survey.....	116
3.4.3	Industries of interest.....	127
<b>4</b>	<b>CHAPTER 4: CONCLUSIONS AND RECOMMENDATIONS.....</b>	<b>130</b>
<b>5</b>	<b>LIST OF REFERENCES.....</b>	<b>134</b>
<b>6</b>	<b>APPENDIX: .....</b>	<b>157</b>
6.1	APPENDIX A – LITERATURE TABLE OF COMPOUNDS OR WASTEWATERS TREATED BY <i>R. PALUSTRIS</i> OR OTHER PNS BACTERIA.....	157
6.2	APPENDIX B – APPENDICES FOR MATHEMATICAL MODEL .....	173
6.2.1	Modelling procedures.....	173
6.2.2	Coefficients for density and viscosity .....	187
6.2.3	Derivation of the mathematical model .....	189
6.2.4	Final mathematical model Matlab code.....	193
6.3	APPENDIX C – APPENDICES FOR CFD MODEL .....	200
6.3.1	Computational Fluid Dynamics modelling methodology .....	200
6.3.2	Experimental fluid dynamic studies .....	203
6.3.3	UDF source code.....	215

## LIST OF FIGURES

Figure 1: Diagrammatic representation of the division cycle of <i>Rhodospseudomonas palustris</i> . Reproduced from (Westmacott and Primrose, 1976). See text for description of stages a-f. ....	7
Figure 2: Schematic diagram of the main processes related to hydrogen metabolism in <i>R. palustris</i> under photoheterotrophic, anaerobic, nitrogen fixing conditions. The straight black arrows indicate electron flow, through electron transporter flow. The straight blue arrows indicate CO <sub>2</sub> or fixed carbon flow. The straight red arrows indicate H <sup>+</sup> flow. The curved black arrows indicate reactions. The curved purple arrows indicate the cyclic electron transport system, as part of the photosynthetic apparatus. The yellow lightning indicates light excitation. The thick grey line indicates the inner cell membrane. Abbreviations: Hup = external uptake hydrogenase; LH1 = Light harvesting complex 1; LH2 = Light harvesting complex 2; RC = reaction centre; Cytbc <sub>1</sub> = cytochrome b/c <sub>1</sub> complex; ATPase = ATP synthase; TCA cycle = tricarboxylic acid cycle (Krebs cycle); CBB pathway = Calvin-Benson-Bassham cycle (Calvin cycle); Com. I = Complex I; N <sub>2</sub> ase = nitrogenase; Fd = ferredoxin; Q = ubiquinone; QH <sub>2</sub> = reduced ubiquinone; cytc = cytochrome c. Reproduced from (Pott, 2014). ....	10
Figure 3: Diagram of A. Bubble column, B. Internal loop (draft tube) airlift, C. Spilt Colum, D. External loop airlift, A. Air lift flat panel PBR, B. Pump driven flat panel PBR redrawn from (Wang et al., 2012). ....	19
Figure 4: Tubular PBR with horizontal tubes modified from (Chisti, 2008). ....	19
Figure 5: A). Hypothetical thermosiphon system by (Close, 1962)., B). Initial reactor geometry for thermosiphon PBR adapted from Close, 1962., C). Final reactor geometry of thermosiphon PBR adapted from Close, 1962. ....	21
Figure 6: Schematic of density variation in a rectangular thermosiphon loop with a low level heated section and a high level heat sink modified from (Budihardjo et al., 2007) ....	24
Figure 7: Schematic of the various natural circulation loops modified from (Zvirin, 1982). ....	25
Figure 8: Schematic diagram of test photobioreactor rig, showing: 1 – inverted measuring cylinder for gas capture, 2 – water bath, 3 – magnetic stirrer, 4 – magnetic flea, 5 – culture bottle, 6 – gas and liquid ports, 7 – light board, 8 – incandescent lightbulbs, 9 – heater circulator ....	29
Figure 9: Tubular photobioreactor for testing light intensities. ....	30
Figure 10: Growth of <i>R. palustris</i> on 50 mmol glycerol and 10 mmol glutamate under various temperatures. ....	32
Figure 11: Gas production of <i>R. palustris</i> on 50 mmol glycerol and 10 mmol glutamate under various temperatures ....	32
Figure 12: Specific hydrogen production rate of <i>R. palustris</i> under varying temperature conditions, grown on 50 mmol glycerol and 10 mmol glutamate. ....	33
Figure 13: Specific hydrogen production at each time point of <i>R. palustris</i> under varying temperature conditions, grown on 50 mmol glycerol and 10 mmol glutamate. ....	33
Figure 14: Glycerol concentration of <i>R. palustris</i> media when grown under varying temperature conditions on 50 mmol initial glycerol concentration and 10 mmol initial glutamate concentration. ....	34

Figure 15: Transmittance (spectrophotometer – 875 nm) of light through <i>R. palustris</i> cultures of varying cell concentrations with Van Niels medium as the blank. The culture used for these measurements was grown in a 500 mL Schott bottle with bioreactor fittings in modified Van Niels medium at a temperature of 35°C and light intensity of 200 W/m <sup>2</sup> with illumination provided by incandescent light bulbs (EUROLUX – 100 W bulbs). The CDW of the varying light intensities over times is provided in this figure. Data points represent the mean of triplicate repeats. The error bars show the uncertainty associated with the CDW measurements and the transmittance measurements. ....	35
Figure 16: Growth curves (CDW vs time) of <i>R. palustris</i> 11774 with illumination provided by incandescent light bulbs (EUROLUX – 60 W or 100 W depending on the light intensity required) for varying light intensities, i.e. 30, 70, 100, 200, 400 and 600 W/m <sup>2</sup> . <i>R. palustris</i> was cultivated using modified Van Niels medium and filtered sterile with argon at varying light intensities. The CDW of the varying light intensities over times is provided in this figure. All experiments were completed at a constant temperature of 35°C and a volumetric flow rate of 2 L/min. Data points represent the mean of quadruple repeats. The error bars show the uncertainty associated with the CDW measurements.....	38
Figure 17: Maximum CDW of <i>R. palustris</i> achieved with illumination provided by incandescent light bulbs (EUROLUX – 60 W or 100 W depending on the light intensity required) for varying light intensities, i.e. 30, 70, 100, 200, 400 and 600 W/m <sup>2</sup> . <i>R. palustris</i> was cultivated using modified Van Niels medium and filtered sterile with argon at varying light intensities. All experiments were completed at a constant temperature of 35°C and a volumetric flow rate of 2 L/min. Data points represent the mean of quadruple repeats. The error bars show the uncertainty associated with the CDW measurements. ....	39
Figure 18: Natural logarithm of <i>R. palustris</i> CDW within the exponential phase with illumination provided by incandescent light bulbs (EUROLUX – 60 W or 100 W depending on the light intensity required) for varying light intensities, i.e. a) 30, b) 70, c) 200, d) 400 and e) 600 W/m <sup>2</sup> . <i>R. palustris</i> was cultivated using modified Van Niels medium and filtered sterile with argon at varying light intensities. All experiments were completed at a constant temperature of 35°C and a volumetric flow rate of 2 L/min. Data points represent the mean of quadruple repeats. ....	42
Figure 19: Maximum specific growth rate of <i>R. palustris</i> achieved with illumination provided by incandescent light bulbs (EUROLUX – 60 W or 100 W depending on the light intensity required) for varying light intensities, i.e. 30, 70, 200, 400 and 600 W/m <sup>2</sup> . <i>R. palustris</i> was cultivated using modified Van Niels medium and filtered sterile with argon at varying light intensities. All experiments were completed at a constant temperature of 35°C and a volumetric flow rate of 2 L/min. Data points represent the mean of quadruple repeats. The error bars show the propagated uncertainty originally associated with the CDW measurements. ....	44
Figure 20: Light spectrum of the sun for full days (measurement every 10 minutes): a) light intensity over time during the month of May (autumn) and b) light intensity over time during the month of July (winter). Outdoor light meter placed on the roof of a story building at the Department of Process engineering in Stellenbosch. ....	46
Figure 21: Light spectrum of the sun for full days (measurement every 10 minutes): a) light intensity over time during the month of May (autumn) and b) light intensity over time during the month of July (winter). Outdoor light meter placed on the roof of a story building at the Department of Process engineering in Stellenbosch. ....	47

Figure 22: Growth of <i>R. palustris</i> on various wastewaters, either at 50% dilution with growth medium, or at 100% strength. (□ and Δ) indicate wine-making wastewater, (◇ and ○) indicate anaerobic digestate, (-) indicates dye wastewater.....	59
Figure 23: Growth of <i>R. palustris</i> on various wastewaters, either at 50% dilution with growth medium, or at 100% strength. (□ and ○) indicate fish processing wastewater, (◇ and -) indicate tannery wastewater, (Δ and line) indicate olive mill wastewater. ....	60
Figure 24: Photograph of the TPBR during biological hydrogen production with the annotated number (1-6) corresponding to water chiller, reservoir, halogen light panel, sample port, water flowmeter and hydrogen collection unit respectively. ....	63
Figure 25: Schematic diagram of the flat plate fin design used for the outdoor TPBR showing the fin spacing $z$ , fin thickness $\sigma$ , fin height $L$ , and fin base length $W$ . ....	66
Figure 26: Schematic diagram of the outdoor TPBR showing 1) sampling port, 2) solar radiation, 3) flat plate fin, 4) ambient air cooling, 5) fluid of heavier density falling down, 6) fluid of lighter density rise up, and 6) sparing port. ....	67
Figure 27: Schematic of geometrical development for novel Thermosiphon PBR.....	68
Figure 28: Schematic diagram of the outdoor TPBR showing 1) sampling port, 2) solar radiation, 3) flat plate fin, 4) ambient air cooling, 5) fluid of heavier density falling down, 6) fluid of lighter density rise up, and 6) sparing port. ....	69
Figure 29: Cultivation time profile of biomass and glycerol concentrations in TPBR.....	70
Figure 30: Photograph (left to right) of the cooling and down comer section showing deep purple coloration.....	71
Figure 31: Cultivation time profile of biomass concentration and hydrogen production within the TPBR. ....	72
Figure 32: Photograph of cooling and down-comer sections of the TPBR showing regions of deep purple coloration signifying biomass settling.....	73
Figure 33: Physical dimensions of TPBR .....	74
Figure 34: Temperature difference of the various data sets.....	77
Figure 35: Temperature at temperature probe $T_a$ of the various data sets .....	77
Figure 36: Velocity of the fluid at varying average temperatures .....	78
Figure 37: Velocity of the fluid at varying temperature differences.....	79
Figure 38: Correcting the initial assumptions of the model .....	81
Figure 39: Results of the mathematical model.....	82
Figure 40: Adjusting the frictional coefficient in the mathematical model .....	83
Figure 41: Final configuration for the Matlab model.....	84
Figure 42: Final model and experimental velocity based on viscosity.....	85
Figure 43: Final model and experimental velocity based on temperature difference.....	86
Figure 44: Surface plot of model results with experimental data.....	88
Figure 45: Two-phase final model and experimental velocities.....	92
Figure 46: Blackbody radiation curve of halogen lamp used as solar simulators at a color temperature of 2900K .....	94
Figure 47: Linear regression between absorbance ( $A_b$ ) and biomass concentration ( $X$ ) at various wavelength (400 to 900 nm).....	96
Figure 48: Spectral extinction coefficient of <i>Rhodospseudomonas palustris</i> measured at five different biomass concentrations from 400 to 900 nm .....	97

Figure 49: Temperature of thermosiphon PBR as a function of time for the three thermocouple sensor positions. Experimental data (average temperature, $T_{av}$ and stabilization temperature, $T_{stab}$ ): from startup to thermal equilibrium indicated with symbols while theoretical curve (model); illumination switch off after 15000 s indicated with a solid line. ....	98
Figure 50: Temperature of the hot water in thermosiphon PBR as a function of times for the three thermocouple sensor positions. The experimental data (average temperature, $T_{av}$ ) and theoretical curve (model) are indicated with symbols and lines respectively. ....	99
Figure 51: Temperature contours of CFD steady state simulations showing the temperature notation points, which correspond to the thermocouple positions in the experimental set-up. ....	101
Figure 52: Temperature contours distribution with magnified areas of high temperature gradient within the thermosiphon PBR's CFD simulation. ....	103
Figure 53: Velocity vectors of the CFD simulations showing the direction of flow due to thermosiphoning. ....	104
Figure 54: Velocity contours of the CFD simulations showing the two velocity notation points and the riser's flow profile. ....	106
Figure 55: Flow visualization photographs of the TPBR at intervals of 15s, operating under $0.5 \text{ kg/m}^3$ intervals under for active and inactive bacterial cells with pink to blue color dissipation showing indicating fluid flow through the riser. ....	109
Figure 56: Flow visualization photographs of 45s and 60s compared with CFD simulation results. ....	112
Figure 57: Flow visualization photograph of the storage and mixing tank sections compared with CFD simulation results. ....	113
Figure 58: Heating rate: startup to steady temperature-time profile for active and inactive bacterial cells within the thermosiphon PBR and under the same operating conditions. ....	114
Figure 59: Initial configuration for the Matlab model. ....	176
Figure 60: Experimental setup of prototype thermosiphon photobioreactor. ....	180
Figure 61: Biomass calibration curve for <i>R. palustris</i> . ....	184
Figure 62: Density correlation. ....	188
Figure 63: viscosity correlation. ....	189
Figure 64: A single element in the thermosiphon photobioreactor, adapted from Figure 3 (Dobson, 1993). ....	190
Figure 65: Final configuration for the Matlab model. ....	193
Figure 66: (A) and (B) are the 3D and 2D Thermosiphon PBR reactor geometries while (B) and (C) are the element meshing used at the top and bottom sections of the reactor respectively. ....	201
Figure 67: Schematic diagram of the experimental setup: (1) Computer, (2) Data acquisition unit, (3) Halogen lamps, (4) Water Chiller, (5) Reservoir, (6) Cooling water jacket, (7) Riser, (8) Down comer, (9) Storage tank, (10) Thermocouples, (11) Thermal insulation, (12) Cooling section, (13) Cooling water outlet, (14) Cooling water inlet, 15. Submersible water pump. ....	203
Figure 68: Schematic view of light radiating the TBPR front the front surface $z=0$ , to the rear surface $z=l$ , with $A$ , $I_0(\lambda)$ , $I_z(\lambda)$ , and $q(I)$ being the irradiated area, incident radiant illumination, radiant illumination at any point $z$ , and volumetric sensible heat generated at that point $z$ within the riser respectively. ....	204
Figure 69: Photograph of the thermosiphon PBR in full operation for heat transfer analysis with indicated the indicated positions of measuring position. ....	206

Figure 70: Schematic of the thermosiphon PBR's heating and cooling curve illustrating all the various sections where the heat transfer equations are applied .....	207
Figure 71: Schematic of thermosiphon PBR's cooling curve illustrating the application of newton's law of cooling for modeling the riser's heat transfer coefficient .....	208
Figure 72: Schematic diagram of the halogen lamp's emission spectral in the photosynthetically active region with the shared area showing the region for numerical computation of the radiant flux density .....	209
Figure 73: Schematic diagram of the box model applied to the photosynthetically active region of the halogen lamp spectrum .....	210
Figure 74: Photograph of (A) active and (B) inactivated <i>Rhodopseudomonas palustris</i> under a light microscope with a magnification of 40× .....	211
Figure 75: Photographs of (A) <i>Rhodopseudomonas palustris</i> incubated on agar and (B) planktonic <i>Rhodopseudomonas palustris</i> biomass used for all experimental testing .....	212
Figure 76: Schematic diagram for the estimation of local flow velocity through the riser section .....	213
Figure 77: Schematic diagram for the estimation of biomass settling rate .....	214
Figure 78: Photograph of the experimental setup illustrating the estimation of biomass settling .....	214

## LIST OF TABLES

Table 1: Modes of growth of PNS bacteria .....	8
Table 2: Summary of Single Factor ANOVA on maximum specific growth rate at various light intensities .....	45
Table 3: Summary of some industrial wastewaters of interest, indicating important wastewater components, a green-orange-red (good, intermediate, bad) assessment of the potential for treatment of each wastewater by photofermentative methods, and whether hydrogen production from each wastewater is likely possible.....	53
Table 4: Specific waste streams used in experimentation .....	58
Table 5: Summary of experimentation on wastewaters, indicating whether (Green-orange-red) scale growth of <i>R. palustris</i> occurred on the WW, whether WW treatment (as characterized by COD decrease) occurred, and whether hydrogen was produced from the WW.....	61
Table 6: Segment parameters for initial model .....	75
Table 7: Single phase results .....	76
Table 8: Mathematical model validation .....	85
Table 9: Effect of a 15°C error on the calculated velocity .....	89
Table 10: Effect of a 1°C error on the calculated velocity .....	90
Table 11: Effect of a 5 mm error on the calculated velocity .....	91
Table 12: Two-phase results .....	92
Table 13: Summary of average weighted radiant flux density numerically computed with the box model .....	95
Table 14: Spectral attenuation parameters of <i>Rhodopseudomonas palustris</i> .....	96
Table 15: Comparison of measured and CFD simulated temperatures .....	111
Table 16: Comparison of measured and CFD simulated velocities.....	111
Table 17: South African industry wastewaters, with their estimated volumes, principle components, current treatment methodologies, and pollutant loads. Additionally, literature citations of PNSB metabolizing key components or whole wastewaters, and green-orange-red estimations of treatment potential and hydrogen production potential.	117
Table 18: Rates of hydrogen gas production from various carbon containing components as well as by various photo-fermentative bacteria. ....	157
Table 19: Mesh quality details.....	200
Table 20: Thermophysical properties of water (Lide, 2003).....	200

## LIST OF ABBREVIATIONS

Symbols		
<i>A</i>	Area	$m^2$
<i>D</i>	Diameter	$m$
<i>m</i>	Mass	$kg$
<i>V</i>	Volume	$m^3$
<i>F</i>	Force	$N$
<i><math>\dot{m}</math></i>	Mass flow rate	$kg/s$
<i>a</i>	Acceleration	$m/s^2$
<i>v</i>	Velocity	$m/s$
<i>g</i>	Acceleration due to gravity	$m/s^2$
<i>P</i>	Pressure	$Pa$
<i>Per</i>	Perimeter	$m$
<i>L</i>	Length	$m$
<i>R</i>	Frictional force	$N$
<i>f</i>	Friction coefficient	Dimensionless
<i>Re</i>	Reynolds number	Dimensionless
<i>K</i>	Friction loss factor	Dimensionless
<i>C</i>	Coefficients for the density of water	NA
<i>B</i>	Coefficients for the viscosity of water	NA
Greek symbols		
$\rho$	Density	$kg/m^3$
$\theta$	Angle between the horizontal and flow direction	$^\circ$
$\mu$	Dynamic viscosity	
Subscripts and superscripts		
<i>C</i>	Cross section	
<i>r</i>	Reference	
–	Average	
<i>in</i>	Flow of the stream into the system	
<i>out</i>	Flow of the stream out of the system	
<i>k</i>	Segment of the thermosiphon	
<i>max</i>	Maximum	
<i>ave</i>	Average	

---

<b><i>L</i></b>	Loss
<b><i>z</i></b>	In the z direction
<b>Acronyms</b>	
<b>DCFROR</b>	Discounted Cash Flow Rate of Return
<b>NPV</b>	Net Present Value
<b>PNS</b>	Purple non-sulphur
<b>ROROI</b>	Rate of Return on Investment
<b>TPBR</b>	Thermosiphon Photobioreactor

---

## CHAPTER 1: INTRODUCTION AND OBJECTIVES

### 1.1 Background

Industrial and municipal wastewaters often contain significant concentrations of organic compounds, which require treatment or removal before the water can be safely reused or disposed of in natural waterways. In a South African context the issue of water reuse, in particular, is becoming especially pressing, since due to global climate change our water supplies are reducing concurrently with an increased demand from growing populations and industry. There is therefore a growing need to develop water treatment technologies which can purify wastewaters, to allow for their reuse.

In addition to the imperative to increase water recycling, through treatment, there has been a global shift in paradigm away from simply treating wastewaters to within required emission levels, and rather there is a recognition that the contaminants in wastewaters can be used to produce valuable products additionally. Indeed, closing the nutrient cycles in wastewater treatment has been a focus for the WRC in several previous projects.

### 1.2 Rationale

Hydrogen has been identified not only as a valuable commodity chemical, but one that is proposed as a future energy carrier as a potential replacement for fossil fuels. While there are significant limitations to the current use of hydrogen-based technologies, there is still an interest and potential applications internationally. However, most hydrogen is currently produced through the steam reformation of natural gas, so there is also a need to develop processes which produce hydrogen from renewable resources.

Owing to rapid industrialization and urbanization, environmental pollution is a growing concern. South African industries ranging from textile producers to sugar refineries are both major users and polluters of water, and often produce wastewater streams which are rich in organics such as phenols and organic acids. Furthermore, these wastewater streams have often proven difficult to treat within legislative discharge standards using current technologies. Current wastewater treatment methodologies are also often expensive, energy intensive and, crucially, seldom are the nutrients in the wastewater beneficiated into saleable products.

The purple non-sulfur (PNS) bacterium *Rhodopseudomonas palustris* displays a great metabolic repertoire, being able to metabolise a huge array of organic compounds; many of which other organisms find toxic. In addition, this organism has been shown to efficiently convert organic

substrates into high purity hydrogen gas, as part of its normal photofermentative metabolic functioning.

Phototrophic organisms require cultivation in specialised photobioreactors, however the vast majority of work in photobioreactor design and operation has focused on the optimal cultivation of microalgae or cyanobacteria. Very little work to date has been done on designing a photobioreactor optimised for PNS bacterial cultivation. This work will adapt a phenomenon utilised in solar powered water heaters, the thermosiphon effect to passively circulate fluid within a novel thermosiphon photobioreactor (TPBR).

This project aims to develop a reactor which facilitates biotechnology which is able to both clean and purify wastewater as well as produce a clean, high energy fuel in the form of hydrogen gas. The reactor is designed based on the operation of thermosiphon water heaters, where absorbed light causes passive circulation. This new photobioreactor will allow for the cultivation of anaerobic photosynthetic bacteria, able to convert wastewaters into hydrogen or other valuable products.

### **1.3 Aims and Objectives**

#### **AIM 1:**

Conduct a survey of local industry to determine what organic waste-streams there is a need to treat.

Objectives:

- a) Identify and approach local industries which may produce wastewaters which could potentially be purified using *R. palustris*.
- b) Assemble approximate volumetric flowrates and compositions for local industries' wastewaters, and compare to legislated discharge compositional limits.
- c) Collect samples of approximately representative wastewaters for compositional analysis, as well as growth and hydrogen production studies.
- d) Investigate the literature use of photosynthetic bacteria for metabolism for each component in these waste streams, or the waste streams as a whole.
- e) Evaluate the potential use of photosynthetic bacteria (and *R. palustris* in particular) for i) the treatment of each waste stream and ii) hydrogen production from each waste stream.

#### **AIM 2**

Evaluate the ability of *R. palustris* to metabolise a variety of waste organic materials.

Objectives:

- a) Collect and analyse various industrial wastewater samples. For instance, anaerobic digestate effluent, vinasse, olive mill wastewater, textile and tannery wastewater, fruit juicery wastewaters and paper mill wastewaters.
- b) Evaluate the growth of *R. palustris* on each wastewater, with and without dilution with synthetic media, to evaluate nutrient limitations and inhibitory compound presence.
- c) Evaluate hydrogen production by *R. palustris* on each wastewater, once potential growth has been shown.

### **AIM 3**

To design, construct and test a photobioreactor based on the thermosiphon effect.

Objectives:

- a) Develop a simulation of a thermosiphon based photobioreactor, to predict fluid velocities, temperature profiles and the effect of bacterial loading, so that appropriate design criteria can be met for optimal bacterial photofermentation.
- b) Construct a test thermosiphon photobioreactor to validate the model, and to observe the interfering effects of bacterial metabolism (which is difficult to capture in a simulation).
- c) Test the operational limits and characteristics of the test TPBR.
- d) Iterate the design methodology to propose modifications to the test reactor.

### **AIM 4**

Evaluate the hydrogen production of *R. palustris* used in the novel photobioreactor, in comparison to standard photobioreactors.

Objectives:

- a) Using synthetic media of known composition, evaluate and compare the hydrogen productivity and growth characteristics of the test organism in the TPBR designed and constructed in Aim 3.

### **AIM 5**

Evaluate the treatment of waste-waters by *R. palustris*.

Objectives:

- a) Using the wastewaters tested in Aims 1 and 2, test the hydrogen productivity of *R. palustris* in comparison to known laboratory-based photobioreactors.
- b) Determine the treatment efficiency of *R. palustris* when cultivated in the novel TPBR by examining the wastewater composition over time.

## CHAPTER 2: LITERATURE REVIEW

This review will cover the current state of the art with regards the three main topics integrated within this project:

- i. Photofermentation, and the metabolic activity of *R. palustris*.

In this section the metabolism of our test organism will be discussed, and linked with the wastewater treatment focus of the project. In particular, which organic compounds and wastewaters might be suitable for treatment and reformation into hydrogen by this organism will be discussed.

- ii. What wastewaters are available and in need of treatment in a local context.

If the information is available, the volumes, concentrations, legislative effluent limits and variance of a variety of South African wastewaters are recorded, so that a sensible linking of wastewaters to the possibility of treatment by *R. palustris* can be made. In addition, the potential for an additional photofermentative step to current wastewater treatment is discussed.

- iii. Photobioreactors, and thermosiphon technologies.

This section will deal with the current state of the art with regards photobioreactor design as well as the use of the thermosiphon effect, in addition to any theory required to link these two subjects. Any literature on the use of modelling to design either thermosiphons, or appropriately similar photobioreactors is also considered.

### 2.1 Hydrogen

Hydrogen is regarded as a clean, high energy fuel as it produces only water on combustion (Hosseini and Wahid, 2016). It is particularly useful in fuel cells owing to very high conversion efficiencies (Zaidi and Rauf, 2009). However, it must be noted that although there is currently a large research drive looking at hydrogen as a potential fuel, it does have limitations which make it difficult to use. Since it is a gas at room temperatures and pressures, it requires significant compression to be used as a vehicular fuel. Furthermore, because of its low molecular weight, it is difficult to contain, requiring expensive materials to house it.

Currently most hydrogen is produced by steam reforming of natural gas or light oil, which, rather than reducing the use of fossil fuels, merely shifts them from end use to an earlier production step. Therefore methods for producing hydrogen which are not dependent on fossil feedstocks are being investigated, such as the reforming of biomass, the electrolysis of water and biological hydrogen production (Crabtree et al., 2004).

### 2.1.1 Hydrogen production by photofermentation

The study of the hydrogen-producing metabolism of photosynthetic bacteria has been conducted since the 1940s (Van Neil, 1944). Much of the hydrogen produced by these bacteria is produced by the enzyme nitrogenase, which, under nitrogen limitation, reduces atmospheric nitrogen to ammonia, with the concomitant obligate production of molecular hydrogen. When no molecular nitrogen is available for fixation, hydrogen is reduced according to:



This conversion can be generalised as the complete oxidation of the carbon source to hydrogen, represented by the equation:



The energy deficit, delivered in the form of ATP to these reactions, is provided by photosynthesis.

One organism which exploits photofermentation is the purple non-sulphur bacterium *Rhodopseudomonas palustris*. Under photoheterotrophic growth conditions – that is, under illumination, accompanied by the anaerobic breakdown of organic molecules as both carbon source and electron donor – *R. palustris* is able to produce hydrogen. For the most part, growth and hydrogen production from *R. palustris* have been reported using organic compounds such as glycerol (Sabourin-Provost and Hallenbeck, 2009) or organic acids, such as acetic, lactic, succinic, butyric or malic acids as substrates (Carlozzi and Lambardi, 2009; Carlozzi and Sacchi, 2001; C. Chen et al., 2008; Chen et al., 2007; Vincenzini, 1982) (Vincenzini, 1982, Carlozzi and Sacchi, 2001; Carlozzi and Lambardi, 2009; Chen et al., 2007, Chen et al., 2008a).

### 2.1.2 *Rhodopseudomonas palustris*

#### 2.1.2.1 Taxonomy, ecology and reproduction

Purple non-sulphur bacteria mainly belong to the taxonomic grouping alphaproteobacteria, although several genera fall into the group betaproteobacteria. They are facultative phototrophic anaerobes, mostly found in aquatic environments high in soluble organic matter, often at the oxic-anoxic interface, although they can also be found in soils and sediments, and some species have been known to live in a variety of extreme conditions, from hyper-saline waters to thermal springs or cold polar waters (Imhoff, 2006; Madigan and Jung, 2009).

With regards their taxonomical designation as purple non-sulphur (PNS) bacteria, the Gram-negative *R. palustris* has been found to be able to use inorganic sulphur compounds as electron donors for growth. The fact that they can oxidise sulphide, thiosulphate and elemental sulphur

lays bare the somewhat spurious nomenclature of their being purple “non-sulphur” (as in non-sulphur oxidising) bacteria, although it must be noted that in general they have a lower tolerance to sulphide than the purple bacteria (Sander and Dahl, 2009). The species name *palustris* is derived from the Latin for ‘swamp’ or ‘marsh’, signifying the habitat generally inhabited by the species-aquatic environments rich in organic matter.

The reproduction of *R. palustris* follows a budding cell cycle, producing two morphologically-distinct phases, a ‘mother-cell’ which is non-motile and a smaller, motile ‘swarmer-’ or ‘daughter-cell’. The morphological development of *R. palustris* has been described as cyclical by Whittenbury and McLee (1967) and is presented in Figure 1, reproduced from Westmacott and Primrose (1976). The life cycle is such that the swarmer cell (a) exudes a short phase contrast-translucent tube, somewhat narrower than the original cell (b,c). At the end of this tube a bud develops (d) which will eventually become opaque and large enough to give the whole structure a dumbbell shape (e). Division between the mother cell and swarmer cell then occurs (f), giving rise to a smaller, motile swarmer cell, which has a single polar or sub-polar flagellum, whilst the mother cell is always immotile. On the opposite pole to the tube, the mother cell has a sticky “holdfast”. Several mother cells will often join into a rosette affixed to one another by their “holdfasts”. Swarmer cells were found to reproduce (in their first generation) at an average time of 3 hours 41 minutes, while mother cells reproduced at an average of 3 hours and 30 minutes. The time difference is accounted for by the swarmer cells’ growing the extruding tube, which mother cells retain (Whittenbury and McLee, 1967). This complex cyclic system may account for some of the non-exponential growth seen in cultures, and informs some decisions around reactor design, since some of the life cycle is non-motile.

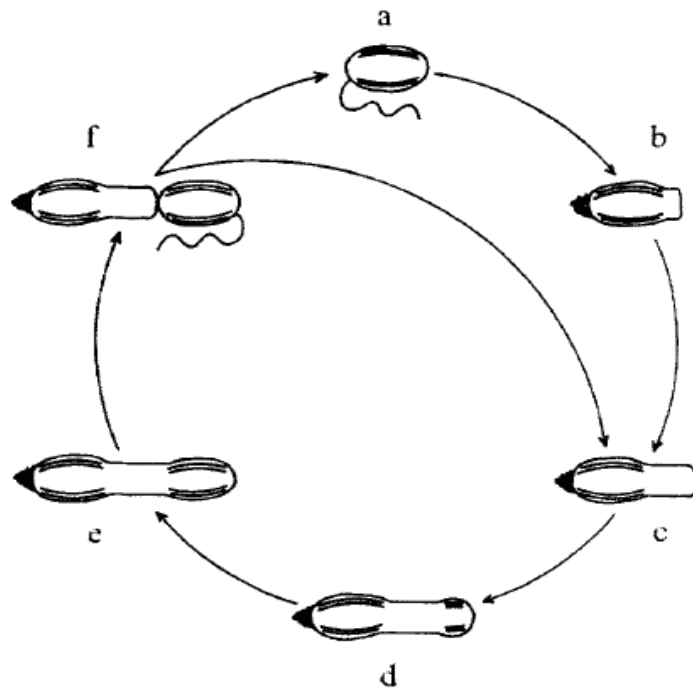


Figure 1: Diagrammatic representation of the division cycle of *Rhodospseudomonas palustris*. Reproduced from (Westmacott and Primrose, 1976). See text for description of stages a-f.

### 2.1.2.2 Overview of modes of growth

The work by Larimer et al. (2004) in sequencing the genome of *R. palustris* CGA009 has allowed insights into the diverse metabolism of these bacteria. They are able to grow chemoheterotrophically, chemoautotrophically, photoautotrophically, and photoheterotrophically, summarised in Table 1. Thus, in the presence of oxygen PNS bacteria operate chemoheterotrophically and do not express their photosystem, but rather synthesise ATP through oxygenic respiration by using oxygen as a terminal electron acceptor in the oxidation of organic compounds.

The second regime where the bacterium is unable to utilise its photosystem is during chemoautotrophism in dark anoxic conditions. In this case electron acceptors other than oxygen are used. These electron acceptors include substrates such as reduced sulphur, nitrogen, iron or carbon monoxide, hydrogen or other compounds such as DMSO (dimethylsulfoxide) or TMAO (trimethylamine-N-oxide).

Photoautotrophism, also labelled photolithoautotrophic growth, occurs when the organism uses reduced inorganics such as  $S^{2-}$ ,  $H_2$ , or  $Fe^{2+}$  as electron donors and  $CO_2$  as the sole carbon source under illumination (Adessi and De Philippis, 2012).

The preferred regime for both growth and hydrogen production is photoheterotrophism, which occurs under illumination by the breakdown of organic molecules, such as organic acids, for use

as both a source of carbon and of reducing potential. During respiration, the carbon compounds are often oxidised rather than assimilated, although in order to maintain redox poise carbon dioxide is fixed by the enzyme RuBisCo. However, when there is an inorganic electron donor present then the carbon source is primarily used for carbon assimilation rather than being oxidised to carbon dioxide.

Under nitrogen limitation the nitrogen fixation pathway is expressed. The nitrogenases, which represent the major enzymatic constituent in this pathway, reduce atmospheric nitrogen to ammonia, with the concomitant obligate production of molecular hydrogen. Hydrogen production also serves as an electron sink, which the bacteria utilise to maintain redox poise by funnelling excess energy and reducing potential into the production of molecular hydrogen.

Table 1: Modes of growth of PNS bacteria

<b>Growth mode</b>	<b>oxygen required</b>	<b>Light required</b>	<b>Carbon Source</b>	<b>Electron source/ Energy source</b>	<b>Hydrogen production</b>	<b>Notes</b>
<b>Chemoheterotrophic</b>	Aerobic	No Light	Organic carbon	Organic carbon	None	can occur without oxygen if there is another terminal electron acceptor, such as nitrate, although growth is limited under this condition
<b>Chemoautotrophic</b>	Aerobic	No Light	CO <sub>2</sub>	H <sub>2</sub> , thiosulphate, other inorganic electron donors	Hydrogen consumption	high expression of RuBISCO
<b>Photoautotrophic</b>	Anaerobic	Light	CO <sub>2</sub>	H <sub>2</sub> , thiosulphate, other inorganic electron donors/ light	Hydrogen consumption	high expression of RuBISCO
<b>Photoheterotrophic</b>	Anaerobic	Light	Organic carbon	Organic carbon/ light	Significant hydrogen production, in the absence of ammonia	Preferred growth mode. CBB pathway still in operation to maintain redox poise

### 2.1.2.3 Metabolism involved in hydrogen production

Hydrogen production by *R. palustris*, and other PNS bacteria, occurs *via* two metabolic routes. The first is through the biological water-gas shift reaction, whereby the bacterium utilises the reducing power of carbon monoxide, under fermentative conditions, to produce hydrogen (Jung et al., 1999; Oh et al., 2002). The second pathway, which is more suited to the reformation of organic compounds to hydrogen, is photofermentation. This occurs under illumination, in an anaerobic atmosphere and results in the breakdown of reduced substrates, such as organic acids. The culture should either be under nitrogen limitation, or the nitrogen source should be glutamic acid, so as to stimulate the synthesis and activation of nitrogenase. Under these conditions the bacteria maintain redox poise by routing excess energy and reducing power to the nitrogenase-catalysed production of hydrogen. Several components make up the hydrogen production system; for simplicity of analysis these can be grouped as: the enzymes; the photosystem; and the Calvin-Benson-Bassham (CBB) cycle and storage compounds. The overall metabolism related to hydrogen production is illustrated in Figure 2.

In Figure 2, light is absorbed by light harvesting complexes 1 and 2 (LH1, LH2) and the reaction centre (RC) and is used to drive to a charge separation across the cell membrane, where reducing equivalents are transported by ubiquinone (Q), and a proton gradient is created by cytochrome *b/c1* (cytbc1). This proton gradient is utilised by ATP synthase (ATPase) to produce ATP. While the photosystem operates a cyclic electron transport chain (purple curved arrows), there is a flux of reducing equivalents which leaves the ubiquinone pool (black straight arrows). The photosystem is denoted as 'cyclic' not because it is a closed loop, but rather because there is no terminal electron acceptor and so electrons are cycled back to the light harvesting complex. The reducing equivalents leaving the cyclic transport chain, transported by ferredoxin (Fd), are used by nitrogenase ( $N_2$ ase) to fix dinitrogen to ammonia, with the concurrent obligate production of hydrogen. Some of this hydrogen is hydrolysed back to electrons and protons by an uptake hydrogenase (Hup). Reducing potential is also used by the cell to fix  $CO_2$  in the Calvin cycle (CBB pathway), and store the carbon as poly(hydroxybutrate) (PHB) and glycogen. The Krebs cycle (TCA cycle) makes up the electrons lost to the photosystem by metabolising organic substrates.

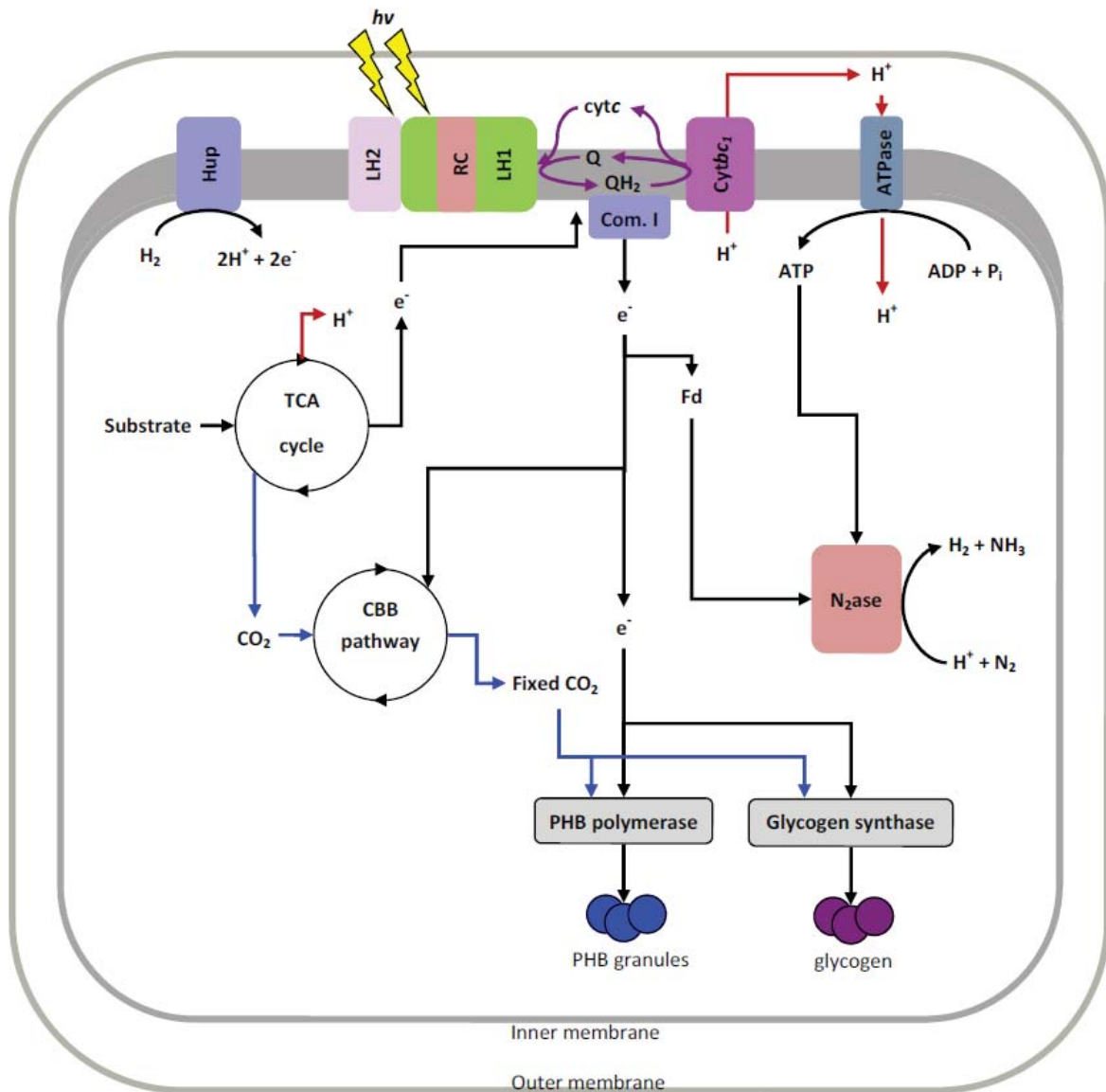


Figure 2: Schematic diagram of the main processes related to hydrogen metabolism in *R. palustris* under photoheterotrophic, anaerobic, nitrogen fixing conditions. The straight black arrows indicate electron flow, through electron transporter flow. The straight blue arrows indicate CO<sub>2</sub> or fixed carbon flow. The straight red arrows indicate H<sup>+</sup> flow. The curved black arrows indicate reactions. The curved purple arrows indicate the cyclic electron transport system, as part of the photosynthetic apparatus. The yellow lightning indicates light excitation. The thick grey line indicates the inner cell membrane. Abbreviations: Hup = external uptake hydrogenase; LH1 = Light harvesting complex 1; LH2 = Light harvesting complex 2; RC = reaction centre; Cytbc<sub>1</sub> = cytochrome b/c<sub>1</sub> complex; ATPase = ATP synthase; TCA cycle = tricarboxylic acid cycle (Krebs cycle); CBB pathway = Calvin-Benson-Bassham cycle (Calvin cycle); Com. I = Complex I; N<sub>2</sub>ase = nitrogenase; Fd = ferredoxin; Q = ubiquinone; QH<sub>2</sub> = reduced ubiquinone; cytc = cytochrome c. Reproduced from (Pott, 2014).

## 2.1.2.4 Enzymes involved in hydrogen metabolism

### 2.1.2.4.1 Hydrogenase

The presence of hydrogenase has been found to be common in PNS bacteria, located both internally, in the cytoplasm, and externally (Koku, 2002; Vignais and Toussaint, 1994). Several isozymes of hydrogenase have been identified, differentiated by the metal at the active sites, which has been found to be either nickel or iron, or a combination thereof (Kim and Kim, 2011). Hydrogenase catalyses the reversible reaction:

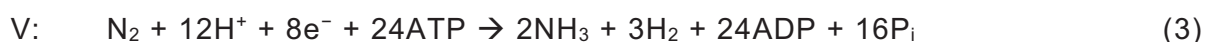
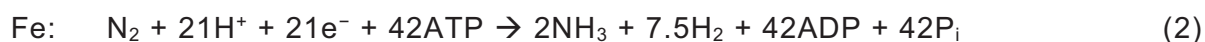
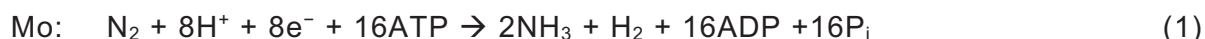


The turnover number of [NiFe]-hydrogenase, as a representative example, was found to be extremely rapid, in the region of 1500-9000 s<sup>-1</sup> at 30°C (pH 5-8) (Pershad et al., 1999). Hydrogenase is inhibited by the presence of O<sub>2</sub> or CO, which irreversibly inactivates the enzyme (Kim and Kim, 2011).

Organisms expressing hydrogenase have been found to be capable of both hydrogen consumption and production. However, under the conditions generally utilised for photofermentation, hydrogenase (in particular external uptake hydrogenase) consumes hydrogen, allowing the organism to regain some reducing equivalents lost to hydrogen production. This has been confirmed by the mutation of organisms to remove their facility for hydrogenase production. In many cases this manipulation has resulted in improved hydrogen production (Kim et al., 2006a; Liu et al., 2010; Rey et al., 2006).

### 2.1.2.4.2 Nitrogenase

Diazotrophic organisms use the highly-conserved enzyme nitrogenase to convert atmospheric nitrogen to ammonia and hydrogen (Burriss, 1991; Igarashi and Seefeldt, 2003). The action of the enzyme entails the obligate concomitant production of hydrogen while producing ammonia, according to the following reactions, the stoichiometry of which is dependent on the metal cofactor (Wall, 2004):



The most frequently-occurring isozyme across diazotrophic organisms, and the most often expressed nitrogenase in PNS bacteria, is the Mo-cofactor based isozyme as the energy requirement for this isozyme to catalyse the reaction is lower than that of other isozymes.

However, if the cell is starved of molybdenum, it will express the other nitrogenase isozymes instead (Oda et al., 2005). The rate of catalysis by the enzyme is comparatively slow, with a turnover number in the region of  $5 \text{ s}^{-1}$ . The slow speed of catalysis necessitates a large enzyme concentration (Heiniger et al., 2012).

In the absence of molecular nitrogen, for example under an argon atmosphere, the enzyme continues to operate; however, the yield of hydrogen to ATP consumed increases 4-fold, according to:



This nitrogenase-catalysed production of hydrogen forms the major source of hydrogen in photofermentation in PNS bacteria (Koku, 2002).

The reaction is an energetically-expensive one for the organism, requiring significant amounts of ATP and reducing potential in the form of reduced ferredoxin, and so is subject to a number of metabolic regulatory systems (Burris, 1991; Igarashi and Seefeldt, 2003; Koku, 2002). Similarly to hydrogenase, the most effective inhibitor of nitrogenase, and repressor of its expression, is oxygen, which irreversibly inactivates the enzyme. As another regulatory mechanism, lack of light also prevents the expression of nitrogenase, as without light as an energy source, the organism is unable to bear the energetic burden of operating nitrogen fixation (Burris, 1991; Masepohl et al., 2002).

One of the inhibitors of nitrogenase, and therefore of hydrogen production, is ammonia (as  $\text{NH}_4^+$ ). The presence of fixed nitrogen induces three levels of regulation: (i) at the first level transcription of the *nifA1*, *nifA2* genes, which encode the transcriptional activators for nitrogenase expression, are suppressed in the presence of  $\text{NH}_4^+$  through the two-component NtrB and NtrC system. (ii) at the second level, independent of the NtrB/C system, the presence of  $\text{NH}_4^+$  induces structural changes to NifA1 and NifA2 which prevent the transcriptional activator from binding to its binding site and activating the nitrogenase gene transcription. (iii) at the third level of regulation, GlnB and GlnK, expressed in the presence of  $\text{NH}_4^+$ , control the DraT/DraG system which mediates the reversible ADP-ribosylation of already expressed nitrogenase (Heiniger et al., 2012; Leigh and Dodsworth, 2007; Masepohl et al., 2002). This inhibition has implications for wastewater treatment concurrent with hydrogen production, since many wastewaters are rich in nitrogen compounds, and will therefore not produce significant hydrogen.

Heiniger et al. (2012) have shown that it is possible to modify *R. palustris* genetically so that post-translational nitrogenase inactivation does not occur, even in the presence of fixed nitrogen sources, such as ammonium salts.

### **2.1.3 Industrial applications of *R. palustris***

While the use of *R. palustris* for hydrogen production is a fairly recent research priority, the bacterium has been used industrially for a variety of other purposes. The most frequent application of PNS bacteria in general is that of wastewater treatment (Hiraishi et al., 1989; Oh et al., 2004; Siefert et al., 1978; Vincenzini et al., 1981). *R. palustris* is not only applicable in the treatment of sewage, but also industrial wastewaters. Some examples of this that have been gaining interest in the literature are the treatment of dyes (Kim et al., 2002; Oda et al., 2001), of latex wastewater (Kantachote et al., 2005), and of waste streams from various foodstuff factories (Adessi et al., 2012; Getha et al., 1998; Keskin and Hallenbeck, 2012). Another application which is being investigated in the literature is the use of *R. palustris*, or other PNS bacteria, in aquaculture either as a protein-rich feedstuff (Kim and Lee, 2000) or as a probiotic (Wang, 2011). Many of these waste streams will be considered later in this literature review.

### **2.1.4 Substrates for hydrogen production by *R. palustris***

The metabolic diversity of *R. palustris*, and PNS bacteria in general, means that a large number of compounds can be metabolised by these organisms, and the derived energy utilised for hydrogen production. Therefore a diverse number of substrates have been investigated in the literature, although the majority of research has concerned the use of organic acids. Other substrates include some sugars, waste streams, biomass of various types and crude glycerol.

#### **2.1.4.1 Organic acids**

These compounds, which include acetic, butyric, malic, and succinic acids, are frequently found in *R. palustris*'s habitat, as they are the by-products of fermentative, particularly anaerobic, metabolism. Accordingly, *R. palustris* is able to metabolise them, and, under the correct conditions, produce hydrogen as a product. Many studies have examined the production of hydrogen from acetic acid (Barbosa et al., 2001; Carlozzi et al., 2006; C.-Y. Chen et al., 2008; Gosse et al., 2007; Lo et al., 2011; Oh et al., 2004), butyric acid (C.-Y. Chen et al., 2008; Chen et al., 2007; Lo et al., 2011), malic acid (Basak and Das, 2009; Carlozzi et al., 2010b, 2010a; Carlozzi and Lambardi, 2009; Kim and Lee, 2000; Vincenzini et al., 1982), succinic acid (Melnicki et al., 2008; Vincenzini et al., 1982) or lactic acid (Fascetti et al., 1998; Lo et al., 2011; Vincenzini et al., 1982).

Several studies have examined so called 'two-stage' processes (Rai and Singh, 2016), which ferment a substrate by one (or more) organism(s) into hydrogen, with the obligate concurrent production of organic acids which can then be photofermented by PNS bacteria to hydrogen. Examples of such two-stage conversions include algal biomass fermented by *Clostridium butyricum* and photofermented by *Rb. sphaeroides* (Kim et al., 2006b), palm oil mill effluent (Mishra et al., 2016), cassava ethanol wastewater (Lin et al., 2016), sugars fermented by *Clostridium pasteurianum*, *Enterobacter cloacae* or *Caldicellulosiruptor* sp. and photofermented by *R. palustris*, *Rb. Sphaeroides* or *Rb. capsulatus* respectively (Boran et al., 2012; C.-Y. Chen et al., 2008; Nath, 2008), and starch or cellulose (Cheng et al., 2010; Hitit et al., 2017).

#### **2.1.4.2 Sugars**

There have been several studies examining the photofermentation of glucose, sucrose, or waste streams containing sugars by a variety of PNS bacteria (Abo-Hashesh et al., 2011; Jeong and Jouanneau, 2000; Keskin and Hallenbeck, 2012; LI and Fang, 2008; Oh et al., 2002; Ooshima et al., 1998; Pott et al., 2013; Yetis et al., 2000). The majority of these studies utilise PNS bacteria other than *R. palustris*, as *R. palustris* exhibits limited ability to grow on these substances due to the lack of glucose or fructose transporters (although it does have a mannose transporter system which may operate on other sugars at higher concentrations), hexokinase genes or the genes for the Entner-Doudoroff pathway, all of which are important for sugar metabolism (Larimer et al., 2004).

#### **2.1.4.3 Waste streams**

There are a great many potential waste streams which may be suitable for photofermentation with PNS bacteria (Kapdan and Kargi, 2006a; Tao et al., 2008), considering their metabolic diversity. Some of the waste resources which have been investigated in the literature include the digestate from anaerobic digesters or dark fermenters (Adessi et al., 2012; Boran et al., 2012; C.-Y. Chen et al., 2008; Cheng et al., 2010; Fascetti et al., 1998; Kim et al., 2006b; Lee et al., 2002; Maeda et al., 1998; Nath and Das, 2004), sugar or food production effluent (Abo-Hashesh et al., 2011; Eroglu et al., 2004; Keskin and Hallenbeck, 2012; Oh et al., 2002; Singh et al., 1994; Xu et al., 2013; Yetis et al., 2000; Zhu et al., 1999), sewage water and sludge (Kim et al., 2006b; Nagadomi et al., 2000), wastewater from dye manufacture (Wang et al., 2008), olive mill wastewaters (Eroglu et al., 2004; Pintucci et al., 2015) aromatic-containing wastewaters (Mutharasaiah et al., 2012; Oda et al., 2001), and crude glycerol (Ghosh et al., 2011; Pott et al., 2013; Sabourin-Provost and Hallenbeck, 2009).

## **2.2 Wastewaters for treatment in a South African context**

South Africa has significant resources in the form of waste streams, for example industrial or agricultural effluents. These effluents require treatment before they can be safely disposed of. *R. palustris* can be used to simultaneously treat these effluents while producing hydrogen as a commodity chemical as well as other valuable by-products (DEA, 2015).

### **2.2.1 Wastewater characteristics**

#### **2.2.1.1 Water quality and threats to water quality**

Water quality is threatened by many factors, most prominently from chemical pollution. Chemical pollution from heavy metals, solvents, dyes and pesticides enter aquatic environments in many ways. For instance, industrial wastewaters are often dumped directly into water sources or effluents are released from wastewater treatment plants which do not adhere to discharge requirements. Additionally, pollutants enter aquatic systems by means of agricultural pesticides and fertilizers. Discharge resulting from poor enforcement of laws and illegal practices also adds to water contamination (Oller et al., 2011).

Previously, much focus was placed on identification of extreme individual polluting components. However, current focus is placed on remediation strategies aimed at chronic environmental issues related to the continual emission of pollutants. Additionally, greater amounts of recalcitrant compounds are being found at long distances from their discharge sources. The major avenues for decreasing toxic components in wastewater are biodegradation and photo-degradation. Photo-degradation has proven successful for the treatment of aromatic hydrocarbons, chlorinated aromatic hydrocarbons, chlorinated phenols, and many pesticides. Biodegradation refers to the process where chemicals are broken down via the metabolic metabolism of living organisms such as bacteria and fungi which are naturally found in aquatic and terrestrial environments. Special consideration has to be given to the type of microorganism used as well as to the source of the industrial wastewater. Many organic compounds produced by industry are toxic or resilient to biological treatment, thereby requiring pre-treatment steps or specific experimental operating conditions (Oller et al., 2011).

At present, industrial wastewaters are treated through advanced technologies based on chemical oxidation, such as the advanced oxidation processes. Organic contaminants are degraded through the formation of hydroxyl radicals which are extremely reactive and non-selective. These processes have significant drawbacks, most noteworthy being the formation of oxidation intermediates which are even more resilient to degradation. This means that additional energy and chemical reagents are required which renders these processes expensive and economically

unfeasible. A promising prospect is the use of advanced oxidation processes as a pre-treatment step for biological oxidation processes. The aim would be to convert initially toxic and persistent organic components into more suitable biodegradable compounds. It is estimated that a pre-treatment step could significantly lower the costs associated with the overall process. Alternatively, for the case of non-toxic recalcitrant compounds, advanced oxidation processes could be implemented as a post-treatment step. For these cases, the highly biodegradable portion of the wastewater is initially eliminated via a biological process followed by the degrading of recalcitrant pollutants in an advanced oxidation process (Oller et al., 2011).

#### **2.2.1.2 Industrial wastewater treatment considerations**

The properties of industrial wastewaters vary depending on the industry generating them as well as within the specific industry. Compared to domestic wastewater which generally has a similar composition, the quantitative and qualitative characteristics of industrial wastewater are much more diverse. This results in treatment technologies being complex owing to the vast variety of compounds and concentrations found in industrial wastewater. For instance, industrial wastewater could contain various other organic substrates which compete with the target pollutant for the oxidising agent resulting in a decrease to process efficiency (Oller et al., 2011).

Industrial wastewater can be classified into three varieties. Firstly, wastewater comprising of recalcitrant substances such as large macromolecules which are not readily biodegradable owing to their large size and lack of active centres. Secondly, easily biodegradable wastewater containing high quantities of organic substances as well as low concentrations of recalcitrant substances. Finally, wastewater comprising of inhibitory compounds which are toxic to certain microbial cultures. Recently, research (Gogate and Pandit, 2004) and interest into industrial wastewater treatment through biological processes has significantly increased. This is owing to the real likelihood of reusing the wastewater as a safe and valuable water source (Oller et al., 2011).

The most useful and important biodegradation processes are based on microorganisms such as bacteria and fungi. Important factors to take into consideration when selecting a biodegradation system are the concentration of the species required, their enzyme activity and their ability to acclimatize once they have been exposed to a specific chemical component. Further, microorganisms are very sensitive to environmental changes such as temperature, salinity, pH, oxygen concentration, redox potential, the concentration and types of various substrates and nutrients and the presence of toxic compounds (Oller et al., 2011).

Most commonly, general measures such as biological oxygen demand (BOD), chemical oxygen demand (COD) and dissolved organic carbon (DOC) are used to characterise industrial wastewater. Furthermore, the ratio of BOD/COD (average oxidation state) provides insight towards the portion of organic compounds present in wastewater which are biodegradable (Oller et al., 2011).

## **2.2.2 Wastewater sources**

Availability, cost, carbohydrate content and biodegradability are the main conditions for the choice of waste materials for use in bio-hydrogen production processes. Photosynthetic hydrogen generating bacteria have been found appropriate for the purification of organic waste streams. Favoured substrates for the production of hydrogen include simple sugars such as lactose, sucrose and glucose which are easily biodegradable. Alternatively, pure carbohydrates are also a feasible option for hydrogen production but are more costly raw materials when compared to simple sugars. The main waste materials which can be used for bio-hydrogen gas production are discussed in this section (Kapdan and Kargi, 2006b).

Various photosynthetic and fermentative bacteria can make use of waste materials such as municipal solid wastes, industrial effluents and sewage sludge. Both batch experiments and continuous experiments have shown that organic acid containing aqueous streams acquired from such waste was a suitable substrate for the growth of photosynthetic bacteria. These cases were demonstrated using the photosynthetic bacteria *Rhodobacter sphaeroides* which shares many characteristics with *Rhodospseudomonas palustris* (Kapdan and Kargi, 2006b).

## **2.3 Photobioreactors**

### **2.3.1 Introduction**

Modern biotechnological developments and advances in the mass culturing of microorganisms for food and fuel production was initiated around the early 1940s by research teams at Stanford-USA, Essen-Germany and Tokyo-Japan as an optimal means for maximum biomass productivity (Hagendijk, 2015). Reactors in which bacteria are used as the active component are referred to as bioreactors. They are usually large reactor vessels used in a continuous process but depending on the process requirements are also suitable for batch systems. The feed material flows through the bioreactor bed and the bacteria either remain stationary within the reactor or leave the bioreactor in a sludge stream. The product produced by the bacteria is removed in either a liquid or a gas stream (Mitchell et al., 2006).

A photobioreactor is a specific type of bioreactor. These bioreactors are used for bacteria that require light to grow, live and multiply. These reactors are built from material allowing light to penetrate through to the bacteria and are designed to increase the surface area exposed to the light. Photobioreactors can be closed or open, however the work covered here will focus on closed photobioreactors, due to the requirement to capture any hydrogen gas produced.

Closed photobioreactors can be classified as technical systems providing an artificial environment for phototropic microorganisms to perform chemical conversions (Mortuza et al., 2011) and are cut off from the atmosphere preventing evaporative loss, contamination and pollution (Pulz, 2001). Also, they enable the controlling of growth parameters like optimal temperature, pH level, culture density, nutrient supply, mixing regime, CO<sub>2</sub> and water supply to overcome evaporative losses (Rameshaiah, 2015) thereby significantly improving biomass productivity. Reason why they are preferable over their open systems counterparts despite their very high capital and operational cost (Wang et al., 2012).

Much research has been done on the design and modelling of photobioreactors (Bitog et al., 2011; Molina Grima et al., 1999; Nyce and Rosenberger, 1991; Ugwu et al., 2008; Yugoslav Committee for Chemical Engineering. et al., 2007). However, the vast majority of this work has focussed on the cultivation of microalgae or cyanobacteria, with very little attention paid to other photosynthetic organisms, such as the photofermentative purple non-sulphur bacteria.

Photobioreactors in general use sparging gas to create a flow pattern within the reactor, as well as to transfer required carbon dioxide into the liquid medium. Some classifications of these reactors are known as airlift photobioreactors and are commonly used in industry.

There is a significant demand for the mass culturing of phototrophic microorganisms, since they present a good option not just for food and fuel production but also for the development of new products in the cosmetic, pharmaceutical, agricultural, energy and bioremediation industries (Reyna-Velarde et al., 2010). This project in particular focusses on two aspects of this potential: fuel production, in the form of hydrogen, and bioremediation of wastewaters. The specific design and construction of a photobioreactor must therefore be tied to the required usage, products formed, and organism cultivated.

Several photobioreactor designs have been developed from the three standard designs namely: flat plate, annular and tubular reactors as reviewed by Posten (2009) to meet up with the different physiological demands of these microorganism cells for growth and product development with regards to the value of the products and their field of application. A detail classification of these

new designs according reactor geometry was reported by (B. Wang et al., 2012), as illustrated in Figure 3 and Figure 4, below, with vertical columns PBR [bubble column, internal-loop (draft-tube) airlift, split column airlift and external-loop airlift], flat panel PBR (airlift and pump-driven) and tubular PBR (horizontal and vertical).

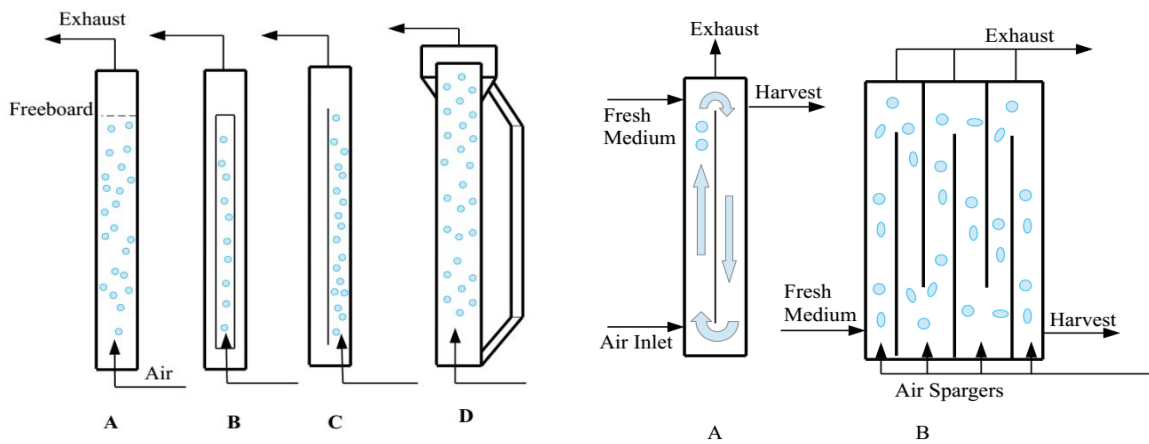


Figure 3: Diagram of A. Bubble column, B. Internal loop (draft tube) airlift, C. Split Column, D. External loop airlift, A. Air lift flat panel PBR, B. Pump driven flat panel PBR redrawn from (Wang et al., 2012).

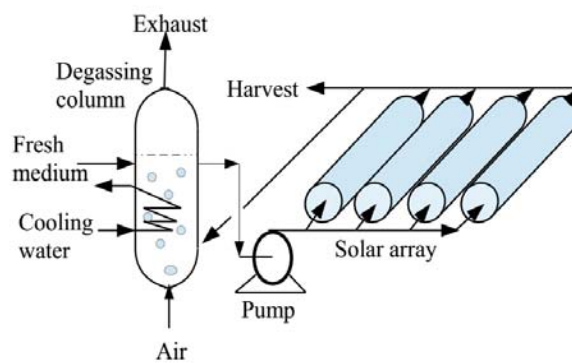


Figure 4: Tubular PBR with horizontal tubes modified from (Chisti, 2008).

Despite the advent of these photobioreactor designs, low production efficiency has been recorded as the major limiting factor due to the many engineering problems which must still be resolved in order to developed low-cost efficient systems at industrial scale (Reyna-Velarde et al., 2010).

High energy consumption is one of those contributing factors to the high capital and operational cost of closed photobioreactors (Acien Fernández et al., 2013; Reyna-Velarde et al., 2010). It results from the main goal of improving biomass productivity by improving mass transfer through

mixing which requires energy to be supplied for aeration and/or agitation by pneumatic and mechanical devices (Acien Fernández et al., 2013). The aeration and/or agitation from these pneumatic and mechanical devices has also been reported to cause cell damage when bubbles detachment from the spargers during breakup or coalescence with liquid and when the bubble burst on culturing surface (Acien Fernández et al., 2013; L.N. Tsoglin, B.V. Gabel, 1996) and hydrodynamic stress produce by mechanical forces from stirrers, impellers or pumps subsequently result to cell damage, restriction to cell growth and metabolic activities. (Reyna-Velarde et al., 2010; Acien Fernández et al., 2013). Therefore, new photobioreactor designs which are less energy consuming, uses light more efficiently and have adequate mass transfer for photosynthetic microorganism biomass production are needed (Reyna-Velarde et al., 2010).

The thermosiphon effect is a physical effect with which fluids flow due to their temperature, and therefore density, differences. The first work on the use of this natural circulation effect in the performance of solar water heaters was done by Close (1962). This project will apply the physical effect of fluid flow in the development and characterization of a novel photobioreactor called Thermosiphon Photobioreactor (TPBR) consisting of a tank, down-comer and riser which is structurally similar to the original formulation by Close (1962). The use of the thermosiphon effect in a photobioreactor has not been reported in the literature previously, and has the potential to significantly decrease energy use in the operation of the photobioreactor.

As a result, this single-phase closed loop thermosiphon could be exploited in the designing of a more complex TPBR as a method to address the high energy consumption supplied for aeration and agitation. A photobioreactor geometry could be developed with a tank, down comer and riser, vertical oriented with respected to gravity which structurally similar to the original formulation by (Close, 1962). Therefore, the proposed thermosiphon PBR could be classified under the reactor geometries of (Wang et al., 2012) as vertical tubular PBR, illustrated below in Figure 5.

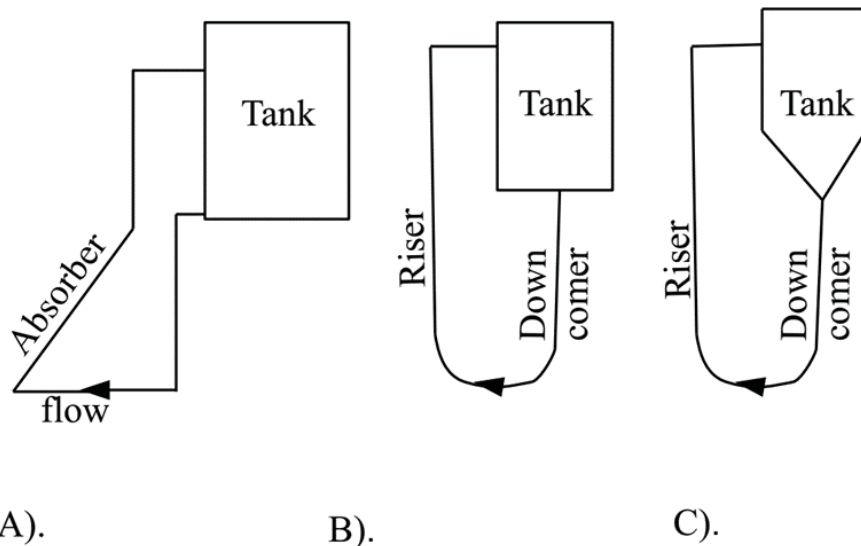


Figure 5: A). Hypothetical thermosiphon system by (Close, 1962); B). Initial reactor geometry for thermosiphon PBR adapted from Close 1962; C). Final reactor geometry of thermosiphon PBR adapted from Close, 1962.

### 2.3.2 Current designs in industry

The use of any bacteria on an industrial scale requires a suitable bioreactor. Different organisms require different living conditions and therefore bioreactors are designed specific to a group of bacteria. This ensures that the designed reactor meets the needs of the bacteria. These reactors must be optimised for optimal cell growth and product yield. Currently in literature there have been few designs proposed for a system based on photosynthetic anoxygenic bacteria, such as *R. rubrum* but an understanding of the currently operated bioreactors can be used to develop such a bioreactor.

Traditionally photobioreactors have been designed for the cultivation of microalgae biomass. The majority of research done on the design and optimisation of a photobioreactor are focused on microalgae systems (Molina Grima et al., 1999; Pulz, 2001; Ugwu et al., 2008).

Photobioreactor designs are limited by their large dependency on light availability and distribution. There are two main methods in which this need is being met. The first design is an open system often referred to as a pond system. This is a large flat reactor resembling a pond with a depth ranging between 15 and 20 cm.

These systems are being replaced by closed systems due to various problems associated with open ponds. Due to the large surface area of the pond that was open to the environment a significant amount of fluid evaporated, the gasses produced could not be captured, preventing

contamination and pollution was impossible and the pond required a large amount of land. These problems were easily avoided a closed system (Pulz, 2001).

Major advances have been made in closed systems in the past years. Two main configurations exist to increase the surface area of a photobioreactor and thereby the illumination. These two configurations are the tubular and flat plate reactor (Pulz, 2001). Within these respective categories there is further differentiation. These variations include the airlift, bubble-column and stirred-tank reactor these variations are aimed to increase the mass transfer of the gas required for microalgae growth (Ugwu et al., 2008).

In the design of a photobioreactor, that aims to operate anaerobically, illumination must be maximised but the mass transfer of gas is not applicable. The configuration is important for maximum light penetration and is relevant to all photobioreactors. The mixing and sparging methods is designed to maximise gaseous mass transfer and is not applicable to an anaerobic bioreactor.

### **2.3.3 Tubular photobioreactors**

A tubular reactor was found to be better suited to outdoor application than flat plate reactors (Ugwu et al., 2008). Tubular reactors are preferred because flat plate reactors are difficult to scale up, they require compartments and multiple support materials. Maintaining a small temperature gradient adds further complication as mixing is difficult within the flat plate. Each system has benefits and limitations but a tubular reactor is favoured for outdoor application (Adessi and De Philippis, 2012; Ugwu et al., 2008).

Ideally a photobioreactor uses sunlight as its source of illumination. A photobioreactor is therefore designed for possible outdoor applications. This study decided to use a tubular photobioreactor design in the hope that the production of hydrogen using this method will only require renewable energy adding to the environmentally friendly nature of hydrogen as a fuel source.

### **2.3.4 Typical circulation methods**

A tubular reactor requires circulation within the reactor (Ugwu et al., 2008). Mechanical mixing, as used in a stirred-tank reactor or aeration as in an airlift or bubble column reactor, can achieve this. Using a propeller to create movement not only requires electrical power but also damages the cells (Molina et al., 2001a). Both the bubble and airlift column involve gas being pumped through the system. This is done to ensure movement and mixing in the reactors as well as supplying the bacteria or algae with the required oxygen or carbon dioxide (Ugwu et al., 2008).

In the case of *R. palustris*, gas is not required, anaerobic conditions are required for optimal growth and therefore using an airlift column or a bubble column reactor is not feasible.

### **2.3.5 Specific anaerobic circulation**

Circulation is necessary for the proper operation of a bioreactor. As neither circulation by a pump nor aeration are suitable for application to promote the growth of *R. palustris* in a bioreactor an alternative method for circulation must be investigated. Sufficient circulation is required while utilising the minimal amount of utilities.

Illumination is required for the operation of a photobioreactor. When energy is converted to light a large portion is lost to heat (Tredici and Zittelli, 1998). If this energy can be used to generate circulation within the reactor the photobioreactors efficiency of light utilisation will increase and no additional utilities will be required.

The thermosiphon principle uses heat to create movement within a fluid. This principle can be applied to a photobioreactor. The thermosiphon principle has the possibility of providing the photobioreactor with sufficient circulation while minimising the utility requirement.

### **2.3.6 Thermosiphons**

The terms thermosiphon, thermosiphon or natural circulation loops are often used interchangeably. For consistency this report will refer to this as the thermosiphon principle.

Thermosiphons are most commonly used in solar water heating systems. The movement is a result of the temperature gradient within the system. These systems are well researched and many correlations are available to model such a system. These models first relate the flow pattern within the tubes to a temperature difference and ultimately to the heat absorbed.

Natural or free convection flows (natural circulation) arise due to the effect of a density difference in a body field (e.g. gravity) and the density difference can be brought about by a temperature difference or heterogeneous multiphase flow (Gandhi et al., 2011; Louisos et al., 2013; Zvirin, 1982). In practice, creating natural circulation within rectangular and cylindrical enclosures, square cavities or any loop can be attainable through heating of the working fluid from the bottom and cooling it from above (Gandhi et al., 2011; Louisos et al., 2013; Zvirin, 1982). The continuous process of heating and cooling establishes a temperature difference within the loop and consequently creates a density gradient thereby enabling the lighted fluid to rise up and be replaced by the heavier fluid as it falls down with the fluid motion being governed by buoyancy

forces (Başaran and Küçüka, 2003; Budihardjo et al., 2007; Louisos et al., 2013) as illustrated in Figure 6.

Natural circulation has gained significant attention in engineering applications such as solar energy systems, cooling of electrical and electronic equipment, thermal energy storage, and heat removal systems in nuclear power plants, as a result of their high reliability, low maintenance costs and absence of moving parts. Some of these natural circulation loops are displayed in Figure 7.

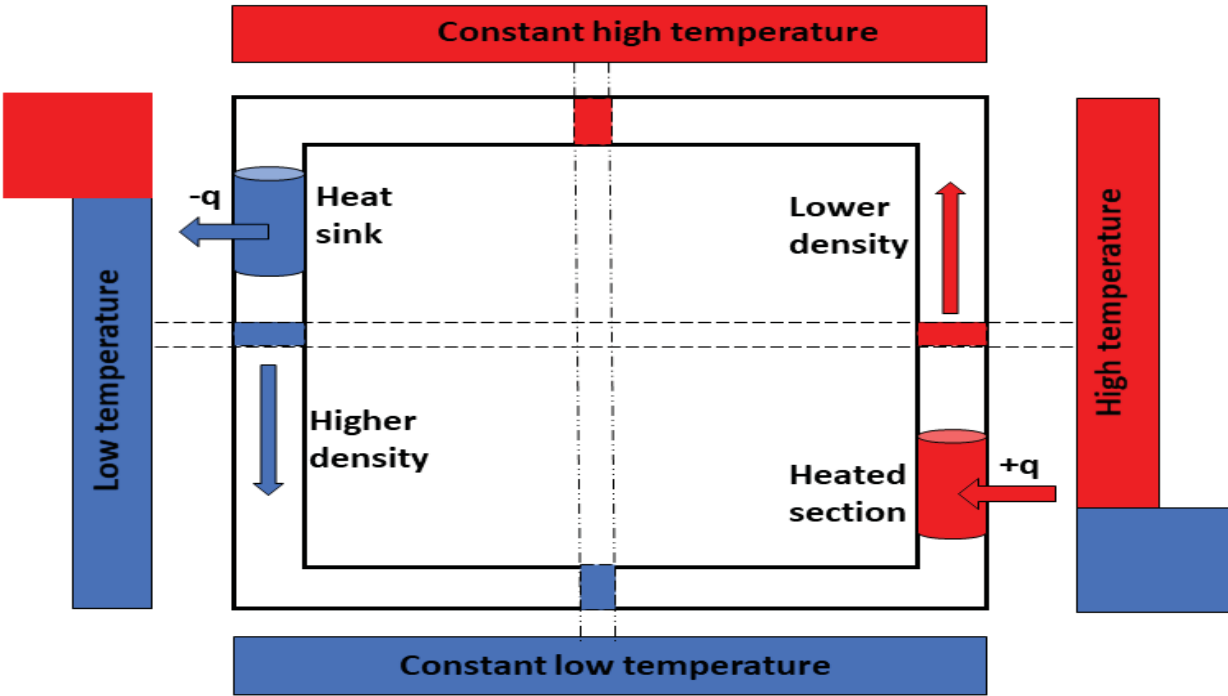


Figure 6: Schematic of density variation in a rectangular thermosiphon loop with a low level heated section and a high level heat sink modified from (Budihardjo et al., 2007)

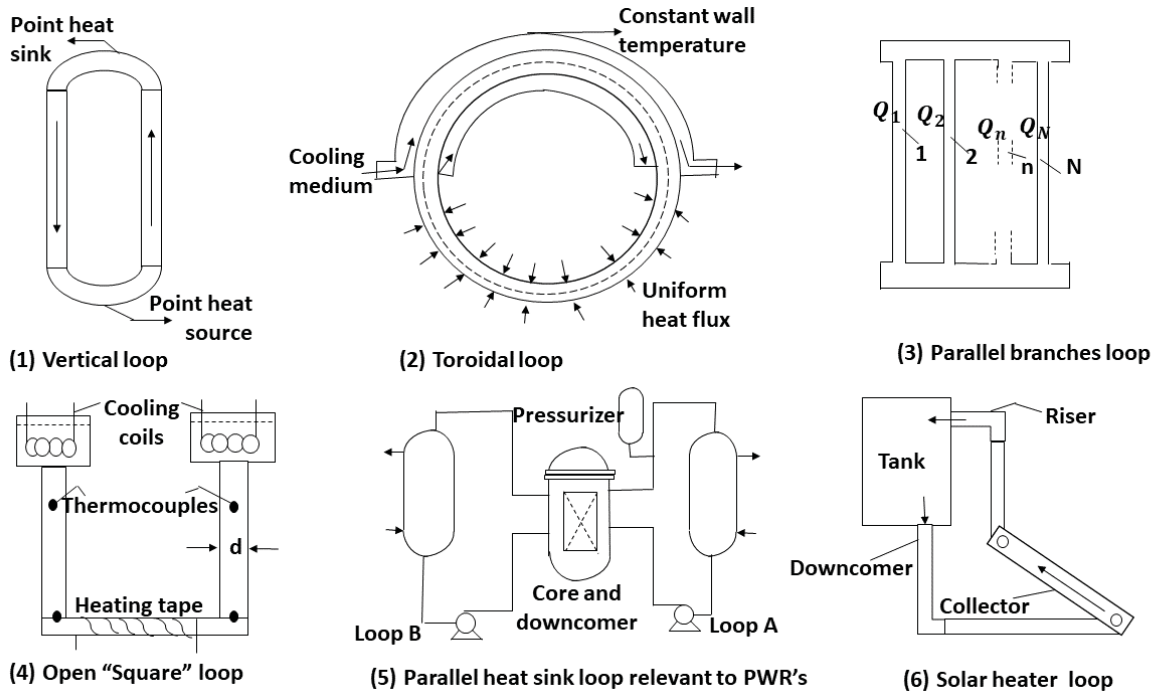


Figure 7: Schematic of the various natural circulation loops modified from (Zvirin, 1982).

Since the very 1<sup>st</sup> work on the performance of solar water heaters (SWH) with natural circulation (figure 23 (6)) was published by close in 1962, SWH in numerous industrial and domestic applications have drastically increased over the last 30 years (Shukla et al., 2013). This is mainly driven by the relative abundance of solar radiation which is harnessed as alternative renewal energy. China leads the global SWH market (118  $GW_{th}$ ) while the European Union, Japan, India and Brazil have recorded a significant expansion (Shukla et al., 2013). Closed thermosiphon loops are characterized by three main sections which forms the basic structural units of a thermosiphon solar water heaters namely (i) storage tank, (ii) connecting pipes (downcomer and upriser), and (iii) collector/absorber whereby thermosiphon is exploited to transport the heat gain by the heat transfer fluid (HTF) from the solar collector to the storage tank (Ogueke et al., 2009; Shukla et al., 2013). Among the commonly used HTFs like water, air, glycol/water mixture, hydrocarbon and refrigerant or phase change liquids (Shukla et al., 2013), water standards out as the favorite HTF for SWH systems because of its high specific heat capacity, low viscosity, less expensive and non-toxic features (Shukla et al., 2013). As a result, water was chosen for this thesis since as it's the growth medium for naturally occurring photosynthetic bacteria. Therefore, all the thermophysical properties pertinent to water will be used.

There are complexities involve in designing thermosiphon SWH systems since as the system performance is affected by the interaction of multiple factors, namely: (i) design parameters, (ii) operating conditions, and (iii) metrological data (Shariah and Shalabi, 1997). For this reason experimental studies on the development of thermosiphon systems (Asfia and Dhir, 1996;

Başaran and Küçüka, 2003; Morrison and Braun, 1985; Samanci and Berber, 2011; Vijayan et al., 2007) are performed on trial and error basis. However, this approach can be expensive and timing consuming. An alternative method of investigation is the use of fundamental theoretical CFD modeling, to predict and characterize thermosiphon and natural convection systems. There have been some investigations using a modeling approach of these systems for water heating, and other engineering applications, however, none have been performed with the aim or characterizing systems designed for photosynthetic organisms (Alizadehdakhel et al., 2010; Budihardjo et al., 2007; Fadhl et al., 2013; Freegah et al., 2013; Gandhi et al., 2011; Louisos et al., 2013; Morrison et al., 2005; Morrison and Braun, 1985; Pilkhwal et al., 2007; Rek et al., 2012; Williamson and Wilson, 2009).

While the CFD modeling methodology has been well established in literature, most of these investigations make use of a simplified boundary condition such as uniform constant wall temperature and surface flux as the heating source on the absorber/collector sections. This approach works well under certain experimental conditions of electric heating, nuclear fuel element, heat exchangers, or boiling water heating. However, it is not well suited for the modeling of natural or artificial externally illuminated systems like a thermosiphon PBR, for which light penetration, absorption and scattering by the working fluid brings about non-uniform volumetric heating at the collector/absorber sections and must be accounted for by solving a relevant radiation transfer equation (equation (4),(5) or (6)).

#### **2.3.6.1 Thermosiphon principle**

Thermosiphons are often referred to as passive systems as they use natural convection to transport fluid (Kalogirou, 2009). The fluid is often heated in one region and cooled in another. This creates a density gradient in the fluid. The colder fluid has a higher density and warmer fluid a lower density. Under the effects of gravity the lighter fluid rises and the heavier fluid falls. This movement results in the fluid circulating as long as there is a temperature difference (Greif, 1988; Kalogirou, 2009). This process as a whole is called the thermosiphon effect.

#### **2.3.6.2 Current applications**

The most common application of thermosiphons is in solar water-heating systems (Kalogirou, 2009). These systems are very common and the thermosiphon principle is rarely mentioned without reference to a solar water heating system. Most of the available literature and mathematical models of thermosiphons are specific to this application.

Thermosiphons are also used as heat transferring elements. These are commonly found in large industries to recover heat as well as in air conditioning units (Lin and Faghri, 1997). Heat

transferring elements usually involves two-phase flow. The density difference between two phases is significantly larger than within one phase resulting in higher flow rates. Additionally a greater amount of heat is absorbed during boiling and condensing than heating and cooling the same volume of fluid making his application well suited for heat transfer.

There are various other niche applications where the thermosiphon is design to specifically meet their required need. One research paper investigates growing protein crystals in a closed loop thermosiphon (Nyce and Rosenberger, 1991). This system has more similarities with a thermosiphon photobioreactor than a solar water heating system.

### **2.3.6.3 Fundamental differences between a solar water heater and a photobioreactor**

The application of a thermosiphon to a bioreactor is not the same as when heating water. In a solar water heating system the collector is used to heat water from the base of a geyser that is then fed back to the top of the geyser. This cycle continues until the water has reached the desired temperature. In a solar water-heater the thermosiphon effect is used to heat water (Zerrouki et al., 2002). This is different in a photobioreactor where the focus will be on sustained circulation, maintained at a constant temperature.

## CHAPTER 3: RESULTS, TREATMENT OF RESULTS AND DISCUSSION

### 3.1 Treatment of wastewaters by *R. palustris*

#### 3.1.1 Materials and methods

##### 3.1.1.1 Bacterial cultivation

*Rhodospseudomonas palustris* strain NCIMB 11774 was obtained from the DSMZ, and grown in modified Rhodospirillacea medium as described by (Pott et al., 2013). Growth medium was adjusted to pH 7.3 with NaOH before autoclaving. Cultures were grown in 500 ml bioreactors comprised of glass reagent bottles (Simax, Czech Republic) fitted with airtight lids containing liquid and gas sampling ports. Anaerobic, and dinitrogen-free conditions were induced by sparging with argon through a 0.22 µm PTFE filter (Pall Corp.) for 10 min. Agitation was provided by magnetic stirring and illumination by 100 W tungsten-filament incandescent bulbs. Irradiance intensity was calibrated to a baseline of 200 W/m<sup>2</sup> (± 20) in the wavelengths between 500-1100 nm, corresponding to the photosynthetic range utilised by *R. palustris*, by means of a compact spectrometer with cosine correcting probe (RGB photonics Qmini VIS-NIR). Temperature was controlled by immersion of culture vessels in a water-filled glass tank fitted with heating circulator and cooling as required to maintain temperature to within ± 0.5°C of stated. Gas produced was collected by displacement of water in inverted 1 L measuring cylinders connected to each gas sampling port with low hydrogen-permeability tubing (Tygon 3603, Saint Gobain).

Culture growth was quantified by optical density at 660 nm, and correlated to dry cell weight using a calibration curve.

##### 3.1.1.2 Test photobioreactors

###### 3.1.1.2.1 Temperature and light controlled photobioreactor for metabolism testing

Photobioreactors with controlled temperature and light intensity were designed and fabricated for these experiments. The photobioreactors consisted of a temperature controlled water bath, containing bottles of cultured bacteria. Each bottle has a gas and a liquid port. The gas port has a tubing line which extends to an inverted measuring cylinder, containing water, to capture any gas produced. A light-board with incandescent lights produces light at the specified light intensity. The culture bottles are placed on top of magnetic stirrers, which keep the cultures in suspension via a magnetic flea.

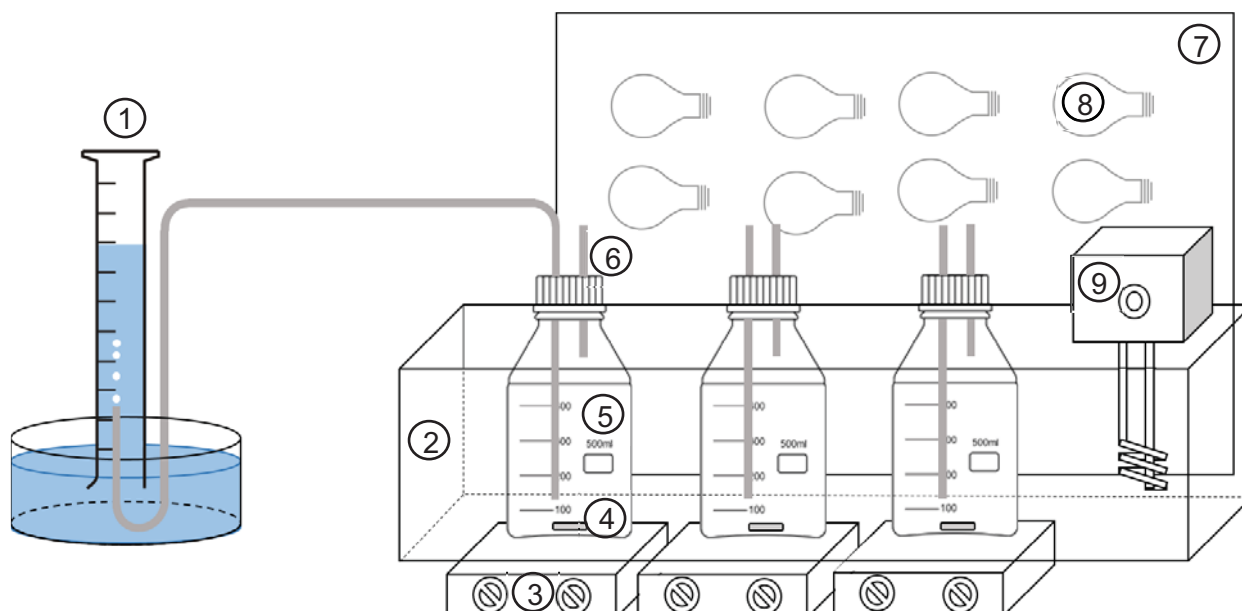


Figure 8: Schematic diagram of test photobioreactor rig, showing: 1 – inverted measuring cylinder for gas capture, 2 – water bath, 3 – magnetic stirrer, 4 – magnetic flea, 5 – culture bottle, 6 – gas and liquid ports, 7 – light board, 8 – incandescent lightbulbs, 9 – heater circulator

### 3.1.1.2.2 Tubular photobioreactor setup and procedure

Borosilicate glass tubing was used to make the tubular photobioreactor system used in this investigation. The reactor had a total active volume of 500 mL with the following dimensions: 3 m long with an internal diameter of 0.022 m and a wall thickness of  $1.8 \times 10^{-3}$  m. Figure 9 below provides a schematic of the experimental setup used for the tubular photobioreactor system. The system consisted of a clear glass water bath with a heat circulator (Julabo) used to control the temperature at which the experiment was set to operate at. The system was set up to operate as a batch type system with a 1 L schott bottle as the reservoir for the returning outlet stream and the exiting inlet stream. The schott bottle lid also housed a liquid sampling port which was used to sparge the system with argon through a  $0.22 \mu\text{m}$  PTFE filter for 10 minutes to induce anaerobic and dinitrogen-free conditions as well as a gas outlet port. Tygon A60 tubing was used for transportation of the culture medium in and out of the reservoir. Tygon A60 has a low gas permeability, was purpose fit for peristaltic pumps and could also withstand the high temperatures experienced during autoclaving. An added benefit of the Tygon A60 tubing was that it was opaque so the bacterial culture only experienced light when it was in the active section of the tubular photobioreactor. A peristaltic pump was used to transport the bacterial culture from the reservoir to the tubular reactor with the outlet of the reactor returning to the reservoir. A peristaltic pump was used due to its non-invasive nature which limits the possibility of contamination of the system. Circulation through the reactor was kept constant throughout all experiments done using this setup at a flowrate of 2 L/min.

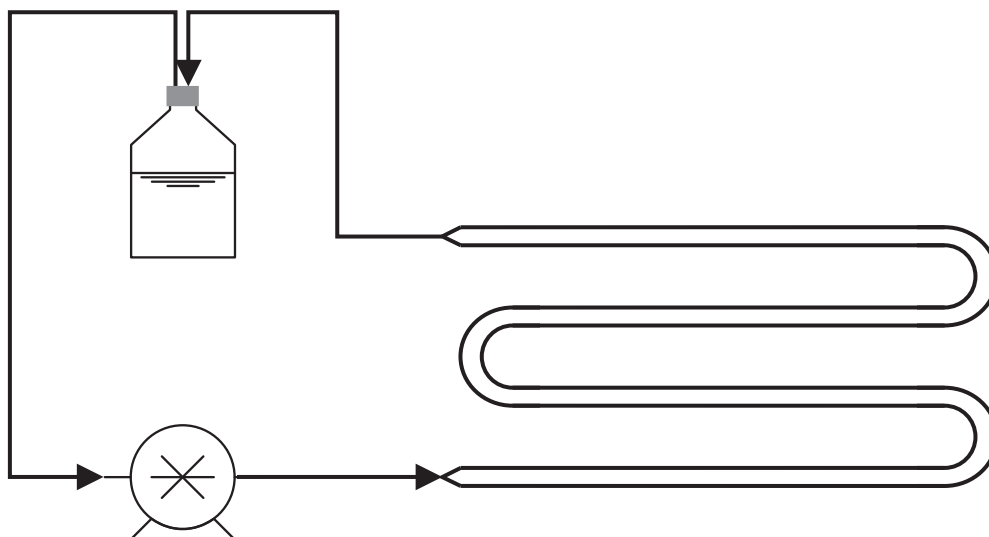


Figure 9: Tubular photobioreactor for testing light intensities.

Illumination of the photobioreactor system was done using 100 W tungsten-filament incandescent light bulbs (EUROLUX). Two rows of seven bulbs were used to illuminate the external surface of one side of each tubular bioreactor. The light intensity was an investigated parameter and therefore was adjusted as required by either shifting the light board closer or further from the surface of the bioreactor. The illuminated surface area of the tubular photobioreactor was approximated as half of the total surface area of the tubular reactor as it was assumed that exactly half of the reactor would receive direct illumination with the light coming from one side only. Equation 8 illustrates how the surface area was calculated.

$$\text{Surface Area of TBR} = \frac{2\pi \times \text{internal radius} \times \text{length}}{2} \quad (5)$$

During the experimental setup procedure the entire photobioreactor system was assembled and then autoclaved (Speedy autoclave) for 50 minutes at a temperature of 121°C and pressure of 101kPa. Once autoclaved the reactor system was sparged with argon before being loaded with either inoculated Van Niels medium or minimal medium depending on which experiment was being run.

### 3.1.1.3 Sampling & measurement

During photofermentation runs, at each time point to be measured, 3 ml of medium was drawn, of which 1 ml was used for biomass quantification by optical density. The remaining 2 ml was centrifuged at 14000 x g for 5 min, the cell-free supernatant decanted and frozen at -20°C for later substrate quantification.

The volume of evolved gas was measured periodically, using an inverted measuring cylinder, with gas samples taken at the end of each run for compositional analysis by gas chromatography.

#### **3.1.1.4 Analysis and statistics**

Glutamate concentration was determined by modified ninhydrin assay (Moore and Stein, 1954). 200 µl of 4 mM ninhydrin (in absolute ethanol) was added to 40 µl of sample in 1.5 ml microfuge tubes and incubated at 80°C for 15 min. 200ul of each reaction was pipetted into a well of a standard 96 well plate (Greiner) and absorbance read at 590 nm in a microplate reader (ELx800, BioTek instruments).

Glycerol concentration was measured using a colorimetric assay based on periodate and acetyl acetone, as described by Pott et al. (Pott et al., 2013), modified from Bondioli et al. (Bondioli and Della Bella, 2005).

A Global Analyser Solutions CompactGC with argon carrier stream and thermal conductivity detector (TCD) was employed to determine the relative composition of the gas produced. H<sub>2</sub> and CO<sub>2</sub> were quantified and reported as relative percentages; any contaminating nitrogen or oxygen was discounted as artefact of the sampling procedure, and no other gases were detected.

Data analysis was performed in GraphPad Prism 7.00. Where appropriate, two-way ANOVA followed by Sidak's multiple comparisons tests was used to determine statistical significance with a 95% confidence interval.

#### **3.1.2 Reactor operating conditions**

In order to appropriately choose reactor conditions for optimal hydrogen production and wastewater treatment, a fundamental study of how temperature effects the growth of our study organism was needed, since the literature has not yet investigated this rigorously. This section therefore deals with the growth and hydrogen production of *R. palustris* under various temperature conditions, when grown on glycerol and glutamate as test carbon and nitrogen sources, respectively. Glycerol is a useful test substrate, since it is a significant waste material, particularly in biodiesel producing countries (Taylor, 2008).

##### **3.1.2.1 Effect of temperature on growth and hydrogen production**

Using the temperature controlled photobioreactor set-up described in the Experimental section of this document, the temperature of the photofermentations was controlled, and varied, between 30 and 45°C. From the figures below it can be seen that *R. palustris* is able to grow and produce hydrogen up to a temperature of around 42°C, while 45°C is high enough to prevent the organism from growing, likely from heat degradation of proteins.

Examining the specific hydrogen production rate in Figure 12, it is clear that the higher the temperature, the greater the specific hydrogen production rate, up to 42°C, where the organism is still able to metabolise. This adds a key piece of information to the body of knowledge of this organism, since previous studies only conducted photofermentations at 30 or 35°C, therefore giving a lower specific hydrogen production rate. The implication of this is that higher reactor temperatures will result in better hydrogen production, and faster wastewater purification, and these higher temperatures will be comparatively easy to achieve, since direct sunlight will tend to raise photobioreactor temperatures above 35°C.

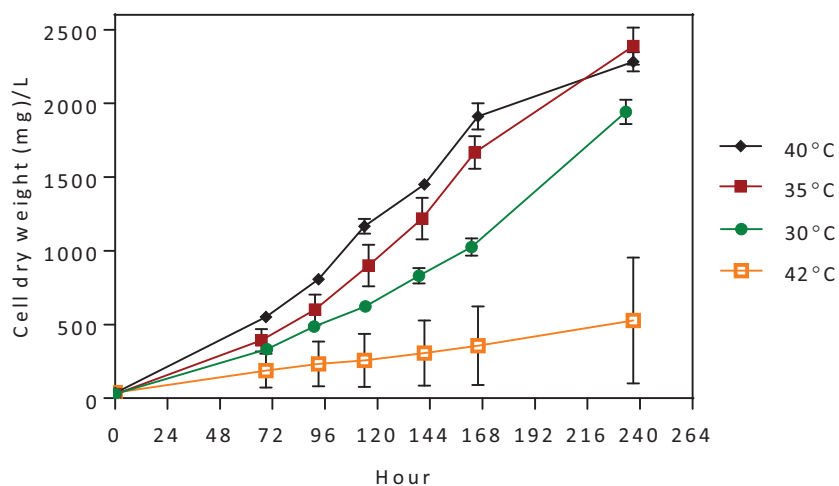


Figure10: Growth of *R. palustris* on 50 mmol glycerol and 10 mmol glutamate under various temperatures

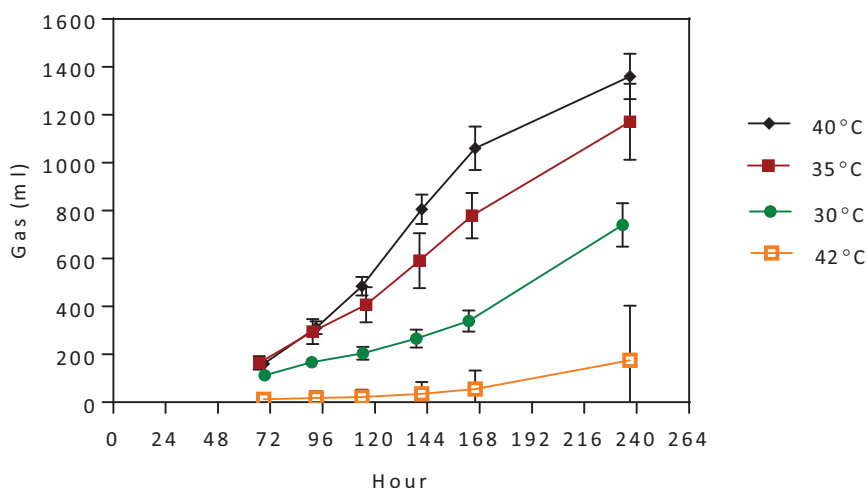


Figure 11: Gas production of *R. palustris* on 50 mmol glycerol and 10 mmol glutamate under various temperatures

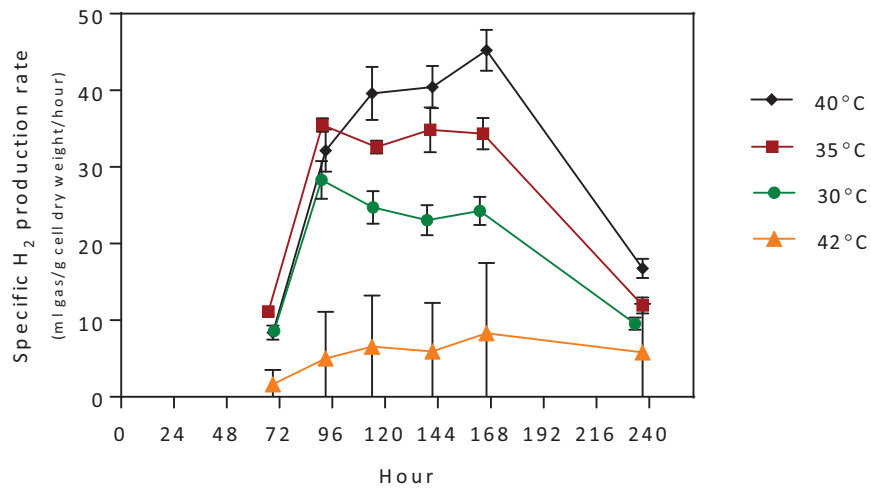


Figure 12: Specific hydrogen production rate of *R. palustris* under varying temperature conditions, grown on 50 mmol glycerol and 10 mmol glutamate.

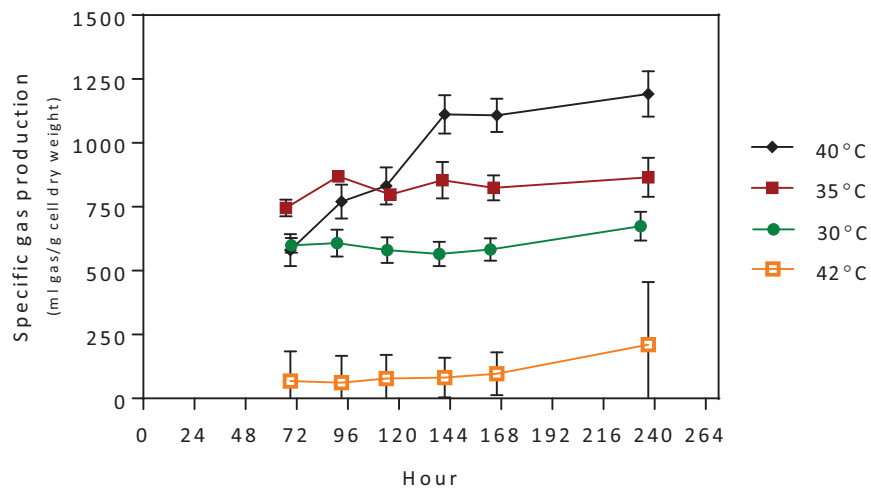


Figure 13: Specific hydrogen production at each time point of *R. palustris* under varying temperature conditions, grown on 50 mmol glycerol and 10 mmol glutamate.

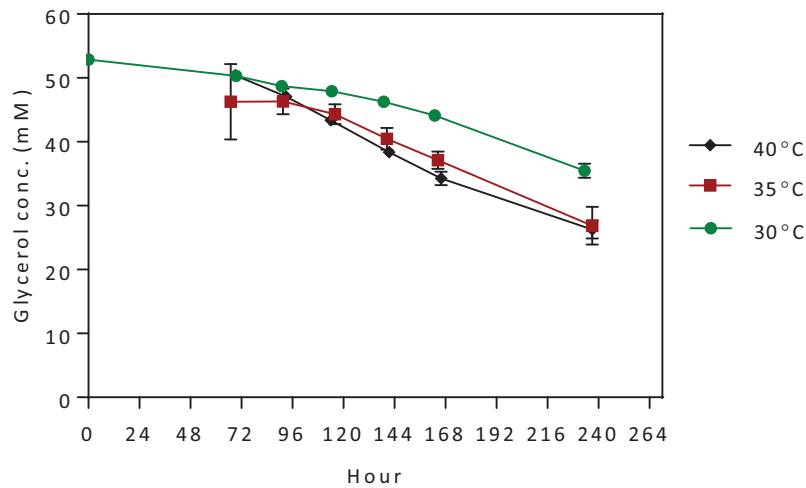


Figure 14: Glycerol concentration of *R. palustris* media when grown under varying temperature conditions on 50 mmol initial glycerol concentration and 10 mmol initial glutamate concentration.

The glycerol consumption trends, shown in Figure 14, correspond with the hydrogen production rate, showing higher consumption rates at higher temperatures. This indicates that the likely limiting factor in these reactors is enzymatic, rather than light, since the light intensity remained the same between these experiments. The likely limiting enzyme in this cascade is the hydrogen producing nitrogenase, since its turnover number is in the region of around 5 molecules per second (McKinlay and Harwood, 2010).

To counteract this limitation further work has been proposed to genetically modify the organism to overexpress the nitrogenase isozymes, and so increase the effective nitrogenase concentration and eliminate or mitigate this limitation.

### 3.1.2.2 Effect of Light intensity on growth and hydrogen production

To investigate the effect of the incident light intensity on the cell growth of *R. palustris* the reactor system described in section 3.1.1.2.2 was employed. A tubular reactor with a very small inner diameter (ID) relative to common lab bioreactor systems (Schott bottle bioreactors) was designed to reduce the effect of light attenuation through the reactor as the cell concentration of the culture increased. Rapid light drop off through a densely grown *R. palustris* culture would be expected purely based on visual inspection of the intense red/purple colour that is completely opaque. Classification of the transmittance of light is discussed in more detail.

Figure 15 below provides a graphical representation of how transmittance (%) of light through an *R. palustris* culture changes as the concentration of cells in the culture increase. The transmittance was measured using a spectrophotometer (UV/Vis spectrophotometer, Varian®)

at a wavelength of 875 nm corresponding to the bacteriochlorophyll  $\alpha$  adsorption peak. At cell concentrations as low as 0.01 g/L approximately 20% of the light is absorbed by the culture and at 0.92 g/L 97.53% of the light is already absorbed by the culture. This illustrates how much light is absorbed over a linear distance of 1cm (standard cuvette) even when the culture density is less than 1 g/L. Therefore, the larger the diameter of the reactor the greater the effect of mutual shading. Mutual shading is where cells closer to the face of the reactor that is receiving direct illumination absorb and/or scatter all the light entering the reactor which results in the remaining cells to be shaded from light. This is far from ideal as the *R. palustris* cell requires the energy from the light to grow and produce the desired by-product hydrogen.

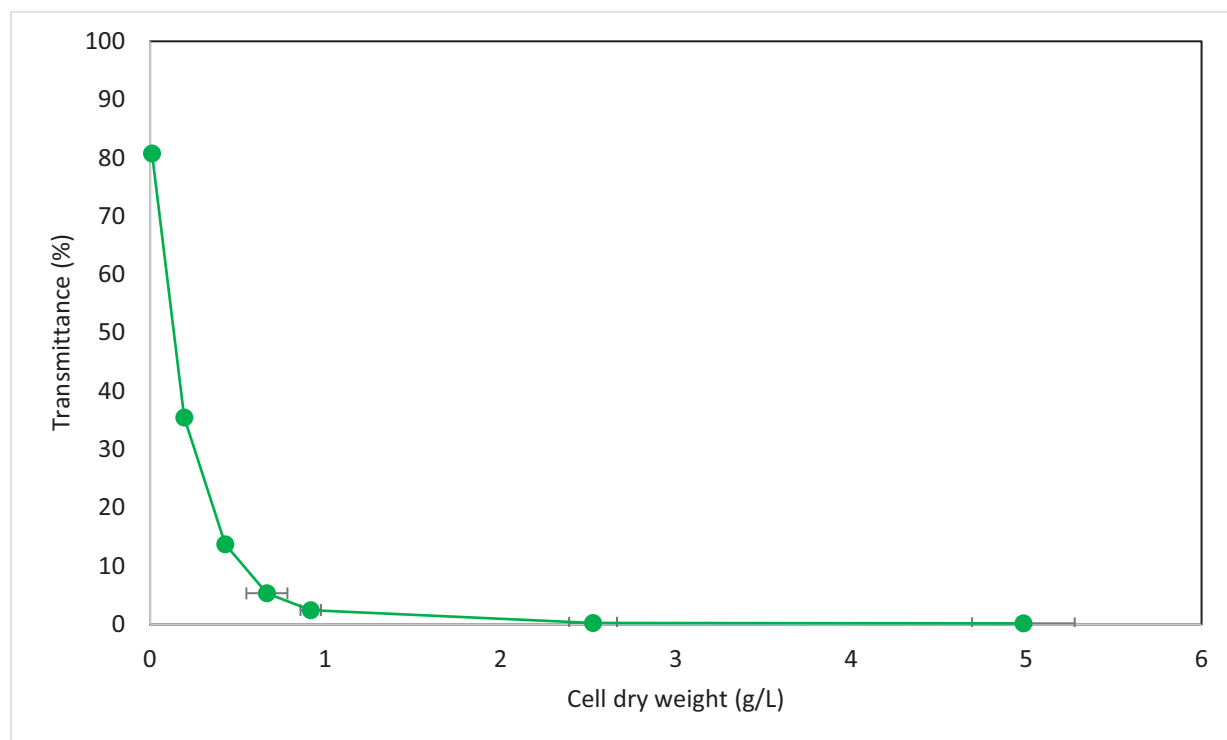


Figure 15: Transmittance (spectrophotometer – 875 nm) of light through *R. palustris* cultures of varying cell concentrations with Van Niels medium as the blank. The culture used for these measurements was grown in a 500 mL Schott bottle with bioreactor fittings in modified Van Niels medium at a temperature of 35°C and light intensity of 200 W/m<sup>2</sup> with illumination provided by incandescent light bulbs (EUROLUX – 100 W bulbs). The CDW of the varying light intensities over times is provided in this figure. Data points represent the mean of triplicate repeats. The error bars show the uncertainty associated with the CDW measurements and the transmittance measurements.

The experimental rig discussed in 3.1.1.2.2 was used for all experiments pertaining to the investigation into the effect of light intensity on *R. palustris* growth. The incident light intensity was measured using a light meter over the wavelength range of 500 nm to 1000 nm. The selection of the wavelength range was due in part to the limitation of the light meter but was mainly based on the range where *R. palustris* can absorb light. The illumination was provided by incandescent light bulbs (EUROLUX) with the light intensity being altered by adjusting the

distance between the incident surface and the light bulbs. For high light intensities (200, 400 and 600 W/m<sup>2</sup>) 100 W incandescent light bulbs were used and for the lower light intensities (30 and 70 W/m<sup>2</sup>) 60 W incandescent light bulbs were used.

Five light intensities were investigated namely 30, 70, 200, 400 and 600 W/m<sup>2</sup>. The minimum and maximum values in this range, i.e. 30 and 600 W/m<sup>2</sup>, correspond to the limits of the experimental setup. The effect of light intensity on *R. palustris* 11774 growth metabolism will be investigated through the comparison of the general growth behaviour, substrate utilisation, maximum specific growth rate and pigment formation at the varying light intensities selected.

### 3.1.3 Growth curves

The growth curves of *R. palustris* 11774 grown in modified Van Niels medium at varying light intensities using the tubular bioreactor system can be seen in Figure 16 below. For each light intensity it can be noted that what is typically described as the trend of batch bacterial growth cultures is followed. That is that there are distinct growth phases namely: the acceleration phase, exponential phase, deceleration phase, stationary phase and in some instances a death phase. Batch cultures often have a period of stasis at the start of culturing where no cell division occurs, here cells are merely adapting to the culture conditions and synthesising required enzymes for growth. This period is known as the lag phase. In most cases steps are taken during culturing to minimise or remove this lag phase entirely to reduce the time it takes for the culture to enter exponential growth phase. This was done by culturing the *R. palustris* inoculum in the same medium and conditions as the actual experimental environment and inoculating when the inoculum was in the exponential phase of growth, thus cells could begin to divide almost immediately after inoculation. It can be seen in Figure 16 that the lag phase was successfully minimised. An in-detail discussion of the growth curve of each light intensity investigated follows:

i. 30 W/m<sup>2</sup>

The acceleration phase starts from time zero and has a duration of 48 hours after which the exponential phase is reached. The exponential phase is where the maximum growth rate is achieved. The exponential phase then ends at the 72 hour mark corresponding to a 24 hour exponential phase. The growth of the cells then begins to decrease as it enters the deceleration phase which continues for 48 hours which corresponds to a total incubation period of 120 hours. A short 9 hour long stationary phase then follows which is where the rate of cell division is equal to the rate of cell death. This is then succeeded by the death phase which is where the rate of cell death is higher than the rate of cell division and often results in a linear decrease. The maximum CDW achieved at a light intensity of 30 W/m<sup>2</sup> was 4.182±0.157 g/L after 120 hours of culturing.

ii. 70 W/m<sup>2</sup>

The acceleration phase starts from time zero and has a duration of 48 hours after which the start of exponential phase is reached. The exponential phase then ends at the 72 hour mark corresponding to a 24 hour exponential phase. The growth of the cells then begins to decrease as it enters the deceleration phase which continues for 31 hours which corresponds to a total incubation period of 103 hours. The deceleration has almost plateaued to the stationary phase at this point. No data was collected in the death phase. The maximum CDW achieved at a light intensity of 70 W/m<sup>2</sup> was 4.319±0.311 g/L and was achieved at the end of the experimental run which was after 103 hours.

iii. 200 W/m<sup>2</sup>

The acceleration phase starts from time zero and has a duration of 48 hours after which the start of exponential phase is reached. The exponential phase then ends at the 72 hour mark corresponding to a 24 hour exponential phase. The growth of the cells then begins to decrease very gradually as it enters the deceleration phase which continues for only 24 hours. At this point in the culture growth (96 hours) a very abrupt stationary phase is reached which plateaus for 9 hours before gradually decreasing as it enters the death phase after a total incubation time of 103 hours. After 96 hours of biomass culturing the maximum CDW achieved at a light intensity of 200 W/m<sup>2</sup> was 4.923±0.338 g/L.

iv. 400 W/m<sup>2</sup>

The acceleration phase starts from time zero and has a duration of 48 hours after which the start of exponential phase is reached. The exponential phase then ends at the 72 hour mark corresponding to a 24 hour exponential phase. The growth of the cells then begins to decrease gradually as it enters the deceleration phase which continues for only 24 hours. After 96 hours of biomass culturing the maximum CDW was reached: 5.015±0.061 g/L. No stationary phase was observed as the culture immediately enters the death phase.

v. 600 W/m<sup>2</sup>

The acceleration phase starts from time zero and has a duration of 48 hours after which the start of exponential phase is reached. The exponential phase then ends at the 72 hour mark corresponding to a 24 hour exponential phase. The growth of the cells then begins to decrease as it enters the deceleration phase which continues for 50 hours which corresponds to a total incubation period of 122 hours. The deceleration has almost plateaued to the stationary phase at this point. No data was collected in the death phase. The maximum CDW achieved at a light

intensity of  $600 \text{ W/m}^2$  was  $4.172 \pm \text{g/L}$  and was achieved at the end of the experimental run which was after 122 hours.

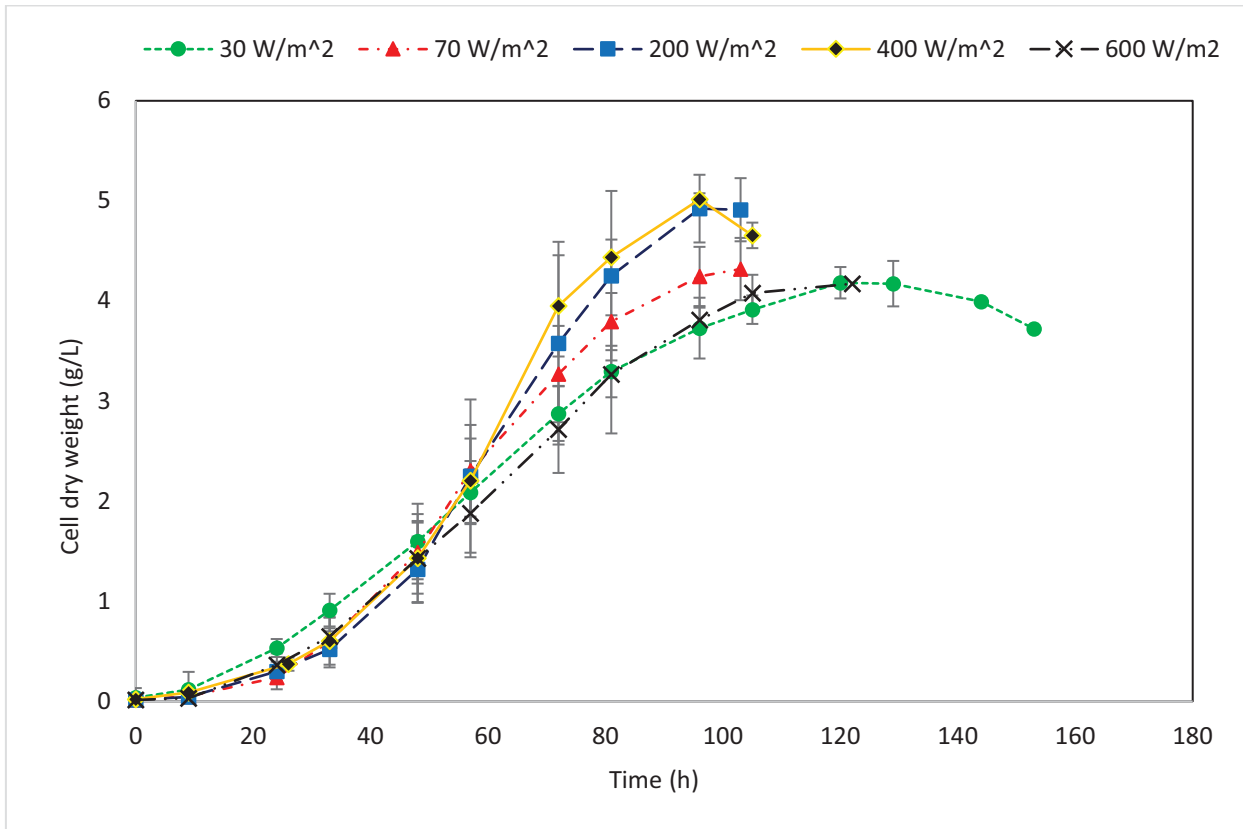


Figure 16: Growth curves (CDW vs time) of *R. palustris* 11774 with illumination provided by incandescent light bulbs (EUROLUX – 60 W or 100 W depending on the light intensity required) for varying light intensities, i.e. 30, 70, 100, 200, 400 and  $600 \text{ W/m}^2$ . *R. palustris* was cultivated using modified Van Niels medium and filtered sterile with argon at varying light intensities. The CDW of the varying light intensities over times is provided in this figure. All experiments were completed at a constant temperature of  $35^\circ\text{C}$  and a volumetric flow rate of  $2 \text{ L/min}$ . Data points represent the mean of quadruple repeats. The error bars show the uncertainty associated with the CDW measurements.

From the detailed discussion on each individual growth curve it can be noted that there are clear similarities between all the light intensities investigated with regards to the timespan of the acceleration phase and the exponential phase. This implies that the period of these phases is not affected by the incident light intensity even though the rate of growth is. More sample points within these phases could possibly illustrate that the period is affected by light although these influences would likely be miniscule.

Almost identical growth curves were achieved for the  $200 \text{ W/m}^2$  and  $400 \text{ W/m}^2$  experimental runs which indicates that the growth rate likely saturates when the light intensity increases to beyond a certain level. This will be discussed later in more detail in section 3.1.4 which divulges into the maximum specific growth rates achieved at each light intensity investigated.

Figure 17 below provides a graphical representation of how the maximum CDW (g/L) achieved changes as the incident light intensity changes. As the light intensity increases the maximum CDW that can be achieved increases until saturation occurs at 200 W/m<sup>2</sup>, saturation then continues until 400 W/m<sup>2</sup> after which photo-inhibition (of some type – since *R. palustris* does not produce oxygen during photosynthesis, photo-inhibition as described in the algal literature it not applicable here. this is an area which requires further investigation) occurs which causes the maximum achievable CDW to decrease. There is an upward trend in the maximum CDW from 30 W/m<sup>2</sup> to 200 W/m<sup>2</sup> which corresponds to a CDW increase of 15.04% from 4.182±0.157 g/L to 4.923±0.338 g/L. The maximum CDW achieved then plateaus between 200 W/m<sup>2</sup> to 400 W/m<sup>2</sup> where there is a difference of only 1.84% between the two light intensities. The maximum CDW then decreases by 16.82% from 5.015±0.061 g/L to 4.172± g/L when the light intensity increases to 600 W/m<sup>2</sup>. This trend aligns with literature, however exact saturation intensities and the point at which photo-inhibition begins to occur cannot be compared as most studies to report light intensities with units such as lux that cannot be converted to W/m<sup>2</sup> without the conversion factor that is light source specific.

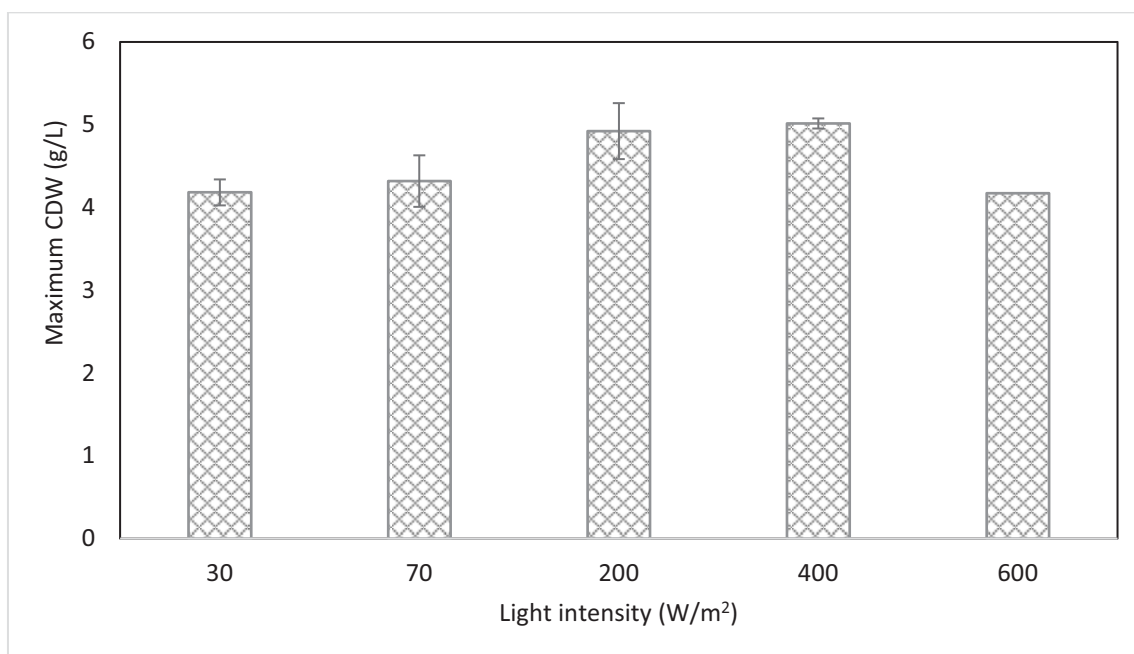


Figure 17: Maximum CDW of *R. palustris* achieved with illumination provided by incandescent light bulbs (EUROLUX – 60 W or 100 W depending on the light intensity required) for varying light intensities, i.e. 30, 70, 100, 200, 400 and 600 W/m<sup>2</sup>. *R. palustris* was cultivated using modified Van Niels medium and filtered sterile with argon at varying light intensities. All experiments were completed at a constant temperature of 35°C and a volumetric flow rate of 2 L/min. Data points represent the mean of quadruple repeats. The error bars show the uncertainty associated with the CDW measurements.

The ability of *R. palustris* 11774 to have relatively similar growth curves and maximum CDW with only a ±15% difference between a large range of light intensities is extremely positive. This would mean that if *R. palustris* was cultured in outdoor photobioreactors that the large variation in the

intensity of direct sunlight may not have a significant effect on the growth of the bacterium. This is of course if it is below a possible light intensity that limits growth altogether.

### 3.1.4 Maximum specific growth rates

As discussed previously the maximum specific growth rate is when the rate of cell division is at a maximum and corresponds to the exponential growth phase on the growth curve. The maximum specific growth rate of each light intensity investigated was determined using the graphical method.

Figure 18 shown below demonstrates how this graphical method was employed for determination of the maximum specific growth rates for each of the light intensities investigated. The natural logarithm of the CDW values in the exponential phase were plotted versus the corresponding times. Microsoft™ Excels built in linear regression function was used to plot a linear regression line through the necessary data points to obtain an equation where the gradient is the maximum specific growth rate.

Figure 18 contains five subplots that are labelled a, b, c, d and e. Each subplot represents the graphical method used for determining the maximum specific growth rate of each individual light intensity investigated. These plots have been separated for ease of viewing. Below a small discussion on the linear regression of each light intensity can be found – lettering corresponds with the subplot labelling. A broader discussion on the effect of the change in incident light intensity on the maximum specific growth rate follows.

#### a) 30 W/m<sup>2</sup>

As discussed above the exponential growth stage fell within the 48 hour and 72 hour experimental time points, therefore the graphical method for determining the maximum specific growth rate was employed over this timespan. This can be seen in Figure 18a with a linear regression line passing through the three experimental points. Equation 9 provided below is the equation that describes the linear regression line with a coefficient of determination of  $R^2 = 0.9918$  which indicates a good fit to the data.

$$y = 0.0242x - 0.6732 \quad [9]$$

The maximum specific growth rate is equal to the gradient of the linear regression line provided in Equation 9, therefore  $\mu_{max} = 0.0242$  at a light intensity of 30 W/m<sup>2</sup>.

#### b) 70 W/m<sup>2</sup>

The exponential growth stage fell within the 48 hour and 72 hour experimental time points, therefore this timespan was used for determination of the maximum specific growth rate. This

can be seen in Figure 18b with a linear regression line passing through the three experimental points. Equation 10 provided below is the equation that describes the linear regression line with a coefficient of determination of  $R^2 = 0.958$  which indicates a good fit to the data.

$$y = 0.0318x - 1.0706 \quad [6]$$

The gradient in Equation 10 provides the maximum specific growth rate, i.e.  $\mu_{max} = 0.0242$  at a light intensity of  $70 \text{ W/m}^2$ .

c)  $200 \text{ W/m}^2$

The exponential growth phase once more fell within the 48 hour and 72 hour experimental time points. Thus, this timespan was used for determination of the maximum specific growth rate, this can be seen in Figure 18c with a linear regression line passing through the three experimental points. Equation 11 below describes the linear regression line fitted to this data with a coefficient of determination of  $R^2 = 0.9665$  which indicates a good fit to the data.

$$y = 0.0405x - 1.6009 \quad [7]$$

The gradient in Equation 11 provides the maximum specific growth rate, i.e.  $\mu_{max} = 0.0405$  at a light intensity of  $200 \text{ W/m}^2$ .

d)  $400 \text{ W/m}^2$

The exponential growth stage fell within the 48 hour and 72 hour experimental time points. This timespan was used for determination of the maximum specific growth rate, this can be seen in Figure 18d with a linear regression line passing through the three experimental points. Equation 12 below describes the linear regression line fitted to this data with a coefficient of determination of  $R^2 = 0.9967$  which indicates a good fit to the data.

$$y = 0.042x - 1.6355 \quad [8]$$

The gradient in Equation 12 provides the maximum specific growth rate, i.e.  $\mu_{max} = 0.042$  at a light intensity of  $400 \text{ W/m}^2$ .

e)  $600 \text{ W/m}^2$

The exponential growth stage fell within the 48 hour and 72 hour experimental time points, therefore this timespan was used for determination of the maximum specific growth rate. This can be seen in Figure 18d with a linear regression line passing through the three experimental points. Equation 13 provided below is the equation that describes the linear regression line with a coefficient of determination of  $R^2 = 0.9965$  which indicates a good fit to the data.

$$y = 0.0266x - 0.9067 \quad [9]$$

The gradient in Equation 13 provides the maximum specific growth rate, i.e.  $\mu_{max} = 0.0266$  at a light intensity of  $600 \text{ W/m}^2$ .

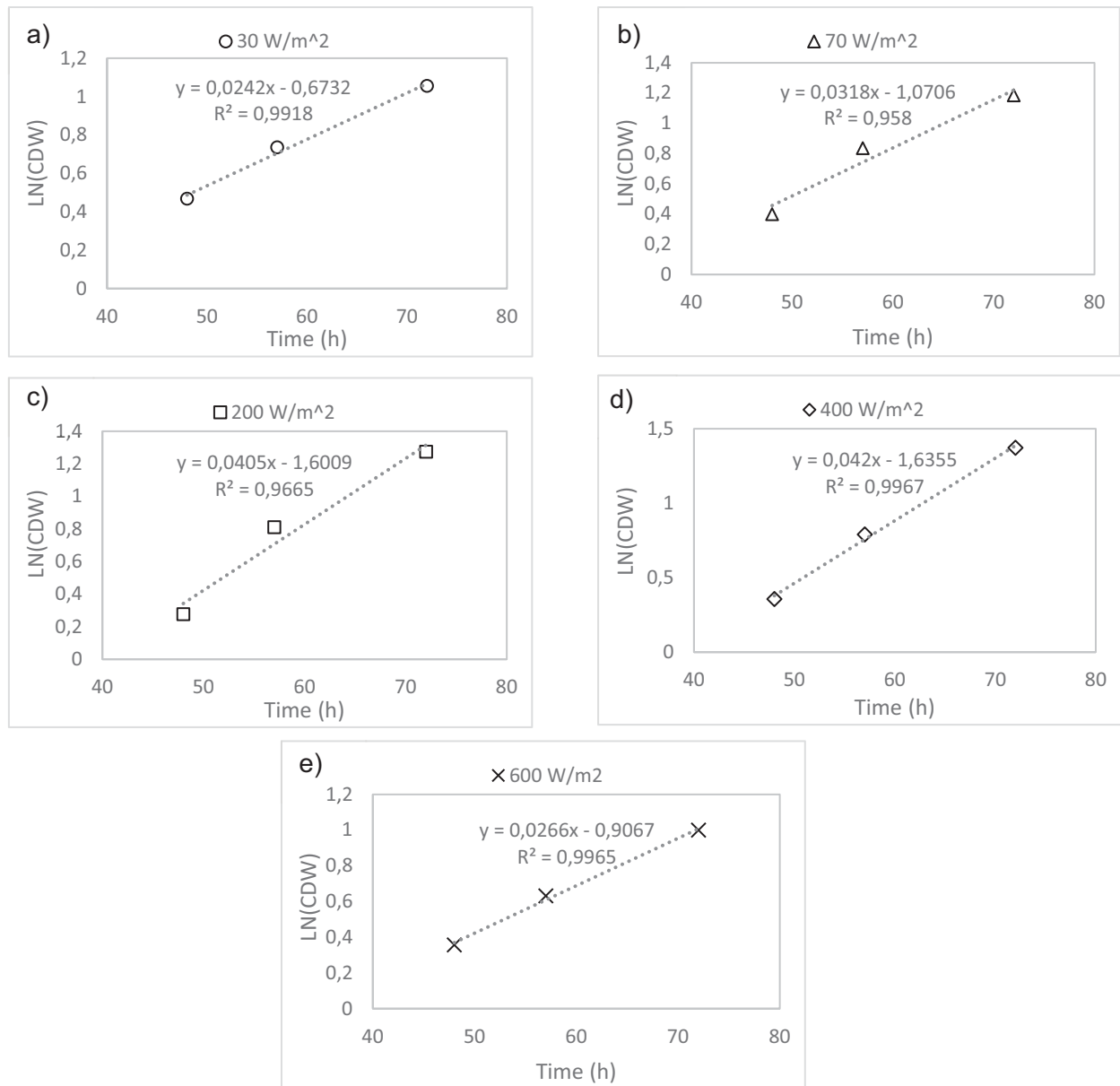


Figure 18: Natural logarithm of *R. palustris* CDW within the exponential phase with illumination provided by incandescent light bulbs (EUROLUX – 60 W or 100 W depending on the light intensity required) for varying light intensities, i.e. a) 30, b) 70, c) 200, d) 400 and e)  $600 \text{ W/m}^2$ . *R. palustris* was cultivated using modified Van Niels medium and filtered sterile with argon at varying light intensities. All experiments were completed at a constant temperature of  $35^\circ\text{C}$  and a volumetric flow rate of  $2 \text{ L/min}$ . Data points represent the mean of quadruple repeats.

Figure 19 provides the maximum specific growth rates achieved during the culturing of *R. palustris* at the five light intensities investigated. The general trend in Figure 19 is that the maximum specific growth rate increases from the minimum light intensity investigated ( $30 \text{ W/m}^2$ )

through 70 W/m<sup>2</sup> and 200 W/m<sup>2</sup> before reaching a maximum at 400 W/m<sup>2</sup>. After this the maximum specific growth rate decreases when the incident light intensity increases to 600 W/m<sup>2</sup>.

From Figure 19 a steep increase in the specific growth rate (+23.99%) when the incident light intensity more than doubles in intensity from 30 to 70 W/m<sup>2</sup> can be seen. The increase in maximum specific growth rate from 0.0242±0.0077 h<sup>-1</sup> at 30 W/m<sup>2</sup> to 0.0318±0.0034 h<sup>-1</sup> at 70 W/m<sup>2</sup> indicates that at these low light intensities *R. palustris* is photo-limited and therefore any increase in light intensity from 30 W/m<sup>2</sup> sees an increase in energy available for growth and division of the cell leading to an increase in the specific growth rate.

An increase in incident light intensity from 70 W/m<sup>2</sup> to 200 W/m<sup>2</sup>, which corresponds to a 185% increase in intensity, sees the maximum specific growth rate increase by 21.12% from 0.0318±0.0034 h<sup>-1</sup> to 0.0405±0.0095 h<sup>-1</sup>. This indicates that increase in the light intensity is beginning to have a reduced effect on the specific growth rate however the effect is still significant.

The next increase in incident light intensity sees a doubling in the light intensity (100% increase) from 200 W/m<sup>2</sup> to 400 W/m<sup>2</sup>. This change in light intensity causes a very slight increase in the maximum specific growth rate from 0.0405±0.0095 h<sup>-1</sup> to 0.0420±0.0139 h<sup>-1</sup> which corresponds to a mere 6.36% increase. The sudden reduction in the effect of increasing light intensity on the maximum specific growth rate indicates that *R. palustris* 11774 becomes photo-saturated in this reactor system at these incident light intensities. Photo-saturation of *R. palustris* means that the bacterium is converting the maximum possible amount of light to energy for growth and enzymatic activity.

The final increase in incident light intensity is from 400 W/m<sup>2</sup> to the maximum light intensity investigated, 600 W/m<sup>2</sup>. This is only a 50% increase in light intensity and was the maximum possible with this experimental setup. This change in light intensity causes a sudden decrease in the maximum specific growth rate from 0.0420±0.0139 h<sup>-1</sup> to 0.0226±0.00505 h<sup>-1</sup> which corresponds to a 37.88% decrease. The significant reduction in the maximum specific growth rate indicates that *R. palustris* 11774 becomes photoinhibited in this reactor system at this incident light intensity. Photoinhibition is likely brought upon by visible light the inhibition of the electron transport and/or possible damage to protein subunits.

The response of the growth metabolism of *R. palustris* to changing incident light intensity is similar to the response of the hydrogen production metabolism. As discussed in the literature, when the effect of light intensity on hydrogen production rate was investigated it was determined

that the hydrogen production increased as light intensity increased from 26 W/m<sup>2</sup> to 65 W/m<sup>2</sup> after which the hydrogen production rate saturated with increasing light intensity up to 285 W/m<sup>2</sup>. Thus, the results with regards to the effect of changing incident light intensity on the maximum specific growth rate align well with literature as similar a response was obtained. Saturation of the hydrogen metabolism was found to be at lower light intensities (65 W/m<sup>2</sup>) than the growth metabolism (200 W/m<sup>2</sup>) and this is due to the difference in bioreactor geometry. In the previous study a larger diameter bioreactor was used, and thus mutual shading would likely cause saturation to occur at lower light intensities. Photoinhibition has also been observed in the literature at around 500 W/m<sup>2</sup> with regards to the hydrogen production rate. This once again aligns well with the findings in this investigation that saw the maximum specific growth rate as well as the maximum CDW drastically decrease between 400 W/m<sup>2</sup> and 600 W/m<sup>2</sup>.

The impact of these results on the eventual culturing of *R. palustris* in outdoor photobioreactors with sunlight as the light source is discussed in more detail below with reference to Figure 20, and the light intensities experienced in the South Africa, more specifically Stellenbosch.

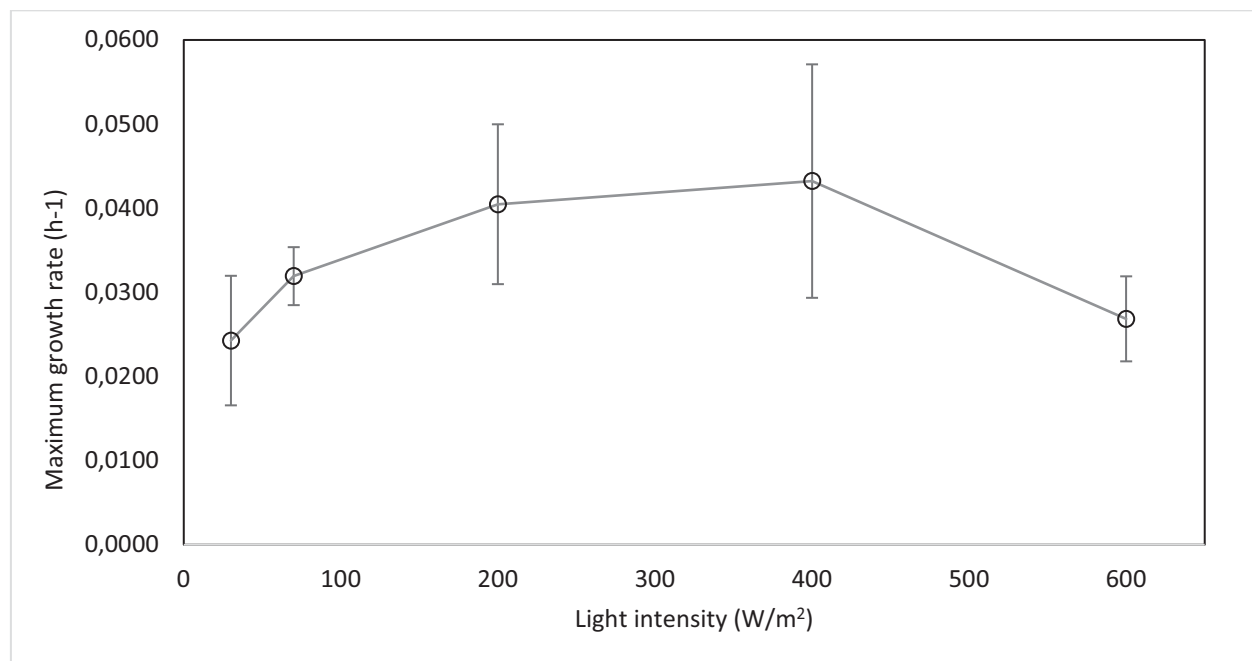


Figure 19: Maximum specific growth rate of *R. palustris* achieved with illumination provided by incandescent light bulbs (EUROLUX – 60 W or 100 W depending on the light intensity required) for varying light intensities, i.e. 30, 70, 200, 400 and 600 W/m<sup>2</sup>. *R. palustris* was cultivated using modified Van Niel's medium and filtered sterile with argon at varying light intensities. All experiments were completed at a constant temperature of 35°C and a volumetric flow rate of 2 L/min. Data points represent the mean of quadruple repeats. The error bars show the propagated uncertainty originally associated with the CDW measurements.

Table 2: Summary of Single Factor ANOVA on maximum specific growth rate at various light intensities

ANOVA						
<i>Source of Variation</i>	<i>SS</i>	<i>df</i>	<i>MS</i>	<i>F</i>	<i>P-value</i>	<i>F crit</i>
Between Groups	0,001013	4	0,000253	8,321858	0,001182	3,11225
Within Groups	0,000426	14	3,04E-05			
Total	0,00144	18				

Figure 20 below provides data obtained from an outdoor light meter that measures the intensity of direct sunlight over a full 24-hour period. The meter was placed on the roof of a four-story building located in Stellenbosch, South Africa in order to obtain intensities over the entire period with no possible interruptions from shading. Figure 20a provides the direct sunlight intensities in the wavelength range of 500 to 1000 nm over a 7-day period in the month of May (falling in autumn). In this seasonal period the average maximum light intensity is approximately 550 W/m<sup>2</sup>. This indicates that in these seasonal periods' good growth of *R. palustris* is likely to be the culture will only experience light intensities that may cause photoinhibition for a brief period with all other sun exposure times being within the range of 30 to 500 W/m<sup>2</sup>.

Figure 20b provides the direct sunlight intensities in the wavelength range of 500 to 1000 nm over a 26-day period in the month of July (falling in winter). In this seasonal period the average maximum light intensity is approximately 86 W/m<sup>2</sup>. This indicates that in this seasonal period, that is usually associated with overcast weather with limited direct sunlight, relatively good growth of *R. palustris* would still be possible although there would be photo-limitation such as that seen in the range of 30 to 70 W/m<sup>2</sup> in the above experiments. This is extremely positive as it would mean that outdoor culturing would not be limited by light intensity and culturing could be done all year round.

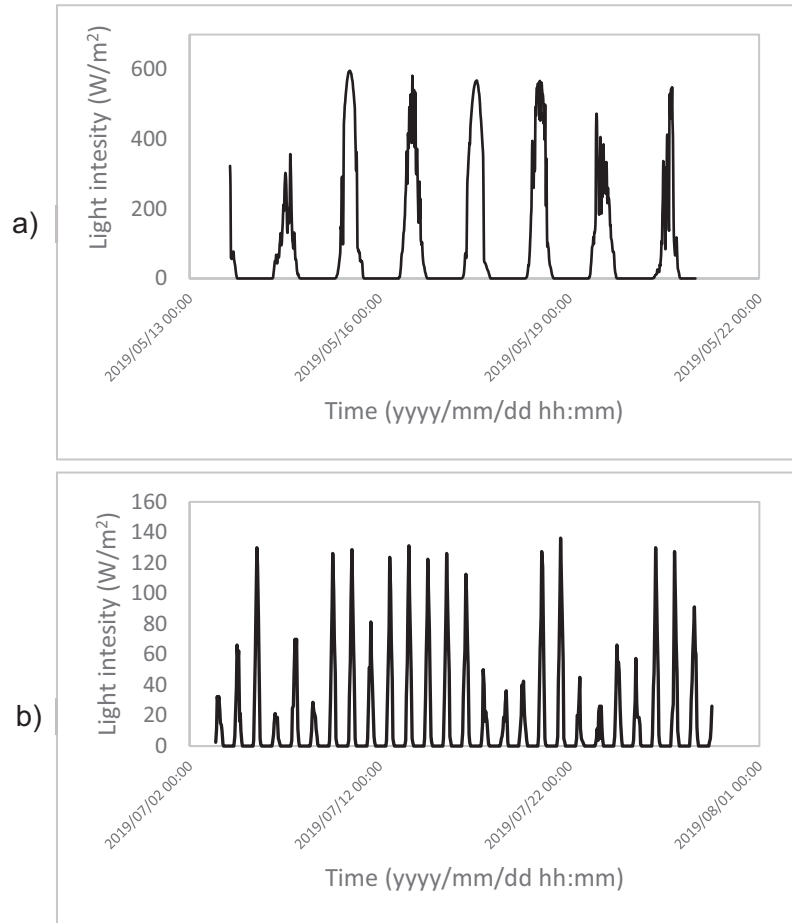


Figure 20: Light spectrum of the sun for full days (measurement every 10 minutes): a) light intensity over time during the month of May (autumn) and b) light intensity over time during the month of July (winter). Outdoor light meter placed on the roof of a story building at the Department of Process engineering in Stellenbosch.

Continuing from the above discussion a more detailed look into the profile of incident sunlight intensity over a single day was examined. Figure 21 provides the change in light intensity over a 24-hour time period for a day in May (•) and in July (▲). Superimposing these two graphs illustrates the drastic difference in the amplitude of the light intensity over a day with direct sunlight throughout versus a day with overcast conditions. The decrease in the duration of daylight between a day in May and July is also noticeable with a 3-hour reduction. This of course results in a reduction in the amount of photo-fermentation that is possible within a single day. With regards to the light intensity profile from the month of May, approximately four hours incident sunlight is above 500 W/m<sup>2</sup>. Thus, outdoor photobioreactors would experience photoinhibition during this period. This is however dependent on reactor size and whether or not high pulsing exposure of light will have the same effect as continuous high light intensity exposure.

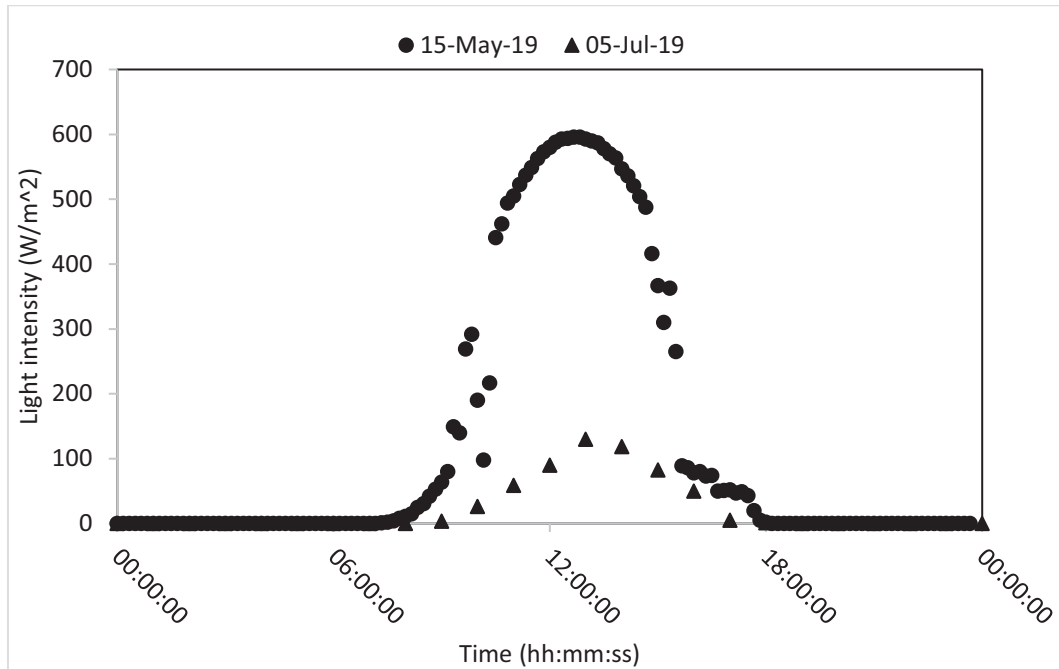


Figure 21: Light spectrum of the sun for full days (measurement every 10 minutes): a) light intensity over time during the month of May (autumn) and b) light intensity over time during the month of July (winter). Outdoor light meter placed on the roof of a story building at the Department of Process engineering in Stellenbosch.

### 3.1.5 Identification of wastewaters for treatment

#### 3.1.5.1 Wastewater sources

Availability, cost, carbohydrate content and biodegradability are the main conditions for the applicability of waste waters for treatment by photofermentative bio-hydrogen production processes. Photosynthetic hydrogen generating bacteria have been found appropriate for the purification of several organic waste streams, in the literature, however, the full picture of photofermentative wastewater treatment is unclear. Favoured substrates for the production of hydrogen include VFAs, or organic acids, easily biodegradable by these organisms. Other waste materials may not yet have been characterised in terms of photofermentative degradation, or hydrogen production. Nonetheless, some of the main waste waters which might be treated by photofermentation, and used for bio-hydrogen gas production, are discussed in this section (Kapdan and Kargi, 2006a).

Various photosynthetic and fermentative bacteria can make use of waste materials such as municipal solid wastes, industrial effluents and sewage sludge. Both batch experiments and continuous experiments have shown that organic acid containing aqueous streams acquired from such waste was a suitable substrate for the growth of photosynthetic bacteria. These cases are

often demonstrated using the photosynthetic bacteria *Rhodobacter sphaeroides* which shares many characteristics with *Rhodospseudomonas palustris* (Kapdan and Kargi, 2006).

This section will examine, in turn, various sources of wastewater, as identified in the wastewater survey. The relative merits of photofermentative treatment are then discussed, and finally a summary of the information is presented. The following section will present some industrially sourced wastewaters, and the results of phototermentation on these wastestreams.

#### **3.1.5.1.1 Industrial effluents rich in carbohydrates**

Industrial effluents which are non-toxic (to photofermentative bacteria), rich in carbohydrates and biodegradable such as the dairy industry, olive oil processing industry and winery industry wastewaters can be used as raw substrates for bio-hydrogen gas generation. The above mentioned industrial wastewaters may require pre-treatment steps and processes in order to remove unwanted, or inhibitory, constituents as well as to ensure an environment suitable for the used bacteria in terms of nutrition. Ideally, high concentration carbohydrate food industry wastewaters should be processed in order to convert the carbohydrate loading to organic acids. This can be accomplished (with value addition) in anaerobic digestors. The resulting organic acid rich digestate can then be converted to hydrogen gas by means of photofermentation (Kapdan and Kargi, 2006).

Photofermentative production of hydrogen has also shown to be feasible when utilizing distillery waste water as the substrate. Hydrogen generation from whey by photosynthetic bacteria such as *Rhodobacter capsulatus* and hydrogen production from starch based substrates has also been shown to be feasible (Das and Veziroglu, 2001).

#### **3.1.5.1.2 Paper mill wastewater**

The paper and pulp manufacturing industry is an extremely water intensive industry. In terms of clean water use and withdrawal, this industry is globally ranked third and is only behind the metals and chemical industries. Great quantities of wastewater are therefore generated by the paper and pulp industry and water usage lies between 75 m<sup>3</sup>/ton and 227 m<sup>3</sup>/ton of product (Oller et al., 2011).

The production of paper based products generate a great number of pollutants which are described by COD, BOD, suspended solids, toxicity and colour. The COD of paper and pulp industry wastewater can be as high as 11 000 mg/L (Oller et al., 2011; Pokhrel and Viraraghavan, 2004). The most toxic compounds are produced during the pulp bleaching stage where chlorine is used. In addition, numerous toxic compounds such as resin acids, diterpene alcohols,

unsaturated fatty acids, juvaniones and chlorinated resin acids are produced during the pulping process. However, the composition of the wastewater is largely dependent on the type of process, type of wood used, the technologies applied, management practices, internal recycling of the recovered effluent and the volumes of water used in the process (Oller et al., 2011).

Currently, effluent treatment methods consist of ozonation, Fenton's reagent application, adsorption and membrane technologies. These methods are efficient but often expensive. Despite individual treatment methods improving and cleaning the wastewater to some extent, none of them were able to produce treated effluents which meet the condition of a COD content less than 200 mg/L. Therefore, there is a requirement for alternative processes such as biological treatments which have the potential to degrade the recalcitrant compounds found in paper mill effluents (Pokhrel and Viraraghavan, 2004). There has been some work on the use of photofermentative organisms in paper mill wastewater treatment (Hay et al., 2016), however, the wastewater is often very recalcitrant, and further work is needed in this area.

#### **3.1.5.1.3 Olive mill wastewater**

The extraction of olive oils is an agricultural industry with economic importance to South Africa. Olive oil extraction produces great amounts of wastewater which are often released to natural waterways, or simply treated by ponding (Dellagreca et al., 2001), to the detriment of local ecosystems. Annual olive mill wastewater generated in the Mediterranean is estimated to be in excess of 30 000 000 m<sup>3</sup> with the COD content of this effluent as high as 220 000 mg/L (Manuel Brenes et al., 1999), and while South Africa's industry is significantly smaller, wastewaters produced by the local industry are also significant. The organic material in this wastewater largely consists of polysaccharides, sugars, polyphenols, polyalcohols, proteins, organic acids and oil (Mantzavinos and Kalogerakis, 2005).

The treatment of olive mill wastewater is complex and multifaceted with no single optimum solution immediately obvious. Presently, the use of advanced oxidation processes is only partially able to decrease the toxicity and enhance the biodegradability olive mill wastewater. The use of photofermentative organisms in the treatment of olive mill wastewater has gathered some interest in the research community, with several researchers showing water treatment and simultaneous hydrogen production (Dermeche et al., 2013; Pintucci et al., 2015, 2013).

#### **3.1.5.1.4 Winery and distillery wastewater**

Wineries and distilleries present a number of obstacles for their wastewater treatment. This industry produces wastewater highly rich in organics, the concentrations and composition of which is largely dependent on process operating conditions and production activities. The vast

majority of effluent, usually above 80%, is generated during production and generally lasts for 3 months per annum. The wastewater contains sugars, ethanol, organic acids, aldehydes, other microbial fermentation products as well soaps and detergents from clean-up operations. Usually, winery effluent has a low pH (3-4) owing to the production of organic acids during natural fermentation and it typically has relatively large quantities of phosphorous. However, the wastewater is deficient of nitrogen and other trace minerals which are essential for effective biological treatment systems (Oller et al., 2011).

The COD content of winery effluent is usually between 800 mg/L and 1200 mg/L, however, cases of CODs up to 25 000 mg/L have been reported. The COD content is mainly dependent on harvest load and processing activities. Biological treatment systems which have been investigated, for instance activated sludge reactors, are efficient in terms of BOD removal but require extended retention times (Petruccioli et al., 2000). Additionally, the capital and operating cost associated with this treatment method are not trivial. As a result, there is no generally accepted and standardized treatment method for winery wastewater (Oller, Malato and Sánchez-Pérez, 2011). Photofermentative treatment of these wastewaters has not yet been explored in the literature.

#### **3.1.5.1.5 Textile wastewater**

The textile industry is an extremely high consumer of both water and energy and is responsible for the release of many polluting compounds. Water consumption of these industries is often in the range of 80-100 m<sup>3</sup>/ton of finished textile is consumed (Savin and Butnaru, 2008). Throughout the textile dyeing and production process, water is used for cleaning the raw material and for many flushing steps. Many different dyes and chemicals are added to water used in textile production, which results in textile effluent having a chemical composition which poses many environmental, and treatment, challenges. Most pollutants are added during dyeing and finishing processes, where finishing incorporates bleaching, dyeing, printing and stiffening of textile products. Usual textile effluents can be characterised by a COD content between 150 mg/L and 12 000 mg/L, total suspended solids between 2900 mg/L and 3100 mg/L, total nitrogen between 70 mg/L and 80 mg/L and BOD between 80 mg/L and 6000 mg/L. This results in a BOD/COD ratio of approximately 0.25 which indicates high quantities of non-biodegradable organic material (Bisschops and Spanjers, 2003).

Textiles are given colour through the use of reactive azo dyes which account for approximately 70% of total dyes produced. Reactive azo dyes are used for their ease of application, high wet fastness profiles, their wide variety of colour shades and for minimal energy consumption. Approximately 20-50% of the initial reactive dyes are washed out in the dyeing process. This is

owing to the easy hydrolyzation of the dyes and their consequential low affinity for the textile fibres. Therefore, reactive azo dyes remain in the dye bath effluent and are discharged into municipal drainage systems. Effluents containing dyes pose a number of serious problems to both people and the environment. The effluent streams are aesthetically unpleasing and the split of azo bonds results in aromatic amines some of which are considered to be carcinogenic and mutagenic (Wang et al., 2007).

In terms of treating textile wastewater for decolourization and detoxification, many physiochemical methods have been tried and tested. These include advanced oxidation processes using the Fenton reagent, hydrogen peroxide or ozone as well as coagulation-flocculation, activated carbon adsorption, membrane filtration, ion exchange, irradiation, and electro-kinetic coagulation. However, these treatments are often not realistic or achievable due to their high operating costs and their production of a further undesired waste stream in the form of chemical sludge (Wang et al., 2007).

Conversely, it has been shown (Fu and Viraraghavan, 2001) that azo dyes can be biologically transformed. Initially, White-rot fungus (*Pleurotus spp.*) was identified as a promising organism able to degrade a vast variety of recalcitrant compounds by their extracellular enzyme system. However, it has proven challenging to keep the fungus functional in activated sludge systems owing to the unique nutrients and environmental conditions which are required for fungal growth. Further, it has also been shown (Kocyigit and Ugurlu, 2015) that azo dyes can be decolourized by azo reductase under anaerobic conditions which results in the formation of aromatic amines. These aromatic amines can be further biodegraded through hydroxylation and ring-opening (Wang et al., 2007).

Decolourization and mineralization of textile wastewater through a biological process is understood to be an encouraging technology since it is not costly and poses no harm to the environment. Bacteria related to this azo dye bio-decolourization process include the photosynthetic bacteria *R. palustris*. However, a strain may be required with a high decolourization capability (Wang et al., 2007). Nonetheless, decolourization efficiencies greater than 80% have been achieved using *R. palustris* as a treatment organism.

#### **3.1.5.1.6 Other wastewaters**

Owing to the wide range of polluted industrial wastewaters which are released into the environment, there are some common industrial wastewaters which have barely been investigated in terms of biological treatment methods. An example of such an industry is the leather industry which produces large volumes of highly complex and highly contaminated

wastewater. Many water intensive processing stages are involved in transforming raw hides into leather products. Effluents discharged from tanneries contain high concentrations of organic material as well as chemicals such as chlorides, bactericides, emulsifiers, ammonia and detergents. Based on their composition, tannery wastewater cannot be discharged into the environment without pre-treatment due to their toxicity. The nature of tannery wastewater is such that the effluent still exceeds the discharge limits in terms of COD, salinity, ammonia and surfactants once conventional treatment methods have been employed (chromium precipitation, primary sedimentation, biological oxidation and secondary sedimentation).

Currently, biological systems are the favoured treatment strategy for tannery wastewaters with advanced oxidation processes considered as a post-treatment step (Oller et al., 2011).

#### **3.1.5.1.7 Summary**

Table 1 provides a summary of the wastewater components found in the effluents from various industries and evaluates the photo-fermentative treatment potential and the hydrogen production potential.

Table 3: Summary of some industrial wastewaters of interest, indicating important wastewater components, a green-orange-red (good, intermediate, bad) assessment of the potential for treatment of each wastewater by photofermentative methods, and whether hydrogen production from each wastewater is likely possible.

Industry	Wastewater components	Photo-fermentative treatment potential	Hydrogen production potential
Malt brewing	Organic material Sugars Carbohydrates Starches Proteins Enzymes Aromatic compounds Alcohol	Good  All components have individually been shown to be degradable by <i>R. palustris</i>	Good  Most components would likely result in hydrogen production. Comparatively little nitrogen in WW
Metal finishing	Immiscible organics, soluble organics, acids and alkalis, metals, complexing agents, nitrogenous materials, cyanides, fluorides, sulphide, phosphate compounds and salts	Bad  Several compounds which would likely hinder microbial growth	Bad  Non-growing cells cannot produce hydrogen
Soft drink	Wasted soft drink Sugar Syrup Wash water Caustic/detergents and machine lubricant Nitrates Phosphates Sodium Potassium	Good  Most components have individually been shown to be degradable by <i>R. palustris</i>	Medium  Nitrogen in the wastewater might hinder hydrogen production
Sorghum beer	Organic material Sugars Carbohydrates Starches Proteins Enzymes	Good  Most components have individually been shown to be degradable by <i>R. palustris</i>	Good  Most components would likely result in hydrogen production. Comparatively little nitrogen in WW

Edible oil	Free fatty acids, residual gums, aromatics, pesticides, residual soaps, emulsifying agents, metal catalysts and sulphuric acid	Good Most components have individually been shown to be degradable by <i>R. palustris</i>	Good Most components would likely result in hydrogen production. Comparatively little nitrogen in WW
Red meat abattoir	Organic matter (excretion) Blood (COD: 400 000 mg/L) Fat	Good Most components have individually been shown to be degradable by <i>R. palustris</i>	Medium Nitrogen in the wastewater might hinder hydrogen production
Laundry	Heavy metals, organic solvents, bleaches, alkalis/builders, antichlors, softeners, sours, starches, detergents, phosphates, salts, soil, nitrogen, ammonia, surfactants, boron, sodium, fats, oils and grease	Medium some components have individually been shown to be degradable by <i>R. palustris</i> , however, several components might prevent microbial growth	Medium Nitrogen in the wastewater might hinder hydrogen production
Tanning and leather finishing	Sulphates, sulphides, chlorides, chromium, acid salts, salts, organic waste, inorganics, ammonium ions, dyestuffs, organic solvents and heavy metals	Medium several components might prevent microbial growth	Medium several components might prevent microbial hydrogen production
Paper and pulp	Lignin organic components from wood chlorine dioxide caustic soda hydrogen peroxide	Medium several components might prevent microbial growth	Good If growth is seen, there are few nitrogen compounds which would hinder hydrogen production
Iron and steel	Heavy metals Hydrocarbons Cyanide compounds Nitrogen compounds Oil/grease	Bad Several compounds which would likely hinder microbial growth	Bad

Cane sugar processing	Inorganics Sugars Sugar metabolites Phosphates	Good Most components have individually been shown to be degradable by <i>R. palustris</i>	Good Most components would likely result in hydrogen production. Comparatively little nitrogen in WW
Textile	Acids, alkalis, bleach, dyes, salts, surfactants, stabilisers, starch, reactive dyes, vat dyes, sulphur dyes, direct dyes, disperse dyes, chromium, copper, zinc, lead and nickel	Medium several components might prevent microbial growth	Medium While some components might prevent microbial growth, there are several which could be photofermented to hydrogen
Poultry	High BOD Salts Nutrients Bacterial contamination	Good Most components have individually been shown to be degradable by <i>R. palustris</i>	Bad Significant amounts of nitrogen would likely prevent hydrogen production

### 3.1.5.2 Industry partners

The industrial wastewater effluents which have been collected for this research are described in this section. The information has been anonymised to preserve our industry contacts' anonymity.

#### 3.1.5.2.1 Olive mill wastewater

Olive mill wastewater was kindly supplied by an olive oil producing farm near Paarl, South Africa. Two fresh 5 L samples were obtained and rapidly frozen in a deep freezer, to store. The first sample consisted of olive processing water from a separation process whereby olive oil is separated from solid material whereas the second sample comprised of the overall wastewater from the plant, including water containing cleaning agents and so forth. The farm estimates that they discharge 1500 L/day of wastewater into the ground. They also have no current wastewater treatment methods and are not monitored.

#### 3.1.5.2.2 Textile dye wastewater

Textile dye wastewater was kindly supplied by a large dyers located in Cape Town. One fresh 5 L sample was obtained and rapidly frozen in a deep freezer. The sample consisted of three dye types. These include Yellow 3RS, Red 3B5 and Navy. The dyers estimate that they discharge

1100 kL/month of wastewater into municipal sewers. They rely on dilution from other process wastewater streams in order to get their solvent, chloride and chemical oxygen demand (COD) levels into an acceptable range. These levels are monitored by the city council.

#### **3.1.5.2.3 Fruit processing wastewater**

Fruit processing wastewater was kindly supplied by a large fruit juice supplier in the Western Cape. Three fresh 5 L samples were obtained and rapidly frozen in a deep freezer. The first sample consisted of the overall process wastewater consisting of organic material as well as cleaning agents such as caustic. The second sample comprised of pure retentate from a separation process which separates clear fruit juice from solid material. It is estimated that this stream has a COD of approximately 80 000 mg/L. The third sample was taken from an anaerobic digester which was fed with apples (10 ton/day), retentate, pomace and cow manure (1 ton/day). It is estimated that this stream has a high loading of organic acids. The company estimate that they discharge 30 000 L/day of retentate and between 50 000 L/day and 60 000 L/day of digestate. Their current wastewater treatment method is that of the anaerobic digester which biodegrades their waste and provides them with methane gas for energy recovery purposes.

#### **3.1.5.2.4 Paper and pulp mill wastewater**

Paper and pulp mill wastewater was kindly supplied by a South African paper making company. Two fresh 5 L samples were obtained and rapidly frozen in a deep freezer. The first sample consisted of entering clarifier effluent whereas the second sample consisted of paper machine effluent.

#### **3.1.5.2.5 Winery wastewater**

Winery wastewater was kindly supplied by a large wine maker, in the Western Cape. Two fresh 5 L samples were obtained and rapidly frozen in a deep freezer. The first sample consisted of winery processing water before any treatment methods were employed. It is estimated that the COD of this water is approximately 12 000 mg/L. The second sample comprised of winery wastewater after the treatment step which takes the form of a settling tank. It is estimated that the COD of the water after the settling tank is approximately 4000 mg/L. The company estimate that they use approximately 12 000 000 L/month of water of which 70% ends up as wastewater. The COD content of their wastewater is monitored by the municipality.

#### **3.1.5.2.6 Fish processing wastewater**

Fish processing wastewater was kindly supplied by a large fishing company based in Cape Town. Two fresh 5 L samples were obtained and rapidly frozen in a deep freezer. The first sample consisted of fish processing wastewater. It is expected that this water has high protein and

organic content. The second sample comprised of ice melt wastewater. It is expected that this wastewater will have minimal to no organic content and have a high concentration of salt. The company estimate that they discharge 900 kL/day of wastewater.

#### **3.1.5.2.7 Tannery wastewater**

Tannery wastewater was kindly supplied by a leather-works in the Western Cape. One fresh 5 L sample was obtained and rapidly frozen in a deep freezer. The sample consisted of the overall tannery processing water from the plant, including water containing cleaning agents, etc. The company estimate that the COD of this wastewater lies between 3000 mg/L and 6000 mg/L depending on process operating conditions. They discharge their wastewater into a dam located near the plant and have no current wastewater treatment methods. The COD content of their wastewater is monitored by the municipality.

#### **3.1.5.2.8 Sugar processing wastewater**

Sugar processing wastewater was kindly supplied by a sugar refinery from KwaZulu-Natal. A fresh 10 L sample was obtained and rapidly frozen in a deep freezer. The sample consisted of vinasse, a waste product generated through the fermentation of sugar processing waste to ethanol.

#### **3.1.5.2.9 Brewing wastewater**

Brewing wastewater was directly supplied by a large brewer in the Western Cape. A fresh 5 L sample was obtained and rapidly frozen in a deep freezer. The sample consisted of liquid pressed from spent brewing grains.

#### **3.1.5.3 Wastewater summary**

Table 4 shows the specific wastewater stream selected from each industry for experimental use. The Industry partners are also listed.

Table 4: Specific waste streams used in experimentation

<b>Industry</b>	<b>Specific waste stream</b>
Textile dye	Dye wastewater containing Yellow 3RS, Red 3B5 and Navy.
Winery	Winery processing water.
Fruit processing	Anaerobic digester (AD) effluent. AD fed with apples, pomace and cow manure.
Olive processing	Overall process wastewater.
Fish processing	Fish processing wastewater.
Tannery	Overall tannery process wastewater.
Sugar processing	Vinasse
Brewing	Liquid pressing from spent brewing grains.
Paper and pulp	Effluent from paper machine

### **3.1.6 Growth of *R. palustris* on wastewaters**

Experimental runs have been conducted on the first six wastewater streams listed in Table 4. These results are shown in Figure 22 and Figure 23. Each data point represents the average of 3 biological repeats.

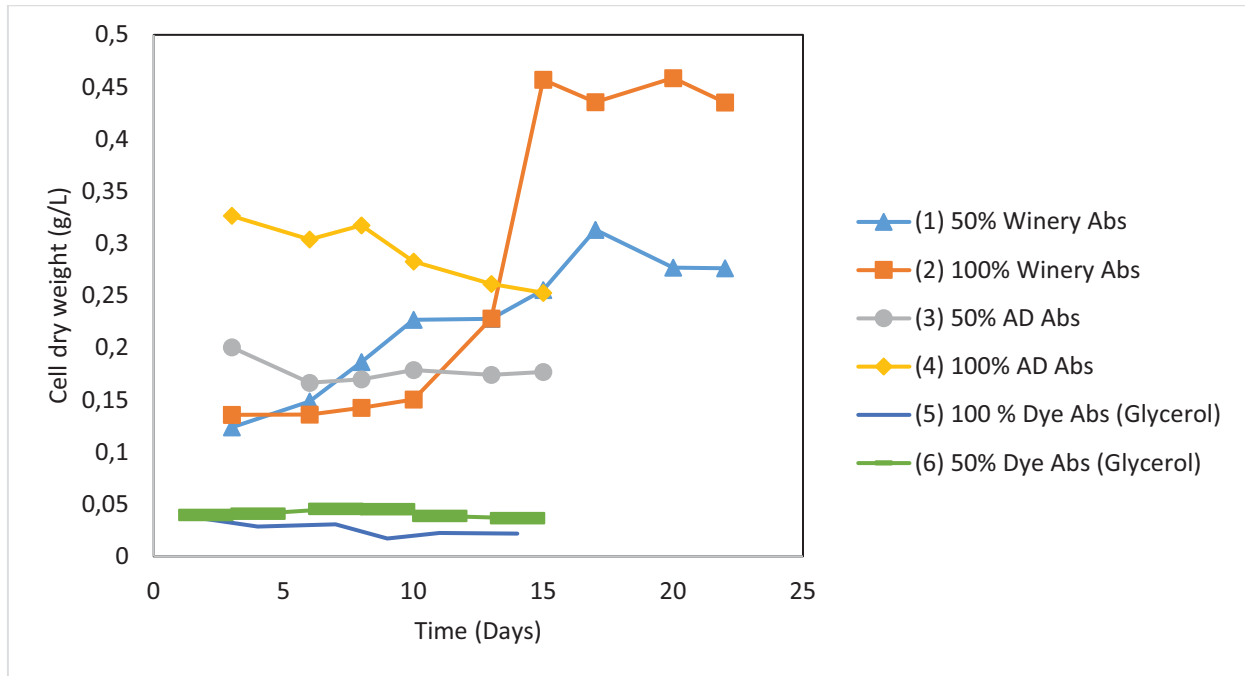


Figure 22: Growth of *R. palustris* on various wastewaters, either at 50% dilution with growth medium, or at 100% strength. ( $\square$  and  $\Delta$ ) indicate wine-making wastewater, ( $\diamond$  and  $\circ$ ) indicate anaerobic digestate, (-) indicates dye wastewater.

As can be seen from Figure 22, growth on winery wastewater resulted in a significant increase in biomass concentration over the test period. This likely corresponds to the availability of both nitrogen and carbon sources in this wastewater. The analyses to determine the carbon and nitrogen concentrations of these streams are underway, and will illuminate the reasons for the significant growth on winery wastewater, and insignificant growth on the other streams. Figure 23 similarly shows that significant growth was seen on tannery wastewater.

What is surprising, however, is that limited growth was seen on anaerobic digester effluent. It would be expected that *R. palustris* would grow exceptionally well on this substrate, since it contains significant amounts of both nitrogen, in the form of ammonia, and volatile fatty acids, both of which are preferred substrates for this organism. It might be the case that there is a contaminating compound, which *R. palustris* finds toxic, in this stream, however, further investigation is needed to conclude this. Another source of AD effluent is being sought to confirm whether this is a general effect, or one specific to this wastewater source.

While no growth was observed on dye wastewater, initial COD measurements indicate that that the biomass that is there is consuming the contaminating components within the wastewater, indicating there may be a potential stationary phase-biomass process which could treat this wastewater.

Some growth was noted on tannery wastewater, however, the results are somewhat inconclusive; the method currently being used to determine biomass concentration (optical density) has been found to not be sufficiently reliable when using these wastewaters. This unreliability can be attributed to solid particles found in the wastes, interfering with the assay, as well as colour changes which can occur during treatment which might further effect the results.

To overcome this, a method for pigment extraction, and biomass determination through that, is being developed, which may circumvent these issues.

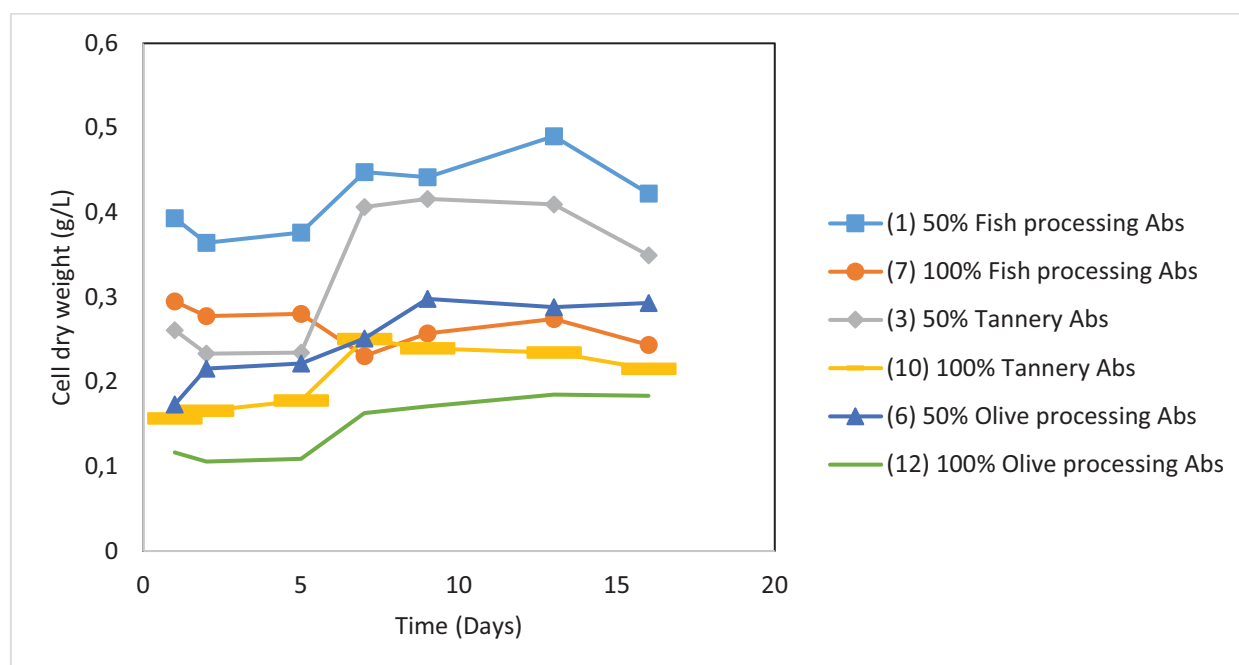


Figure 22: Growth of *R. palustris* on various wastewaters, either at 50% dilution with growth medium, or at 100% strength. ( $\square$  and  $\circ$ ) indicate fish processing wastewater, ( $\diamond$  and  $-$ ) indicate tannery wastewater, ( $\Delta$  and line) indicate olive mill wastewater.

### 3.1.7 H<sub>2</sub> production from wastewaters

Of the media tested, only cultures containing glycerol, or xylose (as a synthetic wastewater from woody biomass treatment) showed significant hydrogen production. This result is not entirely unexpected – in the presence of ammonia or other nitrogen sources, the nitrogenase enzyme (responsible for hydrogen production) is downregulated. Many of the wastewaters tested contain significant quantities of nitrogenous compounds, and so hydrogen production, especially at the start of the culture, is unlikely.

We had hoped that the nitrogen would quickly be consumed, and any remaining COD be converted into hydrogen, but it appears that the nitrogen requirement for the organism is

comparatively low, and so the nitrogen concentration does not drop sufficiently low in the wastewaters we have tested to date.

In collaboration with Prof. Chris Howe, at the University of Cambridge, we hope to repeat these experiments using a strain of *R. palustris* that continues to produce hydrogen even when nitrogen is present. This will improve the process significantly.

Table 5: Summary of experimentation on wastewaters, indicating whether (Green-orange-red) scale growth of *R. palustris* occurred on the WW, whether WW treatment (as characterized by COD decrease) occurred, and whether hydrogen was produced from the WW.

Waste water	Winery	AD Effluent	Dye	Fish processing	Tannery	Olive processing	Glycerol
Growth	Yes	No	No	Yes	Yes	No	Yes
COD decrease	Yes	Medium	Medium	Yes	Yes	No	Yes
H <sub>2</sub> production	TBC	TBC	No	TBC	TBC	No	Yes

## 3.2 Thermosiphon reactor development and fabrication

### 3.2.1 Thermosiphon reactor development

Since both photobioreactors (PBRs) and thermosiphon solar water heaters (SWH) have certain advantages and limitations, and mindful of the unavailability of literature on such a thermosiphon photobioreactor design, the approach utilized in this thesis was to separately examine the existing designs considerations for operational PBRs and SWH systems with the main aim of combining the unique features of these two designs into an integrated design consideration for the novel thermosiphon PBR. The following criteria were outlined to build a high-performance thermosiphon PBR for the purpose of cultivating photosynthetic bacteria:

1. The laboratory scale thermosiphon PBR should have possibility of being autoclaved, which limits the working volume of the prototype to about 1 L (Skjånes et al., 2016; Tamburic et al., 2011).
2. The thermosiphon PBR should have appropriate ports allowing for regular culture sample extraction for the measurement of important parameters during experiments (Skjånes et al., 2016).

3. The thermosiphon PBR should minimize biofilm formation by having smooth internal surfaces and limited bends to increase cleanability (Wang et al., 2012).
4. The thermosiphon PBR should have an optimal surface to volume ratio and light path as features which have been well explored in vertical tubular photobioreactors (Akkerman et al., 2002; Kunjapur and Eldridge, 2010; Skjånes et al., 2016; Tamburic et al., 2011; Wheaton and Krishnamoorthy, 2012).
5. The thermosiphon PBR should have the possibility of insertion of multiple sensors and electrodes for logging and control of multiple culture parameters (Skjånes et al., 2016; Tamburic et al., 2011).
6. The system should be as hydrogen impermeable as possible, by ensuring the use of minimal hydrogen gas penetration materials when in contact with the culturing system and connection joints (Akkerman et al., 2002; Skjånes et al., 2016; Tamburic et al., 2011).
7. All materials used for used for construction and mounting of the experimental setup were assessed for criteria such as availability on the market, transparency whenever needed, weight, resistance to oxidation and corrosion, durability and heat resistance (Skjånes et al., 2016; Tamburic et al., 2011; Wang et al., 2012).
8. The materials should be robust enough to tolerate the intensive use by avoiding tension in breakable materials such as glass caused by contact between these materials and harder materials such as metals (Skjånes et al., 2016; Wang et al., 2012).
9. The thermosiphon PBR should have a simple, low cost solution for temperature control, in the laboratory prototype a cooling water circuit (Skjånes et al., 2016; Wang et al., 2012).

### **3.2.1.1 Thermosiphon testing**

#### **3.2.1.1.1 Experimental setup and procedure**

The experimental setup used for this study was a modification of the original TPBR (Cho and Pott, 2019) to accommodate a hydrogen collection unit as seen in Figure 24. Hence, detail description of the various units except the hydrogen collection unit can be understood by referring to (Cho and Pott, 2019). The hydrogen collection unit comprised of an inverted measuring cylinder filled with demineralized water. The generated gases from the TPBR pass through a hydrogen impermeable tygon tube and displaced the demineralized water in the inverted measuring cylinder. This displacement represents the volume of hydrogen produced since the hydrogen is assumed to be insoluble in water. On the other hand, biomass concentration in the TPBR was monitored with UV-VIS spectrophotometer measurement of the optical density at 660 nm (Cho and Pott, 2019). Demineralized water was used to blank the spectrophotometer reading to zero and an OD of 1.0 corresponded to a dry cell weight (DCW) of 0.7074 g/L.

### 3.2.1.1.2 Organism, strains and medium

*Rhodospseudomonas palustris* strain NCIMB 11774 was the photosynthetic bacteria strain selected for biohydrogen production in this study. It was grown in a synthetic medium containing: Glycerol (50 mM), Na- glutamate (10 mM), yeast extract (0.73 M),  $K_2HPO_4$  (0.98 M),  $KH_2PO_4$  (1.3 M),  $Na_2S_2O_3 \cdot 5H_2O$  (1 M), PABA (15 mM),  $MgSO_4 \cdot 7H_2O$  (0.81 M),  $CaCl_2 \cdot 2H_2O$  (0.34 M),  $NaCl$  (6.8 M),  $FeC_6H_5O_7$  (20 mM),  $ZnCl$  (0.51 mM),  $MnCl_2 \cdot 4H_2O$  (0.51 mM),  $H_3BO_3$  (0.97 mM),  $CoCl_2 \cdot 6H_2O$  (0.84 mM),  $CuSO_4 \cdot 2H_2O$  (0.12 mM),  $NiCl_2 \cdot 6H_2O$  (84 $\mu$ M),  $Na_2MoO_4 \cdot 2H_2O$  (0.17 mM), Vitamin B12 (0.73 $\mu$ M), Thiamine (0.45 mM) and  $H_2O$  (0.98 mL) with the pH at about 7.3. The media was kept sterile by autoclaving at 120°C for 15 mins, except for the vitamins, which were filter sterilized and added after autoclaving. Bacterial colonies cultured on agar were picked and resuspended into an airtight 1 L Schott bottle containing the growth medium, and placed into an incubator set at 35°C with about 2500 lux external illumination from a 100 W tungsten lamp. The bacterial inoculum was allowed to grow for 5 days until it reached mid-logarithmic phase with an optical density at 660 nm of around 1.0, and then used as starter cultures for photofermentation in the TPBR.



Figure 24: Photograph of the TPBR during biological hydrogen production with the annotated number (1-6) corresponding to water chiller, reservoir, halogen light panel, sample port, water flowmeter and hydrogen collection unit respectively.

### 3.2.2 Prototype photobioreactor operation

Photosynthesis still remains the only way to directly convert biomass as energy source from solar radiation and carbon dioxide (Janssen et al., 2003). This phenomena has been continuously exploited in specialize systems called photobioreactors (PBRs) since the 1940s (Zhang et al., 2017). As a result, this biotechnology process has been widely reviewed for their application in renewable energy production, bioremediation and commercial viable products (Alagesan et al., 2013). The global environmental problems such as i) environmental degradation, ii) resource depletion, and iii) energy shortage resulting from the large scale utilization of fossil fuels as energy sources to meet up with the world's energy demand (circa 80%) has further entice the significant biotechnological advancement of these PBR technologies (Gosse et al., 2007; Zhang et al., 2017). However, more engineering still needs to be done in developing efficient PBR which are scalable, required low energy input and utilize maximum sunlight for the large scale production of photosynthetic microorganisms.

Contrary to open systems and lab scale closed PBRs, enclosed outdoor PBRs have demonstrated potentials of exploiting natural sunlight to attain high biomass productivity for several photosynthetic microorganisms such as i) microalgae, ii) cyanobacteria and ii) photosynthetic bacteria (Janssen et al., 2003). Nevertheless, their operational, maintenance and production costs are still being impacted by the high energy consumption associated with mechanical and/or pneumatic pumps employed for agitation and/or aeration (Acien Fernández et al., 2013). Therefore, there is high need to address this bottleneck and making the process more economical viable for large scale production.

The TPBR discussed in this report achieves natural fluid circulation due to the temperature-induced density difference resulting from microbial light absorption (Anye Cho and Pott, 2018). There is a good agreement between the CFD model and experiments plus a satisfactory passive fluid flow capable of maintaining 88% of bacterial cells in free suspension when the TPBR was operated at a biomass concentration of 0.5 g/L. However, these achieved these results via the use of artificial light (four 150 W halogen lamps) and water cooling (submersible water pump and chiller) which amounted to increased electrical energy consumption even though it was quantified in their work. Therefore, the ground work has been laid by proving the concept but there are enormous opportunities to minimize this electrical energy consumption by extending the technology to outdoor operating conditions.

In order to more fully understand the functioning of the novel TPBR a prototype thermosiphon bioreactor was designed, fabricated and tested as part of the photobioreactor modelling section.

On the basis of this work, a larger, 10 litre, TPBR is currently being fabricated for testing. The 10 litre reactor will make use of cooling fins to provide a cooling driving force, rather than the cooling water jacketed as employed by the prototype model.

The sun being a renewable energy which is abundantly available will eliminate the artificial lighting cost on the illuminated area the outdoor TPBR. Since the cooling section of the TPBR is controlled by equation (14) whereby the rate of heat dissipation ( $q$ ) and the magnitude of the temperature difference ( $\Delta T$ ) are governed by the product of the heat transfer coefficient and area ( $hA$ ) (Anye Cho and Pott, 2018; Kraus and Bar-Cohen, 1995). Therefore, to attain high heat dissipation at low excess temperature, one requires either a TPBR cooling section of substantial surface area ( $A$ ) for the dissipation or a coolant possessing a superior heat-transfer property ( $h$ ) (Kraus and Bar-Cohen, 1995).

$$q = hA\Delta T \quad (14)$$

However, achieving this increased heat dissipation via coolants of superior heat-transfer properties are either expensive or not easily achievable meanwhile augmenting the cooling surface via extended surfaces such as fins present a considerable more efficient method for obtaining this increased dissipation (Kraus and Bar-Cohen, 1995).

The exploitation of fins with various shapes (longitudinal fins, spine fins, radial fins, etc.) and materials (copper, aluminium, stainless steel, alloys, etc.) for air cooling has been widely reported in literature (Kraus and Bar-Cohen, 1995; Marcinichen et al., 2014; Wu et al., 2011). Aiming to save electricity of a data cooling centre via cold energy storage, the authors (Wu et al., 2011) used aluminium flat plate (transverse square) fins in a stainless steel tube thermosiphon located at the top condenser section of thermosiphon heat pipe systems for ambient cooling. This system was able to maintain the maximum cold water storage temperature of 25°C in the tank from the 65°C which was ejected by the CPU surface. The fin arrays presented by the authors (Wu et al., 2011) seems applicable for the TPBR with a slight modification of the material composition by making use of only aluminium. This is avoid any microbial culture contamination related issues since as aluminium has already been widely implemented in the internal design of baffles, impellers, and heating coils of bioreactors.

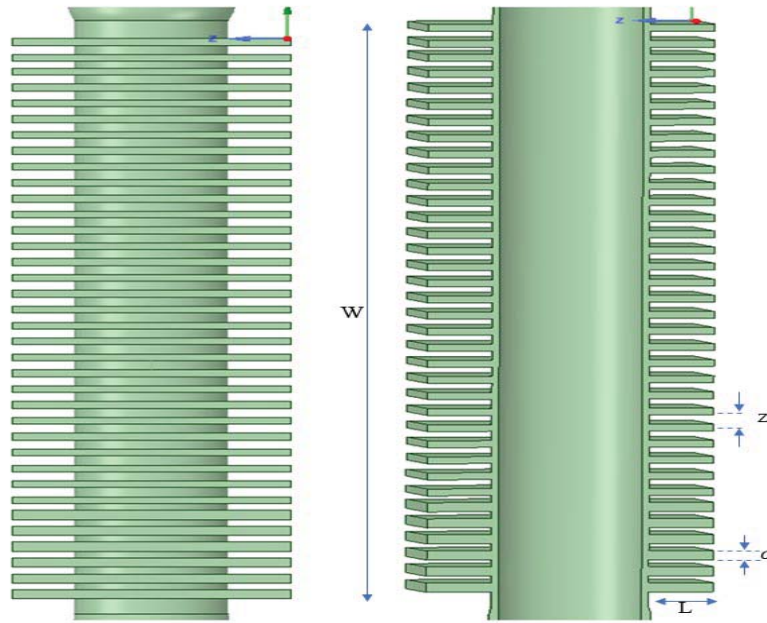


Figure 25: Schematic diagram of the flat plate fin design used for the outdoor TPBR showing the fin spacing  $z$ , fin thickness  $\sigma$ , fin height  $L$ , and fin base length  $W$ .

Nevertheless, the number fins  $n$ , fin spacing  $z$ , fin thickness  $\sigma$ , and fin height  $L$ , as illustrated in Figure 25 will be dependent on the TPBR's operating temperature which is a function of the useful heat gain from the absorb solar radiation and the ambient air temperature. Using the Global Horizontal Irradiation (GHI) of Stellenbosch University (33°55'42.84" S, 18°51'55.08" E, Elevation: 119 m) from the Stellenbosch Weather (see <http://weather.sun.ac.za/>), the TPBR's collector area  $A_c$  and efficiency  $\eta$ , the useful heart gain can be calculated with equation (15).

$$Q_u = \eta \times (GHI \times A_c) \quad (15)$$

Also, the optimum fin spacing  $z_{opt}$  can be calculated from the correlation in equation (16) according to (Kraus and Bar-Cohen, 1995)

$$z_{opt} = 2.714 \times P \quad (16)$$

Where  $P$  is plate-air parameter which is evaluated with equation (17) using the thermal properties of air at the average temperature between the flat plate fin and the surrounding.

$$P = \left[ \frac{\mu K_{fl} L}{c_p \rho^2 g \beta \Delta T} \right]^{\frac{1}{4}} \quad (17)$$

As well, the centerline spacing of the fins  $z_c$ , would be gotten from equation (18), thereby allowing for the number of fins  $n$ , to be calculated with equation (19),

$$z_c = z_{opt} + \sigma \quad (18)$$

Whereby  $n$  spaces for  $n$  should give an integer

$$n = \frac{W}{z_{opt} + \sigma} \quad (19)$$

Figure 28 shows the proposed design of the outdoor TPBR which will be constructed from Plexiglas and aluminium heat sink, mounted on a steel frame which will be inclined to 45° for maximum capture of solar energy at the roof top of Annex building, Department of Process Engineering, Stellenbosch University. Once installed, preliminary heat transfer and passive fluid analysis will be executed to establish the operating conditions for the cultivation of photosynthetic bacteria. This will be followed by the proper cultivation of the photosynthetic bacteria under outdoor conditions.

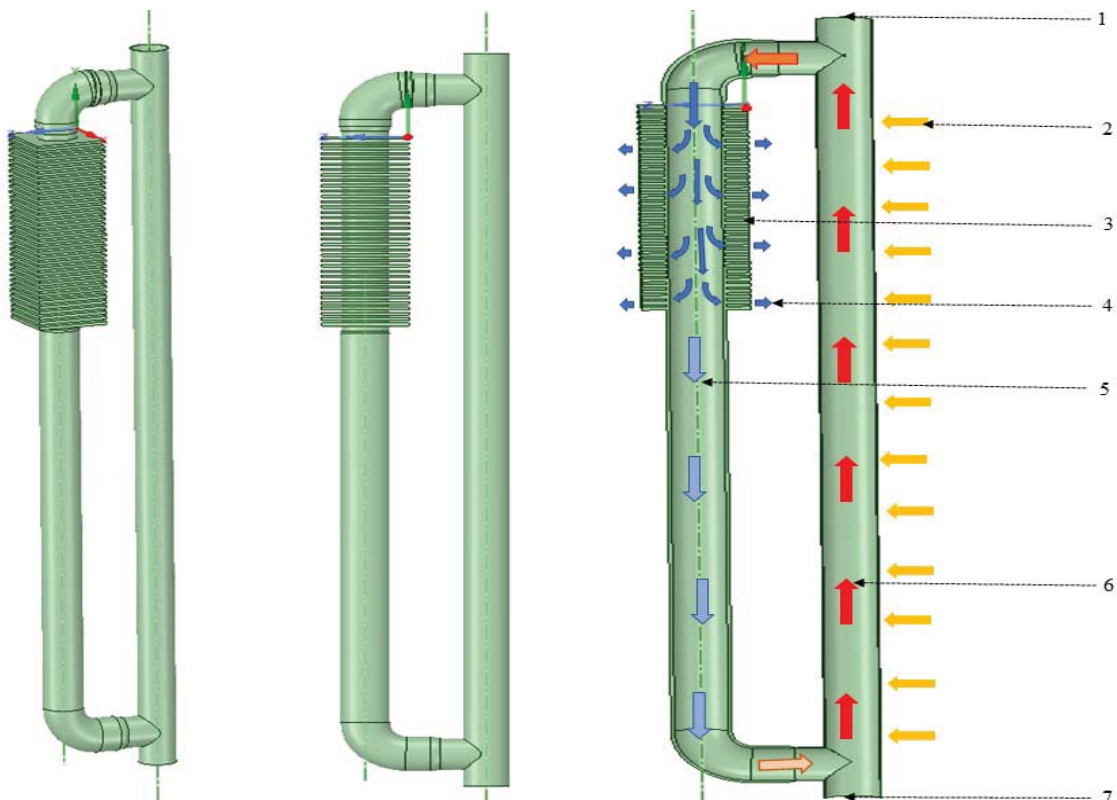


Figure 26: Schematic diagram of the outdoor TPBR showing 1) sampling port, 2) solar radiation, 3) flat plate fin, 4) ambient air cooling, 5) fluid of heavier density falling down, 6) fluid of lighter density rise up, and 6) sparging port.

### 3.2.3 Thermosiphon PBR geometry

The thermosiphon PBR geometry was developed from a structural adaptation of the original thermosiphon loop used by Close (1962), to meet the system's performance of a photobioreactor. This process was captured in the geometrical advancement as shown in Figure 27.

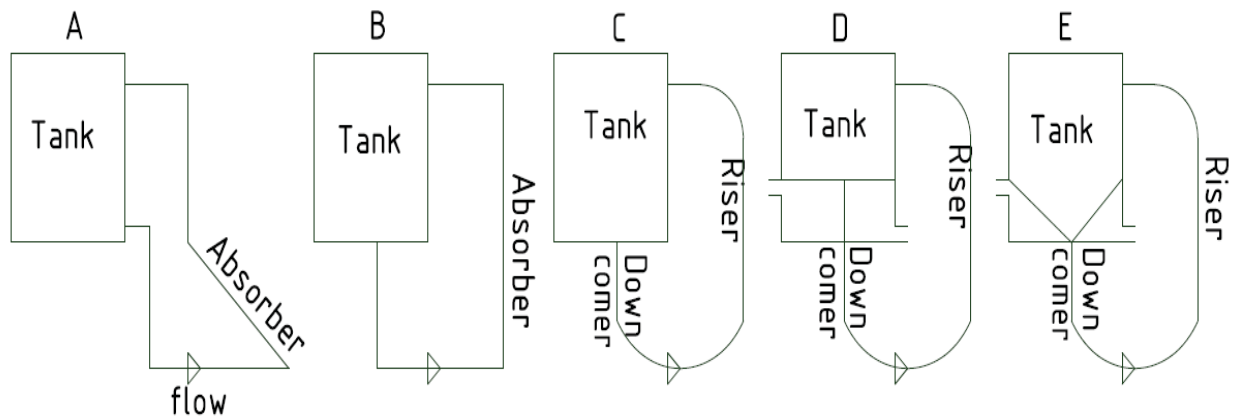


Figure 27: Schematic of geometrical development for novel Thermosiphon PBR

The original thermosiphon loop ((A) of Figure 27 (Close, 1962)) is characterized by three main sections forming the basic structural units of a thermosiphon solar water heaters namely: (i) the storage tank, (ii) connecting pipes (downcomer and upriser), and (iii) collector/absorber (Close, 1962). The downcomer and riser were of tubular shape since previous studies (Fernandes and Dragone, 2010; Ramírez-Duque and Ramos-Lucumi, 2011) have proven them to better allow light penetration at similar biomass concentrations in comparison to their planar counterparts. Loop (B) is a modification of the (A) with the downcomer and upriser connected at the bottom end and side of the storage tank respectively. However, the flat horizontal connecting pipe at the bottom of this configuration poses a possible disadvantage of microbial cell settling and sedimentation (Kunjapur and Eldridge, 2010). Therefore, it was adjusted with a 180° bend curvature (elbow) for increased flow speed (Ramírez-Duque and Ramos-Lucumi, 2011) resulting to loop (C). Applying the vertical cooling and vertical heating (VCVH) sections of (Pilkhwil et al., 2007; Vijayan et al., 2007) to loop (C) resulted to loop (D). As in (B), the flat horizontal bottom of the storage tank in loop (D) connecting the downcomer may bring about microbial cell sedimentation. This was reduced through the implementation of a smooth diameter transition from the storage tank to the downcomer diameters resulting to a truncated cone-shaped bottom storage as seen in loop (E). The describing geometries of (E) are shown in Figure 27. During experimentation, the walls of all the sections except the riser were insulated with 1 cm cotton wool wrapped with aluminium foil to minimize heat flux.

### 3.2.4 Pilot-scale TPBR set-up

A large scale (10 litre) TPBR will be built on the roof top of Annex building, Department of Process Engineering, Stellenbosch University. Figure 28 shows the proposed design of the outdoor TPBR which will be constructed from Plexiglas and aluminium heat sink, mounted on a steel frame which will be inclined to 45°C for maximum capture of solar energy at this latitude. Once installed,

preliminary heat transfer and passive fluid analysis will be executed to establish the operating conditions for the cultivation of photosynthetic bacteria. This will be followed by the proper cultivation of the photosynthetic bacteria under outdoor conditions. A pyranometer will continuously log insolation, while a temperature logger will monitor operating fluid temperatures.

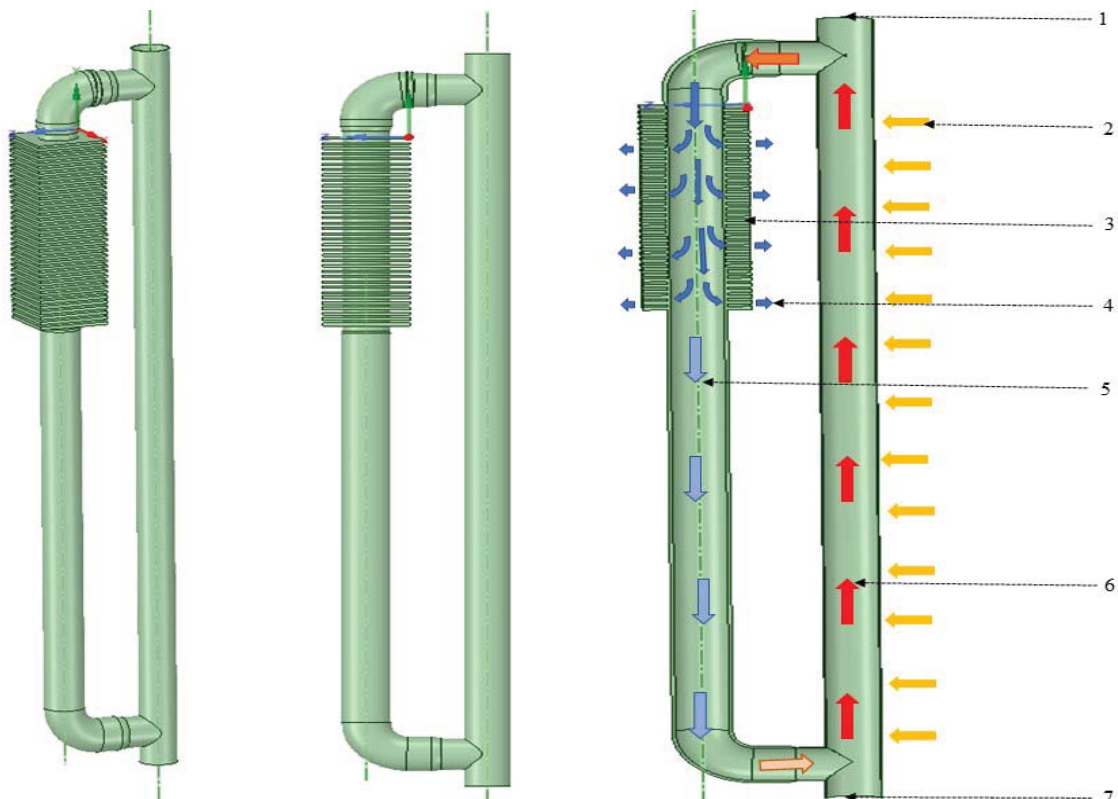


Figure 28: Schematic diagram of the outdoor TPBR showing 1) sampling port, 2) solar radiation, 3) flat plate fin, 4) ambient air cooling, 5) fluid of heavier density falling down, 6) fluid of lighter density rise up, and 6) spring port.

### 3.2.5 Bacteria growth and substrate consumption within the TPBR.

The initial biomass concentration of the starter culture was set at 0.08 g DCW/L. Since this is the very first photofermentation related work with this type of passively circulated bioreactor design, the entire growth bacteria profile including the lag phase, until the death phase were considered for investigation as shown in Figure 29. This was achieved by collecting samples at the center point of the TPBR's storage tank for every 24 hours, thereby corresponding to the biomass in free suspension as a result of thermosiphoning in the TPBR.

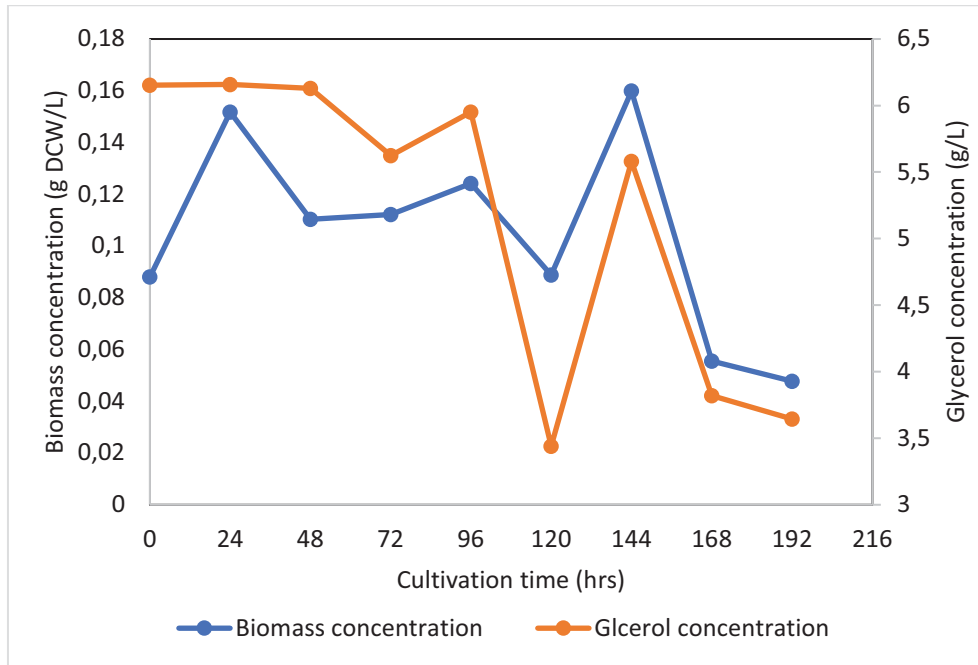


Figure 29: Cultivation time profile of biomass and glycerol concentrations in TPBR.

As per Figure 29, the bacteria growth profile in the TPBR was very unstable with an observed increase in biomass concentration to 0.15 g/L within the first 24 hours of cultivation, followed by a steady decrease to 0.11 g/L within the next 3 days of cultivation. After this point, the biomass concentration experienced a slight decrease before picking at a maximum value of 0.17 g DCW/L and then decreased completely thereafter to 0.15 DCW/L. These results reveal that the bacterial cells did not experienced a lag phase with in the first 24 hours and this was interpreted to occur due to the high initial biomass loading of already active exponential growing cells in the TPBR. Conversely, the drastic drop in biomass concentration after 144 hours of cultivation was interpreted to be death phase. Many factors could have prompted this unstable bacterial growth in the TPBR and therefore, glycerol consumption by bacterial cells in the TPBR was checked.

The glycerol concentration profile on Figure 29 was seen to decrease from an initial concentration of 6 g/L to 3.5 g/L at the end of the experiment. This was expected as glycerol was the only carbon source present in the growth medium for the bacterial cells to feed on. This shows that the bacteria cells were growing in the TPBR as they consumed the glycerol. However, the glycerol concentration did not decrease exponentially as reported by other studies (D Zhang et al., 2015) instead, it revealed an unstable decrease characterized by some peaks and troughs. These phenomena suggest a technical abnormality taking place within the TPBR.

Generally speaking, the bacterial growth profile within the TPBR strongly deviates from the standard microbial growth profile characterized by a lag, accelerated, exponential, stationary and

death phases (Kim Gail Clarke, 2013). This implies that there were some technical abnormalities taking place in the TPBR with respect to quantifying bacterial cell growth since eye inspection of the rig showed deep purple coloration at different sections (cooling and down-comer section) of the TPBR as seen in Figure 30.

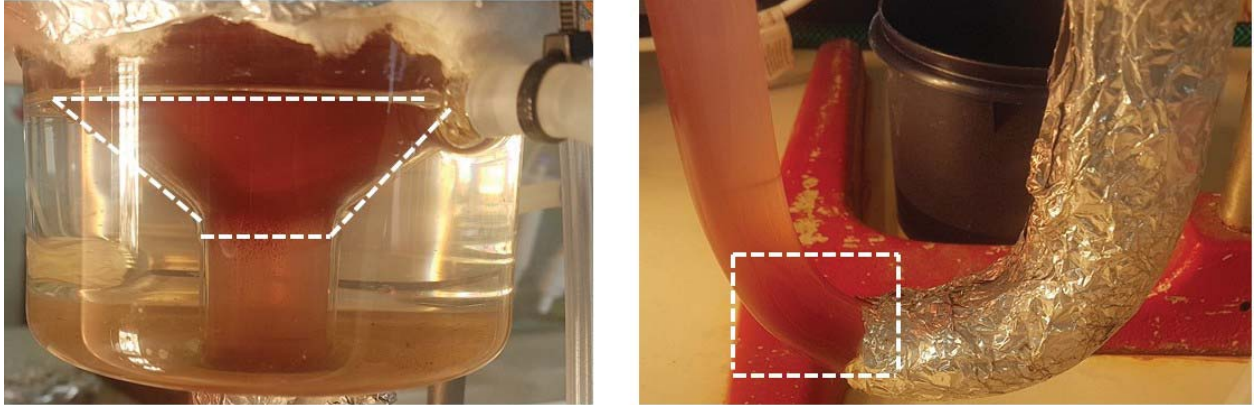


Figure 30: Photograph (left to right) of the cooling and down comer section showing deep purple coloration.

### 3.2.6 Biomass growth and biohydrogen production within the TPBR.

As per Figure 31 the hydrogen production rate was observed to increase with the bacterial growth during the first 24 hours and peak at 60 ml on the 4th day of cultivation meanwhile bacterial growth was slightly constant throughout this period (2<sup>nd</sup> to 4<sup>th</sup> day). This reveals that the hydrogen production was not bacterial growth associated in the TPBR and the same phenomena has reported when *R. palustris* in other photobioreactors (Palamae et al., 2018; D Zhang et al., 2015). After 144 hours of cultivation, both the hydrogen production and bacterial growth were seen to decrease. This was quite unusual because Figure 29 showed that there was still available glycerol for metabolic hydrogen to be produced. Therefore, the bacterial cells were dying due to some other unknown factor (maybe poor mixing and cell settling) since the light intensity was kept constant at  $200 W/m^2$  throughout the run.

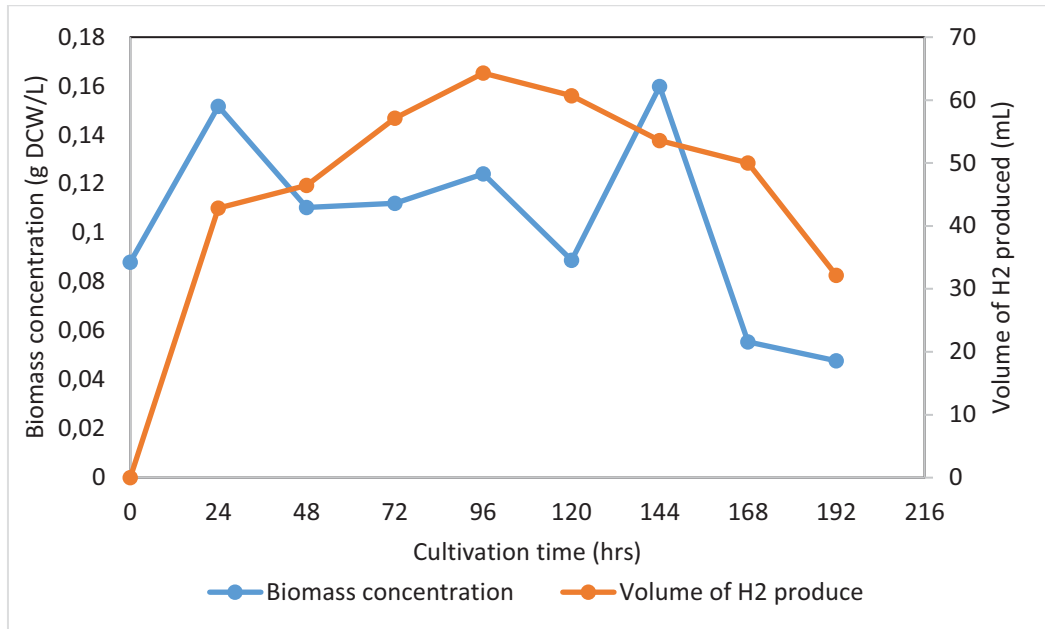


Figure 31: Cultivation time profile of biomass concentration and hydrogen production within the TPBR.

### 3.2.7 Limitations of bacterial free suspension within the TPBR

Figure 32 shows snapshots of the TPBR's cooling and down-comer section during bacterial growth and hydrogen production which were taken at various time intervals (24, 72 and 144 hours respectively). A build-up of deep purple coloration was observed in these regions as the photofermentation progressed. This was interpreted to be biomass settling at these sections with the cooling section showing the greatest effect. In general, bacterial cell settling was anticipated at the TPBR's down-comer since previous works by (Cho and Pott, 2019) on the hydrodynamics had reported some cell sedimentation around the curvature bend of the down-comer. On the other hand, the TPBR's cooling section unexpectedly reveal enormous biomass settling even though previous CFD studies by (Cho and Pott, 2019) had showed enhance fluid flow motion around that section. Also, it can be seen that the truncated cone shape side of the TPBR's cooling section performed poorly compared its vertical tubular side in facilitating the passage biomass to the down-comer section.



Figure 32 : Photograph of cooling and down-comer sections of the TPBR showing regions of deep purple coloration signifying biomass settling.

### 3.3 Photobioreactor modelling

#### 3.3.1 Mathematical modelling

The experimental results were used to determine how the temperature difference and viscosity affected the fluid velocity within the TPBR. The parameters of the mathematical model were determined and then validated based on the experimental results. The final mathematical model was extended to calculate the fluid velocity of a two-phase system.

##### 3.3.1.1 Model parameters

The mathematical model required the definition of ten parameters per segment of the TPBR, listed in Table 6. Six of these parameters were fixed based on the geometry of the TPBR. Four were based on the temperature approximation of each segment. The temperature approximation was adjusted based on the experimental results and therefore these four parameters were susceptible to change.

### 3.3.1.1.1 Physical dimensions

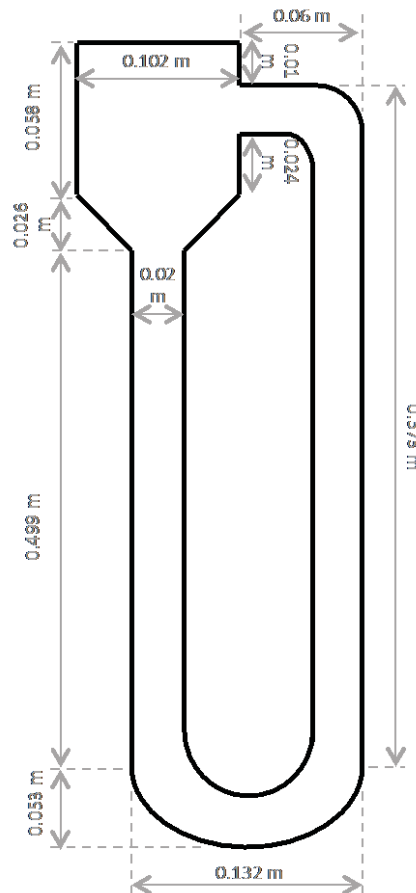


Figure 33: Physical dimensions of TPBR

The dimensions of the TPBR can be seen in Figure 33. The small and large diameter measurements of 20 mm and 102 mm indicated the inner diameter of the narrower and wider tubes respectively. The thickness of the glass was calculated based on the inner and outer diameter of the thinner tubes. The outer diameter of the thin tubes was measured as 24 mm and the inner diameter was determined as 20 mm using the method described in Section 6.2.1.3. The glass was found to be 2 mm thick. It was assumed that the glass had a uniform thickness throughout the TPBR.

The geometry of the TPBR had to be simplified before it could be modelled mathematically. The simplified geometry is shown in Figure 59 in Section 6.2.1.4. The segments were approximated as straight tubes with a constant diameter. The length and inner diameter of each segment was used in the mathematical model.

### 3.3.1.1.2 Parameters per segment

The mathematical model requires ten parameters to be specified per segment as seen in Equation 24 in Section 6.2.1.4. The number of parameters was reduced to nine by assuming that

each segment was perfectly mixed and therefore the density of the fluid leaving the segment was the same as the density of the fluid within the segment. The viscosity and density terms were calculated based on the temperature of the fluid. The temperature, at which the density and viscosity was calculated, was specified and used in the model to calculate the value of the fluid property. The temperature approximations shown in Figure 59 in Section 6.2.1.4 were used for the initial model.

The diameter of the inlet and outlet of each segment was specified as the smallest diameter of the interface through which the fluid was passing. The smaller diameter had the most significant influence on the system in terms of resistance to flow. The lengths were specified as shown in Figure 59 in Section 6.2.1.4. The equivalent lengths were calculated using the method described in Section 6.2.1.4.

Theta indicated the direction of flow with respect to gravity, as defined in the derivation of the model in Figure 64 in 6.2.3 . A theta value of 0° indicates that the fluid was flowing perpendicularly to gravity while a theta value of 90° indicated that the fluid was flowing against the direction of gravity. The parameters of all six segments for the initial model can be seen in Table 6.

Table 6: Segment parameters for initial model

k	$D_{k\text{in}}$ (m)	$D_{k\text{out}}$ (m)	$\rho_{k\text{in}}$ $\left(\frac{\text{kg}}{\text{m}^3}\right)$	$\rho_{k\text{out}} \& \rho_k$ $\left(\frac{\text{kg}}{\text{m}^3}\right)$	$\mu_k$ (Pa.s)	$L_k$ (m)	$\theta_k$ (°)	$D_k$ (m)	$L_{eq\ k}$ (m)
1	0.02	0.061	$Ta$	$Ta$	$Ta$	0.048	270	0.102	0.7018
2	0.061	0.02	$Ta$	$\frac{Ta+Tb}{2}$	$\frac{Ta+Tb}{2}$	0.026	270	0.061	0.148
3	0.02	0.02	$\frac{Ta+Tb}{2}$	$Tc$	$Tc$	0.499	270	0.02	0.859
4	0.02	0.02	$Tc$	$Tc$	$Tc$	0.108	0	0.02	0.748
5	0.02	0.02	$Tc$	$\frac{Ta+Tc}{2}$	$\frac{Ta+Tc}{2}$	0.553	90	0.02	1.193
6	0.02	0.02	$\frac{Ta+Tc}{2}$	$Ta$	$Ta$	0.057	180	0.02	0.377

### 3.3.1.2 Maximum velocity

The mathematical model assumed the fluid within the TPBR was with in the laminar flow regime. The fluid velocity that has a Reynolds number less than 2 100 was classified to lie within the laminar region. The maximum fluid velocity in the thinner tubes was calculated to be  $0.083 \frac{m}{s}$ . The experimental velocities did not exceed  $0.083 \frac{m}{s}$  and the mathematical model could not accurately calculate the fluid velocity if it was faster. The assumption that the system must be modelled for the laminar flow region was validated based on the experimental velocities and found to be correct.

### 3.3.1.3 Single phase experimental results

Multiple readings were taken for each experiment. The time and corresponding distances were recorded. These values were used to determine the velocity of the fluid in the down-comer and the experimental error. The superficial velocity in the down-comer was determined as the average of the calculated velocities. The experimental error was determined as the standard deviation of the velocities from the average velocity. The superficial velocity and standard deviation was calculated for each experiment. The results are shown in Table 7 (below).

Table 7: Single phase results

Experiment	1	2	3	4	5	6	7	8	9
$T_a$ ( $^{\circ}C$ )	38.9	28.5	30.9	22.3	31.6	30.9	34.0	33.1	31.3
$T_b$ ( $^{\circ}C$ )	34.4	25.6	24.3	17.6	27.7	27.3	30.2	29.5	26.9
$T_c$ ( $^{\circ}C$ )	34.8	26.0	26.8	18.8	28.9	28.3	29.1	30.0	28.4
$T$ average ( $^{\circ}C$ )	36.0	26.7	27.3	19.5	29.6	28.8	31.1	30.9	28.9
$v$ (m/s)	0.011	0.007	0.013	0.010	0.010	0.008	0.012	0.009	0.009
Experimental Error (m/s)	0.0010	0.0006	0.0011	0.0014	0.0007	0.0002	0.0015	0.0007	0.0010
$\Delta T$ ( $^{\circ}C$ )	4.5	2.9	6.6	4.7	3.9	3.6	3.8	3.6	4.4

Where  $\Delta T$  ( $^{\circ}C$ ) =  $T_a$  ( $^{\circ}C$ ) –  $T_b$  ( $^{\circ}C$ ) is the temperature difference as defined in Section 6.2.1.5.3. Experiments 5, 6, 7 and 8 were identified as having a similar temperature differences and therefore a similar driving force. The temperature difference was investigated based on the temperature difference between the temperature reading at temperature probe  $T_a$  and  $T_b$ . The temperature difference was plotted for each experiment in Figure 34 (below). The temperature differences of these four condition sets varied from  $3.3^{\circ}C$  –  $3.9^{\circ}C$ . It was not possible to have a constant temperature difference in the various experiments, due to the way in which the temperature was controlled. Using experiments with similar temperature differences minimised the influence of the temperature difference on the experimental results. Experiments 5, 6, 7 and 8 were identified as the first set of experiments and used to determine the effect of viscosity on the fluid velocity.

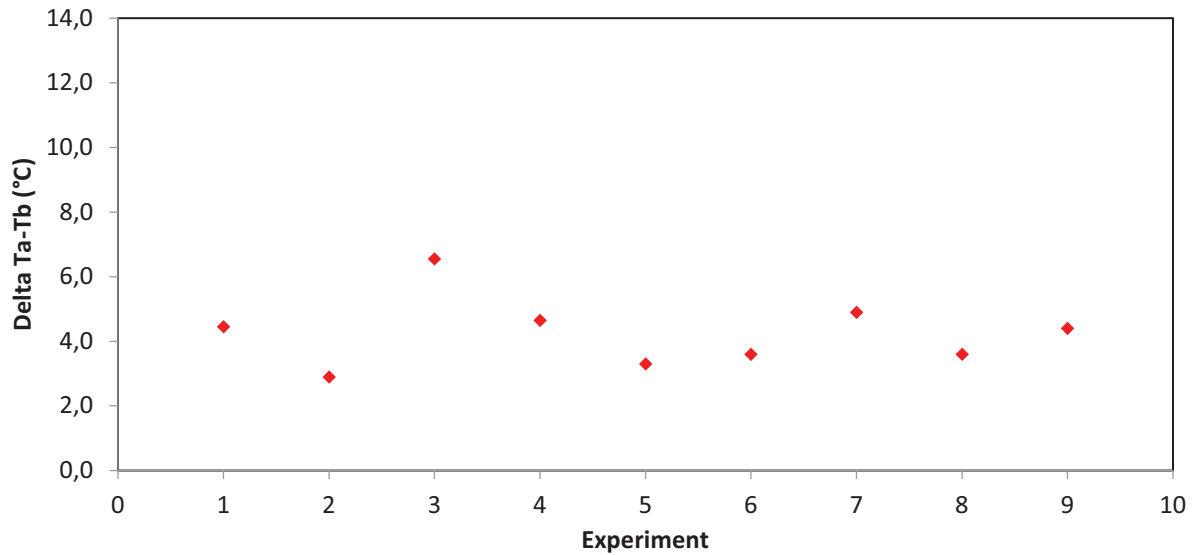


Figure 34: Temperature difference of the various data sets

Ideally the average temperature would have been kept constant to minimise the effect of viscosity on the fluid velocity. This was not possible, as the average temperature of each experiment could not be controlled and the large variation can be seen in Table 7. The temperature readings of temperature probe Ta were used instead to identify experiments with similar viscosities. The temperature readings, of temperature probe Ta for the different experiments, was plotted in Figure 35. From Figure 35 experiments 3, 5, 6 and 9 were identified as having the most similar readings at temperature probe Ta. These experiments were identified as the second set of experiments and used to determine the effect of the driving force on the fluid velocity.

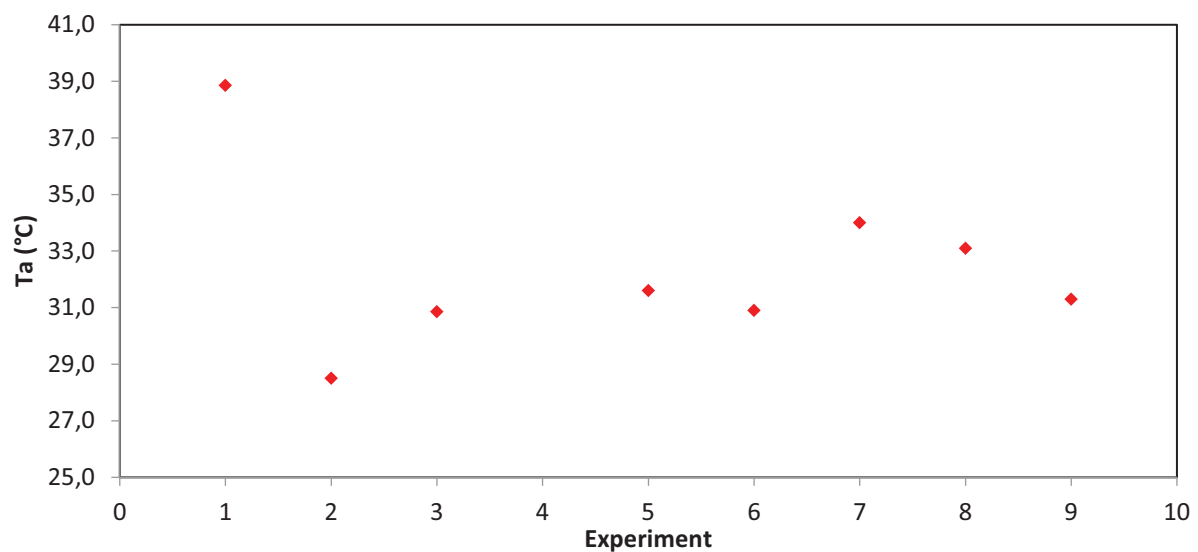


Figure 35: Temperature at temperature probe Ta of the various data sets

The variation in both the temperature difference and average temperature prevented the two effects from being investigated separately. This influenced the results and was considered during

the interpretation of them. The two effects were discussed separately to determine how each effect influenced the fluid velocity.

### 3.3.1.4 Discussion on the effect of viscosity

The effect of the viscosity was investigated using the first set of experiments. The velocity in the down-comer was plotted in Figure 36 with respect to the average temperature of the fluid. The effect of the viscosity on the fluid velocity is seen in Figure 36.

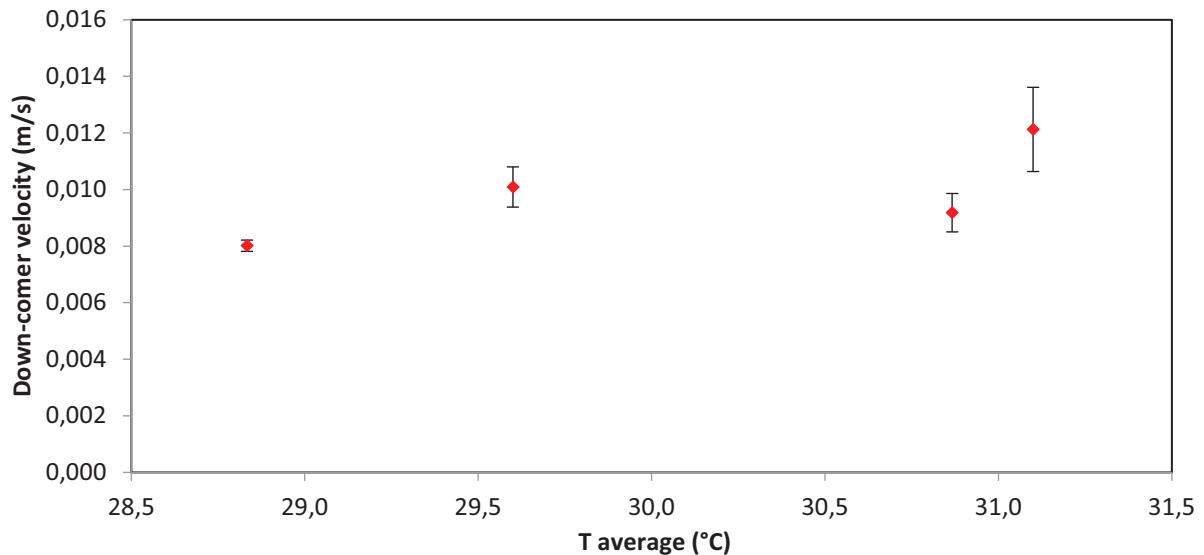


Figure 36: Velocity of the fluid at varying average temperatures

From Figure 26 it was seen that the fluid velocity increased as the average temperature of the TPBR increased. This was expected based on the literature. As the temperature of the fluid increased, the viscosity of the fluid decreased. The friction of the fluid in the TPBR depends on the fluid viscosity. The friction decreased at the higher average temperature and therefore the velocity increased. These results are supported by the literature discussed in the literature review.

The velocity for an average temperature of  $30,9^{\circ}\text{C}$  is slightly lower than expected while the velocity for an average temperature of  $29,6^{\circ}\text{C}$  is slightly higher. These readings are from experiments 8 and 5 respectively. These deviations from the trend may be accounted to the temperature differences that were not constant or the experimental error as indicated by the error bars.

The average temperature difference, for these four experiments, was calculated as  $3,7^{\circ}\text{C}$ . In Table 7 it is seen that the temperature difference of experiment 8 was slightly lower than the average temperature difference ( $3,6^{\circ}\text{C}$ ) and the temperature difference of experiment 5 was

slightly higher ( $3.9^{\circ}\text{C}$ ). The lower temperature difference of experiment 8 may have resulted in the slower fluid velocity. Similarly, the higher temperature difference of experiment 5 may have caused the fluid velocity to be slightly higher than the expected velocity based on the observed trend.

The mathematical model incorporated both the effect of the temperature difference and the viscosity. The mathematical model was able to determine whether the slight variation in temperature difference resulted in the deviations from the expected trend. This is discussed in Section 3.3.1.7 and determined that the variation was not the cause of the deviations from the trend. The deviation resulted from the experimental error.

**3.3.1.5 Discussion of the effect of the driving force**

The effect of the driving force on the fluid velocity was investigated by plotting the fluid velocity versus the temperature difference for experiments 3, 5, 6 and 9, in Figure 37. The average temperature was assumed to be constant for the experiments plotted in order to investigate the effect of the driving force on the system separately from that of viscosity.

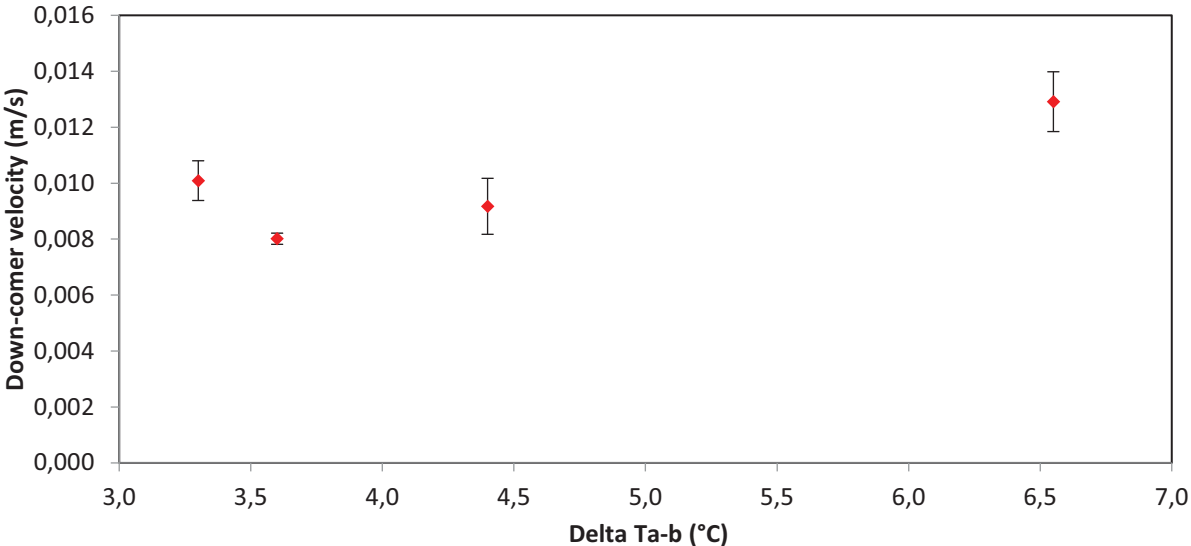


Figure 37: Velocity of the fluid at varying temperature differences

From Figure 37 it was seen that the fluid velocity increased as the temperature difference increased. This was expected, as the temperature difference was the driving force for the movement of the fluid in the TPBR. The increased driving force of the thermosiphon therefore resulted in higher velocities, corresponding to the literature understanding of the system.

The two velocities that deviate from the general trend correspond to a temperature difference of  $3.3^{\circ}\text{C}$  and  $4.4^{\circ}\text{C}$ . These are the results of experiments 5 and 9 respectively. The error bars show that the velocity measured for experiment 9 was not very precise. The velocity measurements had a deviation of  $0.0010\text{ m/s}$  and experimental error of 11% from Table 8. The deviation may therefore be due to experimental error. The velocity readings for experiment 5 may also have included an experimental error as discussed in Section 3.3.1.4.

The overall trend shows that the fluid velocity increased as the temperature difference increased and these findings are supported by the literature. The fluid velocity was therefore found to increase with an increased temperature difference. The significance of the two effects of temperature on fluid velocity was investigated further and quantified using the mathematical model.

### **3.3.1.6 Parameterising the model**

During the derivation of the mathematical model in Section 6.2.1.4 two approximations were made that had to be validated based on the experimental results. The first approximation was made to determine the amount of friction acting on the system. The values, for the frictional term, were initially determined from literature values by representing the friction as an equivalent length. The frictional term in the mathematical model was then adjusted based on the experimental results as described in Section 6.2.1.4. The equivalent length of each segment was multiplied by a correction factor. This correction factor is referred to as the frictional coefficient and the same value was used for all the segments of the modelled TPBR.

The second approximation was made to determine the temperature of each segment based on the three temperature readings available. The initial model used an initial estimate as discussed in Section 6.2.1.4. The degree to which the fluid velocity depended on the temperature difference or the viscosity was adjusted by altering how the temperature of each segment was approximated. The approximations were adjusted based on the experimental results.

The first set of experiments, experiments 5, 6, 7 and 8, was used to update the frictional coefficient and temperature approximations. The method used to update the model is shown below, in Figure 38. Once the correct frictional coefficient and best approximation of the temperature of each segment were determined, the mathematical model was used to calculate velocities for the second set of experiments, experiments 3, 5, 6 and 9. The model was validated based on how well the calculated velocities predicted the experimental velocities of the second set of experiments.

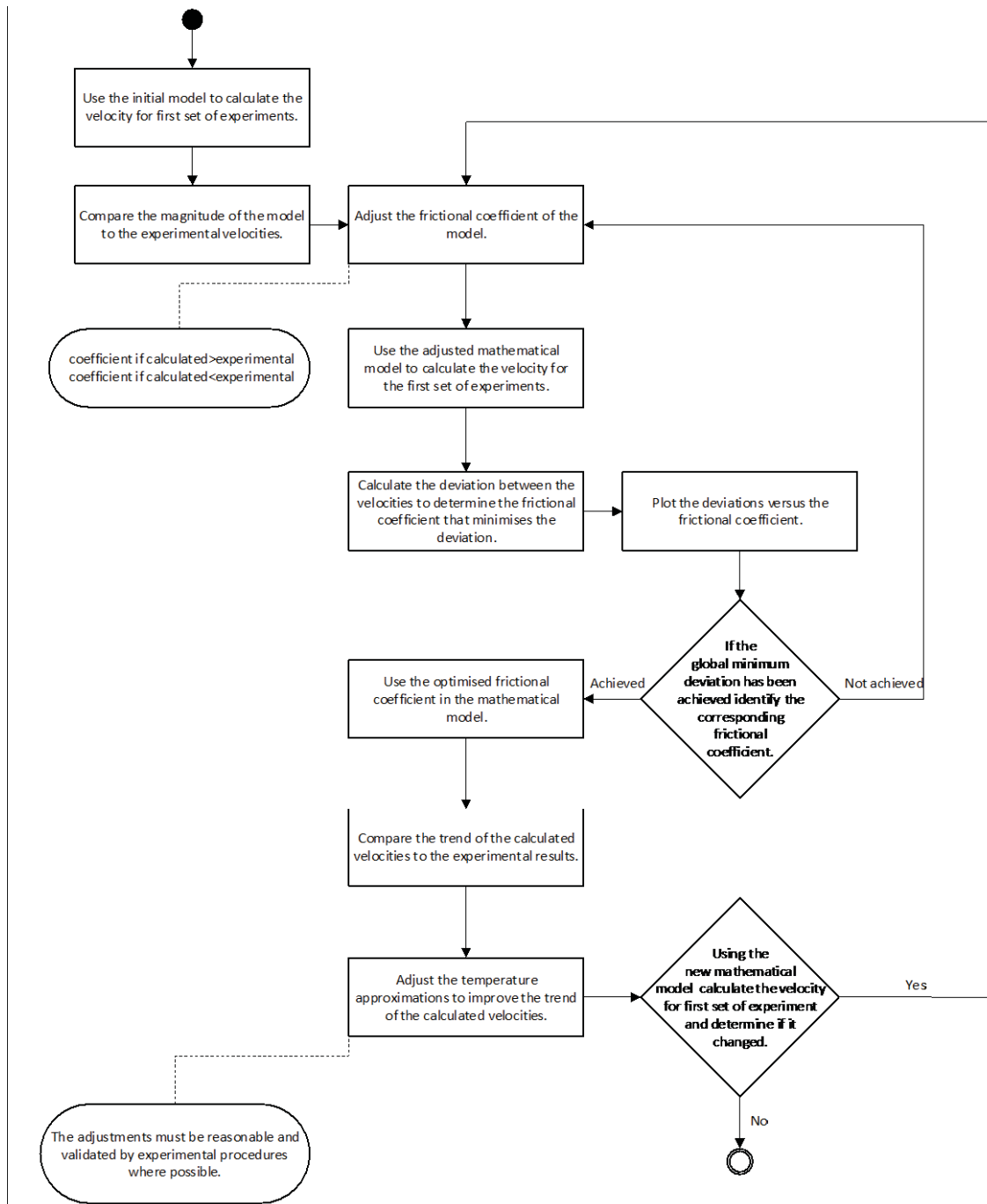


Figure 38: Correcting the initial assumptions of the model

Figure 39 shows how the calculated velocities changed as the mathematical model was adjusted. The results of the initial model are represented as the 1<sup>st</sup> mathematical model. The experimental velocities can also be seen in Figure 39. Figure 39 shows the effect of adjusting the frictional coefficient and the temperature approximation on the accuracy of the mathematical model.

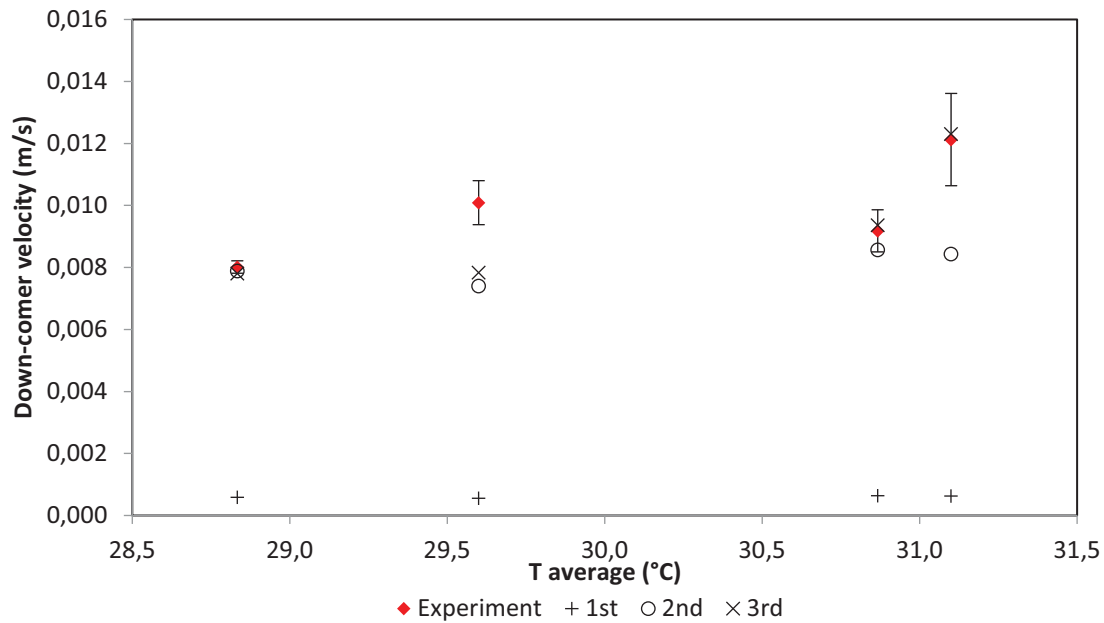


Figure 39: Results of the mathematical model

The frictional coefficient was reduced from 1 in the 1<sup>st</sup> model to 0.071 in the 2<sup>nd</sup> model plotted in Figure 39. Decreasing the frictional coefficient decreased the magnitude of the frictional term in the mathematical model. The force opposing the fluid motion was therefore calculated to be less, resulting in a higher fluid velocity in the down-comer of the TPBR. The increased velocity can be seen in Figure 39 represented by the 2<sup>nd</sup> mathematical model. This adjustment increased the magnitude of the calculated velocities and reduced the deviation between the modelled and experimental velocities.

The frictional coefficient was adjusted based on the deviation of the modelled velocities from the experimental velocities. The deviation was calculated as the sum of the differences squared. The effect of the frictional coefficient on the deviation of the modelled velocities is shown in Figure 40 (below).

Figure 40 shows the optimisation of the frictional coefficient for the final mathematical model. From Figure 40 it is clear that there exists an optimal frictional coefficient that minimised the error between the modelled and experimental velocities. The deviation decreased as the magnitude of the modelled velocities approached those of the experimental velocities. The deviation increased once the magnitude of the modelled velocities exceeded the magnitude of the experimental velocities. The frictional coefficient that corresponded to the minimum deviation was used in the final mathematical model.

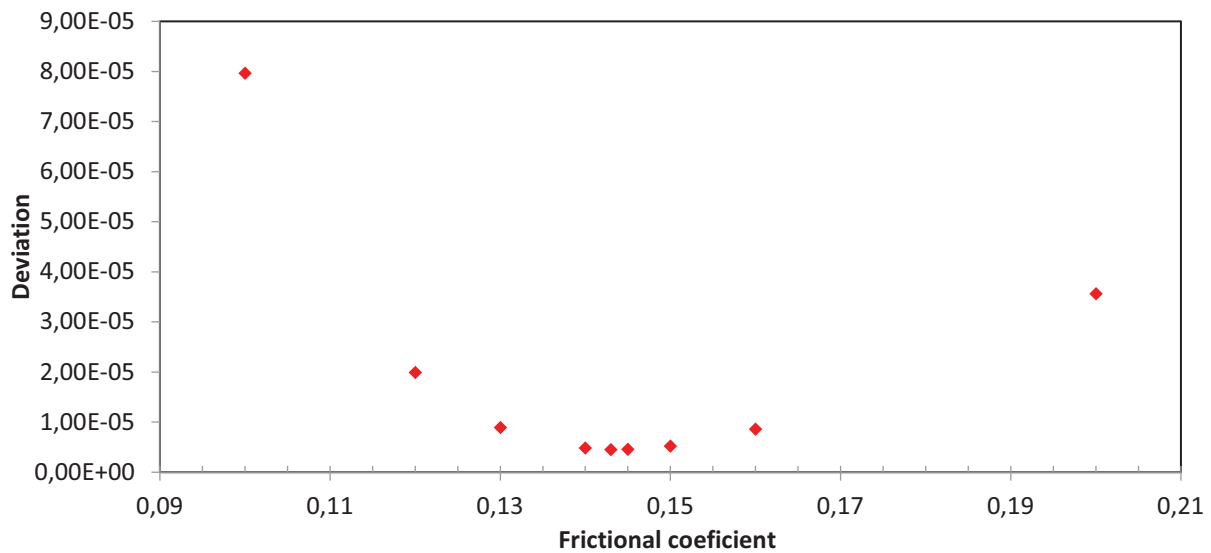


Figure 40: Adjusting the frictional coefficient in the mathematical model

The temperature approximation was adjusted based on how the viscosity influenced the fluid velocity. This was assessed by comparing the experimental trend in Figure 39 (above) to the trend determined by the modelled velocities. In Figure 39 the velocities of the 2<sup>nd</sup> model do not follow the same trend as that of the experimental results. The experimental velocities increased with a steeper gradient than the modelled velocities. The experimental fluid velocity therefore increased more significantly with an increased average temperature than predicted by the mathematical model. The temperature approximations were therefore adjusted from the 2<sup>nd</sup> mathematical model to the 3<sup>rd</sup>, as seen in Figure 39.

The modelled velocity for the average temperature of 31.1°C was slower than the experimental velocity and very similar to the other velocities calculated by the mathematical model. The mathematical model was therefore underestimating the effect of viscosity on the fluid velocity. The viscosity significantly affected the fluid velocity, as seen in the experimental results and discussed in Section 3.3.1.4. The mathematical model had to be corrected to model the effect of viscosity correctly.

The temperature approximation of the two segments in which heat was added or removed was adjusted, segment 2 and 5. These temperatures were changed, from being approximated as the average of two temperature readings, to the temperature of the outlet fluid from the segment. The outlet temperature of both segments was measured during the experimental procedure by temperature probes Tc and Ta respectively. The corrected temperatures can be seen indicated for each segment in Figure 41 (below). The mathematical model was updated accordingly and the results are shown in Figure 39 as the results of the 3<sup>rd</sup> model.

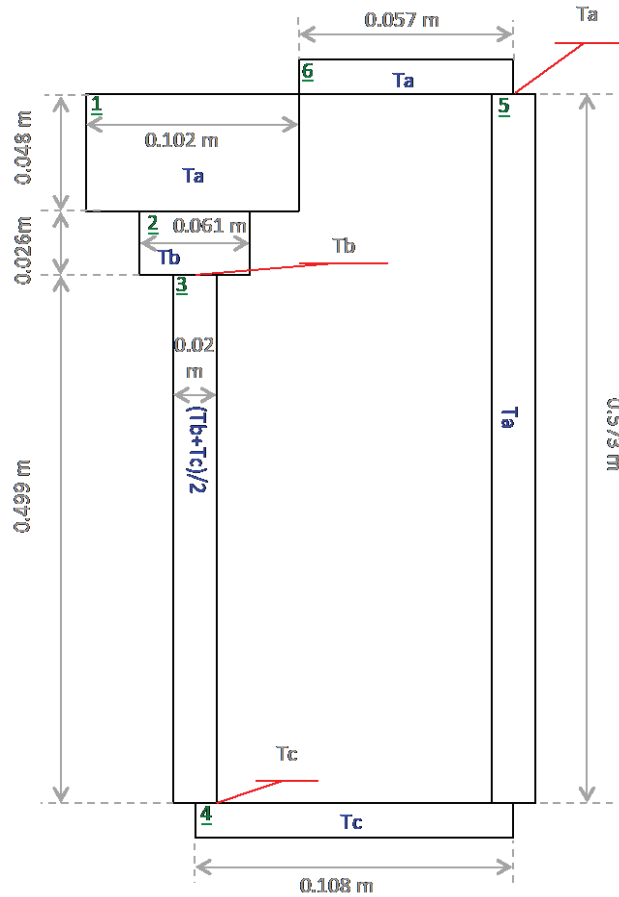


Figure 41: Final configuration for the Matlab model

The final mathematical model was determined by following the method described and summarised in Figure 38 (above). The frictional coefficient was optimised for the final model and determined to be 0.143, the minimum deviation was  $4.55 \times 10^{-6}$ , as seen in Figure 40 (above). The temperature approximations were adjusted as discussed and indicated in each segment in Figure 41. The Matlab code for the final model is included in Appendix 6.2.4 and the results shown in Figure 43 (below).

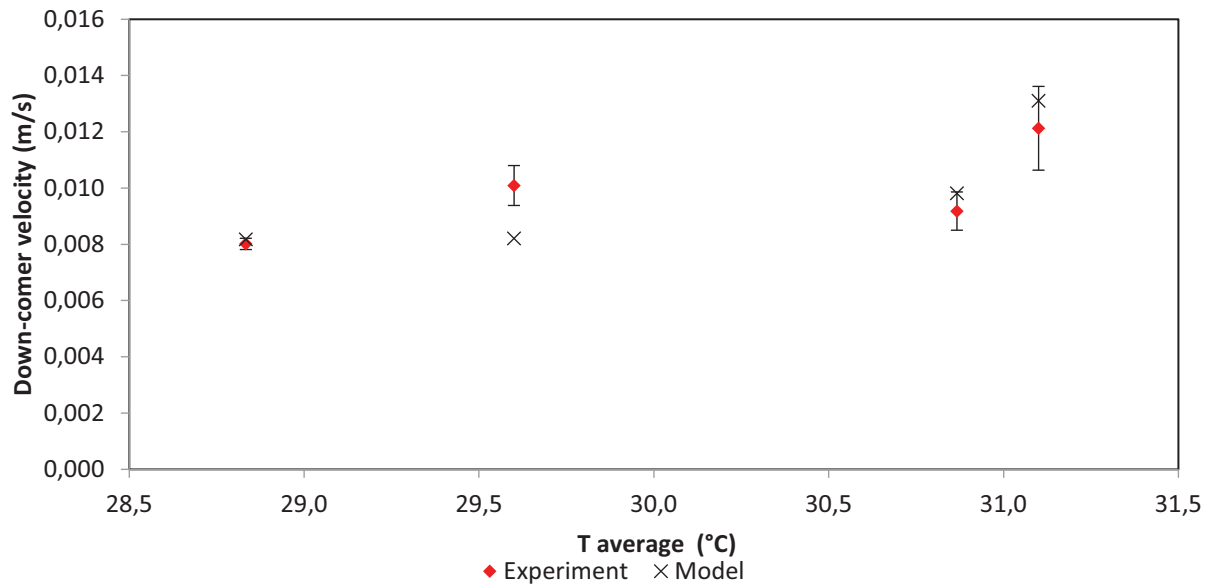


Figure 42: Final model and experimental velocity based on viscosity

### 3.3.1.7 Model validation

The mathematical model was validated by comparing the modelled velocities to the experimental velocities. It was also validated by using the second set of experiments. This determined how well the model accounted for the effect of the temperature difference on the fluid velocity. Two of the experiments in the second set of experiments were also used to determine the parameters of the model, namely experiments 5 and 6. The results are shown in Table 8 and Figure 43.

Table 8: Mathematical model validation

Experiment	1	2	3	4	5	6	7	8	9
$T_a$ (°C)	38.9	28.5	30.9	22.3	31.6	30.9	34.0	33.1	31.3
$T_b$ (°C)	34.4	25.6	24.3	17.6	28.3	27.3	29.1	29.5	26.9
$T_c$ (°C)	34.8	26.0	26.8	18.8	28.9	28.3	30.2	30.0	28.4
Experimental velocity ( $\frac{m}{s}$ )	0.011	0.007	0.013	0.010	0.010	0.008	0.012	0.009	0.009
Matlab velocity ( $\frac{m}{s}$ )	0.016 4	0.006 3	0.013 4	0.006 3	0.008 2	0.008 2	0.013 1	0.009 8	0.009 7
Experimental error	9%	8%	8%	14%	7%	2%	12%	7%	11%
Deviation	32%	19%	3%	51%	23%	2%	6%	6%	6%

$$Deviation = \frac{|Experimental\ velocity - Matlab\ velocity|}{Experimental\ velocity} \times 100\% \quad [20]$$

The error between the modelled and experimental fluid velocity was calculated using Equation 20. The shaded area in Table 8 represents the experiments that were used to determine the parameters of the model. From the values in the table the model was able to predict the experimental velocities of experiments 2, 3 and 9. The error for experiments 3 and 9 were less than the experimental error and therefore the model was sufficiently accurate for these velocities. The model however did not predict the velocities for experiments 1 and 4 accurately.

The mathematical model was used to calculate the velocities for the second set of experiments, namely experiments 3, 5, 6 and 9. The calculated velocities were compared to the experimental velocities in Figure 43 to determine how well the model accounted for the effect of temperature difference on the system.

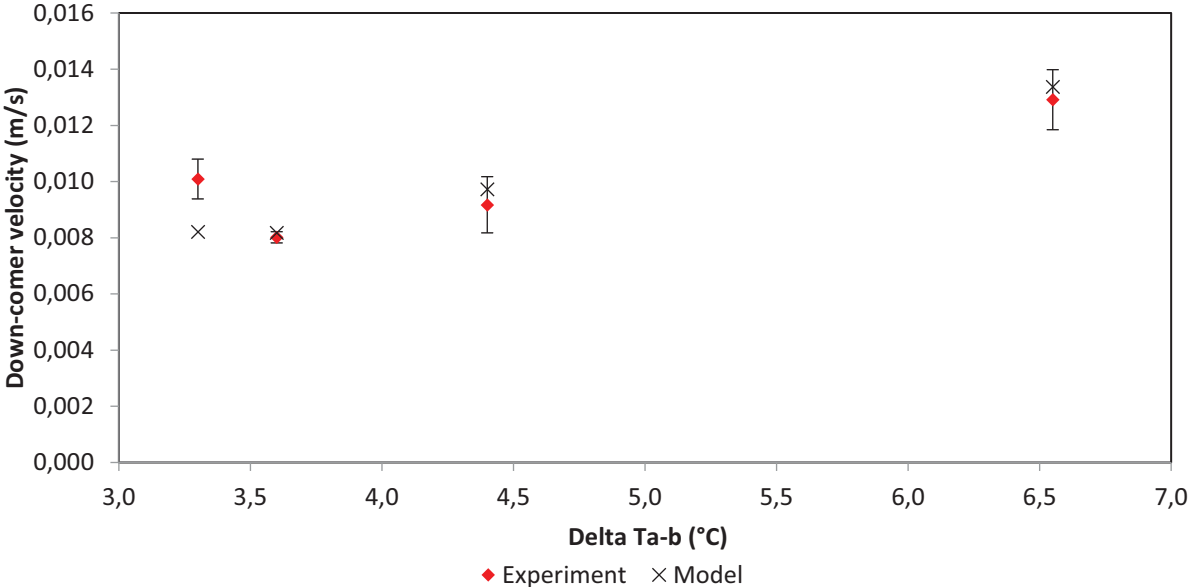


Figure 43: Final model and experimental velocity based on temperature difference

Figure 43 shows that the mathematical model accurately captured the effect of temperature difference on the fluid velocity within a TPBR. The model was accurate as it was parameterised to predict the effect of viscosity on the fluid velocity and still managed to capture the effect of temperature difference on the fluid velocity. In both Figure 42 and Figure 43 the only data point where there is a large discrepancy between the experimental and modelled velocity is from experiment 5.

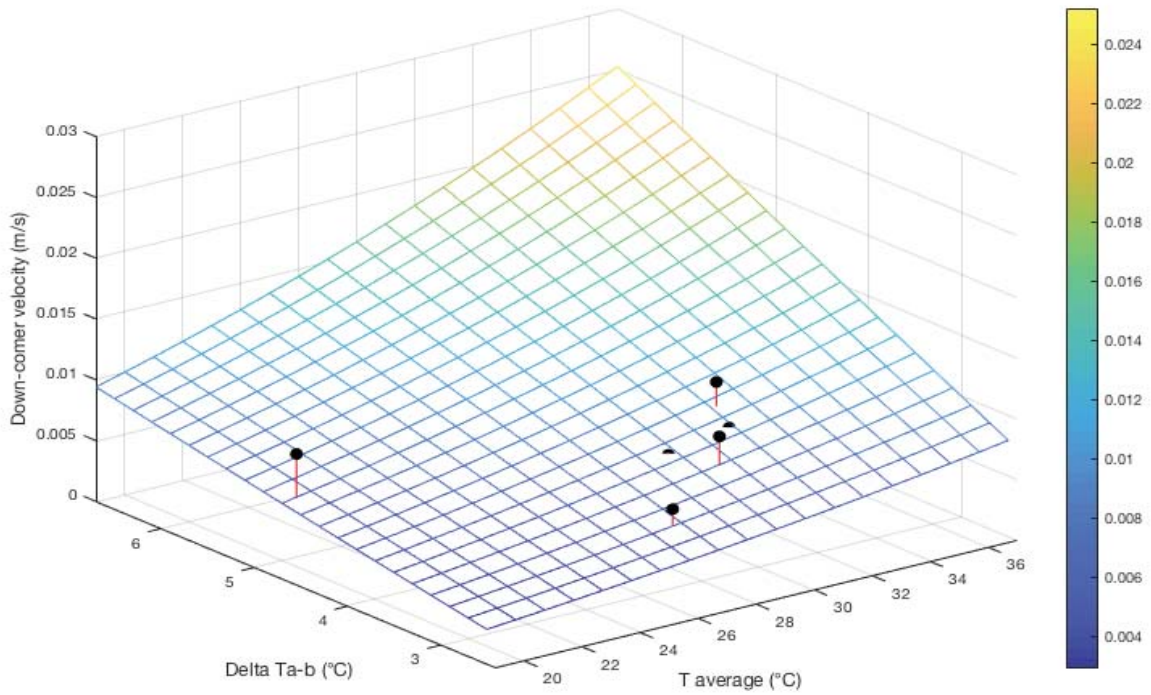
As the model predicted the velocity of experiment 5 to follow the expected trend, the deviation of the experimental velocity was not due to variations in the temperature difference as discussed in Section 3.3.1.4. The error may therefore result from experimental error. Repeated readings, of the flow rate, were taken and therefore it is unlikely that the experimental velocity was measured

incorrectly. The sensitivity of the fluid velocity to the temperature measurements was investigated to determine if an error in the recorded the temperature readings may have the caused the deviation.

The final model was used to predict the velocity of the fluid in the TPBR for various average temperatures and temperature differences. These results assumed a constant rate of heat transfer in the down-comer of the TPBR.  $T_c$  was therefore assumed to be  $1^\circ\text{C}$  warmer than  $T_b$ . A surface plot was created from the results of the mathematical model and is shown in Figure 44. Figure 44 shows the effect of the viscosity and temperature difference on the fluid velocity based on the model and experiments.

Figure 44a and Figure 44b show the same results. Figure 44a shows the results from the front and clearly displays how the velocity increased as both the temperature difference and average temperature increased. Figure 44b shows the results from a different angle so that the deviation between the model and experimental results can be seen clearly. Some of the deviation was due to the assumption that  $T_c$  was  $1^\circ\text{C}$  warmer than  $T_b$  but as the average temperature difference between  $T_b$  and  $T_c$  was  $1^\circ\text{C}$  the effect, on the deviation, due to this assumption was negligible.

a)



b)

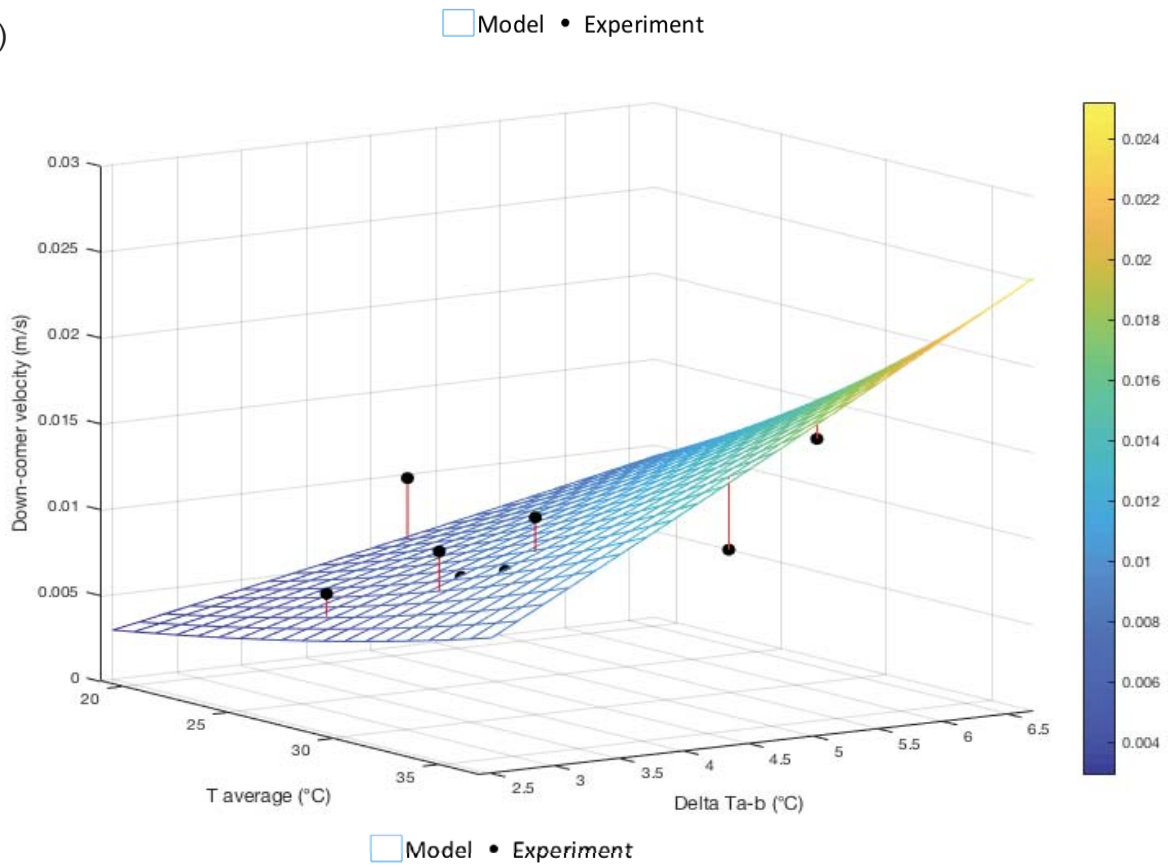


Figure 44: Surface plot of model results with experimental data

### 3.3.1.8 Model sensitivity

The sensitivity of the fluid velocity, with respect to the temperature readings at temperature probes Ta, Tb and Tc, was determined. In order to use the model the effect of measurement error had to be investigated. It was also important to determine how an error in the experimental temperature would have affected the velocity calculated for that experiment. The sensitivity analysis was performed based on experiment 5 and the uncertainty calculated using Equation 21.

$$Uncertainty = \frac{|Adjusted\ velocity - Original\ velocity|}{Original\ velocity} \times 100\% \quad [21]$$

The sensitivity of the system, to the three temperature readings, was investigated by comparing the velocities calculated at various temperature readings. The uncertainty of the calculated velocity due to the uncertainty in the temperature reading, of 0.15°C, was determined to be a maximum of 5% for experiment 5, in Table 9. From Table 9 it was also seen that the model is more sensitive to the temperature reading at Ta than Tb and Tc. The uncertainty resulting from the 0.15°C uncertainty in the temperature readings was small as it was less than the experimental errors in Table 8.

Table 9: Effect of a 0.15°C error on the calculated velocity

	Original values	Increase				Decrease			
		Ta	Tb	Tc	All	Ta	Tb	Tc	All
Ta (°C)	31.60	31.75	31.60	31.60	31.75	31.45	31.60	31.60	31.45
Tb (°C)	28.30	28.30	28.45	28.30	28.45	28.30	28.15	28.30	28.15
Tc (°C)	28.90	28.90	28.90	29.05	29.05	28.90	28.90	28.75	28.75
v (m/s)	0.0082	0.0087	0.0080	0.0080	0.0083	0.0078	0.0084	0.0084	0.0082
Uncertainty	0%	5%	2%	2%	0.8%	5%	2%	2%	1%

During the experiments the temperature readings fluctuated after the drop of base was added. These fluctuations may have results in the temperature deviating from the recorded temperature reading. It was therefore possible that for some experiments the temperature deviation was significant enough to cause the model velocity to deviate from the experimental velocity. A sensitivity analysis on a temperature deviation of 1°C was conducted to determine how this would effect the velocity calculated by the mathematical model.

The sensitivity analysis was also conducted based on experiment 5. It was determined that an error of 1°C can result in an error of up to 37% in the calculated velocity as shown in Table 10. The deviation between the calculated and experimental velocities may be caused by an error in the temperature reading recorded or temperature fluctuation during the experiment. The model was found to be the most sensitive to the temperature reading  $T_a$  and the uncertainty of the temperatures measured by the temperature probes were not significant compared to the experimental errors.

Table 10: Effect of a 1°C error on the calculated velocity

	Original values	Increase				Decrease			
		$T_a$	$T_b$	$T_c$	All	$T_a$	$T_b$	$T_c$	All
$T_a$ (°C)	31.60	32.60	31.60	31.60	32.60	30.60	31.60	31.60	30.60
$T_b$ (°C)	28.30	28.30	29.30	28.30	29.30	28.30	27.30	28.30	27.30
$T_c$ (°C)	28.90	28.90	28.90	29.90	29.90	28.90	28.90	27.90	27.90
$v$ ( $\frac{m}{s}$ )	0.0082	0.0112	0.0069	0.0070	0.0087	0.0053	0.0095	0.0094	0.0078
Uncertainty	0%	37%	16%	15%	5%	35%	16%	14%	5%

The deviation between the model and experimental velocities for experiments 1, 4 and 5 were analysed as these experiments had the largest deviation. The deviations of these experiments were 32%, 51% and 23% respectively. An error in the temperature reading could possibly have resulted in the deviation of experiments 1 and 5.

The deviation of experiment 4 exceeds the error that could reasonably be expected due to an error in the temperature reading. It is therefore possible that the system had not reached steady state yet when this reading was taken or the drop of base that was added influenced the fluid velocity. The deviation of experiment 4 alone was not enough to prove that the mathematical model was not accurate.

Due to the method used to measure the dimensions of the TPBR the dimensions include a level of uncertainty. The uncertainty could not be determined but it was prudently estimated that each dimension could vary with 5 mm either direction. The velocity of experiment 5 was calculated for the two extreme cases, if all the dimensions were 5 mm too large or too small. The results are shown in Table 11.

Table 11: Effect of a 5 mm error on the calculated velocity

	Segment length $m$						$v \left( \frac{m}{s} \right)$	Uncertainty
	1	2	3	4	5	6		
Original	0.048	0.026	0.499	0.108	0.573	0.057	0.0082	0%
Smaller 5 mm	0.047	0.025	0.496	0.103	0.568	0.052	0.0083	1%
Larger 5 mm	0.049	0.027	0.502	0.113	0.578	0.062	0.0081	1%

### 3.3.1.9 Two-phase results

The two-phase experiments were performed using a solution of water and deactivated bacteria at a concentration of  $0.5 \text{ g/L}$ . A different indicator was used and tested on a single-phase experiment with temperature readings similar to experiment 8. The velocity was also measured as  $0.009 \text{ m/s}$ . The different indicator was therefore assumed to have a negligible influence on the experimentally measured velocity. The mathematical model had to be updated to account for the addition of solids to the fluid.

The parameters discussed in Section 3.3.1.1.2 and Equation 24 were considered for the two-phase model. The addition of solids did not influence the derivation of Equation 24 and therefore the same equation was used. The addition of the solids affected the fluid properties and the internal friction in the system but not the geometry of the TPBR.

The effect of the solids on the density and viscosity of the fluid were considered. The density and viscosity of solids do not change with temperature. The only effect of the solids on the density and viscosity terms was identified to be the decrease in the volume of water in the fluid due to the volume of solids. As the volume of the solids was negligible in comparison to the volume of fluid, the density and viscosity terms of the two-phase model were assumed to be the same as those of the single-phase model.

The modelled and experimental velocities of the three, two-phase experiments were plotted in Figure 45 and the results shown in Table 12. Figure 45 shows that the mathematical model, modelled the experimental velocities well. Table 12 shows the calculated experimental error and model error calculated using Equation 20.

Table 12: Two-phase results

Experiment	1	2	3
$T_a$ ( $^{\circ}C$ )	38.0	38.2	31.5
$T_b$ ( $^{\circ}C$ )	34.6	34.6	27.5
$T_c$ ( $^{\circ}C$ )	35.6	35.0	29.0
Experimental velocity ( $\frac{m}{s}$ )	0.012	0.012	0.010
Matlab velocity ( $\frac{m}{s}$ )	0.011	0.012	0.009
Experimental error	24%	9%	12%
Deviation	9%	4%	13%

The modelled velocities fall within the error bars in Figure 45. The deviation between the average velocity and the calculated velocity was therefore smaller than the deviation of the experimental results. The mathematical model can therefore be used to calculate the velocity for two-phase systems as well as single-phase systems.

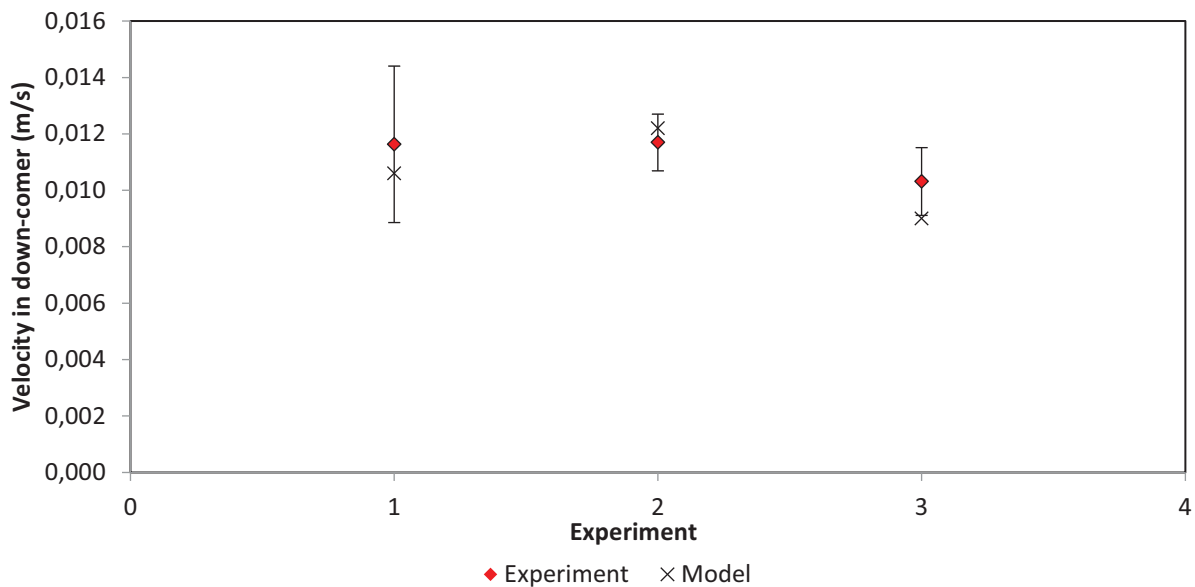


Figure 45: Two-phase final model and experimental velocities

### 3.3.2 Fluent modelling

The use of CFDs and experimental validation for the development of the thermosiphon PBR led to a series of investigations which the results are presented and discussed in this chapter of the thesis. This chapter is broken down into six subchapters: parameters used for CFD model, CFD simulation results, flow visualization results, validation results, and effects of light absorption on the heating rate and thermosiphoning cells respectively.

### **3.3.2.1 Spectral parameters used in CFD modelling**

This section contains the results and discussion of the experiments designed for the investigation of the relevant CFD modeling parameters. It starts by discussing the results of the halogen lamps as an illumination source for the thermosiphon PB, followed by the spectral attenuation properties of active *Rhodospseudomonas palustris* cells and finally the measured heat transfer coefficient of the thermosiphon PBR system.

#### **3.3.2.1.1 Results of Halogen lamp radiation model**

The spectral emittance,  $I(\lambda, T)$  which is the flux of power per unit area per wavelength predicted by the Planck's radiation equation for a perfect blackbody at a color temperature of 2900K is displayed in Figure 46. This emission spectral of the halogen lamp compares very well with that reported in literature (Cengel and Ghajar, 2011; MacIsaac et al., 1999). The spectral existence is seen to be lowest in the ultraviolet region, small in the visible region and highest in the infrared wavelengths regions. This implies that the emission spectra of the halogen lamps produce mostly long wavelength than short wavelength radiations as was expected. This confirms that they are not suitable for plants and microalgae whose absorption is in the visible region (relatively short wavelength region) but highly efficient for photosynthetic bacteria whose absorption is in the visible region, as well infrared region (long wavelength region). Also, with the specific energy content being inversely proportional to wavelengths, the photosynthetic pigment molecules of the bacteria: carotenoid and bacteriochlorophylls, will each experience minimal ionizing effects but however, immensely thermal effects respectively. Therefore, the sensible volumetric heat generation will be greatest for the thermosiphon PBR being illuminated by halogen lamps as to compare to other existing light sources like cool white fluorescent, Gro-lux, AlInGAP II LED and GaAlAs LED, etc.

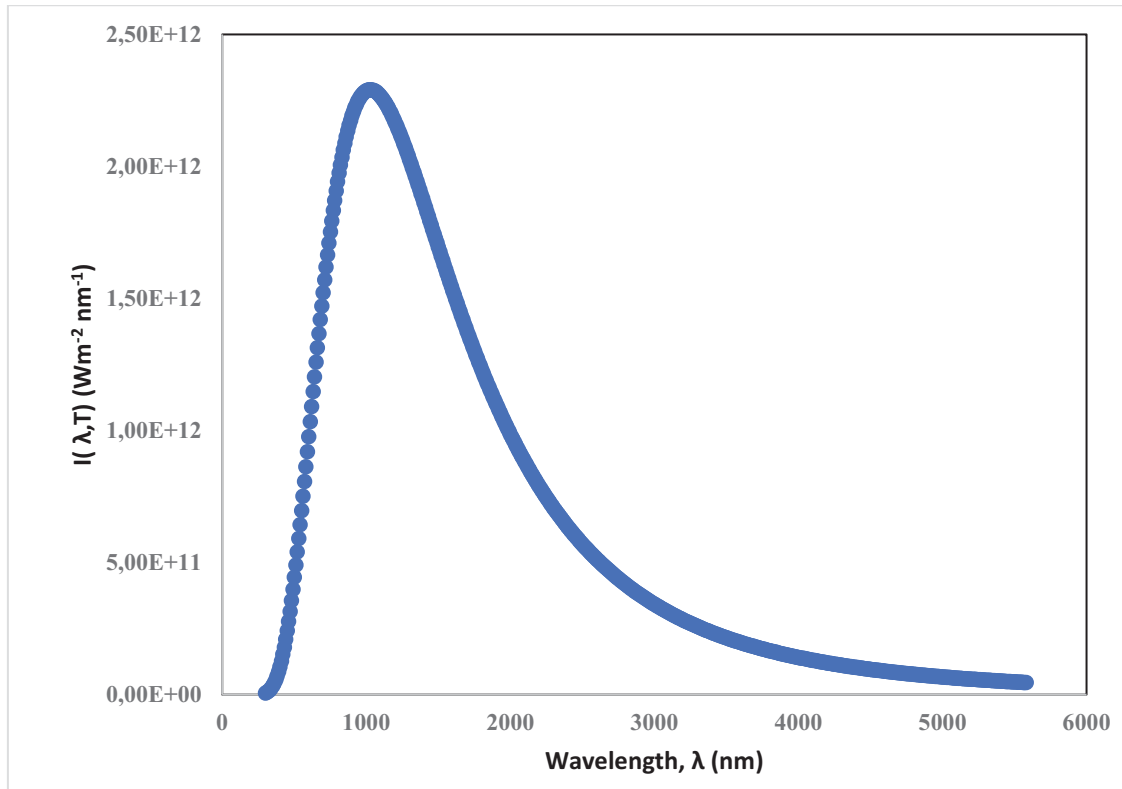


Figure 46: Blackbody radiation curve of halogen lamp used as solar simulators at a color temperature of 2900K

However, the emission spectrum in Figure 46 extends to wavelength regions of over 600 nm where the photosynthetic bacteria do not absorb. Therefore, using this entire spectrum for radiant flux calculation will result to an over estimation of radiant flux which is either not been produced by the experimental halogen lamp or available for absorption by the photosynthetic bacteria. With the box method applied to easily perform the numerical integration over the PAR (Table 13), the actual average weighted radiant flux density ( $W/m^2$ ) available for bacterial absorption is reported in Table 13. The data reveals that the available radiant flux for bacterial absorption increases with an increasing wavelength. This confirms that the volumetric heating effect will be minimal at the short wavelengths, 400 nm but increases as the wavelength approaches 900 nm. This was then used as irradiance on the riser section of the thermosiphon PBR for the radiative transport equation as shown in the UDF (see Appendix C).

Table 13: Summary of average weighted radiant flux density numerically computed with the box model

Box	Wavelength, $\lambda_c$ (nm)	Radiant flux, $I(T)$ ( $10^3 W/m^2$ )
1	400	1.43
2	500	5.25
3	600	11.06
4	700	16.94
5	800	21.45
6	900	24.12

### 3.3.2.2 Spectral extinction coefficient determination

The governing radiative transport equation (RTE) takes into account the spectral intensity as well as the spectral extinction properties of the medium. Therefore, the spectral extinction coefficient of *Rhodopseudomonas palustris* was measured to accurately model the light transfer within an absorbing medium. The absorbance of *Rhodopseudomonas palustris* at five different biomass concentrations ( $Kg/m^3$ ): 0.16, 0.27, 0.38, 0.49 and 0.59 in the spectral range from 400 to 900 nm were measured with UV spectrophotometer. The measurements were performed in triplicates and the arithmetic mean of the result was plotted against its wavelength absorbance as illustrated in Figure 47. This showed the bacterial wavelength absorbance to increase with an increasing biomass concentration. This pattern has been reported for another photosynthetic bacteria like *Rhodobacter sphaeroides* ATCC 49419 (Berberoglu and Pilon, 2007), and even cyanobacteria like *Anabaena variabilis* ATCC 29413-U (Berberoglu and Pilon, 2007).

This confirms that more light is being absorbed in an optical thick medium and contributes greatly to increasing the sensible volumetric heating of photobioreactors via fluorescence and waste metabolic heat. The linear regression between absorbance (Ab) at each wavelength and biomass concentration (X) was performed to estimate the spectral mass extinction coefficient  $K_b$ , as defined in (equation (20)), and reported in Table 14. Figure 48 shows the spectral mass extinction coefficient of *Rhodopseudomonas palustris* within the spectra range from 400 to 900 nm. This mass extinction coefficient includes the specific wavelength absorbance of the photosynthetic pigments plus the light scattered within that wavelength. Generally, the bacteria's mass extinction coefficient levels from 400 to 500 nm, decreases from 500 to 700 nm, peaks at 800 nm and then decreases to 900 nm. This implies that *Rhodopseudomonas palustris* has two light absorptions peaks: around 500 nm and 800 nm which falls in the visible and infrared regions of the

electromagnetic spectrum respectively. Also, they correspond to the absorption peaks of carotenoid and bacteriochlorophylls which are the main photosynthetic pigments responsible for that light absorption in photosynthetic bacteria like *Rhodopseudomonas palustris*. This conforms several published literature about the bacteria's photosynthetic activity region (PAR)(Nogi et al., 1985; Pilon et al., 2011).

Table 14: Spectral attenuation parameters of *Rhodopseudomonas palustris*

Wavelength (nm)	Slope ( $m^3/Kg$ )	$K_b(m^2/Kg)$
400	2.2042	220.42
500	2.2344	223.44
600	1.7231	172.31
700	1.2378	123.78
800	1.7758	177.58
900	1.2465	124.65

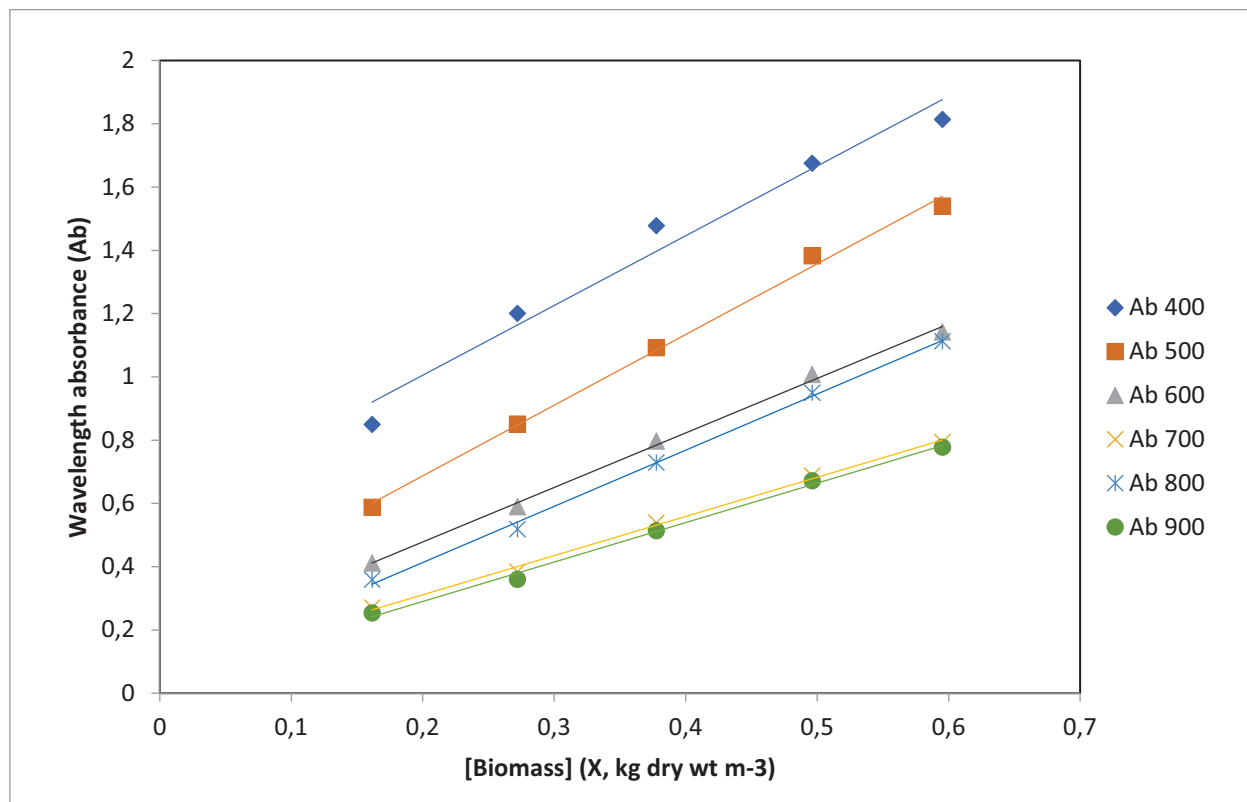


Figure 47: Linear regression between absorbance (Ab) and biomass concentration (X) at various wavelengths (400 to 900 nm)

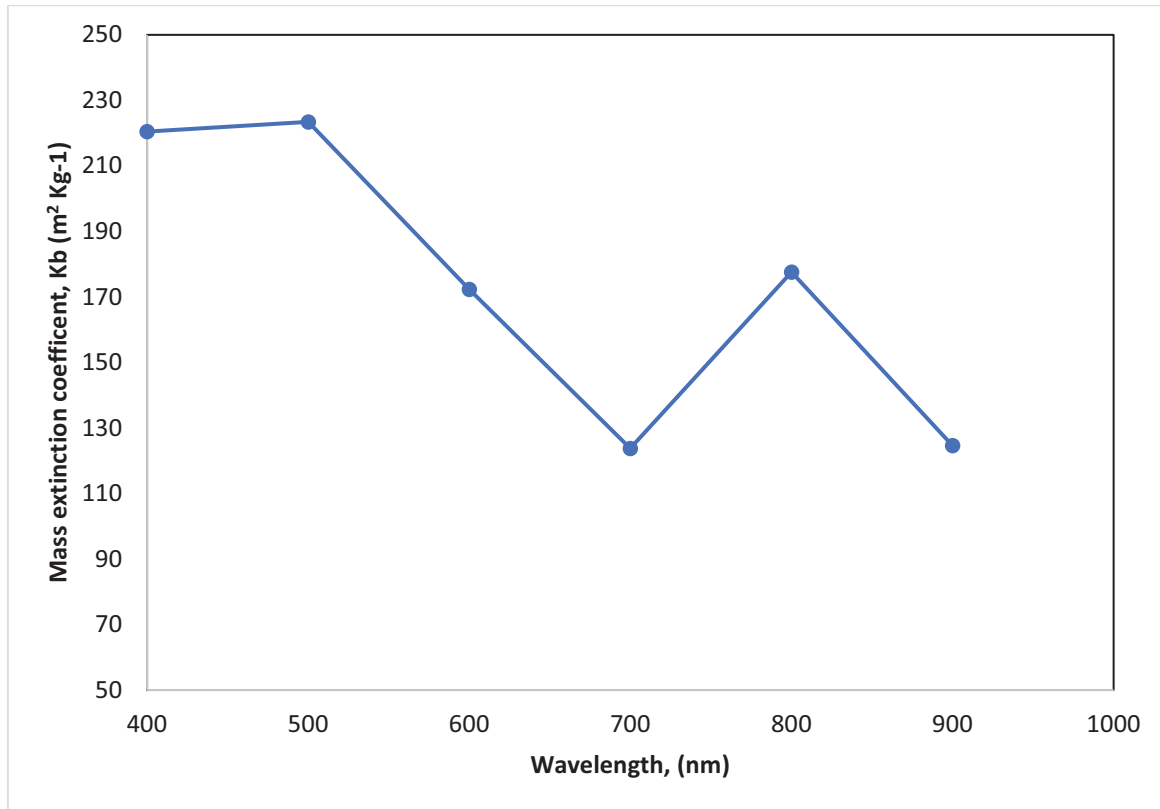


Figure 48: Spectral extinction coefficient of *Rhodospseudomonas palustris* measured at five different biomass concentrations from 400 to 900 nm

### 3.3.2.3 Heat transfer measurements

The thermal balance on the thermosiphon PBR system showed that its medium temperature is controlled by (i) radiative heat transfer from the halogen lamps, (ii) metabolic heat exchange within the system, (iii) convection heat transfer from the air surrounding the thermosiphon PBR, and (iv) convection heat transfer to circulating water at the cooler section of the thermosiphon PBR. Also, the heat transfer and natural fluid circulation within the thermosiphon PBR are directly coupled since as it's responsible for the temperature-induced density variation. Most modeling studies assume the existence of a forced convection correlation which enables them to calculate the heat transfer coefficient by knowing the flow regime and flow profile. However, this approach is inappropriate for the TPBR because of the direct coupling between the external heat transfer and the circulating fluid's density, which are unique for the experimental setup. Therefore, the heat transfer coefficient of thermosiphon PBR's cooler and riser sections were estimated with Newton's law of cooling by curve fitting equation (24) and (25) respectively with experimental data. For heat transfer coefficient of the cooling walls, the arithmetic mean of the three different center-pipe temperature vs time data for the thermosiphon PBR operating under biomass loading of  $0.5 \text{ Kg/m}^3$  active *Rhodospseudomonas palustris* cells was calculated and used for the curve fitting.

Figure 49 shows that the curve fits very well from the steady state temperature of 315.06k to the ambient cooling water temperature. Hence, the numerical estimation of the cooling wall's heat transfer coefficient was  $202 W/m^2K$ . This value implies that the thermosiphon PBR's cooling walls were experiencing heat transfer to the circulating subcooled water by forced convection since as its heat transfer coefficient fell within the range of forced convection by external means ( $10-75,000 W/m^2K$ ) (Ansys Fluent, 2016). On the other hand, for the heat transfer coefficient of the thermosiphon PBR's riser walls, the arithmetic mean of the three different center-pipe temperature vs time data for the thermosiphon PBR operating under hot water at about 341.7K and cooling to environment's ambient temperature was calculated and used for the curve fitting.

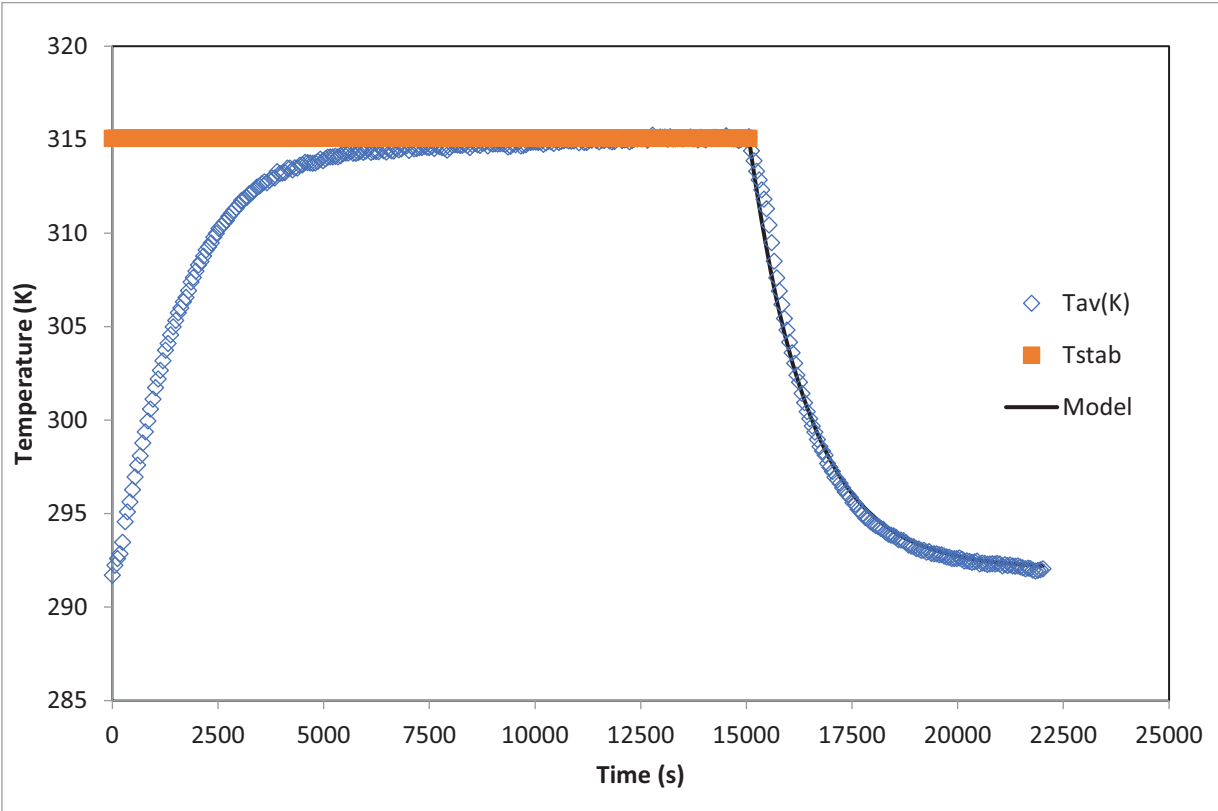


Figure 49: Temperature of thermosiphon PBR as a function of time for the three thermocouple sensor positions. Experimental data (average temperature,  $T_{av}$  and stabilization temperature,  $T_{stab}$ ): from startup to thermal equilibrium indicated with symbols while theoretical curve (model); illumination switch off after 15000 s indicated with a solid line.

Figure 50 shows that the curve fits very well and the heat transfer coefficient of the riser walls was numerically estimated to be  $2 W/m^2K$ . This value implies that the thermosiphon PBR's riser walls were losing heat to the environment via natural convection since as its heat transfer coefficient is far below that of forced convection. This was in accordance with our expectations

and the values were used for the CFD simulations of thermosiphon PBR's heat transfer and buoyancy driven flow.

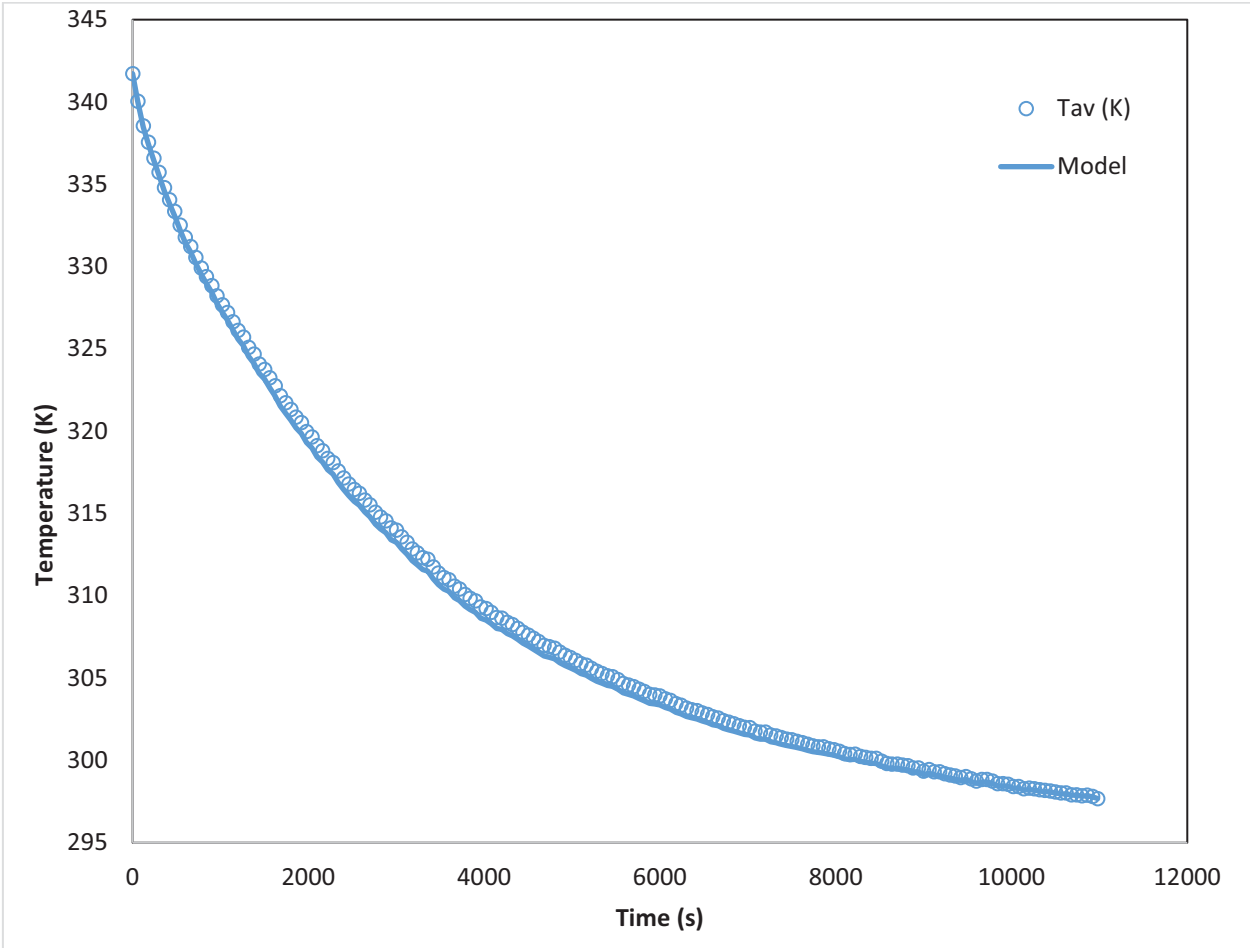


Figure 50: Temperature of the hot water in thermosiphon PBR as a function of times for the three thermocouple sensor positions. The experimental data (average temperature,  $T_{av}$ ) and theoretical curve (model) are indicated with symbols and lines respectively.

### 3.3.3 CFD simulation results

This section contains the thermosiphon BPR's CFD simulation results and discussion. The model was setup in ANSYS Fluent version 17.2 and activated for 2D, transient, bousinessq approximation, thermophysical properties of water, radiation transfer User-Defined Function (UDF), heat transfer coefficient of the riser and cooling walls. The converged solution was post-processed to allow for simple interpretation of the results. The results were obtained in terms of temperature (K) and velocity (m/s) distributions in the working fluid and presented by the means of contours and vectors plots for the modeled variables. This allowed for qualitative analysis by providing a more comprehensive visualization of the thermosiphon PBR operation. (see the attached compact disk (CD) for the ANSYS reported html file for the CFD simulations results).

### **3.3.3.1 Temperature distribution**

The CFD predicted temperature distribution of the thermosiphon PBR is discussed here. As well, the CFD simulated temperature distribution was probe at three positions corresponding to the three experimental center-pipe thermocouple locations for monitoring the thermosiphon PBR's five main sections (storage tank, cooling, downcomer, riser and upper bend sections).

Figure 51 shows the temperature distribution of the working fluid within the thermosiphon PBR and it can be seen that the circulating fluid is thermally heterogeneous. However, areas of high temperatures are observed to occupy the thermosiphon PBR's top section (upriser and storage tank section) while those of relatively lower temperature settle in the bottom (downcomer section). This simulation result verifies the hypothesis that buoyancy effects characterize the temperature distribution and fluid flow within the thermosiphon BPR since as fluid of lower density is floating while that of higher density is settling. This is even more conspicuous at the cooling wall sections where parallel temperature lines show the decrease of the working fluid's temperature as it propagates through the downcomer.

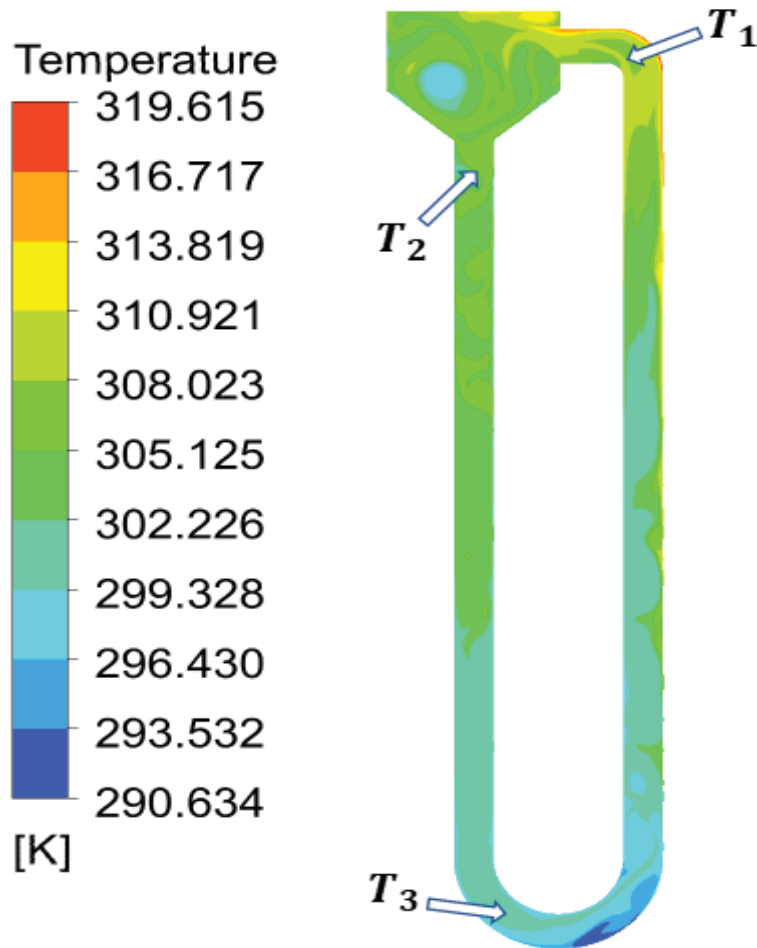


Figure 51: Temperature contours of CFD steady state simulations showing the temperature notation points, which correspond to the thermocouple positions in the experimental set-up

Another important observation is made at the cooling and riser section where the working fluid's temperature distribution is observed to be highly stratified as seen in Figure 52. This is presumed to be the result of force convection of the subcooling water at the cooling walls and light attenuation in the riser section respectively. The defined heat transfer coefficient of the cooling walls brought about its rapid cooling as the sidewalls had a significantly lower temperature as to compare to the inner annulus of cooling section. On the other hand, the UDF implemented radiative transfer equation (RTE) was responsible for the non-uniform, left to right temperature stratification through the riser's cross section. This is in accordance with the hypothesis of the non-uniform volumetric heating being dependent on the attenuated light from the front irradiated wall surface to the reactor center and rear surface according the famous Beer-Lambert law (Luo and Al-Dahhan, 2011, 2004) which is highly heterogeneous in the presence of bacterial cells (Benson and Rusch, 2006) and for buoyancy forces in these cases.

The stratified nature of the riser's temperature predicted by the CFD model agrees very well with the results presented by (Roldán et al., 2014) in the thermal analysis of a volumetric solar absorber. However, their result cannot be directly used to match the thermosiphon PBR's CFD model since their solar absorber was made of a solid material with gradual changing porosity. Other thermosiphon CFD analyses focus mostly on the quantitative validation of probed temperature readings, mainly because the temperature distribution in the absorber/solar collection are very uniform or homogenous since as they defined either a constant wall temperature or uniform surface flux heating. Their modeling methodology is practically limited to situations where the absorbers/solar collectors are coated with black material to enhance solar absorption. However, this was not the practical case for the thermosiphon PBR whose riser walls were transparent to enhance light penetration and available for microbial absorption as the design consideration.

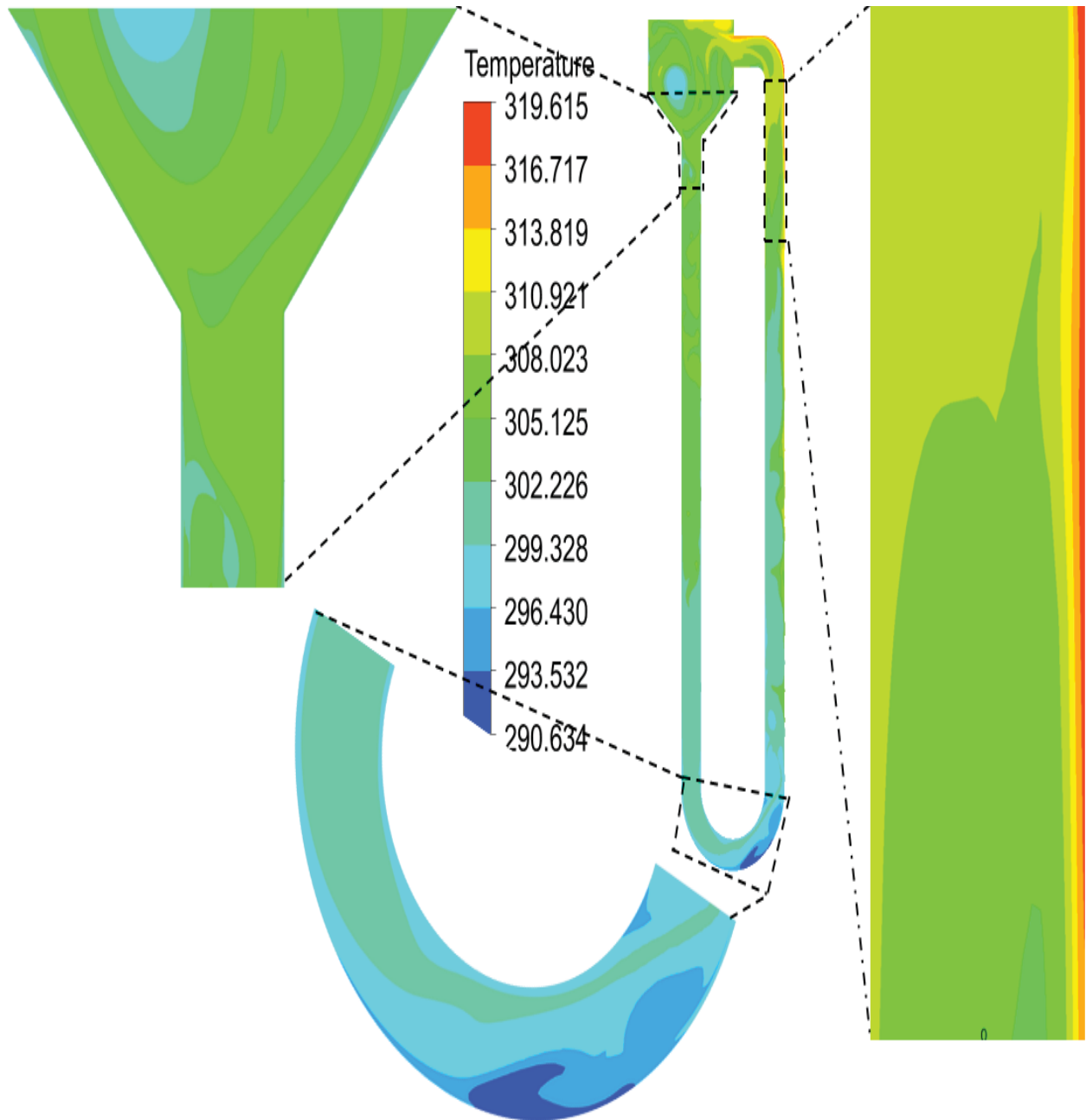


Figure 52: Temperature contours distribution with magnified areas of high temperature gradient within the thermosiphon PBR's CFD simulation

### 3.3.3.2 Velocity profiles

The CFD predicted velocity distribution of the thermosiphon PBR is discussed here. As well, the CFD simulated velocity distribution was probe at two positions corresponding to the bottom and top riser position used to monitoring the thermosiphon PBR's riser local flow velocity.

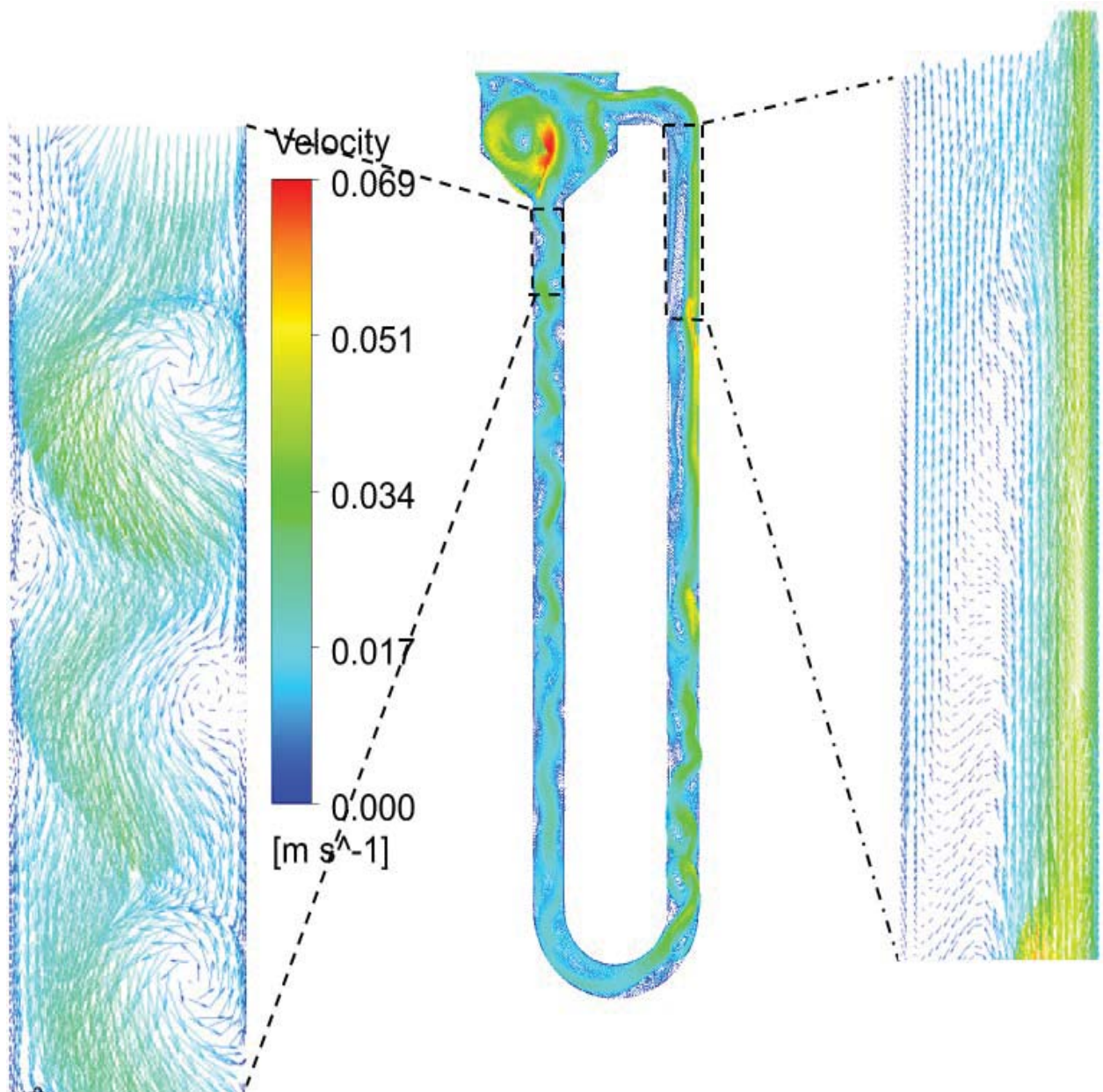


Figure 53: Velocity vectors of the CFD simulations showing the direction of flow due to thermosiphoning

Figure 53 shows the velocity vector distribution of the working fluid within the thermosiphon PBR and it can be seen that the velocity vector distribution varies throughout the domain. However, the velocity vectors indicate an upward movement on the riser section with a corresponding downward movement on the downcomer section. This indicates the presence of buoyancy driven flow which is highly favored towards the forward direction with little or no flow reversals. These results are a better representation of the reality in the TPBR than those presented in literature (Louisos et al., 2013) which make use of constant uniform wall temperature and surface flux by reporting the bulk fluid motion of a 2D thermosiphon to be a chaotic flow regime and associated with flow reversals. This high degree of forward buoyancy driven flow is presumed to exist as a result of the smooth light transfer through the riser section captured by the UDF

radiative transfer equation. The gradual attenuation of this light and subsequent volumetric heat generation guarantees a smooth temperature-induced density gradient which enhances the forward buoyancy flow. At the same time, it eliminates the heat deprived internal core of the absorber/solar collector which brings about flow instabilities in other thermosiphon systems.

The eddies within the downcomer section are seen to be very strong with a serpent-like profile. The defined adiabatic boundary conditions of the downcomer walls prevented heat losses through that section resulting to the almost steady temperature and density of the circulating. However, the effect of gravity was greatest within this section and was interpreted to be responsible for the rapid downward movement of the fluid since it is colder and generally heavier. This was practical impossible to see in experimental setup because the downcomer section of TPBR was thermal insulated with a layer of cotton wool and aluminium foil. However, this revelation provides valuable insights into fluid flow profile within the downcomer section.

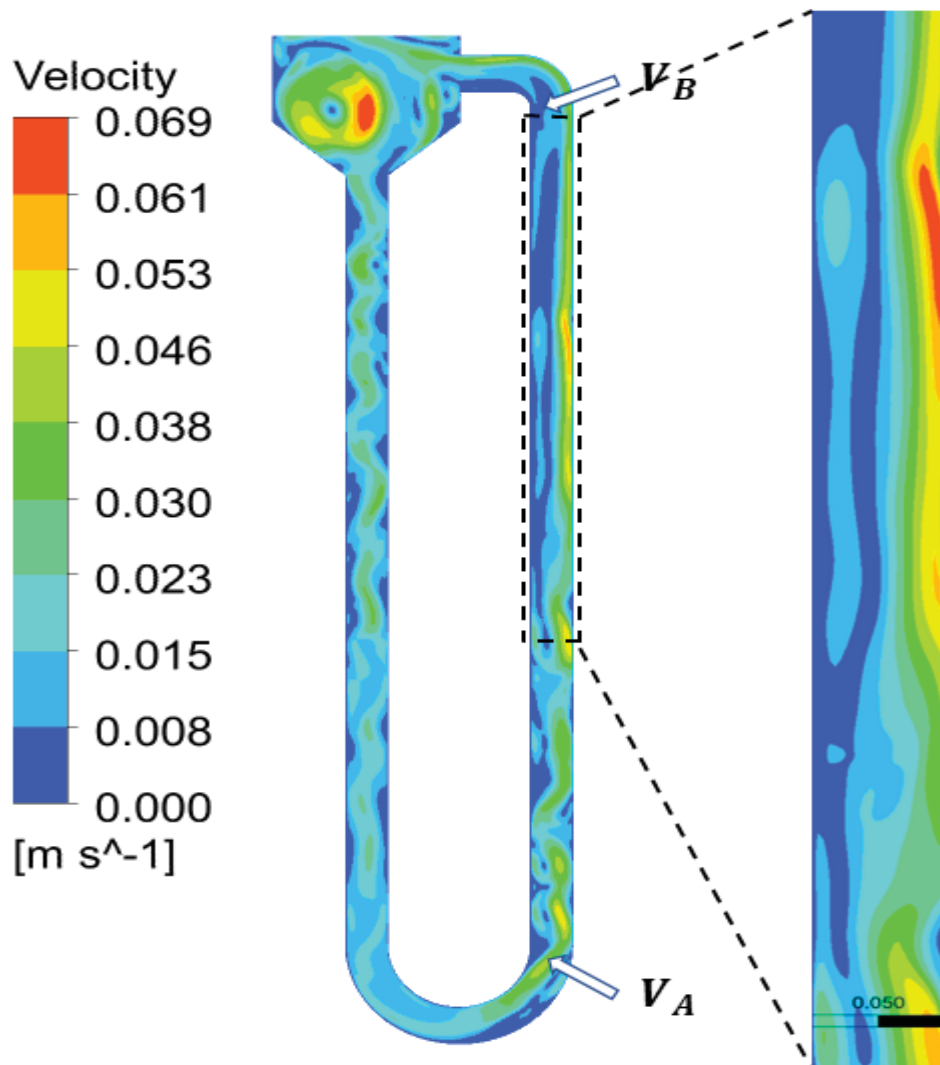


Figure 54: Velocity contours of the CFD simulations showing the two velocity notation points and the riser's flow profile.

Figure 54 shows the velocity contour distribution of the working fluid within the thermosiphon PBR and it can be seen that the velocity of the working fluid varies throughout the domain. This corresponds very well with the natural fluid flow being induced by density gradients which are caused volumetric heating through light absorption and cooling of the working fluid at the riser and cooling section sections respectively. The fluid flow can be attributed mainly to buoyancy effects, agreeing with observation in the flow field visualization experiments. Additionally, it can be noted that the fluid flow velocities predicted by CFD simulation remain laminar, at 0.069 m/s. This velocity falls within the range of other flow velocity studies relating to more conventional photobioreactor designs, at 0.038 m/s, 0.11 m/s and 0.36 m/s for wholly, half and alternately aerated airlift PBRs respectively (Huang et al., 2016). As well, they were in the range of some experimental thermosiphon solar water heating (SWH) systems of  $3.3 \cdot 10^{-2}$  m/s (Morrison et al.,

2005), 0.8 m/s (Gandhi et al., 2011). The 0.8 m/s of Gandhi (2011) is of a larger order of magnitude but this can be likely explained due to their defined outdoor boundary conditions for sunlight which resulted to large temperature differences driving faster flow.

Another important observation is the riser's fluid flow profile which is more tilted towards the front of the riser section. This was expected since as the incident light intensity which when absorbed by the microbial cells is responsible for volumetric heating and buoyancy flow has an inverse relationship with the penetration depth (riser diameter). Therefore, the incident light intensity drops exponentially from the front to the rear surface of the riser according the famous Beer-Lambert law (Luo and Al-Dahhan, 2011, 2004) thereby producing a buoyancy flow which is more tilted towards the front of the riser section. This CFD predicted flow profile agrees very well with in literature for volumetric solar absorber (Roldán et al., 2014).

Another important observation is the swirly eddied fluid flow in the storage tank section, which corresponds well with experimental observation (see section Fluid flow profile validation), and was interpreted to occur as a result of rapid heat lost at a small dimension cooling section bringing about rapid density variations. This occurrence is will highly favor the satisfactory passive fluid flow and keep bacterial cells in suspension within the tank section of the TPBR. Also, it would likely result to improving the mass transfer, and eliminating the light and nutrient gradients through enhanced mixing thereby increasing biomass productivity

### **3.3.4 Flow visualization**

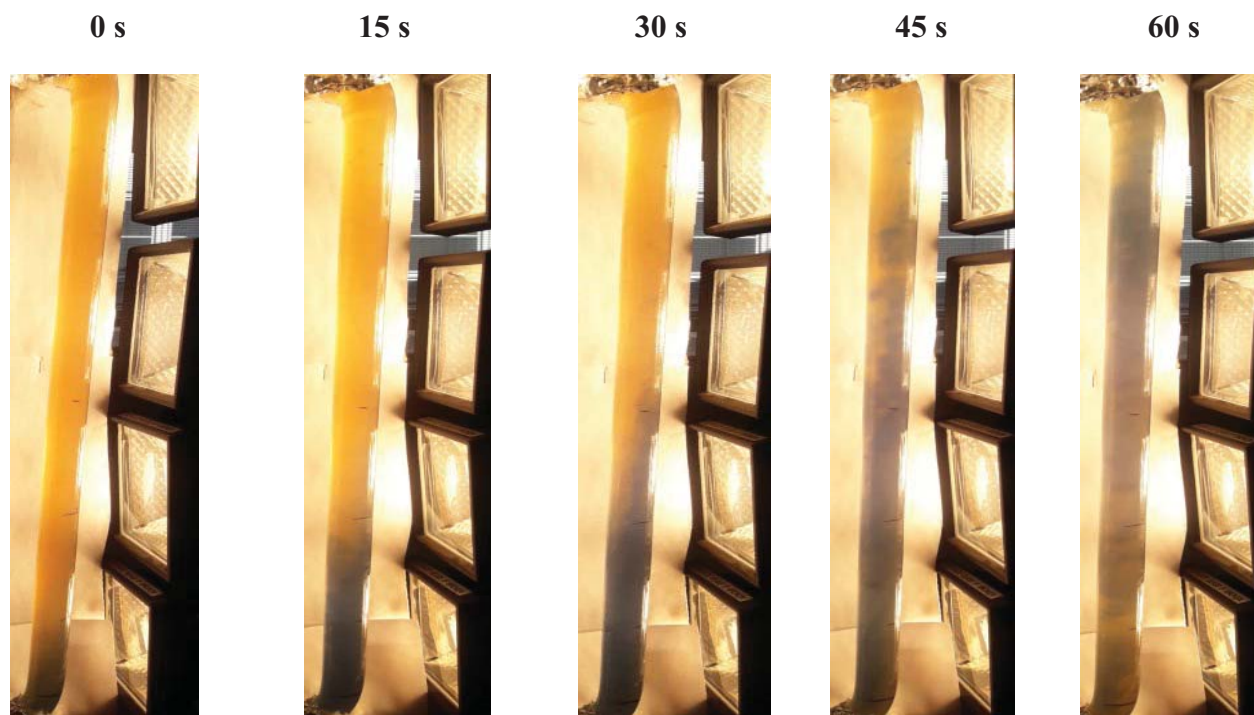
This section contains the results and discussions for the visualization of local circulation patterns generated by the buoyancy flow through the riser section of the thermosiphon PBR. This provides insight into the hydrodynamics of both experimental scenarios: activated and inactivated *Rhodopseudomonas paulustris* cells operating under the same conditions of  $0.5 \text{ kg/m}^3$  of biomass concentration. This experimental fluid dynamic investigation was realized through the nonintrusive technique of 'image maker method' (Joshi et al., 2009). As already stated, the underlying principle of this technique is the measurement of the displacement marked by the fluid particles in consecutive images. A small difference of less than 3% was reported when this image maker method under the name "color dye method" was compared with the commonly used acid tracer method with pH meters for the mixing time characterization of a plat panel airlift PBR (Reyna-Velarde et al., 2010). Therefore, the image marker method was reliable for the hydrodynamic characterization of buoyancy driven flow through the riser section of the TPBR. Conversely, the acid tracer method was inappropriate for this study since as the TPBR's geometry was too constrained for the insertion of a pH meter on the riser section.

The thermosiphon PBR medium content is comprised of a buffered solution, *Rhodospseudomonas palustris* (fresh and dead) which produced a purple color that changes to pale yellow upon addition of the bromothymol blue indicator. This occurrence was expected since the buffer solutions weaken the effect of the *Rhodospseudomonas palustris* media's pH 7.3 to below 6.0 where the bromothymol blue indicator showed a pale-yellow color. The pale-yellow color was observed to change into blue upon the drop wise addition of a 3.5 M NaOH solution from the top septum-sealed port at the cap of the thermosiphon BPR. This pale yellow to blue color change was expected since the presence of NaOH solution brought about a pH shift to some value greater than 7.6 where the bromothymol blue indicator showed a blue color. This color change and dissipation of the thermosiphon PBR medium content was marked by the plug of fluid motion in consecutive images.

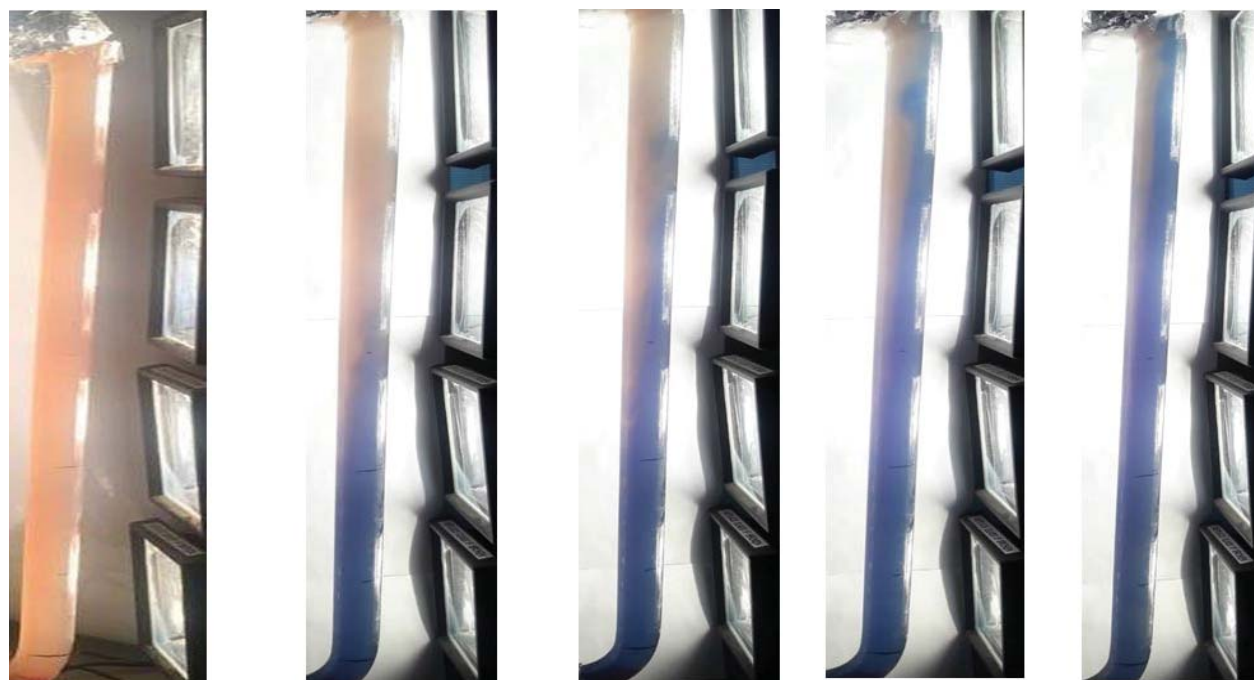
Figure 55 shows snapshots taken at the riser section of the thermosiphon BPR for activated and inactivated bacterial cells operating under the same conditions so that they could be compared. Photographs were taken at intervals of 15s from the time the color change (pink to blue) emerged at the bottom until when it reaches and exit the top of the riser into the storage tank via the up-riser. Photos on the top side of Figure 55 had inactive bacterial cells while the others at the bottom side had active bacterial cells. The overall and specific color change dissipation rates between the various time intervals in one particular case and that of the same time interval between the two cases (active and inactive experiments) were identified as the main features worth observing in the photographs for comparison. In general, this color change dissipation rates provides insights into the fluid velocity as well as TPBR's mixing which are difficult to evaluate independently.

From 0s to 60s of both cases, it is clearly seen that there is a general upward movement of the flow mixing towards storage tank due to buoyancy effect, strong enough to propagate this color dissipation within its main flow. It is important to note that the color dissipation and turbulence is favoured towards the front than to the rear surface of the riser section, corresponding with the anticipated light absorption and, therefore density, gradient. Furthermore, the flow mixing at the same time intervals of the two cases clearly shows the color dissipation and turbulence rate to be slight better for the active than the inactive bacterial cell experiments. This was expected since the active *Rhodospseudomonas palustris* cells were stilling undergoing metabolic heat generation with the light absorption meanwhile the inactivation process halted that for the inactive *Rhodospseudomonas palustris* cells. Also, the inactivated *Rhodospseudomonas palustris* cells may have experience morphological cell damages during the inactivation process which might have affected their photosynthetic pigment molecule and light absorbing potentials. It was

presume that this contribution led to an increased stabilization temperature and enhanced the dissipation and turbulence within the riser section of the thermosiphon PBR.



**Inactivated bacterial cells**



**Active bacterial cells**

Figure 55: Flow visualization photographs of the TPBR at intervals of 15s, operating under  $0.5 \text{ Kg/m}^3$  intervals under for active and inactive bacterial cells with pink to blue color dissipation showing indicating fluid flow through the riser

### 3.3.5 Validation of CFD by comparison with physical experiments

This section contains the results and discussion for the validation of the CFD model via experiments. As already stated, this validation will provide some credibility to the model results and the temperature, velocity, and fluid flow profile were the parameters identified for validation purposes. These model parameters were validated via (i) quantitatively through the measurements of three center-pipe temperatures on the thermosiphon PBR and two points local flow velocity at on the riser's buoyancy flow field, and (ii) qualitatively through flow profile visualization on riser section of the thermosiphon PBR. Since the experimental results of the active *Rhodospseudomonas palustris* were generally better than those of the inactive bacterial cells, their results were used to validate the numerical CFD simulation results in this section using (equation (22)). More to that, the actual thermosiphon PBR will be operated with active bacterial cells absorbing light for photosynthesis while continuously converting substrates to products like biohydrogen

$$\% \text{ Deviation} = \frac{|Experimental \text{ data} - CFD \text{ predicted data}|}{Experimental \text{ data}} \times 100 \quad (22)$$

#### 3.3.5.1 Temperature validation

The experimental temperature readings of three center-pipe locations ( $T_1, T_2, \text{ and } T_3$ ) were measured and compared to the CFD predicted temperatures as presented in Table 15. The CFD simulations results were able to predict the thermosiphon PBR's thermal performance for all three points with a relatively small difference of less than 5% as observed. In addition to the experimental measurement error, the thermal radiation, heat transfer coefficients and buoyancy fluid flow influences the temperature value obtained. More to that, the numerical simulation was a 2D model, and the radiation heat transfer and extinction coefficient by *Rhodospseudomonas palustris* for attenuating light have been included in the UDF volumetric heat source. These conditions have been reported to bring about some deviations of less than 5% for volumetric solar absorber (Roldán et al., 2014). However, the reported deviation of this study is still significantly lower than that reported in literature for thermosiphon heat pipes and natural convection industrial oven with 10.78% (Fadhil et al., 2013) and 15% (Rek et al., 2012) respectively. However, smaller deviation of less than 3% have been reported for volumetric absorber solar absorber (Roldán et al., 2014). This shows that the 2D CFD simulation results are in appreciable agreement with the experimental results. Generally, the CFD simulations under predicted the TPBR's thermal performance. This was a result of the model not accounting for the radiation concentration of 4 halogen lamps as well as their spectral emissivity factors. This

limitation could be improved by making use of a pyrometer to experimentally determine the radiation amplification while accounting for the emissivity at every glass interface.

Table 15: Comparison of measured and CFD simulated temperatures

Measuring point	Experiment (K)	CFD simulation (K)	Deviation (%)
$T_1$	$317.7 \pm 0.5$	307.9	3.1
$T_2$	$313.8 \pm 0.6$	305.5	2.7
$T_3$	$312.6 \pm 2$	299.5	4.2

### 3.3.5.2 Velocity validation

The local flow velocities at two center-pipe points (bottom and top) of the riser section were used to quantitatively compare the CFD simulation results as presented in Table 16. Note that, the experimental local flow velocity was unmeasured at the starting point (bottom riser) since it is the first point of distance-time velocity measurement. The time taken for the color change and dissipation rate to travel the riser distance to the top point (end point) was measured and recorded as  $V_2$ . The local flow velocities between these two points were then compared to the probed CFD simulation results at the same points which were generally less than 9%. Nevertheless, these results are still acceptable although there is certainly room for improvement through the use of more sophisticated non-invasive fluid flow measurement techniques like the high resolution digital Particle image Velocimetry (PIV)(Gandhi et al., 2011; Joshi et al., 2009; Morrison et al., 2005)

Table 16: Comparison of measured and CFD simulated velocities

Measuring point	$V_1$	$V_2$	Local velocity $ V_2 - V_1 $
Experiment (m/s)	Unmeasured	$0.011 \pm 0.0010$	$0.009 \pm 0.0004$
CFD simulation (m/s)	0.0161	0.00763	0.0085
Overall deviation (%)			9.2

### 3.3.5.3 Fluid flow profile validation

Photographs of the local fluid flow profile at 45s and 60s intervals passing through the riser section were assumed fully developed and therefore used to qualitatively compare the CFD simulation results as illustrated in Figure 56. It is clear that this 2D CFD simulation agrees with

experimental data by revealing a fluid flow profile which is more tilted towards the front of the riser section. This is in agreement with literature analysis of light penetration through organisms since the density gradient is strongly dependent on the temperature rise, which is itself a function of light absorption, which drops exponentially from the front to the rear surface of the riser.

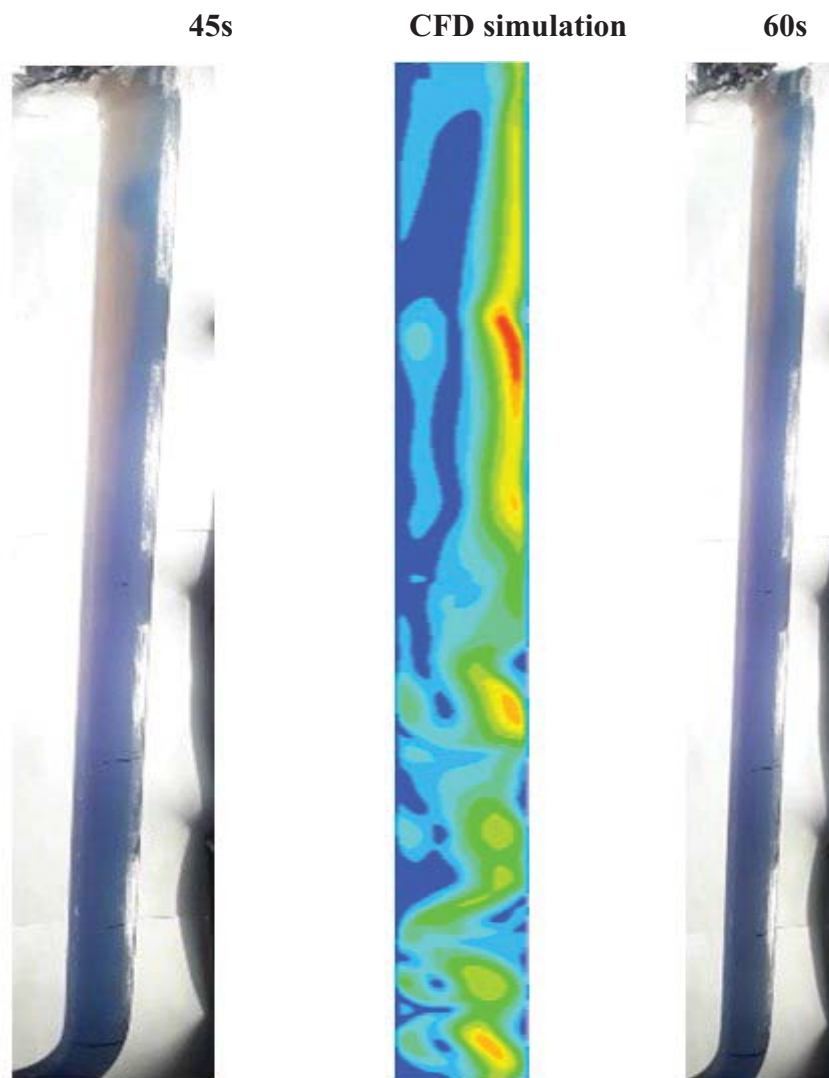


Figure 56: Flow visualization photographs of 45s and 60s compared with CFD simulation results

Also, photographing the thermosiphon PBR's storage tank and cooling tank section shows a swirling and serpentine fluid flow which enhances the mixing intensity around those areas. This was not expected but however matches well with the numerical simulation Figure 57. This was interpreted to occur as a result of rapid heat lost at a small dimension cooling section bringing about rapid density variations, combine to the gravitational pull of the working fluid which enhances its circulation velocity while propagating through the downcomer. This implies that the thermosiphon PBR's mixing speed is highest at the storage tank section and induces the bacterial cells to freely circulate from the illuminated surface to the dark center. This would likely result to

improving the mass transfer, and eliminating the light and nutrient gradients through enhanced mixing thereby increasing biomass productivity.

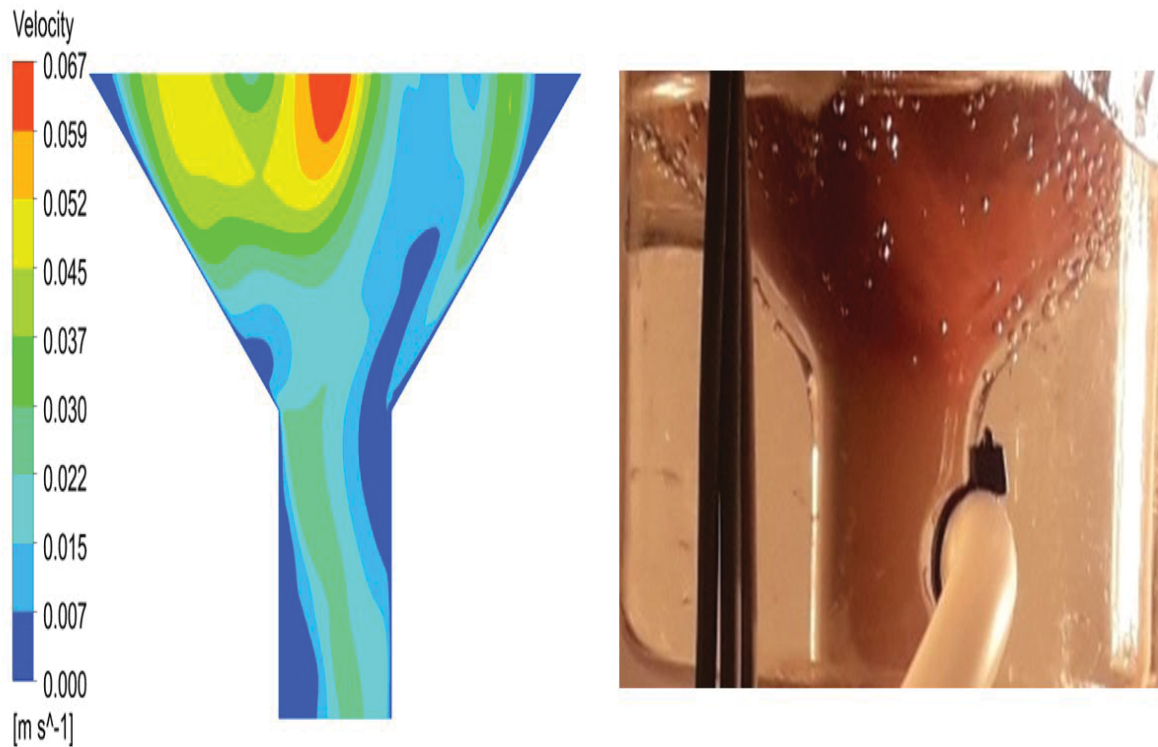


Figure 57: Flow visualization photograph of the storage and mixing tank sections compared with CFD simulation results

### 3.3.6 Effect of light absorption on heating rate

This section presents the results and discussion of microbial light absorption and its effects on the heating of the thermosiphon PBR. It provides insight into the metabolic heat contributions the thermosiphon PBR operating efficiency. Since the thermosiphon BPR is unable to absorb light before the system starts-up, evaluating its startup to steady state behavior is a critical variable for evaluating the reliability and efficiency of the thermosiphon PBR. Theoretically, the thermosiphon BPR's efficiency will be low if it requires a long starting to steady state time or if it is unable to attain steady state (Huang et al., 2017). For both systems, the thermosiphon BPR's startup proceeds through an increase of the sensible heat as a result of bacterial light absorption, and subsequent temperature change that was monitored at three different center-pipe locations by thermocouples probes. The arithmetic mean was calculated and examine over the duration of the experiments followed by the numerical estimation of the rate of heating from light absorption as illustrated in Figure 58.

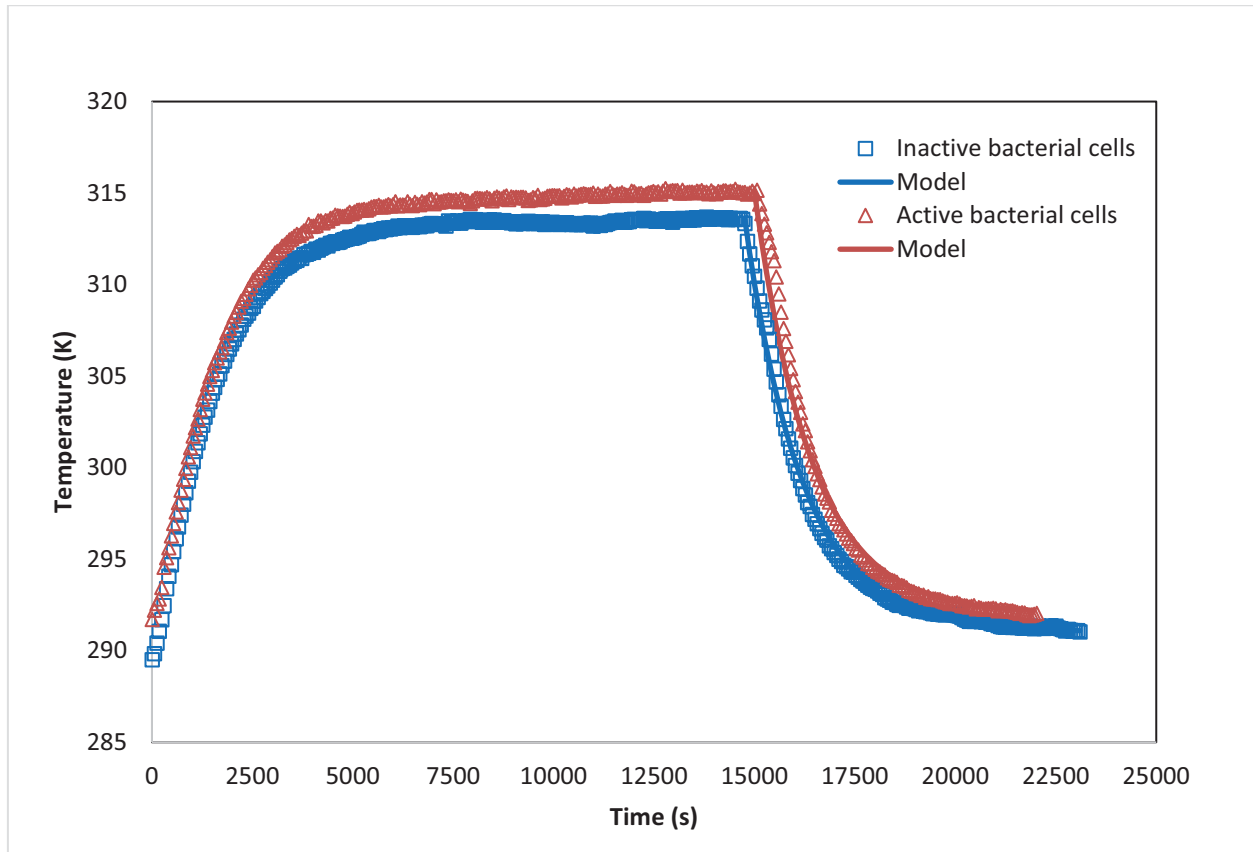


Figure 58: Heating rate: startup to steady temperature-time profile for active and inactive bacterial cells within the thermosiphon PBR and under the same operating conditions.

The startup behavior of the thermosiphon BPR operating with active and inactive bacterial cells were approximately the same by reaching a steady state time of around 5000s. However, their resulting steady state characteristics were slightly different with the highest and lowest steady temperatures of 315.06k and 313.56k attained by the active and inactive bacteria cells respectively. This was expected since as the inactivated bacterial could only absorb light due to their purple color pigmentation which accounted for temperature being lower than that of the activate *Rhodospseudomonas palustris* bacterial cells which able to absorb and generate metabolic heat. Also, the computed heat gain followed the same trend with the highest and lowest being 68.69 J/s and 63.65 J/s for the active and inactive bacteria cells respectively. As a result, there was a 3.7% increase in the steady temperature corresponding to 7.9% increase in heating rate for active and inactive bacterial cells as we earlier hypothesize and this difference was attributed to the metabolic heat generation and fluoresce waste heat for the active bacterial cells as well some morphological damages in the cell structures during the inactivation of the bacterial cells. This is mainly because almost all the photons were assumed to be absorbed by *Rhodospseudomonas palustris* cells and very little light energy is absorbed by the medium because every other parameter (incident radiant illumination, and cooling water flow rate) was relatively constant for both experiments.

Another important observation is that the steady state (315.06K and 313.56K) as well as startup (around 29.15K) temperatures of both cases were of suitable ranges for the cultivation of a wide variety of microbial species including microalgae, cyanobacteria and purple non-sulphur bacteria (Argun and Kargi, 2010; Pires et al., 2017; D Zhang et al., 2015) like *Rhodospseudomonas palustris* which is here investigated. However, the thermosiphon PBR's steady temperatures could even be altered to estimated temperatures of 303.08k where other photosynthetic microbial species have been reported to growth favorably just by increasing the flowrate of the circulating subcooled water.

### **3.3.7 Effect of light absorption on thermosiphoning cells**

This section presents the results and discussion of microbial light absorption and its effects thermosiphoning cells within the thermosiphon PBR. It provides insights into the bacterial cell circulation and free suspension within the thermosiphon PBR as illustrated in Figure 57. Starting the experiment with an initial biomass concentration of  $0.5\text{kg}/\text{m}^3$  for both the active and inactive bacterial cells, the circulating cells in free suspension decreased by 14.2%, and 16.9% corresponding to approximately 86% and 83% of freely circulating bacterial cells within the first 1 hour of operation respectively. Thus, the generated fluid flow from thermosiphoning within the thermosiphon PBR was not sufficiently strong to keep all the biomass in free suspension. However, there was generally a 3% increase of active bacterial cells in free suspension which was maintained throughout the steady state conditions. This was not entirely the case for the inactive bacterial cells as the damage of the cell morphological structure during the inactivation process partially contributed to a further 4.8% in the free suspension circulating cells after 3 hours of operation. Most importantly, the results reveals that a higher stabilization temperature of the thermosiphon PBR leads to an increased thermosiphoning and faster flow rates, which would likely result in enhanced cell circulation, however, bacterial cultures are limited to physiological temperatures. Nonetheless, the thermosiphon PBR did demonstrate the continual and passive circulation of a significant majority of bacterial biomass within the reactor.

## **3.4 Waste survey**

### **3.4.1 Waste survey approach**

#### **3.4.1.1 Data acquisition**

Data was gathered through literature review, focussing on wastewaters produced in South Africa, their volumes, components, concentrations and current treatment methodologies. The National Surveys of each industry were extensively used to give information on each waste stream. Where possible industry partners were contacted, and details were confirmed, and augmented through

informal discussion. Samples of wastewater were taken, and used as point references, to position each waste stream within the context of the studied wastewaters of each industry.

For each waste stream approximate compositions and significant compounds were identified. Each of these compounds was then considered from the literature in terms of photosynthetic bacterial metabolism. If available, investigations into photosynthetic bacterial degradation of full waste streams was also considered.

### **3.4.2 Summary of waste survey**

The following table summarises some of the key literature findings with regards key industrial wastewater effluents. The table includes the industry, the approximate or estimated effluent volumes (either as annual flows or as specific flows, depending on what information was available). The key components of each stream are the identified – the list is not exhaustive, and in many cases there is significant uncertainty about relative concentrations, variability, or even stream content. Nonetheless, for this exercise, some key waste components are identified. The table then identifies the current most common treatment methods, and relative pollutant loads, in order to contextualise this project in the current wastewater treatment field. Then either individual key components, or whole wastewaters, that have been treated by photo-fermentation in the literature are identified. This gives an estimation of the potential for treatment of each waste stream using the proposed process. The final columns give a green-orange-red estimation of the potential for photofermentative treatment, and hydrogen production from, each waste stream.

This table is neither exhaustive, not confident in its estimations. However, it does provide a tool for identifying potentially photo-fermentatively treatable wastewaters, in a South African context.

Table 17: South African industry wastewaters, with their estimated volumes, principle components, current treatment methodologies, and pollutant loads. Additionally, literature citations of PNSB metabolizing key components or whole wastewaters, and green-orange-red estimations of treatment potential and hydrogen production potential.

<b>Industry</b>	<b>WW volumes</b>	<b>Principle WW components</b>	<b>Current treatment methods, if any</b>	<b>Estimated pollutant loads</b>	<b>WW treatment by photo-synthetic bacteria (component or whole stream)</b>	<b>Photo-fermentative treatment potential</b>	<b>Hydrogen production potential</b>
<i>Malt brewing</i>	Beer production: (micro breweries): 17 602 000 L/annum (medium breweries): 351 000 000 L/annum	Organic material Sugars Carbohydrates Starches Proteins Enzymes Aromatic compounds Alcohol	Biological treatment AD	Small breweries: COD: 8049 mg/L SS: 554 mg/L TDS: 255 mg/L Total nitrogen: 48 mg/L Total phosphorous: 30 mg/L TOC: 1295 mg/L Soluble orthophosphate: 15 mg/L Nitrates: 0.1 mg/L	Sugars – <i>R. sphaeroides</i> (Tao 2008, Kim 2004, Keskin 2012) <i>R. palustris</i> (Pott 2013)	Good	Good

*Metal finishing*

Specific water index range: 4.23-399.57 L/m <sup>2</sup>	Immiscible organics: oils, greases, solvents Soluble organics: Wetting agents, brighteners, organic ions and ligands Acids and alkalis Particulate material Complexing agents: Sequestering and chelating agents  Ammonia, Nitrites Cyanides Sulphide	Precipitation, filtration, pH treatment, biological treatment for organics	High pH and low pH High TDS High Cr(vi) High conductivity	None specifically	Medium/unknown (organics may be digestible, however high inorganic content may inhibit growth)	Medium/unknown
--	--	--	--	-------------------	--	----------------

<i>Soft drink</i>	Effluent Discharge (KL/y): 1000-400 000	Sugar Wash water Caustic/detergents and machine lubricant Nitrates Phosphates Sodium Potassium	pH adjustment, settling, AD	COD (mg/L): 87-725 000 TDS (mg/L): 10-19 000 SS (mg/L): 55-3500 pH: 2.8-12.2	Sugars – <i>R. sphaeroides</i> (Tao 2008, Kim 2004, Keskin 2012) <i>R. palustris</i> (Pott 2013)	Good	Good
<i>Sorghum beer</i>	Effluent discharge (KL/y): 483 700 (annual mean)	Sugars Carbohydrates Starches Proteins Enzymes	Discharge to municipal sewer system AD	Chemical oxygen demand (mg/L): 2022 COD pollution load (kg/month): 25 010 Specific pollution load – COD (kg/m <sup>3</sup> ): 3.01 Total dissolved solids (mg/L): 1239 TDS pollution load (kg/month): 15 332 Specific pollution load – TDS (kg/m <sup>3</sup> ): 1.85 Settleable solids (mg/L): 15	Sugars – <i>R. sphaeroides</i> (Tao 2008, Kim 2004, Keskin 2012) <i>R. palustris</i> (Pott 2013)	Good	Good

<i>Edible oil</i>	SEV: 0.04-0.3 m <sup>3</sup> /MT oil	free fatty acids residual gums pigmented and non-pigmented aromatics pesticides degumming acids (phosphoric acid, citric acid) residual soaps emulsifying agents metal catalysts (nickel or palladium)	Flocculation, sedimentation or filtration, WW pond treatment, biological treatment	COD: 6.2-33.2 gO <sub>2</sub> /L FOG/SOG: 5450-41738 mg/L TP, seed oil: 88-1290 mg/L	<i>R. sphaeroides</i> COD reduction olive WW – Tao 2008  <i>R. sphaeroides</i> (COD reduction olive WW) – Karapinar 2006  <i>R. palustris</i> (COD reduction olive WW) – Pintucci 2014  <i>R. sphaeroides</i> (COD reduction olive WW) – Eroglu 2004	Good	Good
<i>Red meat abattoir</i>	7.2 m <sup>3</sup> /annum	Organic matter (excretion) Blood (COD: 400 000 mg/L) Fat	AD	COD: 730-8900 mg/L SS: 1700-3048 mg/L TDS: 595-2805 mg/L	None specifically	Good	Medium/unknown (Nitrogen may inhibit H <sub>2</sub> )

<i>Laundry</i>	200-400 m <sup>3</sup> /day	Heavy metals Organic solvents Alkalis/builders Antichlors Bleaches Softeners Sours Starches Variety of detergents and surfactants Phosphates Salts Soil FOG's Residual textile material	Mostly passed to municipal WWTPs	SS: >1000 mg/L COD: up to 20 000 mg/L BOD: >1300 mg/L FOG: >1100 mg/L TP: 0.5-3.8 mg/L as P TKN: 3.2-80 mg/L as N pH: 8.5-10.6 Absorbance (600 nm): 0.059-0.236 Significant variability between individual laundry processes	None specifically	Poor (low digestible organic content)	Poor
----------------	--------------------------------	---	--	---	-------------------	--	------

Tanning and leather finishing	50 m <sup>3</sup> /1000 kg raw hides	<b>Inorganics</b> Sulphates and sulphides caustic agents Chlorides Chromium sodium bicarbonate Magnesium oxide Ammonium Heavy metals <b>Organics</b> proteolytic enzymes formic acid Surfactants emulsified oils Syntans, resins, tannins Proteins Fats Organic acids Organic solvents Dyestuffs	Screens, filtration and settling Primary treatment: flocculation, pH correction, precipitation, fat traps Secondary treatment: biological treatment, AD, activated sludge	pH: 3.46 12.7 COD: 412-12 091 mg/L TDS: 812-22 244 mg/L TSS: 839-1268 mg/L Sulphates: 702-2780 mg/L Chlorides: 474-12 022 mg/L Total chromium: 1.31-46 mg/L	Dye decolourisation <i>R. palustris</i> (Reactive black as eg) (Wang 2008) Organic acids Many examples – see Appendix A	Medium/unknown	Medium/unknown
-------------------------------	--------------------------------------	--	---	---	--	----------------	----------------

<i>Paper and pulp</i>	SEV: 0.08-84.5 m <sup>3</sup> /t Effluent discharge: 45-92 260 m <sup>3</sup> /d	Lignin organic components from wood chlorine dioxide caustic soda hydrogen peroxide	Clarification Activated sludge Dissolved air flotation Belt press Irrigation Anaerobic digestion	COD: 165-3853 mg/L SS: 34 2260 mg/L Conductivity: 211-4970 uS/cm pH: 6.5-8.5 N: 0.1-1.2 mg/L P: 0.1-0.5 mg/L SO4: 16-565 mg/L Cl: 11-340 mg/L Na: 10-740 mg/L	<i>R. palustris</i> (Degradation of 2-Chlorophenol in effluents from paper and wood industry) – Mutharasaiah 2012	Medium (Undetermined digestibility)	Medium/unknown
<i>Iron and steel</i>	SEV: 0.9-3.6 m <sup>3</sup> /t	Heavy metals Hydrocarbons Cyanide compounds Nitrogen compounds Oil/grease	Clarification Activated sludge Dissolved air flotation Evaporation Ammonia stripper	COD: 13 mg/L Conductivity: 81-3493 uS/cm Fe: 0.02-0.28 mg/L Cr: 0.01-0.14 mg/L Cl: 2.5-145 mg/L Na: 0.12-160 mg/L Mn: 0.03-1.72 mg/L	None specifically	Poor (low organic content)	Poor

*Cane sugar processing*

SEV: 0.1-11.53 kL/ton cane	Inorganics Sugars Sugar metabolites Phosphates	Physiochemical processes (settling and flocculation)  Biological treatment (pond systems, activated sludge system)  Natural percolation through sand  Dilution	COD: 110-6820 mg/L BOD5:COD: 0.08-0.6 mg/L TSS: 5-1480 mg/L TDS: 1008-1480 mg/L TP: 0.8-5.9 mg/L Cl: 50-522 mg/L	Sugar wastewaters  <i>R. sphaeroides</i> Karapinar 2006 Kapdan 2006 Keskin 2012 Yetis 2000  <i>R. palustris</i> Fascetti, 1998 Singh, 1993 Xu, 2013	Good	Good
-------------------------------	---	--	---	--	------	------

Textile industry	80-90% of specific water intake	<b>Inorganics</b> Alkalis and acids Bleach Dyes	Primary: Mechanical, neutralisation, sedimentation	COD: 291-1831 mg/L NH3+: 0.03-31.45 mg/L	<i>R. palustris</i> (Reactive black 5 decolourization of textile effluent) – Wang 2008	Medium/unknown	Medium/unknown
	12 128-284 075 kL/year (dyers and finishers)	Salts Surfactants Stabilisers Starch Chromium, copper, zinc, lead or nickel (some effluets)	Secondary: Biological treatment, WW ponds	PO4-: 1.71-31.29 mg/L pH: 6.62-10.10 Conductivity: 78.52-1159.45 mS/m TSS: 53.00-746.00 mg/L TS: 753.33-7256.00 mg/L			
	29-75 500 kL/year (producers)	<b>Organics</b> detergents natural oils waxes carboxymethyl cellulose polyvinyl alcohol organic solvents volatile organic compounds		Nitrate: 0.45-4.09 mg/L Chlorides: 66.36-3140.45 mg/L Sulphates: 64.24-308.63 mg/L			
	106 800-840 000 kL/year (technical and traditional textiles)						

Poultry	56-10 944 000 kL/annum	High BOD Proteins Fats Salts Bacterial contamination	Biological treatment AD Composting	COD: 1000-6000 mg/L SS: 51-1500 mg/L EC: 75-2000 mS/m TDS: 500-4000 mg/L TKN: 21-250 mg/L NH4-N: 0-100 mg/L TP: 5-50 mg/L PO4-P: 0-250 mg/L Na: 0-500 mg/L Cl: 101-500 mg/L	None specifically	Good	Poor (high nitrogen content)
---------	------------------------	--	--	--	-------------------	------	---------------------------------

**Key:**

---

WW	Wastewater
COD	Chemical oxygen demand
SS	Suspended solids
TDS	Total dissolved solids
TOC	Total organic carbon
AOX	Adsorbable organic halides
SEV	Specific effluent volume
FOG	Fats, oils and grease
SOG	Soaps, oils and grease
TP	Total phosphorous
RP	<i>Rhodopseudomonas palustris</i>
RS	<i>Rhodobacter sphaeroides</i>

### **3.4.3 Industries of interest**

From the current round of work examining wastewaters in a South African context, several industries were highlighted as having waste streams of interest to this project. These wastewaters were flagged to contain components that purple bacteria have been shown to metabolise, and therefore have the potential to be treated in the proposed process. These wastewaters are therefore discussed below.

#### **3.4.3.1 Sugar refining**

The sugar rich wastewaters from sugar refining often are used as feedstock for ethanol production, which in turn produces another wastewater, lower in sugar content. This waste stream, commonly known as vinasse, has a high organic loading (often in the region of 10 000 COD), significant concentrations of phenolic and polyphenolic compounds, as well as organic acids, sugars, proteins, salts and other compounds.

The stream has been found to be difficult to treat using conventional wastewater treatment methods, mostly due to its high phenolic compound component, which can inhibit bacterial growth and metabolism.

There is some evidence, however, that *R. palustris* is able to metabolise some of the organic portions of this wastewater. This study has preliminary data indicating COD reduction, and bacterial growth, when *R. palustris* is cultivated in 50% diluted vinasse. Further testing is required to elucidate which compounds are being metabolised, and to what degree.

#### **3.4.3.2 Abattoir**

This industry is still under investigation, and further information will be added as the project progresses.

#### **3.4.3.3 Brewing**

The production of beer (either sorghum, malt, maize or other cereal beers), produces wastewaters rich in proteins, sugars, carbohydrates and other components. Also of interest is the solid waste, which is sometimes fed to an anaerobic digester (as is the case at the SAB Newlands factory). The effluent from the AD is ideal for treatment by this proposed process.

#### **3.4.3.4 Edible oil industries**

There are various edible oil industries of importance in South Africa, such as canola oil, sunflower oil, olive oil, and to a small degree nut oils such as macadamia oil. These industries produce a

number of wastewaters which often include high concentrations of free fatty acids, as well as residual gums, pigmented and non-pigmented aromatics, pesticides and degumming acids.

Many of these components have not yet been demonstrated to be metabolised by photosynthetic bacteria, and so this study will include these wastewaters for further study.

#### **3.4.3.5 Paper and pulp**

The paper and pulp industry produces several waste streams, at large volumes. These wastes vary in composition from those containing high concentrations of inorganic salts (which would not be treatable using this process), to some which are comprised mainly of cellulose.

There is limited opportunity for the treatment of these waste streams by this process, as they emerge from the plant, since photosynthetic bacteria do not express cellulases, and so are unable to metabolise long cellulosic polymers. However, an opportunity does lie in the combination of a pretreatment step, which hydrolyses the celluloses and lignins to oligomers prior to treatment by *R. palustris*. This study has already shown that *R. palustris* is able to metabolise and grow on xylose, which has not yet been demonstrated in the literature. Further investigations into pre-treatment methods will be conducted, to examine the potential of this process addition.

#### **3.4.3.6 Petrochemical**

Very little concrete information has been forthcoming from South African industry partners in this field. However, what is known (from some informal discussions) is that several wastewater streams are produced during petrochemical refining (for example, by SASOL). Many of these wastewaters are likely to contain linear and branched alkanes, which have not yet been shown to be metabolised by photosynthetic bacteria. However, one stream which shows significant potential is one which contains organic acids in concentrations of around 1-10 g/L. *R. palustris* is well known for its ability to metabolise organic acids, particularly in lower concentrations such as these.

These waste streams therefore constitute a significant opportunity for treatment by this organism. However, due to the limited information available directly from the companies concerned, future work will focus on using literature estimations of petrochemical wastewaters.

#### **3.4.3.7 Pharmaceuticals**

The pharmaceutical (and nutraceutical) industries produce a large number of varied wastewaters, of comparatively small volume, and variable component and concentration profiles. This variability makes analysis of the suitability of these wastewaters for treatment using the proposed

process difficult. Nonetheless, many of the components found in pharmaceutical wastewaters are organic compounds, such as fillers, gelatine from pill formation, colourants, and other compounds. Several of these show promise as substrates for metabolism by photosynthetic bacteria.

Local industry, has to date, been unwilling to allow discussion of wastewater components. Nonetheless, this industry may be of interest for further examination.

#### **3.4.3.8 Fisheries**

Fishery wastewaters contain very high organic loadings, with high protein, fat, salt and some carbohydrates. There has been little research demonstrating the use of photosynthetic bacteria for the treatment, or even metabolism, of such compounds. However, it is highly likely that *R. palustris* will be able to utilise these compounds, since they are likely to be easily accessible to the organism. Indeed some preliminary testing has already shown growth of the organism of fishery wastewater from a local industry partner. Further testing is, however, required.

#### **3.4.3.9 Anaerobic Digestion effluent**

The concentrations of organic acids, and other organic compounds frequently found in AD effluent make it an excellent candidate for further treatment and polishing by *R. palustris*. Many studies have shown metabolism and hydrogen production from individual organic acids by the organism, and some work has shown the growth of the organism on AD effluent. However, AD effluent is often rich in ammonia or nitrate, both of which inhibit hydrogen production by the organism. This can be circumvented by using an *R. palustris* strain which constitutively produces hydrogen, or operating the system in such a way that the ammonia is consumed before reaching the hydrogen production portion of the reactor. These possibilities are being investigated as part of this study.

## CHAPTER 4: CONCLUSIONS AND RECOMMENDATIONS

The project can be considered successful with regards most of its aims, although there is still further work to be done to take this technology to fruition.

In brief, each objective has been achieved, moving towards the goal of developing a novel wastewater treatment methodology using anaerobic photosynthetic bacteria within a novel photobioreactor configuration. The tools, and objectives used to achieve this overarching goal were to: investigate potentially treatable wastewaters in a South Africa context; to develop and model a novel thermosiphon based photobioreactor; to evaluate hydrogen productivity on these wastewaters and using this PBR. While there are still questions around the continuous treatment of wastewaters, and how a scaled up reactor will operate in comparison to the bench-scale reactor, significant strides towards the development of a feasible hydrogen producing process have been made.

A novel photobioreactor, based on the thermosiphon principle was designed and constructed. Initial tests to investigate the growth of photosynthetic bacteria in this reactor in comparison to test reactors were conducted. Hydrogen productivity, and glycerol consumption (as a proxy for metabolism) in the novel bioreactor is comparable to that seen in the test bioreactors.

In order to more fully understand the bioreactor diameter limitations with regards light intensity, and whether this organism suffers from light inhibition, experiments were set up examining growth rate over time, under various light intensities, in a thin tube reactor (to minimise mutual shading). From these experiments it can be seen that *R. palustris* is able to grow well up to a light intensity of around  $500 \text{ w/m}^2$ , which is significantly higher than, for instance, many microalgae. On the basis of this information, and using light attenuation modelling, the optimal diameter of outdoor reactors can be calculated.

In order to better understand the functioning of the novel reactor, a modelling approach was used. Two approaches to modelling a novel thermosiphon based photobioreactor were taken: mathematical modelling, and computational fluid dynamics modelling on the basis of a prototype reactor. Both of these modelling methodologies led to similar results – cross verifying the methods, and indicating a good approach.

The mathematical model used Matlab as a tool to calculate the expected velocity of light absorbing fluid under the assumption of laminar flow, and based on expected heat generation by

light absorbed by the bacteria. This model anticipated fluid velocities of 0.01 m/s, which was verified using experimentation on the prototype reactor.

The CFD model included an energy dissipation term linked to the Beer-Lambert approximation of light dissipation in a fluid. This builds significantly on the previous thermosiphon CFD literature (which has been performed only with respect to thermosiphon heat transfer equipment – not a light absorbing photobioreactor). The CFD model successfully predicted both heat and velocity characteristics of the prototype reactor, indicating the fluid flow characteristics. The system was shown to be suitable for use with photosynthetic bacteria, as the flow profiles are sufficient to keep the vast majority of the biomass in suspension.

Having developed a novel photobioreactor, the project looked towards what wastewaters might be treated in it. From data gathered from various industrial partners, as well as research and industry publications, a conceptual map of what industries are producing significant volumes of organic containing wastewaters emerged. Significant limitations with regards which wastewater can be treated for simultaneous hydrogen production have however been found. Many wastewaters are rich in ammonia or other nitrogenous compounds – these prevent hydrogen production through the inhibition of the nitrogenase enzyme.

Several local wastewaters were gathered, tested for composition, and tested for photofermentation and photofermentative treatment. Some wastewaters have shown promise with regards both treatment and hydrogen production potential. In particular, food-system wastewaters have been shown to be particularly amenable to photofermentative treatment. For instance, winery wastewaters, olive mill wastewaters and anaerobic digestate effluent have all been shown to significantly decrease in both COD and nitrate concentration during photofermentation. However, many wastewaters have high nitrogenous compound concentrations – these compounds inhibit the production of hydrogen by *R. palustris* by inducing the organism's posttranslational modification system, which shuts down the nitrogen fixing enzymes (and therefore hydrogen production).

Studies have been conducted looking at the growth of *R. palustris* in its planktonic form in these wastewaters, as well as using immobilised cells in batch and continuous experiments, in order to verify whether a continuous photofermentative wastewater treatment method would be suitable for these wastewaters. Both olive mill and winery wastewater have shown COD reduction under batch and continuous immobilised cell operation, suggesting that the proposed continuous reactor system will be suitable for use. Continuous hydrogen production has been seen on immobilised cells over almost 2 months, with no decrease in activity.

The technology requires further development and conceptualisation. Nonetheless, this project has demonstrated a novel photobioreactor system which works well with anaerobic, non-sparged photofermentative systems.

This project brings to fruition firstly a new type of photobioreactor based on the thermosiphon effect, and secondly examines a number of wastewaters with potential for treatment using photofermentation (with the aim of both treatment, and simultaneous value creation, through side products – in this case hydrogen). It is a good starting point for the development of a viable technology, however, several areas of work are still required, both scientifically (there are some very interesting fundamental questions raised by this work), as well as technologically (before application in real wastewater treatment systems, up-scaling, and operational questions still need to be answered).

The recommendations flowing from this work can be summarised in the following:

Firstly, within the context of developing the bioreactor, the heat transfer required to cause the fluid flow is facilitated by cooling fins, in the pilot-scale reactor. However, the initial prototype simply assumed a heat transfer – some fundamental investigations into what configuration, the number of fins, the cooling area and so forth, will be needed if these reactors are to be used more widely.

Secondly, it is likely inefficient to run these reactors as CSTRs, with continual biomass growth and production. Instead, since hydrogen is not growth associated, the reactors can be run with biomass held within the reactor. How best to do this is an important question: our laboratory is currently investigating immobilisation of *R. palustris* in PVA-based cryogel beads. This work is very promising, but has focused on the fundamentals of immobilisation. To bring these two ideas together, one could use immobilised biomass within the thermosiphon bioreactor, thus using passive flow as well as stationary phase treatment. There are several possible configurations around how this could be accomplished – for instance, should a packed bed operation or fluidised bed operation be used? And would the thermosiphon produce sufficient flow to overcome pressure losses in these systems?

Following on from the immobilisation work, it may be that planktonic cells remain the best for wastewater treatment or hydrogen productivity. In which case another method for retaining the biomass should be used. One option for this is the use of a membrane, which retains biomass but allows wastewater to pass.

Further fundamental questions around the operation of a thermosiphon (such as transient flows, arising from daylight fluctuations) will also need to be addressed.

In terms of the organism itself, a significant opportunity for investigation lies in investigation of the organism itself. *R. palustris* is amenable to genetic manipulation, and so avenues for improved metabolism exist, for instance:

Creating nitrogen insensitive mutants, which constitutively produce hydrogen even in the presence of nitrogenous compounds. Some work in other laboratories has shown the potential for this – by removing and altering the post-translational modification of nitrogenases (which render them inoperable), hydrogen can continue to be produced even when the substrate contains nitrogenous compounds. The implication is that wastewaters rich in nitrogenous compounds (which is many wastewaters) could then be photofermented and also produce hydrogen.

One significant limitation in photobioreactor development is the limitation due to mutual shading: the organisms at the surface of the reactor shade the ones further in, until they do not have sufficient light to photoferment. This problem is exacerbated in this organism since it contains such intense pigmentation, and very large light harvesting antennae. One method which may improve operability is if the size of these antennae were reduced, limiting the absorbed light per cell, such that light could penetrate more deeply into the reactor, so that more cells could metabolise. This kind of work has been demonstrated in other PNS bacteria, and in principle could easily be applied to *R. palustris* as well.

A final option for genetic manipulation is the insertion of heterologous genes for the production of other interesting products. In these systems it is likely that any product should sit in a separate phase, otherwise downstream recovery will be difficult. However, there are several gas-phase products which may be of interest, such as isoprenoids or terpenes. The insertion of pathways to produce these products is a promising route for the development of *R. palustris* as a chassis biotechnology organism.

## LIST OF REFERENCES

- Abo-Hashesh, M., Ghosh, D., Tourigny, A., Taous, A., Hallenbeck, P.C., 2011. Single stage photofermentative hydrogen production from glucose: An attractive alternative to two stage photofermentation or co-culture approaches. *Int. J. Hydrogen Energy* 36, 13889-13895. doi:10.1016/j.ijhydene.2011.02.122
- Ación, F.G., Garcia Camacho, F., Sanchez Perez, J.A., Fernandez Sevilla, J.M., Molina Grima, E., Fernández, F.G.A., Camacho, F.G., Perez, J.A.S., Sevilla, J.M.F., Grima, E.M., 1998. Modeling of Biomass Productivity in Tubular Photobioreactors for Microalgal Cultures: Effects of Dilution Rate, Tube Diameter, and Solar Irradiance. *Biotechnol. Bioeng.* 58, 605-616.
- Acien Fernández, F.G., Fernández Sevilla, J.M., Molina Grima, E., 2013. Photobioreactors for the production of microalgae. *Rev. Environ. Sci. Biotechnol.* 12, 131-151. doi:10.1007/s11157-012-9307-6
- Ación Fernández, F.G., García Camacho, F., Chisti, Y., 1999. Photobioreactors: light regime, mass transfer, and scaleup. *Prog. Ind. Microbiol.* 35, 231-247. doi:10.1016/S0079-6352(99)80118-0
- Adessi, A., De Philippis, R., 2012. Hydrogen Production: Photofermentation, in: *Microbial Technologies in Advanced Biofuels Production*. Springer US, Boston, MA, pp. 53-75. doi:10.1007/978-1-4614-1208-3\_4
- Adessi, A., McKinlay, J.B., Harwood, C.S., De Philippis, R., 2012. A *Rhodospseudomonas palustris* nifA\* mutant produces H<sub>2</sub> from NH<sub>4</sub><sup>+</sup>-containing vegetable wastes. *Int. J. Hydrogen Energy* 37, 15893-15900. doi:10.1016/j.ijhydene.2012.08.009
- Akkerman, I., Janssen, M., Rocha, J., Wijffels, R.H., 2002. Photobiological hydrogen production: Photochemical efficiency and bioreactor design, in: *International Journal of Hydrogen Energy*. pp. 1195-1208. doi:10.1016/S0360-3199(02)00071-X
- Alagesan, S., Gaudana, S.B., Krishnakumar, S., Wangikar, P.P., 2013. Model based optimization of high cell density cultivation of nitrogen-fixing cyanobacteria. *Bioresour. Technol.* 148, 228-233. doi:10.1016/j.biortech.2013.08.144
- Alizadehdakhel, A., Rahimi, M., Alsairafi, A.A., 2010. CFD modeling of flow and heat transfer in a thermosyphon. *Int. Commun. Heat Mass Transf.* 37, 312-318. doi:10.1016/j.icheatmasstransfer.2009.09.002

- Anderson, G., 2015. Study of Light as a parameter in the growth of algae in a Photo-Bioreactor ( PBR ).
- Anderson, G., 2003. Study of Light as a parameter in the growth of algae in a Photo-Bioreactor ( PBR ) This page is for on-line indexing purposes and should not be included in your printed version . An ASAE Annu. Int. Meet. 1-23.
- Ansys Fluent, 2016. Module 08 : Heat Transfer.
- Anye Cho, B., Pott, R.W.M., 2018. The Development of a Thermosiphon Photobioreactor and analysis using Computational Fluid dynamics. Chem. Eng. J. 136, 23-42.
- Argun, H., Kargi, F., 2010. Photo-fermentative hydrogen gas production from dark fermentation effluent of ground wheat solution : Effects of light source and light intensity. Int. J. Hydrogen Energy 35, 1595-1603. doi:10.1016/j.ijhydene.2009.12.040
- Asfia, F.J., Dhir, V.K., 1996. An experimental study of natural convection in a volumetrically heated spherical pool bounded on top with a rigid wall. Nucl. Eng. Des. 163, 333-348. doi:10.1016/0029-5493(96)01215-0
- Barbosa, M.J., Rocha, J.M., Tramper, J., Wijffels, R.H., 2001. Acetate as a carbon source for hydrogen production by photosynthetic bacteria. J. Biotechnol. 85, 25-33.
- Basak, N., Das, D., 2009. Photofermentative hydrogen production using purple non-sulfur bacteria *Rhodobacter sphaeroides* O.U.001 in an annular photobioreactor: A case study. Biomass and Bioenergy 33, 911-919. doi:10.1016/j.biombioe.2009.02.007
- Basak, N., Jana, A.K., Das, D., 2016. CFD modeling of hydrodynamics and optimization of photofermentative hydrogen production by *Rhodospseudomonas palustris* DSM 123 in annular photobioreactor. Int. J. Hydrogen Energy 41, 7301-7317. doi:10.1016/j.ijhydene.2016.02.126
- Başaran, T., Küçüka, S., 2003. Flow through a rectangular thermosyphon at specified wall temperatures. Int. Commun. Heat Mass Transf. 30, 1027-1039. doi:10.1016/S0735-1933(03)00161-1
- Benson, B.C., Rusch, K.A., 2006. Investigation of the light dynamics and their impact on algal growth rate in a hydraulically integrated serial turbidostat algal reactor ( HISTAR ). Aquac. Eng. 35, 122-134. doi:10.1016/j.aquaeng.2005.09.005

- Berberoglu, H., Gomez, P.S., Pilon, L., 2009. Radiation characteristics of *Botryococcus braunii*, *Chlorococcum littorale*, and *Chlorella* sp. used for CO<sub>2</sub> fixation and biofuel production. *J. Quant. Spectrosc. Radiat. Transf.* 110, 1879-1893. doi:10.1016/j.jqsrt.2009.04.005
- Berberoglu, H., Pilon, L., 2007. Experimental measurements of the radiation characteristics of *Anabaena variabilis* ATCC 29413-U and *Rhodobacter sphaeroides* ATCC 49419. *Int. J. Hydrogen Energy* 32, 4772-4785. doi:10.1016/j.ijhydene.2007.08.018
- Berberoglu, H., Yin, J., Pilon, L., 2007. Light transfer in bubble sparged photobioreactors for H<sub>2</sub> production and CO<sub>2</sub> mitigation. *Int. J. Hydrogen Energy* 32, 2273-2285. doi:10.1016/j.ijhydene.2007.02.018
- Bird, R.B., Stewart, W.E., Lightfoot, E.N., 1971. *Transport phenomena*, 1st ed. J. Wiley.
- Bisschops, I., Spanjers, H., 2003. Literature review on textile wastewater characterisation. *Environ. Technol.* 24, 1399-1411. doi:10.1080/09593330309385684
- Bitog, J.P., Lee, I.-B., Lee, C.-G., Kim, K.-S., Hwang, H.-S., Hong, S.-W., Seo, I.-H., Kwon, K.-S., Mostafa, E., 2011. Application of computational fluid dynamics for modeling and designing photobioreactors for microalgae production: A review. *Comput. Electron. Agric.* 76, 131-147. doi:10.1016/j.compag.2011.01.015
- Bondioli, P., Della Bella, L., 2005. An alternative spectrophotometric method for the determination of free glycerol in biodiesel. *Eur. J. Lipid Sci. Technol.* 107, 153-157. doi:10.1002/ejlt.200401054
- Boran, E., Özgür, E., Yücel, M., Gündüz, U., Eroglu, I., 2012. Biohydrogen production by *Rhodobacter capsulatus* in solar tubular photobioreactor on thick juice dark fermenter effluent. *J. Clean. Prod.* 31, 150-157. doi:10.1016/j.jclepro.2012.03.020
- Budihardjo, I., Morrison, G.L., Behnia, M., 2007. Natural circulation flow through water-in-glass evacuated tube solar collectors. *Sol. Energy* 81, 1460-1472. doi:10.1016/j.solener.2007.03.002
- Burris, R., 1991. Nitrogenases. *J. Biol. Chem.* 266, 9339-42.
- Carlozzi, P., Buccioni, A., Minieri, S., Pushparaj, B., Piccardi, R., Ena, A., Pintucci, C., 2010a. Production of bio-fuels (hydrogen and lipids) through a photofermentation process. *Bioresour. Technol.* 101, 3115-20. doi:10.1016/j.biortech.2009.12.049

- Carlozzi, P., Lambardi, M., 2009. Fed-batch operation for bio-H<sub>2</sub> production by *Rhodospseudomonas palustris* (strain 42OL). *Renew. Energy* 34, 2577-2584. doi:10.1016/j.renene.2009.04.016
- Carlozzi, P., Pintucci, C., Piccardi, R., Buccioni, A., Minieri, S., Lambardi, M., 2010b. Green energy from *Rhodospseudomonas palustris* grown at low to high irradiance values, under fed-batch operational conditions. *Biotechnol. Lett.* 32, 477-81. doi:10.1007/s10529-009-0183-2
- Carlozzi, P., Pushparaj, B., Degl'Innocenti, A., Capperucci, A., 2006. Growth characteristics of *Rhodospseudomonas palustris* cultured outdoors, in an underwater tubular photobioreactor, and investigation on photosynthetic efficiency. *Appl. Microbiol. Biotechnol.* 73, 789-95. doi:10.1007/s00253-006-0550-z
- Carlozzi, P., Sacchi, A., 2001. Biomass production and studies on *Rhodospseudomonas palustris* grown in an outdoor, temperature controlled, underwater tubular photobioreactor. *J. Biotechnol.* 88, 239-249. doi:10.1016/S0168-1656(01)00280-2
- Carvalho, A.P., Silva, S.O., Baptista, J.M., Malcata, F.X., 2011. Light requirements in microalgal photobioreactors : an overview of biophotonic aspects 1275-1288. doi:10.1007/s00253-010-3047-8
- Çengel, Y.A., Cimbala, J.M., 2006. Fluid mechanics fundamentals and applications, 3rd in SI. ed. McGraw-Hill Education.
- Cengel, Y.A., Ghajar, A.J., 2011. Heat and Mass Transfer: Fundamentals and Applications.
- Chen, C.-Y., Lee, C.-M., Chang, J.-S., 2006. Feasibility study on bioreactor strategies for enhanced photohydrogen production from *Rhodospseudomonas palustris* WP3-5 using optical-fiber-assisted illumination systems. *Int. J. Hydrogen Energy* 31, 2345-2355. doi:10.1016/j.ijhydene.2006.03.007
- Chen, C.-Y., Yang, M.-H., Yeh, K.-L., Liu, C.-H., Chang, J.-S., 2008. Biohydrogen production using sequential two-stage dark and photo fermentation processes. *Int. J. Hydrogen Energy* 33, 4755-4762. doi:10.1016/j.ijhydene.2008.06.055
- Chen, C., Lu, W., Wu, J., Chang, J., 2007. Enhancing phototrophic hydrogen production of *Rhodospseudomonas palustris* via statistical experimental design. *Int. J. Hydrogen Energy* 32, 940-949. doi:10.1016/j.ijhydene.2006.09.021

- Chen, C., Saratale, G., Lee, C., Chen, P., Chang, J., 2008. Phototrophic hydrogen production in photobioreactors coupled with solar-energy-excited optical fibers. *Int. J. Hydrogen Energy* 33, 6886-6895. doi:10.1016/j.ijhydene.2008.09.014
- Cheng, J., Su, H., Zhou, J., Song, W., Cen, K., 2010. Hydrogen production by mixed bacteria through dark and photo fermentation. *Int. J. Hydrogen Energy* 1-8. doi:10.1016/j.ijhydene.2010.10.007
- Chisti, Y., 2008. Biodiesel from microalgae beats bioethanol. *Trends Biotechnol.* 26, 126-131. doi:10.1016/j.tibtech.2007.12.002
- Cho, B.A., Pott, R.W.M., 2019. The development of a thermosiphon photobioreactor and analysis using Computational Fluid Dynamics (CFD). *Chem. Eng. J.* 363, 141-154. doi:10.1016/J.CEJ.2019.01.104
- Clarke, K.G., 2013. *Bioprocess engineering: an introductory engineering and life science approach.* Woodhead Publishing.
- Clarke, Kim Gail, 2013. *Microbial kinetics during batch, continuous and fed-batch processes,* Bioprocess Engineering. doi:10.1533/9781782421689.97
- Close, D.J., 1962. The performance of solar water heaters with natural circulation. *Sol. Energy* 6, 33-40. doi:10.1016/0038-092X(62)90096-8
- Cornet, J.F., Dussap, C.G., Gros, J.B., Binois, C., Lasseur, C., 1995. A simplified monodimensional approach for modeling coupling between radiant light transfer and growth kinetics in photobioreactors. *Chem. Eng. Sci.* 50, 1489-1500. doi:10.1016/0009-2509(95)00022-W
- Crabtree, G.W., Dresselhaus, M.S., Buchanan, M. V, 2004. The hydrogen economy. *Phys. Today* 39-44.
- Cui, Z., Fan, L.S., 2004. Turbulence energy distributions in bubbling gas-liquid and gas-liquid-solid flow systems. *Chem. Eng. Sci.* 59, 1755-1766. doi:10.1016/j.ces.2004.01.031
- DAE, 2012. *National Waste Information Baseline Report.* Pretoria, South Africa.
- Das, D., Veziroglu, T., 2001. Hydrogen production by biological processes: a survey of literature. *Int. J. Hydrogen Energy* 26, 13-28. doi:10.1016/S0360-3199(00)00058-6
- DEA, 2015. *EIA Guideline for Renewable Energy Projects.*

- Dellagrecia, M., Monaco, P., Pinto, G., Pollio, A., Previtera, L., Temussi, F., 2001. Phytotoxicity of Low-Molecular-Weight Phenols from Olive Mill Waste Waters. *Corresp. to P. Monaco Bull. Environ. Contam. Toxicol* 67, 352-359. doi:10.1007/s00128-001-0132-9
- Dermeche, S., Nadour, M., Larroche, C., Moulti-Mati, F., Michaud, P., 2013. Olive mill wastes: Biochemical characterizations and valorization strategies. *Process Biochem.* 48, 1532-1552. doi:10.1016/J.PROCBIO.2013.07.010
- Dobson, R.T., 1993. Transient response of a closed loop thermosyphon. *R&D J.* 9.
- Eroglu, E., Gunduz, U., Yucel, M., Turker, L., 2004. Photobiological hydrogen production by using olive mill wastewater as a sole substrate source. *Int. J. Hydrogen Energy* 29, 163-171. doi:10.1016/S0360-3199(03)00110-1
- Fadhl, B., Wrobel, L.C., Jouhara, H., 2013. Numerical modelling of the temperature distribution in a two-phase closed thermosyphon. *Appl. Therm. Eng.* 60, 122-131. doi:10.1016/j.applthermaleng.2013.06.044
- Fascetti, E., D'addario, E., Todini, O., Robertiello, A., 1998. Photosynthetic hydrogen evolution with volatile organic acids derived from the fermentation of source selected municipal solid wastes. *Int. J. Hydrogen Energy* 23, 753-760. doi:10.1016/S0360-3199(97)00123-7
- Fernandes, B.D., Dragone, G.M., 2010. Light Regime Characterization in an Airlift Photobioreactor for Production of Microalgae with High Starch Content 218-226. doi:10.1007/s12010-009-8783-9
- Fernandes, B.D., Dragone, G.M., Teixeira, J.A., Vicente, A.A., 2010. Light regime characterization in an airlift photobioreactor for production of microalgae with high starch content. *Appl. Biochem. Biotechnol.* 161, 218-226. doi:10.1007/s12010-009-8783-9
- Fluent, A., 2016. Module 01 : Overview of the CFD Process.
- Freegah, B., Asim, T., Mishra, R., 2013. Computational Fluid Dynamics based Analysis of a Closed Thermo-Siphon Hot Water Solar System. *26th Int. Congr. Cond. Monit. Diagnostic Eng. Manag.*
- Fu, L., Leutz, R., Ries, H., 2006. Physical modeling of filament light sources. *J. Appl. Phys.* 100. doi:10.1063/1.2364669
- Fu, Y., Viraraghavan, T., 2001. Fungal decolorization of dye wastewaters: A review. *Bioresour. Technol.* 79, 251-262. doi:10.1016/S0960-8524(01)00028-1

- Gandhi, M.S., Sathe, M.J., Joshi, J.B., Vijayan, P.K., 2011. Two phase natural convection: CFD simulations and PIV measurement. *Chem. Eng. Sci.* 66, 3152-3171. doi:10.1016/j.ces.2011.02.060
- Getha, K., Vikineswary, S., Chong, V.C., 1998. Isolation and growth of the phototrophic bacterium *Rhodospseudomonas palustris* strain B1 in sago-starch-processing wastewater. *World J. Microbiol. Biotechnol.* 14, 505-511. doi:10.1023/A:1008855125634
- Ghosh, D., Tourigny, A., Hallenbeck, P.C., 2011. Near stoichiometric reforming of biodiesel derived crude glycerol to hydrogen by photofermentation. *Int. J. Hydrogen Energy* 2-6. doi:10.1016/j.ijhydene.2011.11.011
- Gogate, P.R., Pandit, A.B., 2004. A review of imperative technologies for wastewater treatment I: Oxidation technologies at ambient conditions. *Adv. Environ. Res.* 8, 501-551. doi:10.1016/S1093-0191(03)00032-7
- Gómez-Pérez, C.A., Espinosa, J., Montenegro Ruiz, L.C., van Boxtel, A.J.B., 2015. CFD simulation for reduced energy costs in tubular photobioreactors using wall turbulence promoters. *Algal Res.* 12, 1-9. doi:10.1016/j.algal.2015.07.011
- Gosse, J.L., Engel, B.J., Rey, F.E., Harwood, C.S., Scriven, L.E., Flickinger, M.C., 2007. Hydrogen production by photoreactive nanoporous latex coatings of nongrowing *Rhodospseudomonas palustris* CGA009. *Biotechnol. Prog.* 23, 124-30. doi:10.1021/bp060254+
- Greif, R., 1988. Natural Circulation Loops. *J. Heat Transfer* 110, 1243. doi:10.1115/1.3250624
- Hagendijk, A.A.J., 2015. Design of an optimal photobioreactor.
- Hay, J.X.W., Wu, T.Y., Ng, B.J., Juan, J.C., Md. Jahim, J., 2016. Reusing pulp and paper mill effluent as a bioresource to produce biohydrogen through ultrasonicated *Rhodobacter sphaeroides*. *Energy Convers. Manag.* 113, 273-280. doi:10.1016/J.ENCONMAN.2015.12.041
- Heiniger, E.K., Oda, Y., Samanta, S.K., Harwood, C.S., 2012. How posttranslational modification of nitrogenase is circumvented in *Rhodospseudomonas palustris* strains that produce hydrogen gas constitutively. *Appl. Environ. Microbiol.* 78, 1023-32. doi:10.1128/AEM.07254-11

- Hiraishi, A., Shi, J.-L., Kitamura, H., 1989. Effects of Organic Nutrient Strength on the Purple Nonsulfur Bacterial Content and Metabolic Activity of Photosynthetic Sludge for Wastewater Treatment. *J. Ferment. Bioeng.* 68, 269-276. doi:10.1016/0922-338X(89)90028-7
- Hitit, Z.Y., Lazaro, C.Z., Hallenbeck, P.C., 2017. Single stage hydrogen production from cellulose through photo-fermentation by a co-culture of *Cellulomonas fimi* and *Rhodospseudomonas palustris*. *Int. J. Hydrogen Energy* 42, 6556-6566. doi:10.1016/j.ijhydene.2016.12.035
- Hosseini, S.E., Wahid, M.A., 2016. Hydrogen production from renewable and sustainable energy resources: Promising green energy carrier for clean development. *Renew. Sustain. Energy Rev.* 57, 850-866. doi:10.1016/j.rser.2015.12.112
- Huang, C., Lin, W.K., Wang, S.R., 2017. Two-Phase Closed-Loop Thermosyphon Solar Water Heater with Porous Wick Structure: Performance and Start-Up Time. *Arab. J. Sci. Eng.* 42, 4885-4894. doi:10.1007/s13369-017-2660-6
- Huang, J., Feng, F., Wan, M., Ying, J., Li, Y., Qu, X., Pan, R., Shen, G., Li, W., 2015. Improving performance of flat-plate photobioreactors by installation of novel internal mixers optimized with computational fluid dynamics. *Bioresour. Technol.* 182, 151-159. doi:10.1016/j.biortech.2015.01.067
- Huang, J., Ying, J., Fan, F., Yang, Q., Wang, J., Li, Y., 2016. Bioresource Technology Development of a novel multi-column airlift photobioreactor with easy scalability by means of computational fluid dynamics simulations and experiments. *Bioresour. Technol.* 222, 399-407. doi:10.1016/j.biortech.2016.09.109
- Igarashi, R.Y., Seefeldt, L.C., 2003. Nitrogen Fixation: The Mechanism of the Mo-Dependent Nitrogenase. *Crit. Rev. Biochem. Mol. Biol.* 38, 351-384. doi:10.1080/10409230391036766
- Imhoff, J.F., 2006. The Phototrophic Alpha-Proteobacteria 41-64. doi:10.1007/0-387-30745-1\_2
- Jacobi, A., Steinweg, C., Sastre, R.R., Posten, C., 2012. Advanced photobioreactor LED illumination system: Scale-down approach to study microalgal growth kinetics. *Eng. Life Sci.* 12, 621-630. doi:10.1002/elsc.201200004
- Janssen, M., Tramper, J., Mur, L.R., Wijffels, R.H., 2003. Enclosed outdoor photobioreactors: Light regime, photosynthetic efficiency, scale-up, and future prospects. *Biotechnol. Bioeng.* 81, 193-210. doi:10.1002/bit.10468

- Jeong, H.S., Jouanneau, Y., 2000. Enhanced nitrogenase activity in strains of *Rhodobacter capsulatus* that overexpress the *rnf* genes. *J. Bacteriol.* 182, 1208-14. doi:10.1128/JB.182.5.1208-1214.2000
- Joshi, J.B., Tabib, M. V, Deshpande, S.S., Mathpati, C.S., 2009. Dynamics of Flow Structures and Transport Phenomena , 1 . Experimental and Numerical Techniques for Identification and Energy Content of Flow Structures 8244-8284.
- Jouanneau, Y., Wong, B., Vignais, P.M., 1985. Stimulation by light of nitrogenase synthesis in cells of *Rhodospseudomonas capsulata* growing in N-limited continuous cultures. *BBA-Bioenerg.* 808, 149-155. doi:10.1016/0005-2728(85)90037-4
- Jung, G.Y., Jung, H.O., Kim, J.R., Ahn, Y., Park, S., 1999. Isolation and characterization of *Rhodospseudomonas palustris* P4 which utilizes CO with the production of H<sub>2</sub>. *Biotechnol. Lett.* 21, 525-529.
- Kalogirou, S., 2009. Thermal performance, economic and environmental life cycle analysis of thermosiphon solar water heaters. *Sol. Energy* 83, 39-48. doi:10.1016/j.solener.2008.06.005
- Kantachote, D., Torpee, S., Umsakul, K., 2005. The potential use of anoxygenic phototrophic bacteria for treating latex rubber sheet wastewater. *Electron. J. Biotechnol.* 8, 314-323.
- Kapdan, I.K., Kargi, F., 2006a. Bio-hydrogen production from waste materials. *Enzyme Microb. Technol.* 38, 569-582. doi:10.1016/j.enzmictec.2005.09.015
- Kapdan, I.K., Kargi, F., 2006b. Bio-hydrogen production from waste materials. *Enzyme Microb. Technol.* 38, 569-582. doi:10.1016/j.enzmictec.2005.09.015
- Keskin, T., Hallenbeck, P.C., 2012. Hydrogen production from sugar industry wastes using single-stage photofermentation. *Bioresour. Technol.* 112, 131-136. doi:10.1016/j.biortech.2012.02.077
- Kim, D.-H., Kim, M.-S., 2011. Hydrogenases for biological hydrogen production. *Bioresour. Technol.* 102, 8423-8431. doi:10.1016/j.biortech.2011.02.113
- Kim, J.K., Lee, B., 2000. Mass production of *Rhodospseudomonas palustris* as diet for aquaculture. *Aquac. Eng.* 23, 281-293.

- Kim, M., Baek, J., Lee, J., 2006a. Comparison of H<sub>2</sub> accumulation by *Rhodobacter sphaeroides* KD131 and its uptake hydrogenase and PHB synthase deficient mutant. *Int. J. Hydrogen Energy* 31, 121-127. doi:10.1016/j.ijhydene.2004.10.023
- Kim, M., Baek, J., Lee, J., 2006b. Comparison of H<sub>2</sub> accumulation by *Rhodobacter sphaeroides* KD131 and its uptake hydrogenase and PHB synthase deficient mutant. *Int. J. Hydrogen Energy* 31, 121-127. doi:10.1016/j.ijhydene.2004.10.023
- Kim, T.T.H., Ai, L.T.T., Thuoc, T.L., Ooi, T., Kinoshita, S., 2002. Decolorization of Azo Dyes by Purple Non-Sulphur Bacteria, Annual Report of FY 2002.
- Kocyigit, H., Ugurlu, A., 2015. Biological decolourization of reactive azo dye by anaerobic/aerobic sequencing batch reactor system. *Glob. NEST J.* 17, 1-10.
- Koffi, P.M.E., Andoh, H.Y., Gbaha, P., Touré, S., Ado, G., 2008. Theoretical and experimental study of solar water heater with internal exchanger using thermosiphon system. *Energy Convers. Manag.* 49, 2279-2290. doi:10.1016/j.enconman.2008.01.032
- Koku, H., 2002. Aspects of the metabolism of hydrogen production by *Rhodobacter sphaeroides*. *Int. J. Hydrogen Energy* 27, 1315-1329. doi:10.1016/S0360-3199(02)00127-1
- Kong, B., Vigil, R.D., 2014. Bioresource Technology Simulation of photosynthetically active radiation distribution in algal photobioreactors using a multidimensional spectral radiation model. *Bioresour. Technol.* 158, 141-148. doi:10.1016/j.biortech.2014.01.052
- Kraus, A.D., Bar-Cohen, A., 1995. Design and Analysis of Heat Sinks. JOHN WILEY & SONS, INC., New York.
- Krujatz, F., Illing, R., Krautwer, T., Liao, J., Helbig, K., Goy, K., Opitz, J., Cuniberti, G., Bley, T., Weber, J., 2015. Light-field-characterization in a continuous hydrogen-producing photobioreactor by optical simulation and computational fluid dynamics. *Biotechnol. Bioeng.* 112, 2439-2449. doi:10.1002/bit.25667
- Kunjapur, A.M., Eldridge, R.B., 2010. Photobioreactor Design for Commercial Biofuel Production from Microalgae 3516-3526.
- L.N. Tsoglin, B.V. Gabel, T.N.F. and V.E.S., 1996. Closed photobioreactors for microalgal cultivation. *Russ. J. Plant Physiol.*

- Larimer, F.W., Chain, P., Hauser, L., Lamerdin, J., Malfatti, S., Do, L., Land, M.L., Pelletier, D. a, Beatty, J.T., Lang, A.S., Tabita, F.R., Gibson, J.L., Hanson, T.E., Bobst, C., Torres, J.L.T.Y., Peres, C., Harrison, F.H., Gibson, J., Harwood, C.S., 2004. Complete genome sequence of the metabolically versatile photosynthetic bacterium *Rhodospseudomonas palustris*. *Nat. Biotechnol.* 22, 55-61. doi:10.1038/nbt923
- Lee, C., Chen, P., Wang, C., Tung, Y., 2002. Photohydrogen production using purple nonsulfur bacteria with hydrogen fermentation reactor e uent. *Technology* 27, 1309-1313.
- Leigh, J.A., Dodsworth, J.A., 2007. Nitrogen Regulation in Bacteria and Archaea. *Annu. Rev. Microbiol.* 61, 349-377. doi:10.1146/annurev.micro.61.080706.093409
- LI, R., Fang, Z., 2008. Hydrogen production characteristics of photoheterotrophic *Rubrivivax gelatinosus* L31. *Int. J. Hydrogen Energy* 33, 974-980. doi:10.1016/j.ijhydene.2007.12.001
- Lide, D.R., 2003. *CRC Handbook of Chemistry and Physics*. CRC Handb. Chem. Phys. 1264-1266. doi:10.1021/ja906434c
- Lin, L., Faghri, A., 1997. Steady-state performance in a thermosiphon with tube separator. *Appl. Therm. Eng.* 17, 667-679. doi:10.1016/S1359-4311(96)00084-1
- Lin, R., Cheng, J., Yang, Z., Ding, L., Zhang, J., Zhou, J., Cen, K., 2016. Enhanced energy recovery from cassava ethanol wastewater through sequential dark hydrogen, photo hydrogen and methane fermentation combined with ammonium removal. *Bioresour. Technol.* 214, 686-691. doi:10.1016/j.biortech.2016.05.037
- Linstrom, P.J., Mallard, W.G., 2011. NIST Chemistry WebBook [WWW Document]. [Httpwebbooknistgovchemistry](http://webbook.nist.gov/chemistry). doi:10.5860/CHOICE.35-2709
- Liu, T., Li, X., Zhou, Z., 2010. Improvement of hydrogen yield by hupR gene knock-out and nifA gene overexpression in *Rhodobacter sphaeroides* 6016. *Int. J. Hydrogen Energy* 35, 9603-9610. doi:10.1016/j.ijhydene.2010.06.072
- Lo, Y.-C., Chen, C.-Y., Lee, C.-M., Chang, J.-S., 2011. Photo fermentative hydrogen production using dominant components (acetate, lactate, and butyrate) in dark fermentation effluents. *Int. J. Hydrogen Energy* 1-10. doi:10.1016/j.ijhydene.2011.04.148
- Loeffler, B.H., 2012. *Modeling and Optimization of a Thermosiphon for Passive Thermal Management Systems*. Georgia Institute of Technology.

- Louisos, W.F., Hitt, D.L., Danforth, C.M., 2013. Chaotic flow in a 2D natural convection loop with heat flux boundaries. *Int. J. Heat Mass Transf.* 61, 565-576. doi:10.1016/j.ijheatmasstransfer.2013.02.015
- Lucas, M.S., Peres, J.A., Li Puma, G., 2010. Treatment of winery wastewater by ozone-based advanced oxidation processes (O<sub>3</sub>, O<sub>3</sub>/UV and O<sub>3</sub>/UV/H<sub>2</sub>O<sub>2</sub>) in a pilot-scale bubble column reactor and process economics. *Sep. Purif. Technol.* 72, 235-241. doi:10.1016/j.seppur.2010.01.016
- Luo, H., Al-dahhan, M.H., 2011. Verification and validation of CFD simulations for local flow dynamics in a draft tube airlift bioreactor. *Chem. Eng. Sci.* 66, 907-923. doi:10.1016/j.ces.2010.11.038
- Luo, H., Al-dahhan, M.H., 2004. Analyzing and Modeling of Photobioreactors by Combining First Principles of Physiology and Hydrodynamics. doi:10.1002/bit.10831
- Luo, H.P., Al-Dahhan, M.H., 2011. Verification and validation of CFD simulations for local flow dynamics in a draft tube airlift bioreactor. *Chem. Eng. Sci.* 66, 907-923. doi:10.1016/j.ces.2010.11.038
- Luo, H.P., Al-Dahhan, M.H., 2004. Analyzing and Modeling of Photobioreactors by Combining First Principles of Physiology and Hydrodynamics. *Biotechnol. Bioeng.* 85, 382-393. doi:10.1002/bit.10831
- Maclsaac, D., Kanner, G., Anderson, G., 1999. Basic physics of the incandescent lamp (lightbulb). *Phys. Teach.* 37, 520-525. doi:10.1119/1.880392
- Madigan, M.T., Jung, D.O., 2009. An Overview of Purple Bacteria: Systematics, Physiology, and Habitats. pp. 1-15. doi:10.1007/978-1-4020-8815-5\_1
- Maeda, I., Chowdhury, W.Q., Idehara, K., Yagi, K., Mizoguchi, T., Akano, T., Mlyasaka, H., Furutani, T., Ikuta, Y., Shioji, N., Miura, Y., 1998. Improvement of substrate conversion to molecular hydrogen by three-stage cultivation of a photosynthetic bacterium, *Rhodovulum sulfidophilum*. *Appl. Biochem. Biotechnol.* 70-72, 301-10. doi:10.1007/BF02920146
- Malalasekera, W., Versteeg, H.K., 2006. An Introduction to Computational Fluid Dynamics – The Finite Volume Method, *AIAA Journal*. doi:10.2514/1.22547

- Malik, A.H., Shah, A., Khushnood, S., 2013. CFD analysis of heat transfer within a bottom heated vertical concentric cylindrical enclosure, in: *Journal of Physics: Conference Series*. doi:10.1088/1742-6596/439/1/012004
- Mantzavinos, D., Kalogerakis, N., 2005. Treatment of olive mill effluents: Part I. Organic matter degradation by chemical and biological processes—an overview. *Environ. Int.* 31, 289-295. doi:10.1016/J.ENVINT.2004.10.005
- Manuel Brenes, \*, Aranzazu García, Pedro García, José J. Rios, and, Garrido, A., 1999. Phenolic Compounds in Spanish Olive Oils. doi:10.1021/JF990009O
- Marcinichen, J.B., Szczukiewicz, S., Lamaison, N., Thome, J.R., 2014. Towards development of a passive datacenter cooling technology: On-server thermosyphon cooling loop under dynamic workload. *Thermomechanical Phenom. Electron. Syst. -Proceedings Intersoc. Conf.* 1027-1037. doi:10.1109/ITHERM.2014.6892394
- Masepohl, B., Drepper, T., Paschen, A., Gross, S., Pawlowski, A., Raabe, K., Riedel, K.-U., Klipp, W., 2002. Regulation of nitrogen fixation in the phototrophic purple bacterium *Rhodobacter capsulatus*. *J. Mol. Microbiol. Biotechnol.* 4, 243-8.
- Massart, A., Mirisola, A., Lupant, D., Thomas, D., Hantson, A., 2014. Experimental characterization and numerical simulation of the hydrodynamics in an airlift photobioreactor for microalgae cultures. *ALGAL* 6, 210-217. doi:10.1016/j.algal.2014.07.003
- McKinlay, J.B., Harwood, C.S., 2010. Carbon dioxide fixation as a central redox cofactor recycling mechanism in bacteria. *Proc. Natl. Acad. Sci. U. S. A.* 107, 11669-75. doi:10.1073/pnas.1006175107
- Melnicki, M., Bianchi, L., De Philippis, R., Melis, A., 2008. Hydrogen production during stationary phase in purple photosynthetic bacteria. *Int. J. Hydrogen Energy* 33, 6525-6534. doi:10.1016/j.ijhydene.2008.08.041
- Mishra, P., Thakur, S., Singh, L., Ab Wahid, Z., Sakinah, M., 2016. Enhanced hydrogen production from palm oil mill effluent using two stage sequential dark and photo fermentation. *Int. J. Hydrogen Energy* 41, 18431-18440. doi:10.1016/j.ijhydene.2016.07.138
- Mitchell, D.A., Krieger, N., Berovič, M., 2006. Solid-State Fermentation Bioreactors, *Solid-State Fermentation Bioreactors: Fundamentals of Design and Operation*. doi:10.1007/3-540-31286-2

- Molina-Grima, E., Acien, G., Camacho, Francisco Garcia, Chisti, Y., Molina Grima, E., Acien Fernández, F.G., Camacho, F García, 1999. Hydrogen production from empty fruit bunch hydrolysate by photosynthetic bacteria View project Biotechnology of marine microalgae: development of antibiofouling surfaces for photobioreactors View project Photobioreactors: light regime, mass transfer, and . Artic. J. Biotechnol. J. Biotechnol., Biotechnological Aspects of Marine Sponges 70, 231-247. doi:10.1016/S0168-1656(99)00078-4
- Molina, E., Fernández, J., Acien, F.G., Chisti, Y., 2001a. Tubular photobioreactor design for algal cultures. J. Biotechnol. 92, 113-131. doi:10.1016/S0168-1656(01)00353-4
- Molina, E., Fernández, J., Acien, F.G., Chisti, Y., 2001b. Tubular photobioreactor design for algal cultures. J. Biotechnol. 92, 113-131. doi:10.1016/S0168-1656(01)00353-4
- Molina Grima, E., Fernández, F.G.A., García Camacho, F., Chisti, Y., 1999. Photobioreactors: light regime, mass transfer, and scaleup. J. Biotechnol., Biotechnological Aspects of Marine Sponges 70, 231-247. doi:10.1016/S0168-1656(99)00078-4
- Moore, S., Stein, W.H., 1954. A modified ninhydrin reagent for the photometric determination of amino acids and related compounds. J. Biol. Chem. 211, 907-913.
- Morrison, F.A., 2013. An introduction to fluid mechanics. Cambridge University Press.
- Morrison, G.L., Braun, J.E., 1985. System modeling and operation characteristics of thermosyphon solar water heaters. Sol. Energy 34, 389-405. doi:10.1016/0038-092X(85)90051-9
- Morrison, G.L., Budihardjo, I., Behnia, M., 2005. Measurement and simulation of flow rate in a water-in-glass evacuated tube solar water heater. Sol. Energy 78, 257-267. doi:10.1016/j.solener.2004.09.005
- Mortuza, S.M., Gent, S.P., Kommareddy, A., Anderson, G.A., 2011. Computational and experimental investigation of heat transfer within a column photobioreactor. ASME 2011 Int. Mech. Eng. Congr. Expo. IMECE 2011 4, 1-10. doi:10.1115/IMECE2011-63947
- Murphy, T.E., Berberoğlu, H., 2011. Effect of algae pigmentation on photobioreactor productivity and scale-up: A light transfer perspective. J. Quant. Spectrosc. Radiat. Transf. 112, 2826-2834. doi:10.1016/j.jqsrt.2011.08.012

- Mutharasaiah, K., Govindareddy, V., Chandrakant, K., 2012. Biodegradation of 2-Chlorophenol by *Rhodopseudomonas palustris*. Bioremediat. J. 16, 1-8. doi:10.1080/10889868.2011.628348
- Nagadomi, H., Kitamura, T., Watanabe, M., Sasaki, K., 2000. Simultaneous removal of chemical oxygen demand (COD), phosphate, nitrate and H<sub>2</sub>S in the synthetic sewage wastewater using porous ceramic immobilized photosynthetic bacteria. Biotechnol. Lett. 22, 1369-1374. doi:10.1023/A:1005688229783
- Nath, K., 2008. Kinetics of two-stage fermentation process for the production of hydrogen. Int. J. Hydrogen Energy 33, 1195-1203. doi:10.1016/j.ijhydene.2007.12.011
- Nath, K., Das, D., 2004. Improvement of fermentative hydrogen production: various approaches. Appl. Microbiol. Biotechnol. 65, 520-9. doi:10.1007/s00253-004-1644-0
- Nogi, Y., Akiba, T., Horikoshi, K., 1985. Wavelength dependence of photoproduction of hydrogen by *Rhodopseudomonas rubra*. Agric. Biol. Chem. 49, 35-38. doi:10.1080/00021369.1985.10866684
- Nyce, T.A., Rosenberger, F., 1991. Growth of protein crystals suspended in a closed loop thermosyphon. J. Cryst. Growth 110, 52-59. doi:10.1016/0022-0248(91)90865-3
- Oda, Y., Samanta, S.K., Rey, F.E., Yan, T., Zhou, J., Harwood, C.S., 2005. Functional Genomic Analysis of Three Nitrogenase Isozymes in the Photosynthetic Bacterium *Rhodopseudomonas palustris*. J. Bacteriol. 7784-7794. doi:10.1128/JB.187.22.7784
- Oda, Y., Vries, Y.P., Forney, L.J., Gottschal, J.C., J.D., van E., F.J., de B., K.-H., S., 2001. Acquisition of the ability for *Rhodopseudomonas palustris* to degrade chlorinated benzoic acids as the sole carbon source. FEMS Microbiol. Ecol. 38, 133-139. doi:10.1111/j.1574-6941.2001.tb00891.x
- Ogbonna, J.C., Yada, H., Tanaka, H., 1995. Light supply coefficient: A new engineering parameter for photobioreactor design. J. Ferment. Bioeng. 80, 369-376. doi:10.1016/0922-338X(95)94206-7
- Ogueke, N. V., Anyanwu, E.E., Ekechukwu, O. V., 2009. A review of solar water heating systems. J. Renew. Sustain. Energy 1, 043106. doi:10.1063/1.3167285

- Oh, Y., Seol, E., Kim, M., Park, S., 2004. Photoproduction of hydrogen from acetate by a chemoheterotrophic bacterium *Rhodospseudomonas palustris* P4. *Int. J. Hydrogen Energy* 29, 1115-1121. doi:10.1016/j.ijhydene.2003.11.008
- Oh, Y., Seol, E., Lee, E., Park, S., 2002. Fermentative hydrogen production by a new chemoheterotrophic bacterium *Rhodospseudomonas Palustris* P4. *Int. J. Hydrogen Energy* 27, 1373-1379. doi:10.1016/S0360-3199(02)00100-3
- Oller, I., Malato, S., Sánchez-Pérez, J.A., 2011. Combination of Advanced Oxidation Processes and biological treatments for wastewater decontamination-A review. *Sci. Total Environ.* 409, 4141-4166. doi:10.1016/j.scitotenv.2010.08.061
- Ooshima, H., Takakuwa, S., Katsuda, T., Okuda, M., Shirasawa, T., Azuma, M., Kato, J., 1998. Production of hydrogen by a hydrogenase-deficient mutant of *Rhodobacter capsulatus*. *J. Ferment. Bioeng.* 85, 470-475. doi:10.1016/S0922-338X(98)80064-0
- Palamae, S., Choorit, W., Dechatiwongse, P., Zhang, D., Antonio del Rio-Chanona, E., Chisti, Y., 2018. Production of renewable biohydrogen by *Rhodobacter sphaeroides* S10: A comparison of photobioreactors. *J. Clean. Prod.* 181, 318-328. doi:10.1016/j.jclepro.2018.01.238
- Perry, R., Green, D., Maloney, J., 1997. Perry's chemical engineers' handbook, *Journal of Chemical Education*. doi:10.10360071422943
- Pershad, R., Duff, J., Heering, H., Duin, E., Albracht, S., Armstrong, F., 1999. Catalytic Electron Transport in *Chromatium vinosum* [NiFe]-Hydrogenase: Application of Voltammetry in Detecting Redox-Active Centers and Establishing That Hydrogen Oxidation Is Very Fast Even at Potentials Close to the Reversible H<sup>+</sup>/H<sub>2</sub> Value. doi:10.1021/BI990108V
- Petruccioli, M., Duarte, J., Federici, F., 2000. High-rate aerobic treatment of winery wastewater using bioreactors with free and immobilized activated sludge. *J. Biosci. Bioeng.* 90, 381-386. doi:10.1016/S1389-1723(01)80005-0
- Pilkhwai, D.S., Ambrosini, W., Forgione, N., Vijayan, P.K., Saha, D., Ferreri, J.C., 2007. Analysis of the unstable behaviour of a single-phase natural circulation loop with one-dimensional and computational fluid-dynamic models. *Ann. Nucl. Energy* 34, 339-355. doi:10.1016/j.anucene.2007.01.012

- Pilon, L., Berberoğlu, H., Kandilian, R., 2011. Radiation transfer in photobiological carbon dioxide fixation and fuel production by microalgae. *J. Quant. Spectrosc. Radiat. Transf.* doi:10.1016/j.jqsrt.2011.07.004
- Pintucci, C., Giovannelli, A., Traversi, M.L., Ena, A., Padovani, G., Carlozzi, P., 2013. Fresh olive mill waste deprived of polyphenols as feedstock for hydrogen photo-production by means of *Rhodospseudomonas palustris* 42OL. *Renew. Energy* 51, 358-363. doi:10.1016/J.RENENE.2012.09.037
- Pintucci, C., Padovani, G., Giovannelli, A., Traversi, M.L., Ena, A., Pushparaj, B., Carlozzi, P., 2015. Hydrogen photo-evolution by *Rhodospseudomonas palustris* 6A using pre-treated olive mill wastewater and a synthetic medium containing sugars. *Energy Convers. Manag.* 90, 499-505. doi:10.1016/j.enconman.2014.11.045
- Pires, J.C.M., Alvim-ferraz, M.C.M., Martins, F.G., 2017. Photobioreactor design for microalgae production through computational fluid dynamics : A review. *Renew. Sustain. Energy Rev.* 79, 248-254. doi:10.1016/j.rser.2017.05.064
- Pokhrel, D., Viraraghavan, T., 2004. Treatment of pulp and paper mill wastewater—a review. *Sci. Total Environ.* 333, 37-58. doi:10.1016/J.SCITOTENV.2004.05.017
- Posten, C., 2009. Design principles of photo-bioreactors for cultivation of microalgae. *Eng. Life Sci.* 9, 165-177. doi:10.1002/elsc.200900003
- Pott, R.W.M., 2014. The bioconversion of waste glycerol into hydrogen by *Rhodospseudomonas palustris*. University of Cambridge.
- Pott, R.W.M., Howe, C.J., Dennis, J.S., 2013. Photofermentation of crude glycerol from biodiesel using *Rhodospseudomonas palustris*: Comparison with organic acids and the identification of inhibitory compounds. *Bioresour. Technol.* 130, 725-730. doi:10.1016/j.biortech.2012.11.126
- Pulz, O., 2001. Photobioreactors: Production systems for phototrophic microorganisms. *Appl. Microbiol. Biotechnol.* 57, 287-293. doi:10.1007/s002530100702
- Rai, P.K., Singh, S.P., 2016. Integrated dark- and photo-fermentation: Recent advances and provisions for improvement. *Int. J. Hydrogen Energy* 41, 19957-19971. doi:10.1016/j.ijhydene.2016.08.084

- Rameshaiah, G.N., 2015. Development of Photobioreactors for Improvement of Algal Biomass Production Shabnam Siddiqui G N Rameshaiah Kavya G Engineering 220-226.
- Ramírez-Duque, J.L., Ramos-Lucumi, M.A., 2011. Hydrodynamic computational evaluation in solar tubular photobioreactors bends with different cross sections. *CTyF – Ciencia, Tecnología y Futur.* 4, 59-72.
- Rek, Z., Rudolf, M., Zun, I., 2012. Application of CFD Simulation in the Development of a New Generation Heating Oven. *Strojniški Vestn. – J. Mech. Eng.* 58, 134-144. doi:10.5545/sv-jme.2011.163
- Rey, F.E., Oda, Y., Harwood, C.S., 2006. Regulation of uptake hydrogenase and effects of hydrogen utilization on gene expression in *Rhodospseudomonas palustris*. *J. Bacteriol.* 188, 6143-52. doi:10.1128/JB.00381-06
- Reyna-Velarde, R., Cristiani-Urbina, E., Hernández-Melchor, D.J., Thalasso, F., Cañizares-Villanueva, R.O., 2010. Hydrodynamic and mass transfer characterization of a flat-panel airlift photobioreactor with high light path. *Chem. Eng. Process. Process Intensif.* 49, 97-103. doi:10.1016/j.cep.2009.11.014
- Ribeiro, C.I., 2014. Blackbody Radiation from an Incandescent Lamp 371, 1-3. doi:10.1119/1.4893096
- Roldán, M.I., Smirnova, O., Fend, T., Casas, J.L., Zarza, E., 2014. Thermal analysis and design of a volumetric solar absorber depending on the porosity. *Renew. Energy* 62, 116-128. doi:10.1016/j.renene.2013.06.043
- Rout, S.K., Thatoi, D.N., Acharya, A.K., Mishra, D.P., 2012. CFD supported performance estimation of an internally finned tube heat exchanger under mixed convection flow. *Procedia Eng.* 38, 585-597. doi:10.1016/j.proeng.2012.06.073
- Ruppersberg, J.C., 2008. Transient modelling of a loop thermosyphon : transient effects in single and two phase natural circulation thermosyphon loops suitable for the reactor cavity cooling of a pebble bed modular reactor.
- Sabourin-Provost, G., Hallenbeck, P.C., 2009. High yield conversion of a crude glycerol fraction from biodiesel production to hydrogen by photofermentation. *Bioresour. Technol.* 100, 3513-7. doi:10.1016/j.biortech.2009.03.027

- Samanci, A., Berber, A., 2011. Experimental investigation of single-phase and two-phase closed thermosyphon solar water heater systems. *Sci. Res. Essays* 6, 688-693. doi:10.5897/SRE09.072
- Sander, J., Dahl, C., 2009. *Metabolism of Inorganic Sulfur Compounds in Purple Bacteria*. Springer Netherlands, pp. 595-622. doi:10.1007/978-1-4020-8815-5\_30
- Sato, T., Yamada, D., Hirabayashi, S., 2010. Development of virtual photobioreactor for microalgae culture considering turbulent flow and flashing light effect. *Energy Convers. Manag.* 51, 1196-1201. doi:10.1016/j.enconman.2009.12.030
- Savin, I., Butnaru, R., 2008. Wastewater characteristics in textile finishing mills. *Environ. Eng. Manag. J.* 7, 856-864.
- Shariah, A., Shalabi, B., 1997. Optimal design for a thermosyphon solar water heater. *Renew. Energy* 11, 351-361. doi:10.1016/S0960-1481(97)00005-0
- Shukla, R., Sumathy, K., Erickson, P., Gong, J., 2013. Recent advances in the solar water heating systems: A review. *Renew. Sustain. Energy Rev.* 19, 173-190. doi:10.1016/j.rser.2012.10.048
- Siefert, E., Irgens, R.L., Pfennig, N., 1978. Phototrophic purple and green bacteria in a sewage treatment plant. *Appl. Environ. Microbiol.* 35, 38-44.
- Singh, S.P., Srivastava, S.C., Pandey, K., 1994. Hydrogen production by *Rhodospseudomonas* at the expense of vegetable starch, sugarcane juice and whey. *Int. J. Hydrogen Energy* 19, 437-440. doi:10.1016/0360-3199(94)90020-5
- Skjånes, K., Andersen, U., Heidorn, T., Borgvang, S.A., 2016. Design and construction of a photobioreactor for hydrogen production , including status in the field. *J. Appl. Phycol.* 1, 2205-2223. doi:10.1007/s10811-016-0789-4
- Soman, A., Shastri, Y., 2015. Optimization of novel photobioreactor design using computational fluid dynamics. *Appl. Energy* 140, 246-255. doi:10.1016/j.apenergy.2014.11.072
- Tamburic, B., Zemichael, F.W., Crudge, P., Maitland, G.C., Hellgardt, K., 2011. Design of a novel flat-plate photobioreactor system for green algal hydrogen production. *Int. J. Hydrogen Energy* 36, 6578-6591. doi:10.1016/j.ijhydene.2011.02.091

- Tao, Y., He, Y., Wu, Y., Liu, F., Li, X., Zong, W., Zhou, Z., 2008. Characteristics of a new photosynthetic bacterial strain for hydrogen production and its application in wastewater treatment. *Int. J. Hydrogen Energy* 33, 963-973. doi:10.1016/j.ijhydene.2007.11.021
- Taylor, G., 2008. Biofuels and the biorefinery concept☆. *Energy Policy* 36, 4406-4409. doi:10.1016/j.enpol.2008.09.069
- Tredici, M.R., Zittelli, G.C., 1998. Efficiency of sunlight utilization: Tubular versus flat photobioreactors. *Biotechnol. Bioeng.* 57, 187-197. doi:10.1002/(SICI)1097-0290(19980120)57:2<187::AID-BIT7>3.0.CO;2-J
- Ugwu, C.U., Aoyagi, H., Uchiyama, H., 2008. Photobioreactors for mass cultivation of algae. *Bioresour. Technol.* 99, 4021-4028. doi:10.1016/j.biortech.2007.01.046
- USHIO America, I., 2018. Halogen Lamps Technical Specifications Data [WWW Document].
- van Neil, C., 1944. The culture, general physiology, morphology and classification of the nonsulfur purple and brown bacteria. *Bacteriol. Rev.* 8, 1-118.
- Vignais, P.M., Toussaint, B., 1994. Molecular biology of membrane-bound H<sub>2</sub> uptake hydrogenases. *Arch. Microbiol.* 161, 1-10. doi:10.1007/BF00248887
- Vijayan, P.K., Sharma, M., Saha, D., 2007. Steady state and stability characteristics of single-phase natural circulation in a rectangular loop with different heater and cooler orientations 31, 925-945. doi:10.1016/j.expthermflusci.2006.10.003
- Vincenzini, M., 1982. Hydrogen production by immobilized cells—I. light dependent dissimilation of organic substances by *Rhodospseudomonas palustris*. *Int. J. Hydrogen Energy* 7, 231-236. doi:10.1016/0360-3199(82)90086-6
- Vincenzini, M., Balloni, W., Mannelli, D., Florenzano, G., 1981. A bioreactor for continuous treatment of waste waters with immobilised cells of photosynthetic bacteria. *Experimentia* 2, 710-712.
- Vincenzini, M., Materassi, R., Tredici, M., Florenzano, G., 1982. Hydrogen production by immobilized cells—II. H<sub>2</sub>-photoevolution and waste-water treatment by agar-entrapped cells of *Rhodospseudomonas palustris* and *Rhodospirillum molischianum*. *Int. J. Hydrogen Energy* 7, 725-728. doi:10.1016/0360-3199(82)90021-0

- Wall, J.D., 2004. Rain or shine--a phototroph that delivers. *Nat. Biotechnol.* 22, 40-1. doi:10.1038/nbt0104-40
- Wang, B., Lan, C.Q., Horsman, M., 2012. Closed photobioreactors for production of microalgal biomasses. *Biotechnol. Adv.* doi:10.1016/j.biotechadv.2012.01.019
- Wang, X., Cheng, X., Dezhi, S., Qi, H., 2007. Biodecolorization and partial mineralization of Reactive Black 5 by a strain of *Rhodospseudomonas palustris*. *J. Environ. Sci.* 19, 1014-1019. doi:10.1016/S1001-0742(08)62363-3
- Wang, X., Cheng, X., Sun, D., Qi, H., 2008. Biodecolorization and partial mineralization of Reactive Black 5 by a strain of *Rhodospseudomonas palustris*. *J. Environ. Sci.* 20, 1218-1225. doi:10.1016/S1001-0742(08)62212-3
- Wang, Y., 2011. Use of probiotics *Bacillus coagulans*, *Rhodospseudomonas palustris* and *Lactobacillus acidophilus* as growth promoters in grass carp (*Ctenopharyngodon idella*) fingerlings. *Aquac. Nutr.* 17, e372-e378. doi:10.1111/j.1365-2095.2010.00771.x
- Westmacott, D., Primrose, S.B., 1976. Synchronous Growth of *Rhodospseudomonas palustris* from the Swarmer Phase. *J. Gen. Microbiol.* 94, 117-125. doi:10.1099/00221287-94-1-117
- Wheaton, Z.C., Krishnamoorthy, G., 2012. Modeling radiative transfer in photobioreactors for algal growth. *Comput. Electron. Agric.* 87, 64-73. doi:10.1016/j.compag.2012.05.002
- Whittenbury, R., McLee, A.G., 1967. *Rhodospseudomonas palustris* and *Rh. viridis*-Photosynthetic budding bacteria. *Arch. Microbiol.* 59, 324-334. doi:10.1007/BF00406346
- Williamson, M.E., Wilson, D.I., 2009. Development of an improved heating system for industrial tunnel baking ovens. *J. Food Eng.* 91, 64-71. doi:10.1016/j.jfoodeng.2008.08.004
- Wu, X.P., Mochizuki, M., Mashiko, K., Nguyen, Thang, Nguyen, Tien, Wuttijumnong, V., Cabusao, G., Singh, R., Akbarzadeh, A., 2011. Cold Energy Storage Systems Using Heat Pipe Technology for Cooling Data Centers. *Front. Heat Pipes* 2. doi:10.5098/fhp.v2.1.3005
- Xu, B., Li, P., Waller, P., 2014. Study of the flow mixing in a novel ARID raceway for algae production. *Renew. Energy* 62, 249-257. doi:10.1016/j.renene.2013.06.049
- Xu, J., Feng, Y., Wang, Y., Lin, X., 2013. Characteristics of purple nonsulfur bacteria grown under *Stevia* residue extractions. *Lett. Appl. Microbiol.* 57, 420-426. doi:10.1111/lam.12129

- Yang, Z., Cheng, J., Ye, Q., Liu, J., Zhou, J., Cen, K., 2016. Bioresource Technology Decrease in light/dark cycle of microalgal cells with computational fluid dynamics simulation to improve microalgal growth in a raceway pond. *Bioresour. Technol.* 220, 352-359. doi:10.1016/j.biortech.2016.08.094
- Yetis, M., Gündüz, U., Eroglu, I., Yücel, M., Turker, L., 2000. Photoproduction of hydrogen from sugar refinery wastewater by *Rhodobacter sphaeroides* O.U. 001. *Int. J. Hydrogen Energy* 25, 1035-1041. doi:10.1016/S0360-3199(00)00027-6
- Yu, G., Li, Y., Shen, G., Wang, W., Lin, C., Wu, H., Chen, Z., 2009. A novel method using CFD to optimize the inner structure parameters of flat photobioreactors. *J. Appl. Phycol.* 21, 719-727. doi:10.1007/s10811-009-9407-z
- Yugoslav Committee for Chemical Engineering., J.C., Society of Chemists and Chemical Engineers of Croatia. Biochemical Engineering Section., F., Österreichische Gesellschaft für Bioprozesstechnik., E., Croatian Society of Chemical Engineers., Slovensko kemijsko društvo., 2007. Chemical and biochemical engineering quarterly., Chemical and biochemical engineering quarterly. Association of Chemists and Chemical Engineers of Croatia.
- Yun, G., Su, G.H., Wang, J.Q., Tian, W.X., Qiu, S.Z., Jia, D.N., Zhang, J.W., 2005. Two-phase instability analysis in natural circulation loops of China advanced research reactor. *Ann. Nucl. Energy* 32, 379-397. doi:10.1016/j.anucene.2004.11.002
- Zaidi, S.M.J., Rauf, M.A., 2009. Fuel cell fundamentals, in: *Polymer Membranes for Fuel Cells*. pp. 1-6. doi:10.1007/978-0-387-73532-0\_1
- Zerrouki, A., Boumédién, A., BouhadeF, K., 2002. The natural circulation solar water heater model with linear temperature distribution. *Renew. Energy* 26, 549-559. doi:10.1016/S0960-1481(01)00146-X
- Zhang, Dongda, Dechatiwongse, P., Hellgardt, K., 2015. Modelling light transmission , cyanobacterial growth kinetics and fluid dynamics in a laboratory scale multiphase photobioreactor for biological hydrogen production. *Algal Res.* 8, 99-107. doi:10.1016/j.algal.2015.01.006

- Zhang, D, Xiao, N., Mahbubani, K.T., Rio-chanona, E.A., Slater, N.K.H., Vassiliadis, V.S., 2015. Bioprocess modelling of biohydrogen production by *Rhodospseudomonas palustris* : Model development and effects of operating conditions on hydrogen yield and glycerol conversion efficiency. *Chem. Eng. Sci.* 130, 68-78. doi:10.1016/j.ces.2015.02.045
- Zhang, T., 2013. Dynamics of fluid and light intensity in mechanically stirred photobioreactor. *J. Biotechnol.* 168, 107-116. doi:10.1016/j.jbiotec.2013.07.007
- Zhang, Z., Zhou, X., Hu, J., Zhang, T., Zhu, S., Zhang, Q., 2017. Photo-bioreactor structure and light-heat-mass transfer properties in photo-fermentative bio-hydrogen production system: A mini review. *Int. J. Hydrogen Energy* 42, 12143-12152. doi:10.1016/j.ijhydene.2017.03.111
- Zhu, H., Suzuki, T., Tsygankov, A.A., Asada, Y., Miyake, J., 1999. Hydrogen production from tofu wastewater by *Rhodobacter sphaeroides* immobilized in agar gels. *Int. J. Hydrogen Energy* 24, 305-310. doi:10.1016/S0360-3199(98)00081-0
- Zvirin, Y., 1982. A review of natural circulation loops in pressurized water reactors and other systems. *Nucl. Eng. Des.* 67, 203-225. doi:10.1016/0029-5493(82)90142-X

## APPENDIX:

### 6.1 Appendix A – Literature table of compounds or wastewaters treated by *R. palustris* or other PNS bacteria

Table 19: Rates of hydrogen gas production from various carbon containing components as well as by various photo-fermentative bacteria.

Carbon containing components	Waste type	<i>R. palustris</i>	H <sub>2</sub> production	Water treatment	Author
Glucose	Synthetic medium	No ( <i>R. capsulatus</i> JY91)	3 mol H <sub>2</sub> per mol glucose	Not evaluated	Abo-Hashesh, 2011
Glucose	Synthetic medium	Yes (P4)	29.9 mmol/g cell h	Not evaluated	Oh, 2002
Glucose	Synthetic medium	No ( <i>R. sphaeroides</i> )	75 mL/L	Yes (COD decrease)	Tao, 2008
Glucose	Synthetic medium	No ( <i>R. capsulatus</i> B100)	NA	Yes (COD decrease)	Tao, 2008
Glucose	Synthetic medium	No ( <i>R. capsulatus</i> ST410)	NA	Yes (COD decrease)	Tao, 2008
Glucose	Synthetic medium	No ( <i>R. sphaeroides</i> mutant)	12.6 mL H <sub>2</sub> /L h	Yes (COD decrease)	Tao, 2008
Glucose	Synthetic medium	No ( <i>R. sphaeroides</i> ZX5)	75 mL H <sub>2</sub> /L h	Yes (COD decrease)	Tao, 2008
Glucose	Synthetic medium	No ( <i>R. sphaeroides</i> KD131)	0.53 ml H <sub>2</sub> /mg-cdw	Not evaluated	Kim, 2004

Glucose	Synthetic medium	No (R. sphaeroides KD131)	0.24 ml H <sub>2</sub> /mg-cdw	Not evaluated	Kim,2004
Glucose medium (control)	Synthetic medium	No (R. sphaeroides)	1.9 L H <sub>2</sub> /h m <sup>2</sup> gel	Yes (not explicitly stated)	Zhu, 1999
Glucose and fructose	Synthetic medium	Yes (6A)	11.8 mL/g(dw)/h	Yes (COD decrease)	Pintucci, 2014
Sucrose	Synthetic medium	No (R. capsulatus B100)	NA	Yes (COD decrease)	Tao, 2008
Sucrose	Synthetic medium	No (R. capsulatus ST410)	NA	Yes (COD decrease)	Tao, 2008
Sucrose	Synthetic medium	No (R. capsulatus Z1)	NA	Yes (COD decrease)	Tao, 2008
Sucrose	Synthetic medium	No (R. sphaeroides ZX5)	40 mL H <sub>2</sub> /L h	Yes (COD decrease)	Tao, 2008
Sucrose	Synthetic medium	No (R. capsulatus JP91)	14 mol H <sub>2</sub> /mol sucrose	Not evaluated	Keskin, 2012
Sucrose	Synthetic medium	No (R. sphaeroides KD131)	0.24 ml H <sub>2</sub> /mg-cdw	Not evaluated	Kim, 2004
Sucrose	Synthetic medium	No (R. sphaeroides KD131)	0.49 ml H <sub>2</sub> /mg-cdw	Not evaluated	Kim, 2004
Sucrose	Synthetic medium	No (R. sphaeroides)	40 mL/L	Yes (COD decrease)	Tao, 2008
Glycerol	Synthetic medium	No (R. sphaeroides KD131)	0 ml H <sub>2</sub> /mg-cdw	Not evaluated	Kim, 2004

Glycerol	Synthetic medium	No (R. sphaeroides KD131)	0.13 ml H <sub>2</sub> /mg-cdw	Not evaluated	Kim, 2004
Xylose	Synthetic medium	No (R. sphaeroides)	70 mL/L	Yes (COD decrease)	Tao, 2008
Fructose	Synthetic medium	No (R. sphaeroides)	61 mL/L	Yes (COD decrease)	Tao, 2008
Arabinose	Synthetic medium	No (R. sphaeroides)	0 mL/L	Yes (COD decrease)	Tao, 2008
Cellobiose	Synthetic medium	No (R. sphaeroides)	0 mL/L	Yes (COD decrease)	Tao, 2008
Maltose	Synthetic medium	No (R. sphaeroides)	5 mL/L	Yes (COD decrease)	Tao, 2008
Acetate	Synthetic medium	No (R. sphaeroides KD131)	0.13 ml H <sub>2</sub> /mg-cdw	Not evaluated	Kim, 2004
Acetate	Synthetic medium	No (R. sphaeroides KD131)	0.46 ml H <sub>2</sub> /mg-cdw	Not evaluated	Kim, 2004
Acetate	Synthetic medium	No (R. sphaeroides)	90 mL/L	Yes (COD decrease)	Tao, 2008
Acetate	Synthetic medium	Rhodopseudomonas sp.	25.2 mL H <sub>2</sub> /L h	Yes (COD decrease)	Tao, 2008
Acetate	Synthetic medium	Yes (P4)	NA	Yes (COD decrease)	Tao, 2008
Acetate	Synthetic medium	No (R. capsulata)	45 mL H <sub>2</sub> /L h	Yes (COD decrease)	Tao, 2008

Acetate	Synthetic medium	No (R. capsulatus B100)	NA	Yes (COD decrease)	Tao, 2008
Acetate	Synthetic medium	No (R. capsulatus ST410)	NA	Yes (COD decrease)	Tao, 2008
Acetate	Synthetic medium	No (R. sphaeroides ZX5)	90 mL H <sub>2</sub> /L h	Yes (COD decrease)	Tao, 2008
Acetate	Synthetic medium	Rhodopseudomonas sp.	25.2 mL H <sub>2</sub> /L h	Not evaluated	Kapdan, 2006
Acetate	Synthetic medium	Yes	2.2 mL H <sub>2</sub> /L h	Not evaluated	Kapdan, 2006
Acetate	Synthetic medium	No (R. capsulata)	0.88 mL/h	Not evaluated	Kapdan, 2006
Acetate	Fermentation products of glucose	No (R. sphaeroides O.U. 001)	1.5-1.72 mol H <sub>2</sub> /mol acetic acid	Not evaluated	Nath, 2007
Malate	Synthetic medium	No (R. sphaeroides KD131)	0.80 ml H <sub>2</sub> /mg-cdw	Not evaluated	Kim, 2004
Malate	Synthetic medium	No (R. sphaeroides KD131)	1.16 ml H <sub>2</sub> /mg-cdw	Not evaluated	Kim, 2004
Malate	Synthetic medium	Rhodopseudomonas sp.	1.1 mL H <sub>2</sub> /L h	Yes (COD decrease)	Tao, 2008
Malate	Synthetic medium	Yes	5.8 mL H <sub>2</sub> /L h	Yes (COD decrease)	Tao, 2008
Malate	Synthetic medium	No (R. sphaeroides OU001)	5 mL H <sub>2</sub> /L h	Yes (COD decrease)	Tao, 2008

Malate	Synthetic medium	No (R. capsulatus B100)	90 mL H <sub>2</sub> /L h	Yes (COD decrease)	Tao, 2008
Malate	Synthetic medium	No (R. capsulatus ST410)	130 mL H <sub>2</sub> /L h	Yes (COD decrease)	Tao, 2008
Malate	Synthetic medium	No (R. sphaeroides ZX5)	92 mL H <sub>2</sub> /L h	Yes (COD decrease)	Tao, 2008
Malate	Synthetic medium	No (R. sphaeroides)	92 mL/L	Yes (COD decrease)	Tao, 2008
Malate	Synthetic medium	Rhodopseudomonas sp.	1.1 mL H <sub>2</sub> /L h	Not evaluated	Kapdan, 2006
Malate	Synthetic medium	Yes	5.8 mL H <sub>2</sub> /L h	Not evaluated	Kapdan, 2006
Malate	Synthetic medium	No (R. sphaeroides)	12 mL/L h	Not evaluated	Kapdan, 2006
L-malic acid	Synthetic medium	Yes	Not evaluated (growth evaluated)	Not evaluated	Xu, 2013
Lactate	Synthetic medium	Rhodopseudomonas sp.	10.7 mL H <sub>2</sub> /L h	Yes (COD decrease)	Tao, 2008
Lactate	Synthetic medium	Yes	9.1 mL H <sub>2</sub> /L h	Yes (COD decrease)	Tao, 2008
Lactate	Synthetic medium	No (R. sphaeroides RV)	62.5 mL H <sub>2</sub> /L h	Yes (COD decrease)	Tao, 2008
Lactate	Synthetic medium	No (R. sphaeroides ZX5)	103 mL H <sub>2</sub> /L h	Yes (COD decrease)	Tao, 2008
Lactate	Synthetic medium	Rhodopseudomonas sp.	10.7 mL H <sub>2</sub> /L h	Not evaluated	Kapdan, 2006

Lactate	Synthetic medium	Yes	9.1 mL H <sub>2</sub> /L h	Not evaluated	Kapdan, 2006
Lactate	Synthetic medium	No (R. sphaeroides RV)	1.5 L/L d	Not evaluated	Kapdan, 2006
Lactate	Synthetic medium	No (R. capsulatus IR3)	NA	Not evaluated	Kapdan, 2006
Lactate	Synthetic medium	No (R. sphaeroides GL-1)	0.2 mL/mL PU matrix h	Not evaluated	Kapdan, 2006
Lactate	Synthetic medium	No (R. sphaeroides)	103 mL/L	Yes (COD decrease)	Tao, 2008
Lactate	Synthetic medium	No (R. sphaeroides KD131)	0.47 ml H <sub>2</sub> /mg-cdw	Not evaluated	Kim, 2004
Lactate	Synthetic medium	No (R. sphaeroides KD131)	1.03 ml H <sub>2</sub> /mg-cdw	Not evaluated	Kim, 2004
Butyrate	Synthetic medium	Rhodopseudomonas sp.	7.6 mL H <sub>2</sub> /L h	Not evaluated	Kapdan, 2006
Butyrate	Synthetic medium	No (R. capsulata)	1.28 mL/h	Not evaluated	Kapdan, 2006
Butyrate	Synthetic medium	No (R. sphaeroides)	118 mL/L	Yes (COD decrease)	Tao, 2008
Butyrate	Synthetic medium	Rhodopseudomonas sp.	7.6 mL H <sub>2</sub> /L h	Yes (COD decrease)	Tao, 2008
Butyrate	Synthetic medium	No (R. capsulata)	65 mL H <sub>2</sub> /L h	Yes (COD decrease)	Tao, 2008
Butyrate	Synthetic medium	No (R. sphaeroides ZX5)	118 mL H <sub>2</sub> /L h	Yes (COD decrease)	Tao, 2008
Butyric acid and acetic acid	Synthetic medium	Yes (WP3-5)	7.2 mol H <sub>2</sub> /mol sucrose	Yes (72% COD reduction)	Chen, 2008

Succinate	Synthetic medium	No (R. sphaeroides)	108 mL/L	Yes (COD decrease)	Tao, 2008
Succinate	Synthetic medium	No (R. sulfidophilum)	26.6 mL H <sub>2</sub> /L h	Yes (COD decrease)	Tao, 2008
Succinate	Synthetic medium	No (R. sphaeroides ZX5)	108 mL H <sub>2</sub> /L h	Yes (COD decrease)	Tao, 2008
Succinate	Succinate wastewater	No (R. sphaeroides ZX5)	55 mL/L h	Yes (87.55% COD removed)	Tao, 2008
Succinate	Synthetic medium	No (R. sulfidophilum)	26.6 mL/L h	Not evaluated	Kapdan, 2006
Succinate	Algal fermentative products	No (R. sulfidophilum)	34.3 μmol/mg cell dry wt	Not evaluated	Maeda, 1998
Pyruvic acid	Synthetic medium	No (R. sphaeroides)	110 mL/L	Yes (COD decrease)	Tao, 2008
Propionate	Synthetic medium	No (R. sphaeroides)	112 mL/L	Yes (COD decrease)	Tao, 2008
Valeric acid	Synthetic medium	No (R. sphaeroides)	25 mL/L	Yes (COD decrease)	Tao, 2008
Caproate	Synthetic medium	No (R. sphaeroides)	0 mL/L	Yes (COD decrease)	Tao, 2008
Isovaleric acid	Synthetic medium	No (R. sphaeroides)	0 mL/L	Yes (COD decrease)	Tao, 2008
Isobutyric acid	Synthetic medium	No (R. sphaeroides)	20 mL/L	Yes (COD decrease)	Tao, 2008

Ethanol	Algal fermentative products	No (R. sulfidophilum)	0.46 $\mu$ mol/mg cell dry wt	Not evaluated	Maeda, 1998
Ethanol	Synthetic medium	No (R. sphaeroides)	0 mL/L	Yes (COD decrease)	Tao, 2008
D-mannitol	Synthetic medium	No (R. sphaeroides)	75 mL/L	Yes (COD decrease)	Tao, 2008
Benzoic acid	Synthetic medium	No (R. sphaeroides)	0 mL/L	Yes (COD decrease)	Tao, 2008
Vanillic acid	Synthetic medium	No (R. sphaeroides)	0 mL/L	Yes (COD decrease)	Tao, 2008
Starch	Synthetic medium	No (R. sphaeroides KD131)	0 ml H <sub>2</sub> /mg-cdw	Not evaluated	Kim, 2004
Starch	Synthetic medium	No (R. sphaeroides KD131)	0.03 ml H <sub>2</sub> /mg-cdw	Not evaluated	Kim, 2004
Carbohydrates	Olive wastewater	No (R. sphaeroides OU001)	NA	Yes (35.00% COD removed)	Tao, 2008
Carbohydrates	Olive wastewater	No (R. sphaeroides OU001)	NA	Yes (52.00% COD removed)	Tao, 2008
Carbohydrates	Olive mill wastewater	No (R. sphaeroides OU001)	4 mL/L culture h	Yes (COD decrease)	Kapdan, 2006

Polyphenols, glucose, fructose, mannitol, acetic acid and malic acid but poor in VFA's	Pre-treated fresh olive mill wastewater diluted with water (30% v:v)	Yes (6A)	13.5 mL/g(dw)/h	Yes (COD decrease)	Pintucci, 2014
Organic matter and phenols	Olive mill wastewater (OMW)	No (R. sphaeroides O.U. 001)	13.9 L H <sub>2</sub> /L OMW	Yes (COD decreased from 1100 to 720 mg/L)	Eroglu, 2004
Organic matter and phenols	Olive mill wastewater (OMW)	No (R. sphaeroides O.U. 001)	13.9 L H <sub>2</sub> /L OMW	Yes (BOD decreased from 475 to 200 mg/L)	Eroglu, 2004
Organic matter and phenols	Olive mill wastewater (OMW)	No (R. sphaeroides O.U. 001)	13.9 L H <sub>2</sub> /L OMW	Total recoverable phenol content decreased from 2.32 to 0.93 mg/L	Eroglu, 2004
Sugar refinery effluent + malic acid	Sugar refinery effluent	No (R. sphaeroides OU001)	5 mL/L culture h	Yes (COD decrease)	Kapdan, 2006
Sugar refinery effluent + malic acid	Sugar refinery effluent	No (R. sphaeroides OU001)	3 mL/L culture h	Yes (COD decrease)	Kapdan, 2006
Not given	Sugarcane juice	Rhodopseudomonas sp.	45 ml H <sub>2</sub> /g d w/h	Not evaluated	Fascetti, 1998
Not given	Sugarcane wastewater	Rhodopseudomonas sp.	15 ml H <sub>2</sub> /g Bchl-a/h	Not evaluated	Fascetti, 1998
Not given	Sugar refinery waste	Yes	30 ml H <sub>2</sub> /g d w/h	Not evaluated	Fascetti, 1998

Not specified	Sugarcane juice	Rhodopseudomonas sp. BHU 1-4	45 $\mu$ l H <sub>2</sub> /h mg bacterial cell dry weight	Not evaluated	Singh, 1993
Reduced sugar, formic acid, acetic acid, oxalic acid, tartaric acid, malic acid, ascorbic acid, citric acid	Simulated effluent of stevia residue	Yes	Not evaluated (growth evaluated)	Not evaluated	Xu, 2013
Water 16%, sucrose 51%, amino acids 8%, organic acids 11%, minerals 11.5%	Beet molasses (sugar industry)	No (R. capsulatus JP91)	10.5 mol H <sub>2</sub> /mol sucrose	Not evaluated	Keskin, 2012
Water 20%, sucrose 32%, glucose 15%, fructose 16%, amino acids 3%, organic acids 7%, minerals 8%	Black strap (sugar industry)	No (R. capsulatus JP91)	8 mol H <sub>2</sub> /mol sucrose	Not evaluated	Keskin, 2012
Sucrose + sugar refinery wastewater and L-malic acid + sugar refinery wastewater	Pre-treated sugar refinery wastewater	No (R. sphaeroides O.U. 001)	0.005 l hydrogen/h/l culture	Not evaluated	Yetis, 2000

Carbohydrates	Tofu wastewater	No (R. sphaeroides RV)	NA	Yes (41.00% COD removed)	Tao, 2008
Carbohydrates and proteins	Tofu wastewater	No (R. sphaeroides)	2.1 L/h m <sup>2</sup> gel	Yes (COD decrease)	Kapdan, 2006
Carbohydrates and proteins	Tofu wastewater	No (R. sphaeroides)	15.9 mL/L h	Yes (COD decrease)	Kapdan, 2006
Starch 6750 mg/L, sucrose 800 mg/L, protein 630 mg/L, sugar reductive 250 mg/L, volatile acids 200 mg/L	Tofu wastewater	No (R. sphaeroides)	2.1 L H <sub>2</sub> /h m <sup>2</sup> gel	Yes (TOC removal ratio in 85 h reached 41%)	Zhu, 1999
Glutamate-malate cultivation medium and glucose and peptone treatment conditions	Synthetic sewage wastewater	No (R. sphaeroides S, NR-3)	Not evaluated	Yes (removal of COD 89%, phosphate 77%, nitrate 99% and H <sub>2</sub> S 99.8%)	Nagadomi, 2000
Glutamate-malate cultivation medium and glucose and peptone treatment conditions	Synthetic sewage wastewater	Yes	Not evaluated	Yes (removal of COD 89%, phosphate 77%, nitrate 99% and H <sub>2</sub> S 99.8%)	Nagadomi, 2000

Glutamine or lactate	Textile effluent	Yes (W1)	Not evaluated	Yes (Reactive black 5 (RB5) decolourization)	Wang, 2008
Yeast extract and peptone	Effluents of paper and wood industry	Yes	Not evaluated	Yes ( <i>R. palustris</i> degraded about 97% of the supplemented 2-CP)	Mutharasaiah, 2012
Not given	Straw paper mill effluent	Yes	30 ml H <sub>2</sub> /g d w/h	Not evaluated	Fascetti, 1998
Butyrate and acetate	Effluents from dark fermentation of WW from a fuel ethanol manufacturer	No ( <i>R. sphaeroides</i> ZX5)	48 mL/L h	Yes (84.55% COD removed)	Tao, 2008
Butyrate and acetate	Fermentation effluent from dark fermentation of kitchen waste	No ( <i>R. sphaeroides</i> ZX5)	45 mL/L h	Yes (80.00% COD removed)	Tao, 2008
Acetate and butyrate	Soluble metabolite products of dark fermentation of cassava starch	Yes	489 ml H <sub>2</sub> /g starch (3.54 mol H <sub>2</sub> /mol hexose)	Not evaluated	Cheng, 2010

Organic acids (and ammonia)	Effluent from hydrogen fermentation reactors (CSTR, peptone fed)	Yes (WP2-5 and WP3-5)	No (high ammonia conc. but growth possible)	Not evaluated	Lee, 2002
Organic acids mainly butyric acid	Effluent from hydrogen fermentation reactors (ASBR, sugar fed)	Yes (WP2-5 and WP3-5)	Insignificant H <sub>2</sub> produced due to presence of ammonia and ethanol	Not evaluated	Lee, 2002
Organic acids mainly butyric acid	Effluent from hydrogen fermentation reactors (UASB, sugar fed)	Yes (WP2-5 and WP3-5)	Very low H <sub>2</sub> prod due to use of carbonate as medium buffer which produced CO <sub>2</sub>	Not evaluated	Lee, 2002
Not specified (volatile organic acids)	Effluent from hydrogen fermentation reactors (CSTR, sugar fed)	Yes (WP2-5 and WP3-5)	Yes but due to high ammonia conc. large amounts of H <sub>2</sub> gas not produced	Not evaluated	Lee, 2002
Not specified	Effluent from hydrogen fermentation reactors (CSTR, glucose and beef extract)	Yes (WP2-5 and WP3-5)	Yes (low ammonia conc. and phosphate used as medium buffer)	Not evaluated	Lee, 2002
Not given	Lactic acid fermentation waste	No (Rhodobacter sphaeroides)	1.8 ml H <sub>2</sub> /g d w/h	Not evaluated	Fascetti, 1998
Phenols and organic acids	Dark fermentation effluent from 50% (v/v)	No (R. sphaeroides O.U. 001)	0.008 L/(L h)	Yes	Eroglu, 2006

	activated sludge and olive mill wastewater				
Phenols and organic acids	Effluent of clay pre-treatment process	No (R. sphaeroides O.U. 001)	Yes (not explicitly given)	Yes (52% COD reduction)	Eroglu, 2006
Acetic acid, phenol and ethanol (not consumed)	Thick juice dark fermenter effluent (DFE)	No (R. capsulatus)	0.15 mol H <sub>2</sub> /(m <sup>3</sup> h)	Yes (68% COD reduction)	Boran, 2012
Not specified	Sago-starch processing decanter	Yes (B1)	Not evaluated (growth evaluated)	Yes (77% COD reduction)	Getha, 1998
Not given	Vegetable starch	Rhodopseudomonas sp.	30 ml H <sub>2</sub> /g d w/h	Not evaluated	Fascetti, 1998
Not specified	Potato starch	Rhodopseudomonas sp. BHU 1-4	30 µl H <sub>2</sub> /h mg bacterial cell dry weight	Not evaluated	Singh, 1993
Not specified	Whey	Rhodopseudomonas sp. BHU 1-4	25 µl H <sub>2</sub> /h mg bacterial cell dry weight	Not evaluated	Singh, 1993
Not given	Whey	Rhodopseudomonas sp.	25 ml H <sub>2</sub> /g d w/h	Not evaluated	Fascetti, 1998
Not given	Dairy wastewater	Rhodopseudomonas sp.	16 ml H <sub>2</sub> /g Bchl-a/h	Not evaluated	Fascetti, 1998

Not given	Distillery wastewater	No (Rhodobacter sphaeroides)	10.4 ml H <sub>2</sub> /g d w/h	Not evaluated	Fascetti, 1998
Lactic acid (90%) as well as acetic acid, propionic acid and butyric acid	Lactate from municipal solid waste	No (Rhodobacter sphaeroides)	1.2 ml H <sub>2</sub> /g d w/h	Not evaluated	Fascetti, 1998
Lactic acid (90%) as well as acetic acid, propionic acid and butyric acid	Enriched lactate liquor	No (Rhodobacter sphaeroides)	100 ml H <sub>2</sub> /g d w/h	Not evaluated	Fascetti, 1998
PHB	Synthetic medium	No (R. sulfidophilum)	33 mL/L h	Not evaluated	Kapdan, 2006
Not given	Fermented cow dung	No (R. capsulata)	6.35 ml H <sub>2</sub> /g d w/h	Not evaluated	Fascetti, 1998
Not given	Orange processing effluent	No (Rhodopseudomonas sphaeroides)	133 ml H <sub>2</sub> /g Bchl-a/h	Not evaluated	Fascetti, 1998
Chlorinated benzoic acids – 3-chlorobenzoate (3-	Synthetic medium	Yes	Not evaluated	Yes (degradation of 3-CBA if growth in a	Oda, 2001

CBA) and benzoate (BA). Also 2-CBA and 4-CBA.				substrate containing BA)	
---	--	--	--	--------------------------	--

## **6.2 Appendix B – appendices for mathematical model**

### **6.2.1 Modelling procedures**

#### **6.2.1.1 Mathematical modelling methodology**

Various parameters were investigated to determine whether using a thermosiphon photobioreactor for the production of hydrogen by *R. palustris* is feasible. Mathematical models were derived for the design and optimisation of a thermosiphon photobioreactor. Once a model for a single-phase system had been derived and tested the accuracy and feasibilities were investigated. The model was then extended to investigate the effect of solid particles on the system. This study focuses on the fluid velocity within the thermosiphon photobioreactor for a single phases system and investigates the pertinence of this to a two-phase system.

Two methods were used to determine the relationship between the velocity and temperature of the fluid. A mathematical model was derived for the specific experimental setup. The model was then solved in Matlab. Experiments were performed to determine the actual fluid velocity with respect to temperature in the experimental setup. The experimental results were used to validate the assumptions made during the derivation of the mathematical model. The mathematical model was updated to improve the accuracy of the model with respect to the experimental results.

The model was validated using water as the circulating fluid in the experimental setup for the single-phase investigation. Experimental runs were then conducted with deactivated (non-gas producing) bacteria. The two-phase experiments were conducted to determine how the addition of solids influenced the flow rate of the fluid in the reactor.

#### **6.2.1.2 Modelling the velocity versus temperature**

This study concentrates on relating the fluid velocity within a thermosiphon photobioreactor to the temperature of the fluid within the reactor. It is important to know if the thermosiphon effect will create sufficient movement in a transparent vessel, with low heat absorbance rates. The temperature must also be limited to a reasonable temperature range. The temperature within the reactor drives the thermosiphon effect while the fluid velocity can be measured to determine the force of the thermosiphon principle.

The temperature was therefore the independent variable in this study and the fluid velocity the dependant variable. All other parameters such as the configuration and fluid composition were kept constant in the different experiments. This study investigates the temperature difference required to produce sufficient flow. This information can be combined with heat absorbance rates

to design a thermosiphon photobioreactor that will operate at the required temperatures and therefore fluid velocity during steady state operation.

#### **6.2.1.2.1 The required fluid velocity**

There is not a singular optimal flow rate but a range within which the reactor could operate. The flow rate depends on the required residence time within the reactor as well as the minimum flow rate that ensures solids remain in suspension, the settling rate. This flow rate will vary based on the type of bacteria and feed material being used, as well as the process into which the reactor will be integrated. An ideal velocity range can be determined based on the application of the thermosiphon photobioreactor.

To ensure the system is operating within the laminar flow regime the Reynolds number will be kept below 2 100. Laminar flow was assumed during the derivation of the mathematical model. From this Reynolds number a maximum velocity can be calculated once the system is known. This velocity will be used, as an indication of when the temperature difference is too high and the flow is no longer laminar.

This study focuses on relating the velocity of the fluid to the temperature of the fluid based on a specific reactor configuration. The temperature difference to achieve any velocity that falls within the laminar region can be determined from the model developed. This improves the understanding and conceptualisation of the energy transformation within the thermosiphon photobioreactor.

#### **6.2.1.3 Dimensioning the reactor**

An existing thermosiphon photobioreactor is used for the purpose of this study. The configuration of the reactor used can be seen in Figure 60 and the configuration used for the mathematical model in Figure 59. The geometry of the reactor was required for the mathematical model. The reactor was constructed from glass and the dimensions were not specified before construction. The geometry of the reactor was determined as accurately as possible and the results are included in Figure 33 in Section 3.3.1.1.1. The derived model is therefore specific to the geometry determined during the dimensioning of the reactor.

Direct measurements were taken when possible but due to the small openings of the vessel some measurements had to be inferred based on other measurements. The outer diameter of the reactor was measured using a vernier caliper. This method was used to measure the diameter of the narrower tubes used for the riser and down-comer of the reactor as well as the larger

diameter above the cooling jacket. Measuring the length of the various sections was slightly less accurate as they were measured using a measuring tape.

The inner diameter of the tubes and the dimensions under the cooling jacket had to be inferred. The diameter of the narrower tubes was determined by adding a known volume of water to the water within the reactor. The water level was recorded before and after the addition of the water. The inner diameter was calculated based on the volume of water added and the change in the water level. The cross sectional area was calculated by dividing the volume by twice the height increase. The volume was divided by twice the height increase to account for the water rising in both the riser and the down-comer of the reactor. The inner diameter was calculated from the cross sectional area.

The glass thickness was calculated based on the inner and outer diameter of the narrow tubes. The inner diameter of the section above the cooling jacket was determined from the outer diameter and glass thickness. Determining the dimensions, of the section of the reactor enclosed by the cooling jacket, were the least accurate as these dimensions could not be directly measured. The measurements were taken as accurately as possible through the glass-cooling jacket and based on the surrounding dimensions.

The geometry of the reactor was required in the modelling process. The derived model is therefore specific to the geometry determined in this process. A sensitivity analysis was conducted using the mathematical model to determine the sensitivity of the flow rate to the geometry of the model. This analysis will determine the influence that the uncertainty included in the geometry of the reactor will have on the fluid velocity.

#### **6.2.1.4 The mathematical model**

The principles used to model a thermosiphon are generally understood and well established. To model a bioreactor these models must be extended to incorporate the bacterial loading and gas production as both these factors will have a large influence on the performance of a thermosiphon. A single-phase thermosiphon model was derived for the specific configuration and validated before it was possible to extend the model to account for the effects of solids present in the system.

A thermosiphon can be modelled by performing a momentum balance around the entire reactor system. As the system was modelled during steady state the momentum remains constant. The mathematical model uses a momentum balance, in which there is no change in momentum, to

relate the velocity of the fluid in the riser to the temperature difference across the thermosiphon photobioreactor (Loeffler, 2012; Morrison, 2013; Pilkhwal et al., 2007; Ruppertsberg, 2008).

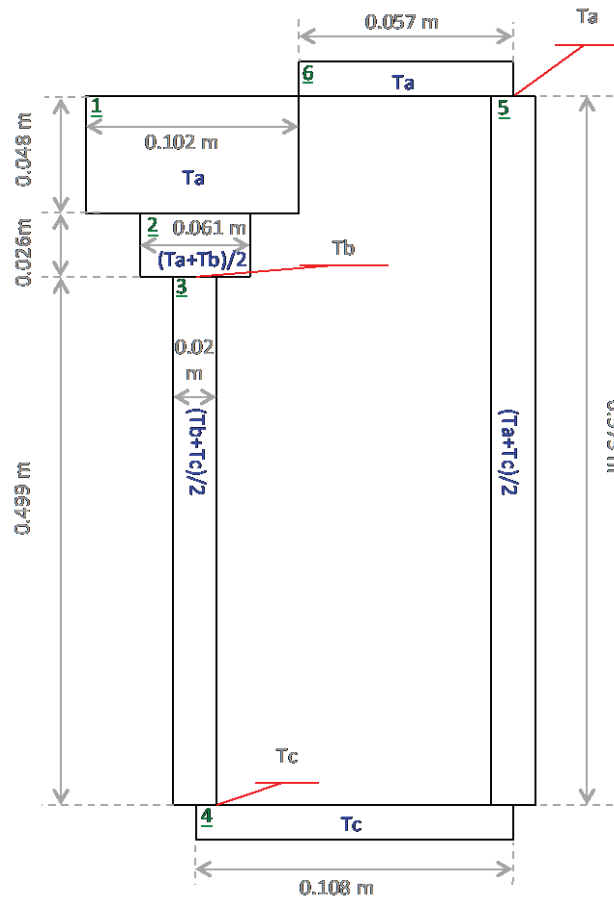


Figure 59: Initial configuration for the Matlab model

In the derivation of the model various assumptions were made. The fluid is assumed to be a single-phase, incompressible fluid that has constant properties within each segment. In this model the fluid flow properties are the density and viscosity. The fluid flow properties depend on the temperature of the fluid. This model made use of the mean fluid flow properties. As discussed below, the reactor was divided into 6 sections shown in Figure 59. The fluid flow properties were therefore assumed to be constant within each segment and calculated based on the average temperature of the segment.

The temperature readings were limited by the experimental setup. As discussed in Section 6.2.1.5.2 three thermocouples were used to measure the temperature of the fluid at three different points. The thermosiphon effect is driven by a temperature difference and depends heavily on the temperature of the fluid. Approximating the temperature of the fluid within each segment was expected to influence the accuracy of the model significantly.

A sensitivity analysis was conducted based on the temperature readings to determine how this assumption influenced the accuracy of the model. The method used to approximate the temperature of each segment was analysed during the validation of the model. This analysis ensured that the temperature of each segment was being represented as accurately as possible within the constraints of the experimental setup.

The temperature approximations were then adjusted to better represent the physical system. In the initial mathematical model the measured temperature was used when possible. If heating or cooling took place within a segment an average temperature was used based on the two relevant temperatures. The temperature of segments whose temperature was not measured nor submitted to heating or cooling was approximated as the closest temperature reading. The initial temperature approximations used for each segment can be seen in Figure 59 above indicated in blue.

The density and viscosity depends on the temperature of the fluid. The density and viscosity had to be written as a function of temperature in order for them to be modelled in Matlab. The relationship was found on the NIST database (Linstrom and Mallard, 2011). A small temperature interval was used to ensure that the error included while approximating the data with a function was minimised. The temperature interval was selected based on the temperature range within which bacteria are reasonably expected to survive and grow. The temperature therefore spans from 17°C to 39°C and the equations are only valid in this narrow temperature range.

The data from the NIST and trend lines that were fitted to the data can be seen in appendix 6.2.2. Coefficients were fitted to the Equations 26 and 27 in appendix 6.2.2. The fit of the trend line was also analysed in appendix 6.2.2. These equations were used for the mathematical model and are only valid for temperatures from 17°C to 39°C.

The thermosiphon investigated was a closed loop. Based on the principle of mass conservation, the mass flow rate is the same throughout the loop at any given time during steady state operation. The model was therefore used to solve for the mass flow rate in the thermosiphon reactor. The velocity was calculated for the various sections using the mass flow rate ( $\dot{m}$ ), density and cross sectional area of the section as shown in Equation 23. Where  $k$  is used to represent the number of the section.

$$v = \frac{\dot{m}}{A_{Ck} \rho_k} \quad [ 23 ]$$

The effects of friction had to be accounted for in the model. The thermosiphon principle is based on the balance between the buoyancy (driving) force and the friction (opposing) force. From

literature it was found that the frictional term accounts for the friction between the fluid and the wall as well as the energy losses when the fluid travels around a bend or travels through a pipe with a constriction or enlargement. The bends, constrictions and enlargements are accounted for by using an equivalent length (Çengel and Cimbala, 2006). A general estimation of these values can be found in literature based on the length and diameter of the pipe, Table C.7 was used from Bird, Stewart and Lightfoot (1971). This provides only an initial estimation and the frictional term must be determined based on the experimental results (Morrison, 2013).

As the friction was accounted for as an equivalent length, this term will be multiplied by a scaling factor. This scaling factor was used to adjust the frictional term so that the frictional term was no longer based on literature values but on the experimental results. This adjustment will be discussed further in Section 3.3.1.6.

The mathematical model was derived for steady state operation in a tubular thermosiphon photobioreactor and resulted in Equation 24. The acceleration term equated to zero as steady state operation was being investigated. The first term in the momentum balance was very small for this configuration due to the small mass flow rate ( $\dot{m}$ ). The model was solved for a mass flow rate that caused the frictional force to be equal to the gravitational force (less the first term). The derivation and discussion of the formula can be found in 6.2.3 and results in Equation 24.

$$0 = \frac{16\dot{m}^2}{\pi^2} \sum_{k=1}^N \left( \left( \frac{1}{\rho_k D_k^4} \right)_{in} - \left( \frac{1}{\rho_k D_k^4} \right)_{out} \right) - g \sum_{k=1}^N (\rho_k L_k \sin \Theta_k) - \frac{128\dot{m}}{\pi} \sum_{k=1}^N \left( \frac{L_{eq_k} \mu_k L_k}{D_k^5 \rho_k} \right) \quad [24]$$

Where  $L$  is the length of the segment and  $L_{eq}$  is the equivalent length accounting for the bends, constrictions and enlargements in the configuration. Both the length and equivalent length of each segment was measured and used in Equation 24 in meters.

The geometry of the system had to be simplified so that the fluid properties and friction factors could be determined per section. The thermosiphon photobioreactor was divided into 6 segments. The number of segments was decided based on the geometry of the shape as well as the segments where heat was added or removed. The segments are shown in Figure 59 (above).

In the formula subscript  $k$  indicates the segment number. The geometry was simplified into pipe segments with uniform diameters as shown in Figure 59. The segment number is indicated in the top right corner of each segment in Figure 59. The simplification of the model was necessary in order for it to be modelled mathematically and will influence the precision of the mathematical model.

The bends, constrictions and enlargements are included in the equivalent length of each segment. When there was a corner between the two segments half of the equivalent length was added to each segment. The change in diameter was accounted for in the equivalent length of segments 1, 2 and 3. These assumptions were chosen to represent the system the most accurately and the equivalent lengths were adjusted based on the experimental results.

The mathematical model was solved using in Matlab using Equation 24. The parameters of Equation 24 are shown in Table 6 in Section 3.3.1.1.2. The results of the code were compared to the experimental results. The initial assumptions were reviewed and adjusted in the development of the final mathematical model and discussed in Section 3.3.1.6.

#### **6.2.1.5 Experimental methods to validate mathematical model**

Experiments were conducted on a single-phase and two-phase system. The single-phase system consisted of fluid and the two-phase consisted of both fluid and solids. The experimental procedure was similar for both the single- and two-phase systems.

The experiments aimed to measure the superficial fluid velocity within the reactor. The fluid velocity was measured for various temperatures. Each experiment was conducted at different fluid temperatures. The temperature of the fluid within the reactor was therefore manipulated, by adjusting the position of the light and flow rate of the cooling water, and the fluid velocity measured. The experimental setup is shown in Figure 60.

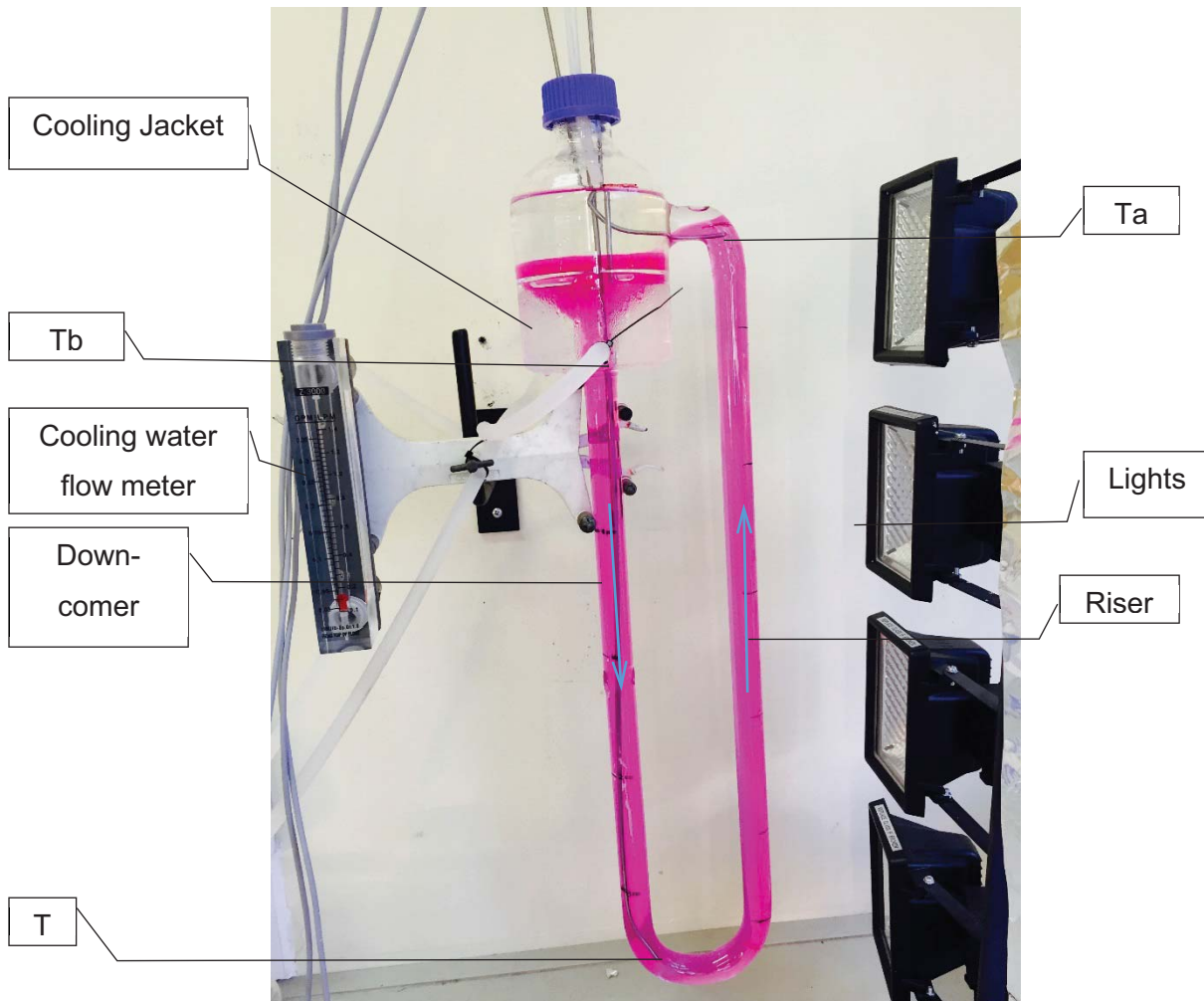


Figure 60: Experimental setup of prototype thermosiphon photobioreactor

### 6.2.1.5.1 Temperature regulation

Heat was added and removed from the fluid within the reactor to control the temperature of the system. The four halogen lights labelled in Figure 60 were used to heat the fluid. Halogen lights were chosen as they produce a full spectrum of light, they emit blackbody radiation similar to the sun (Ribeiro, 2014). The distance between the lights and the reactor determined the amount of heat added to the system. The distance varied between 50 mm and 150 mm. When the lights were placed 50 mm from the reactor the maximum amount of heat was transferred into the reactor. This was done in order to increase the temperature readings at temperature probe Ta. The flow rate and temperature of the cooling water determined the rate at which heat was removed from the system. A 20-litre tank was filled with tap water and this water was recirculate through the cooling jacket. The water recirculates to ensure that water was not wasted unnecessarily during the experimentation.

A 20-litre tank was used to ensure that the volume of cooling water was sufficient to dissipate the absorbed heat. This played an important role in ensuring that the system reached steady state. If the volume of water in the tank were insufficient, the temperature of the cooling water would have increased. The heat removal rate would then have decreased with time and the system would not have reached steady state. An EHEIM pump type 1002.220 series 06063 was used to circulate the cooling water through the cooling jacket seen in Figure 60 (above).

The rate at which heat was removed from the system was controlled by the flow rate and temperature of the cooling water. Increasing the flow rate increased the temperature difference between the temperature readings at temperature probes Ta and Tb. Adjusting the speed of the pump increased the flow rate of the cooling water. This increased the rate of heat removed from the system. When the temperature difference had to be increased further ice was added to the 20-litre tank. The colder water absorbed more heat and the temperature difference was increased.

The temperature was therefore not directly controlled. Achieving a specific temperature was not possible as the relationship of temperature to the heating and cooling system had not been quantified. The imprecise temperature regulation therefore influenced the experiments and interpretation of the results.

#### **6.2.1.5.2 Temperature measurement**

The temperature was recorded using three thermocouples and two data-loggers from WIKA. Class A PT100's were used. The experiments were only performed once the temperature had stabilised, fluctuated within  $0.1^{\circ}\text{C}$ . This was used to indicate that the system had reached steady state. Steady state was reached approximately 4 hours from the initial setup and 2 hours if adjustments were made to the heat addition or removal parameters.

The temperature probes were used to measure the temperature where the most significant temperatures were expected. These locations can be seen in Figure 60 labelled Ta, Tb and Tc. The temperature probe Ta, measures the maximum temperature of the system at the top of the riser after the lights have heated the fluid. Tb measured the temperature of the water after the cooling jacket has cooled the water. The third temperature reading was taken at the base of the reactor so that the heat lost or gained by convection as the fluid travelled down the down-comer was accounted for.

### 6.2.1.5.3 Temperature variation

The temperature affects the velocity in two ways, the driving force as a function of the temperature difference and the viscosity as a function of the average temperature of the fluid. The temperature difference refers to the temperature difference between the highest and lowest temperatures within the reactor. In this study this was defined as the temperature difference between  $T_a$  and  $T_b$ , indicated in Figure 60. The viscosity of a fluid depends on its temperature. The relationship between the viscosity and the temperature of the fluid is shown in Equation 27 in appendix 6.2.2. In this study the average temperature was used to evaluate the effect of the viscosity on the velocity of the fluid. The average temperature was calculated using Equation 25 (below). These two effects were investigated in this study to determine their influence on the fluid velocity.

$$T_{average} = \frac{T_a + T_b + T_c}{3} \quad [25]$$

The effect of the temperature difference on the system was investigated by keeping  $T_a$  constant and manipulating  $T_b$ . In the experiment it was difficult to control the temperature especially the average temperature. This was due to the limitation of the temperature control.  $T_a$  was measured directly and was therefore manipulated by adjusting the lights during the experiments. This was done in an attempt to maintain a constant temperature reading at  $T_a$ . The variation in  $T_a$  was minimised to reduce the effect of the changing viscosity on the fluid velocity, while the temperature difference was being investigated.

The effect of the viscosity was investigated based on the average temperature of the fluid. This was done by increasing the energy supplied to the system in order to increase the temperature at  $T_a$ . The flow rate of the cooling fluid was controlled in an attempt to minimise the variation in the temperature difference between  $T_a$  and  $T_b$ . The effect of the driving was therefore minimised while investigating the effect of the viscosity on the flow rate of the fluid.

Section 6.2.1.5.2 discussed how the temperature was controlled. It is clear that the temperature was not directly controlled but indirectly manipulated. This method of temperature control was used as it was the only way available and mimicked the heating and cooling methods that would ultimately be used in a TPBR but vastly limited the temperature control in this experiment.

Achieving exact temperatures was not possible. The distance of the lights and the flow rate of the cooling water were adjusted until the temperature difference between  $T_a$  and  $T_b$  was within  $0.3^\circ\text{C}$  of the desired temperature difference or when  $T_a$  was within  $0.4^\circ\text{C}$  of the desired temperature. Controlling the temperature therefore limited the extent to which the temperature difference and viscosity could be investigated independently.

#### 6.2.1.5.4 Fluid velocity measurements

The flow rate of the fluid was measured. Using particle-imaging velocimetry was beyond the scope of this project. A device could not be inserted into the reactor to measure the flow rate for two reasons. Firstly the reactor operates at very low velocities, thus the addition of a flow device would result in a significant retardation of the flow. Secondly accessing the internals of the reactor was difficult due to the sharp bend, rigid tubes and small inner diameter. A non-intrusive inexpensive method was required to measure the flow rate. The tracer method was implemented, using dye as the tracer.

Initially a dye was injected into the reactor. The fluid within the reactor therefore had to be replaced after each run. As steady state had to be reached before the readings could be repeated, approximately 4 hours were required between readings. The continual replacement of the fluid within the reactor was therefore not viable.

A pH indicator was used as a replacement to the dye. This was preferred as the colour of the pH indicator could be reverted between runs by adding an acid to the solution. The alkaline plug was used in the same way the dye would have been. This method allowed repeated readings to be taken consecutively. This method vastly increase the number of readings and the fluid only had to be replaced when chloride started to precipitate from the solution.

A pH indicator was added to the water circulating in the reactor. A colour change was observed when the solution changed from acidic to basic. This plug of colour, formed by the addition of the base, was followed as it passed through the reactor. The fluid velocity was determined by recording the time taken for the colour plug to travel 100 *mm*. Lines were draw on the down-comer indicating 0 *mm* up to 300 *mm*. Multiple readings were taken, as multiple colour plugs were formed and various markers used, per run and an average was used as the superficial velocity. The colour change could be revered by the addition of an acid and replacing the fluid was not necessary.

The two different pH indicators were used in the two different systems. For the single-phases system Phenolphthalein was used as this produced a very clear colour change from colourless to pink. The bacteria used as the solid particles were also pink and therefore the colour change would not be observed in the two-phase system. Bromothymol blue was used for the two-phase system as the colour change from yellow to blue was easily traced.

### 6.2.1.5.5 Stock solutions

Four stock solutions were prepared. A hydrochloric acid solution was used to make the system acidic, a sodium hydroxide (NaOH) solution to act as tracer in the reactor and stock solutions of the two pH indicators. These were prepared in excess and used throughout the experimentation. Hydrochloric acid with a molarity of 10.2 M was used as the acidic solution. The Phenolphthalein indicator was used as provided from the manufacturer. A NaOH solution of 3.5 M was prepared by dissolving 14 g NaOH pellets into 100 mL of water. The Bromothymol blue indicator was prepared by dissolving 0.25 g of Bromothymol blue sodium salt powder in 100 mL of water.

A solution of 0.5 g/L solids was required for the two-phase experiments. This concentration was chosen as it fell within the operational concentration range of *R. palustris*. The concentration of *R. palustris* can range up to 2 g/L while producing hydrogen efficiently. Deactivated *R. palustris* was available in the laboratory. The concentration of *R. palustris* in solution was determined using an optical density test. A calibration curve was available from J.P. du Toit. J.P. du Toit constructed this trend line as part of his research towards his Masters in Engineering.

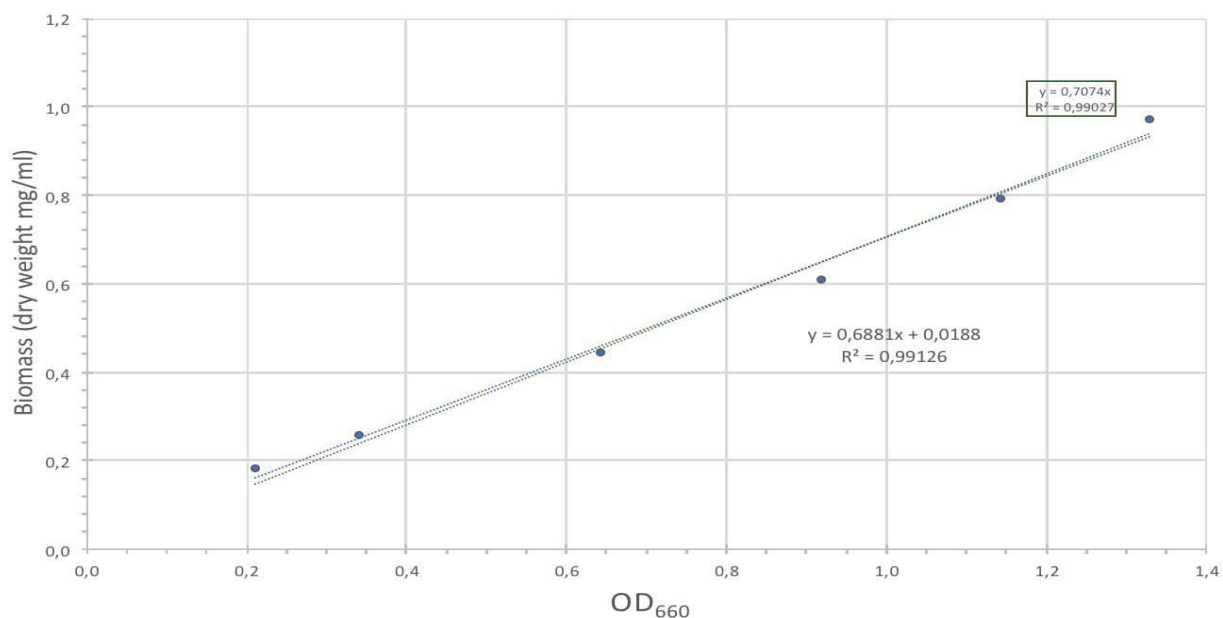


Figure 61: Biomass calibration curve for *R. palustris*

The optical density of the solution was determined by diluting the solution by a factor of 4. 0.1 mL of the stock solution was placed in clear plastic vial and then diluted with 0.9 mL demineralised water. The optical density was measured in the samples using a spectrophotometer at a wavelength of 660 nm. The correlation equation from Figure 61 was used to determine the optical density of the solution and thereby the dilution factor required a solution of 0.5 g/L solids. The dilution factor was calculated as 7.4.

To prepare the two solutions for the reactor the dilution factor of 7.4 was used. The reactor has a volume of approximately 1 L. 130 mL of stock solution was placed in a 1 L flask and the flask was then filled with water. After mixing the solution the solution ready to be decanted into the reactor for the two phase testing.

#### **6.2.1.5.6 Single phase experiments**

The reactor was filled with 1 L of water containing 1 mL of Phenolphthalein indicator and 1 mL of acid solution. The lights were positioned at the desired distance and the pump flow rate set to circulate the cooling water at the specified rate. About 4 hours were given for the system to reach steady state. Once the temperature readings remained constant the system was deemed to have reached steady state.

During this time the NaOH solution was heated to a similar temperature as  $T_b$ . This was done to minimise the influence that the addition of the alkaline solution had on the equilibrium of the reactor. 1 mL of the alkaline solution was added at the top of the reactor using a syringe.

The alkaline solution could be seen immediately by the pink colour. The velocity readings were taken when the plug of colour travelled down the down-comer for the second time. By the second pass it was assumed that the system had returned to steady state and the alkaline solution had equilibrated with the fluid in the reactor. This was done to ensure that the velocity of the plug was representing the velocity of the fluid circulation in the reactor. The first time the alkaline solution travelled down the down-comer the difference in density due to temperature and the effect of gravity caused the plug of colour to have a velocity greater than that of the surrounding fluid.

The plug of colour disintegrated into multiple plugs. This allowed multiple readings to be taken during one run. Multiple readings increased the accuracy of fluid velocity measurements and were used to determine the experimental error incorporated in the velocity measurements.

Once the run was completed the distance of the lights and the cooling water flow rate were adjusted for the next run. Once steady state was reached NaOH solution was added and the velocity was measured again. This was repeated until the fluid within the reactor became permanently pink. The acidic solution was added by drop wise titration to adjust the pH and return the fluid to colourless.

#### **6.2.1.5.7 Two-phase experiments**

The two-phase experiments were performed in a similar manner as the single-phase experiments, described in Section 6.2.1.5.6, with two exceptions. The fluid in the reactor as well

as the indicator used for the velocity readings was different. The reactor was filled with 1 L of the solution containing 0.5 g/L of dead bacteria. The Bromothymol blue indicator was used instead of the 1 mL phenolphthalein indicator. The rest of the methodology remained the same as for the single-phase experiments.

Phenolphthalein was used for the single-phases system as this produced a very clear colour change from colourless to pink. The bacteria used as the solid particles were also pink and therefore the colour change would not be observed in the two-phase system. Bromothymol blue was used for the two-phase system as the colour change from yellow to blue was easily traced and not influenced by the colour of the bacteria.

#### **6.2.1.6 Limitations**

The system will be limited by the experimental setup. The model has to be derived specifically for the experimental setup. The model can be scaled for larger and smaller reactors but will need to be adapted for a reactor with a different configuration. This model will provide insight into the general operation of a thermosiphon photobioreactor but can only be used to calculate velocities for the specific experimental setup.

The velocity depends on the temperature within the experimental setup. Temperature is not easily controlled. The heating and cooling system determines the temperature of the reactor. These systems are insensitive and specific temperatures could not be achieved. This prevented the two different effects from being monitored independently. The temperature at  $T_a$  could not be held steady while the temperature difference between  $T_a$  and  $T_b$  was investigated. The temperature difference between  $T_a$  and  $T_b$  was kept within  $0.3^\circ\text{C}$  of the desired temperature difference and  $T_a$  was within  $0.4^\circ\text{C}$  of the desired temperature. The temperatures achieved by the heating and cooling systems therefore limit the accuracy of the model.

The uncertainty related to any measurement will influence the accuracy of the experimental results. The temperature readings will have a degree of uncertainty related to them. This was expected to be less than  $0.15^\circ\text{C}$  (from the manufacturers information) but as the temperature difference investigated is less than  $7^\circ\text{C}$ , a small uncertainty may have a significant influence.

The temperature was measured at three locations in the reactor. An average or calculated temperature was used for the vast majority of the reactor. Approximating the temperature within the reactor will significantly affect the accuracy of the model. The experimental results can be used to ensure that the model is accurate for the modelled reactor but the model will decrease lose accuracy if it is extended to a different configuration.

Measuring flow rate is known to be imprecise and few methods exist that can measure the superficial velocity with high precision and accuracy. Errors related to the measurement of the velocity are expected. Repeated readings were taken to increase the accuracy of the measurements and minimise the error incorporated in the results. The accuracy of the readings will be determined based on the deviation of the repeated readings. As the model is based on the experimental results the accuracy of the model will be limited to the accuracy of the experimental data.

## 6.2.2 Coefficients for density and viscosity

A polynomial trend line was selected to represent the relationship between the density and the temperature of water. Fitting a polynomial trend line is not a physical representation of this relationship but merely a mathematical tool necessary for the mathematical model. The model requires an equation relating the density to temperature. Equation 26 was derived by fitting a polynomial trend line to the density data found on the NIST database and was used in the mathematical model (Linstrom and Mallard, 2011).

$$\rho = Cw1 \times T^2 + Cw2 \times T + Cw3 \quad [ 26 ]$$

Where  $Cw1 = -0.0045 \frac{kg}{K^2.m^3}$

$$Cw2 = 2.442 \frac{kg}{K.m^3}$$

$$Cw3 = 671.1 \frac{kg}{m^3}$$

The density,  $\rho$ , is calculated in  $\frac{kg}{m^3}$  and  $T$  is the temperature of the fluid in the segment in Kelvin.  $Cw1$ ,  $Cw2$  and  $Cw3$  were the constant determined to best fit the NIST data. Using these constant the  $R^2$  value was calculated as 0.99999. This means that the trend line fits the data well as the  $R^2$  value is close to 1.

Equation 26 is only valid for the range for which it was derived. This equation will therefore not be applied to temperatures below 290K or above 313K. As the temperature range being investigated is small and the trend line fits well the equation can be used with confidence for the relevant temperatures.

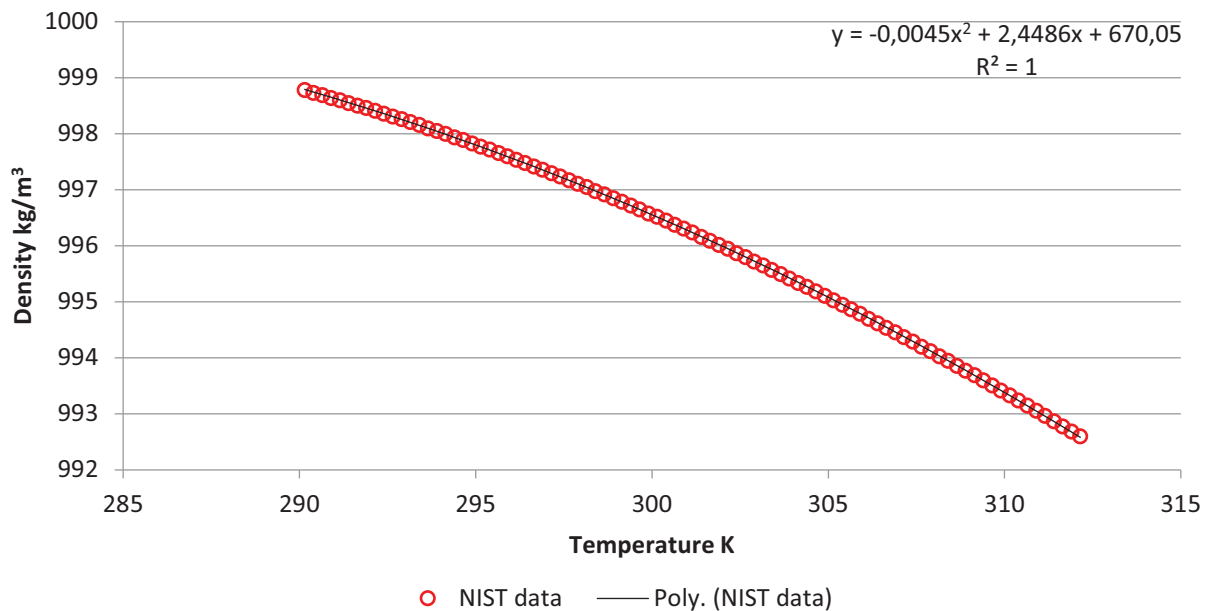


Figure 62: Density correlation

The same procedure was followed to represent the relationship of viscosity to temperature. An exponential function was chosen to represent the NIST data. As the temperatures will extend past the temperature range for which the model was derived the model was sufficiently accurate. The results are shown below in Figure 63 and Equation 27.

$$\mu = C1 \times e^{C2 \times T} \quad [ 27 ]$$

Where  $C1 = 0.6635 \text{ Pa.s}$

$$C2 = -0.02217 \frac{1}{K}$$

The viscosity  $\mu$  is calculated in  $\text{Pa.s}$  and  $T$  is the temperature of the fluid in the segment in Kelvin.  $C1$  and  $C2$  were the constant determined to best fit the NIST data. The resulting equation was shown to fit the data well. The fit can be seen in Figure 63 and the  $R^2$  value was calculated as 0.99847. The resulting equations, Equation 26 and 27, were therefore used to calculate the density and viscosity of the water based for all temperatures falling within the temperature range from 17°C to 39°C.

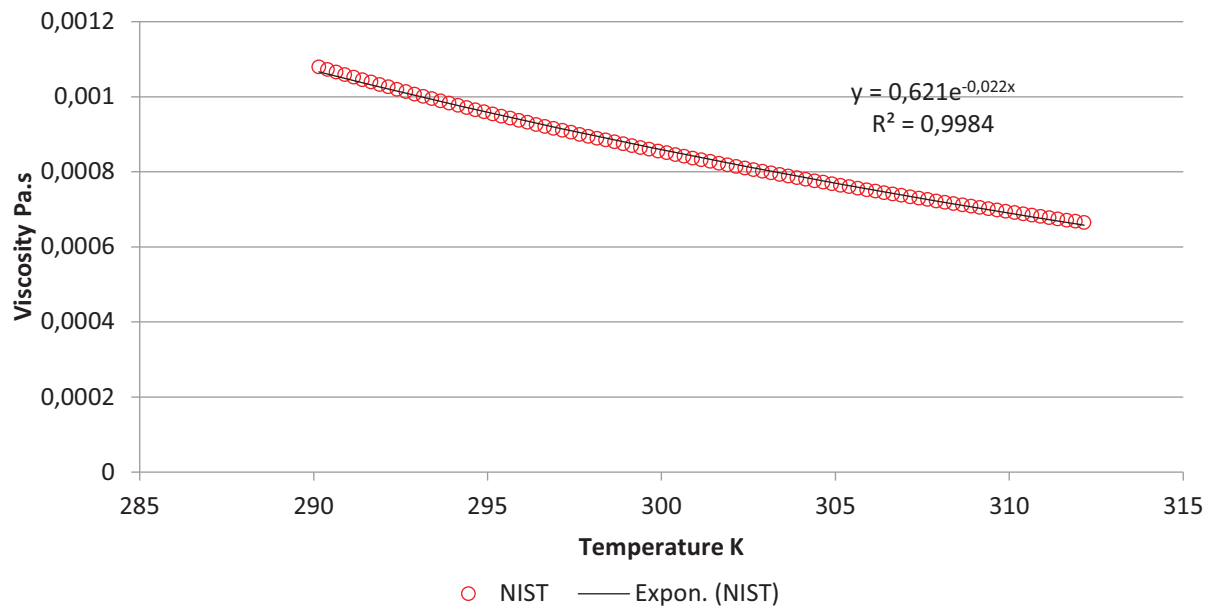


Figure 63: Viscosity correlation

### 6.2.3 Derivation of the mathematical model

Derivation of the momentum balance for a closed loop thermosiphon:

From Newton's 2<sup>nd</sup> law

$$\frac{\Delta(mv)}{\Delta t} = (\dot{m}v)_{in} - (\dot{m}v)_{out} + \sum F \quad [ 28 ]$$

In steady state:

$$\frac{\Delta(mv)}{\Delta t} = 0$$

$$\therefore 0 = (\dot{m}v)_{in} - (\dot{m}v)_{out} + \sum F \quad [ 29 ]$$

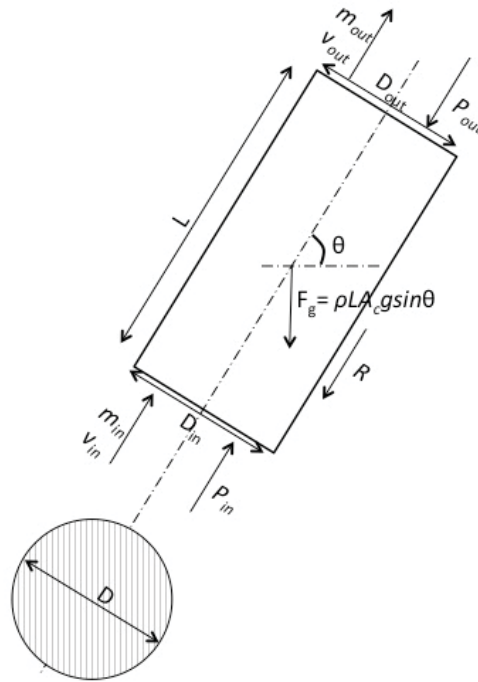


Figure 64: A single element in the thermosiphon photobioreactor, adapted from Figure 3 (Dobson, 1993)

The sum of the all the external forces acting on the control volume can be expressed as (Çengel and Cimbala, 2006; Dobson, 1993; Ruppertsberg, 2008; Yun et al., 2005):

$$\sum F = A_c(P_{in} - P_{out}) - \bar{\rho}LA_c g \sin \theta - R \quad [30]$$

Where R represents the frictional force. In a closed loop the inlet and outlet conditions are equal and therefore the pressure term equates to zero (Dobson, 1993).

$$\therefore A_c(P_{in} - P_{out}) = 0$$

$$\sum F = -\bar{\rho}LA_c g \sin \theta - R \quad [31]$$

Substituting Equations 31 into Equation 29 gives:

$$0 = (\dot{m}v)_{in} - (\dot{m}v)_{out} - \bar{\rho}LA_c g \sin \theta - R \quad [32]$$

The frictional force is equal to the pressure loss multiplied by the surface area (Çengel and Cimbala, 2006; Dobson, 1993):

$$R = \Delta P_L A_z$$

$$R = f \frac{L_{eq} \rho v^2}{D} Per L$$

For laminar flow in pipes the fanning friction factor can be related to the Reynolds number (Budihardjo et al., 2007; Çengel and Cimbala, 2006; Dobson, 1993):

$$f = \frac{16}{Re}$$

$$Re = \frac{\rho v D}{\mu}$$

All the terms are to be written in terms of diameter and mass flow rate:

$$A_c = \frac{\pi D^2}{4}$$

$$Per = \pi D$$

Rewriting the velocity in terms of mass flow rate:

$$v = \frac{\dot{m}}{\rho A_c}$$

$$v = \frac{4\dot{m}}{\rho \pi D^2}$$

Rearranging and substituting for Reynolds number

$$f = \frac{16 \mu}{\rho v D}$$

$$f = \frac{16 \mu \pi D^2}{4 D \dot{m}}$$

Substituting the friction factor into the frictional force term and writing it in terms of diameter:

$$R = \frac{16 \mu \pi D^2 L_{eq} \rho}{4 D \dot{m}} \frac{\dot{m}^2}{D^2 \rho^2 A_c^2} \pi D L$$

$$R = \frac{16 \mu \pi D^2 L_{eq} \rho}{4 D \dot{m}} \frac{\dot{m}^2}{D^2 \rho^2 \pi^2 D^4} \pi D L$$

$$R = \frac{32 L_{eq} \mu \dot{m} L}{D^3 \rho}$$

Substituting the values into Equation 32:

$$0 = \left( \frac{4\dot{m}^2}{\rho \pi D^2} \right)_{in} - \left( \frac{4\dot{m}^2}{\rho \pi D^2} \right)_{out} - \bar{\rho} L A_c g \sin \Theta - \frac{32 L_{eq} \mu \dot{m} L}{D^3 \rho}$$

Divide through by the cross sectional area:

$$0 = \left( \frac{4^2 \dot{m}^2}{\rho \pi^2 D^4} \right)_{in} - \left( \frac{4^2 \dot{m}^2}{\rho \pi^2 D^4} \right)_{out} - \bar{\rho} L g \sin \Theta - \frac{128 L_{eq} \mu \dot{m} L}{\pi D^5 \rho}$$

This balance must be true for across the entire closed loop. Therefore for a loop of N sections the following equation must be true:

$$0 = \frac{16\dot{m}^2}{\pi^2} \sum_{k=1}^N \left( \left( \frac{1}{\rho_k D_k^4} \right)_{in} - \left( \frac{1}{\rho_k D_k^4} \right)_{out} \right) - g \sum_{k=1}^N (\rho_k L_k \sin \Theta_k) - \frac{128\dot{m}}{\pi} \sum_{k=1}^N \left( \frac{L_{eq_k} \mu_k L_k}{D_k^5 \rho_k} \right) \quad [33]$$

### Calculations for model parameters

#### Equivalent length

The equivalent length that accounts for a 90° bend is equal to:

$$L_{eq_k} = 32 \times d_k$$

Half of the equivalent length of the bend was added to the length of tube approaching the bend from either side.

The sudden expansion of the pipe diameter from segment 6 to segment 1 was accounted for in the equivalent length of segment 1 as  $32.69 \times D_k$ . The calculation follows below.

$$\frac{D_6}{D_1} = \frac{0.02 \text{ m}}{0.102 \text{ m}}$$

$$\frac{D_6}{D_1} = 0.196$$

Using linear interpolation between the values in Table C.7 from Bird, Stewart and Lightfoot (1971). Using  $k$  as defined in the table.

$$\frac{0.196-0.1}{0.3-0.1} = \frac{k-0.98}{0.83-0.98}$$

$$k = 0.908$$

The conversion factor relating  $k$  to  $\frac{L_{eq_k}}{D_k}$  was calculated to be approximately 36.

$$\frac{L_{eq_k}}{D_k} = 0.908 \times 36$$

$$L_{eq_k} = 32.69 \times D_k$$

The sudden contraction of the pipe diameter from segment 1 to segment 2 was accounted for, in segment 2 as  $2 \times D_k$ . The contraction was approximated as a type B contraction.

The sudden contraction of the pipe diameter from segment 2 to segment 3 was accounted for, in segment 3 as  $2 \times D_k$ . The contraction was approximated as a type B contraction.

## 6.2.4 Final mathematical model Matlab code

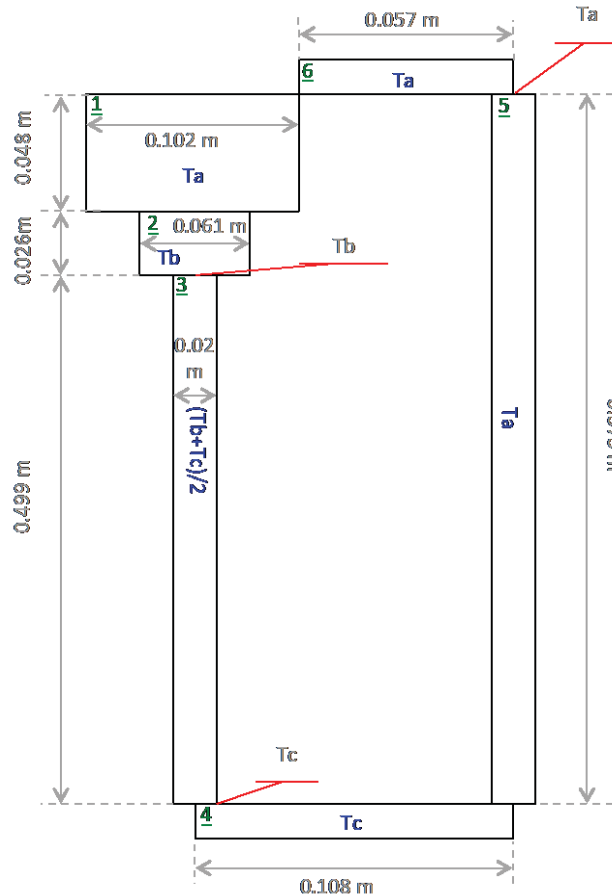


Figure 65: Final configuration for the Matlab model

Main code:

```

%% FINAL DESIGN.
% reactor split into six segments
% three temperatures readings
% equation:
% f = ((16 / (pi())^2)) .* (m.^2) * sum((1 / (de*D^4)) in - (1 / (de*D^4)) out) -
% g * sum(de*L*sin(theta)) ...
% - (128 / pi()) .* m * sum((vis*Leq*L) / (de*D^5));

clc;
clear all;

%% number of segments SPECIFIED BY USER

N = 6; %number of segments

%% Dk    1      2      3      4      5      6 SPECIFIED BY USER

Dk    = [0.102 0.061 0.02 0.02 0.02 0.02]; % m
Dkin  = [0.02 0.061 0.02 0.02 0.02 0.02]; % m
Dkout = [0.061 0.02 0.02 0.02 0.02 0.02]; % m

```

```

%% %Length of each segment SPECIFIED BY USER

%      1      2      3      4      5      6
Lk =[0.048 0.026 0.499 0.108 0.573 0.057]; %m

% frictional coefficient multiplied by the equivalent length
Leqk =0.143*[(Lk(1)+37.69*Dk(1)) (Lk(2)+2*Dk(2)) (Lk(3)+(32/2+2)*Dk(3))
(Lk(4)+32*Dk(4)) (Lk(5)+32*Dk(5)) (Lk(6)+32/2*0.02)]; % m

%% Theta SPECIFIED BY USER

Thetak =[270 270 270 0 90 180]; %degrees define based on orientation of
segments

%% Temperatures SPECIFIED BY USER

% velocity calculation for the surface plot

%T=[20.733 21.733 22.733 23.733 24.733 25.733 26.733 27.733 28.733
29.733 30.733 31.733 32.733 33.733 34.733 35.733 36.733 37.733
38.733
%17.633 18.633 19.633 20.633 21.633 22.633 23.633 24.633 25.633
26.633 27.633 28.633 29.633 30.633 31.633 32.633 33.633 34.633
35.633
%18.633 19.633 20.633 21.633 22.633 23.633 24.633 25.633 26.633
27.633 28.633 29.633 30.633 31.633 32.633 33.633 34.633 35.633
36.633];
%Tas = T(1,:);
%Tbs = T(2,:);
%Tcs = T(3,:);

% velocity calculation for experiments 1-9

Tas=[38.9 28.5 30.9 22.3 31.6 30.9 34.0 33.1 31.3];
Tbs=[34.4 25.6 24.3 17.6 28.3 27.3 30.2 29.5 26.9];
Tcs=[34.8 26.0 26.8 18.8 28.9 28.3 29.1 30.0 28.4];
set=[1 2 3 4 5 6 7 8 9];

%% creating variables to store data

ele=prod(size(set)); % number of data sets investigating
v=zeros(1,ele);
massflow=zeros(1,ele);
y=zeros(1,2);

%% Using a function to solve for the velocity for each set of temperatures
for count=1:ele

Ta = Tas(count)+273.15; %K
Tb = Tbs(count)+273.15; %K
Tc = Tcs(count)+273.15; %K
[mass,y] = soldesFIN(Ta,Tb, Tc, N, Dkin, Dkout, Lk, Thetak, Dk, Leqk,
set(count));
v(1,count) = y; %m/s
massflow(1,count) = mass; %kg/s

end;

```

```

%% printing values for use in Excel

disp([' '])
disp([num2str(v)])
disp([num2str(massflow)])

%% plot summary

subplot(2,2,1);
plot(set, v, '*b');
grid;

xlabel('Experiment');
ylabel('Velocity in down-comer (m/s)');

subplot(2,2,2);
plot(Tas-Tbs, v, '*b');
grid;

xlabel('Maximum Delta T (C)');
ylabel('Velocity in down-comer (m/s)');

subplot(2,2,3);
plot(set, massflow, '*b');
grid;
xlabel('Experiment');
ylabel('Mass flow rate (kg/s)');

subplot(2,2,4);
plot(Tas, v, '*b');
grid;
xlabel('Ta (C)');
ylabel('Velocity in down-comer (m/s)');

%% comparing calculated velocities to experimental results

% first set of experiments
if (set(1)==3)
v1 =[0.0129134 0.0100907 0.0080147 0.0091814]; %experimental result
figure;
plot(Tas-Tbs, v, '*b',Tas-Tbs, v1, 'or');
grid;
%title('Design 5');
xlabel('Maximum Delta T (C)');
ylabel('Velocity in down-comer (m/s)');
legend('model', 'experiment');
end

% second set of experiments
if (set(1)==5)
v2 =[0.0100907 0.0080147 0.0121257 0.0091814]; %experimental result
figure;
plot(Tas, v, '*b',Tas, v2, 'or');
grid;
%title('Design 5');
xlabel('Ta (C)');

```

```

ylabel('Velocity in down-comer (m/s)');
legend('model', 'experiment');
end

% all 9 experiments
if (set(1)==1)
v3 =[0.011  0.007  0.013  0.010  0.0100907  0.0080147  0.0121257
0.0091814  0.009]; %experimental result
figure;
plot(set, v, '*b', set, v3, 'or');
grid;
%title('Design 5');
xlabel('Maximum Delta T (C)');
ylabel('Velocity in down-comer (m/s)');
legend('model', 'experiment');

end

```

Function used to calculate the fluid velocity based on the temperature by solving Equation 24.

```

%% function for calculating the velocity of the fluid in the down-comer

function [massflow, velocity] = soldesFIN(Ta,Tb, Tc, N, Dkin, Dkout, Lk,
Thetak, Dk, Leqk,set)
%% defining variables DO NOT CHANGE

% viscosity constants
C1    =0.663519536;
C2    =-0.022165065;

% density constants
C1w   =-0.004523;
C2w   =2.44818882;
C3w   =671.055;

% gravity
g     =9.81; %m/s^2

%% Define temperature SPECIFIED BY USER

%Tk   = [Ta (Ta+Tb)/2 (Tc+Tb)/2 Tc (Ta+Tc)/2 Ta]; initial temperature
approximation
Tk    = [Ta Tb (Tc+Tb)/2 Tc Ta Ta]; % final temperature approximation

%% Densities SPECIFIED BY USER

% density correlation from NIST data
dek   = (C1w.*(Tk.^2)+C2w.*Tk+C3w); %kg/m^3 (DO NOT ALTER)

% density per segment
%      1      2      3      4 (number of segments)
dein  =[dek(6) dek(1) dek(2) dek(3) dek(4) dek(5)]; %kg/m^3 (adjust based on
number of segments)
deout =dek; %kg/m^3 (adjust based on number of segments)

%% Viscosity
%Tk   = [Ta (Ta+Tb)/2 (Tc+Tb)/2 Tc (Ta+Tc)/2 Ta]; initial temperature
approximation

```

```

Tk = [Ta Tb (Tc+Tb)/2 Tc Ta Ta]; % final temperature approximation

% viscosity per segment
visk = (C1.*exp(Tk.*C2)); %Pa.s

%% An initial check used for model development
if (Ta-Tb==5)
disp('-----')
disp(['For a temperature difference of ', num2str(Ta-Tb), ' Celsius :']);
print(N, Dkin, dein, Dkout, deout, dek, Lk, Thetak, visk, Dk, Leqk);
disp('-----')
end

%% Terms for the equation used to calculate velocity

T1 = (16/(pi())^2)*sum(1./(dein.*((Dkin).^4))-1./(deout.*((Dkout).^4)));
T2 = g*sum(dek.*Lk.*sind(Thetak));
T3 = (128/pi())*sum((visk.*Leqk.*Lk)./(dek.*(Dk.^5)));

func = @(massf) (massf.^2)*(T1)-T2-massf*T3;

%% Solving for the velocity using fzero

x = linspace(0,0.001);
massflow = fzero(func, 0);

disp(' ')
velocity = (massflow*4)/(pi()*dek(3)*(Dk(N-1)^2)); %m/s check that the
segment is that of the riser
Re = (dek(N-1)*velocity*Dk(N-1))/visk(N-1);
disp(['Set DeltaT Ta Mass flow rate Velocity Re']);
disp([num2str(set), ' ', num2str(Ta-Tb), ' ', num2str(Ta-273.15,3), ' ',
', num2str(massflow,3), ' ', num2str(velocity,3), ' ', num2str(Re,3)]);

% check for laminar assumption
if Re<1300
disp('As Re < 1 300 the flow is laminar and the assumption is correct');
else
disp('The flow is not laminar and therefore the assumptions are
incorrect');
end
end

```

Results from the code.

Set	DeltaT	Ta	Mass flow rate	Velocity	Re
1	4.5	38.9	0.00513	0.0164	496

As Re < 1 300 the flow is laminar and the assumption is correct

Set	DeltaT	Ta	Mass flow rate	Velocity	Re
2	2.9	28.5	0.00197	0.00629	151

As Re < 1 300 the flow is laminar and the assumption is correct

Set	DeltaT	Ta	Mass flow rate	Velocity	Re
3	6.6	30.9	0.0042	0.0134	340

As Re < 1 300 the flow is laminar and the assumption is correct

Set DeltaT Ta Mass flow rate Velocity Re  
4 4.7 22.3 0.00199 0.00632 133  
As  $Re < 1300$  the flow is laminar and the assumption is correct

Set DeltaT Ta Mass flow rate Velocity Re  
5 3.3 31.6 0.00257 0.00821 212  
As  $Re < 1300$  the flow is laminar and the assumption is correct

Set DeltaT Ta Mass flow rate Velocity Re  
6 3.6 30.9 0.00256 0.00818 208  
As  $Re < 1300$  the flow is laminar and the assumption is correct

Set DeltaT Ta Mass flow rate Velocity Re  
7 3.8 34 0.00404 0.0129 350  
As  $Re < 1300$  the flow is laminar and the assumption is correct

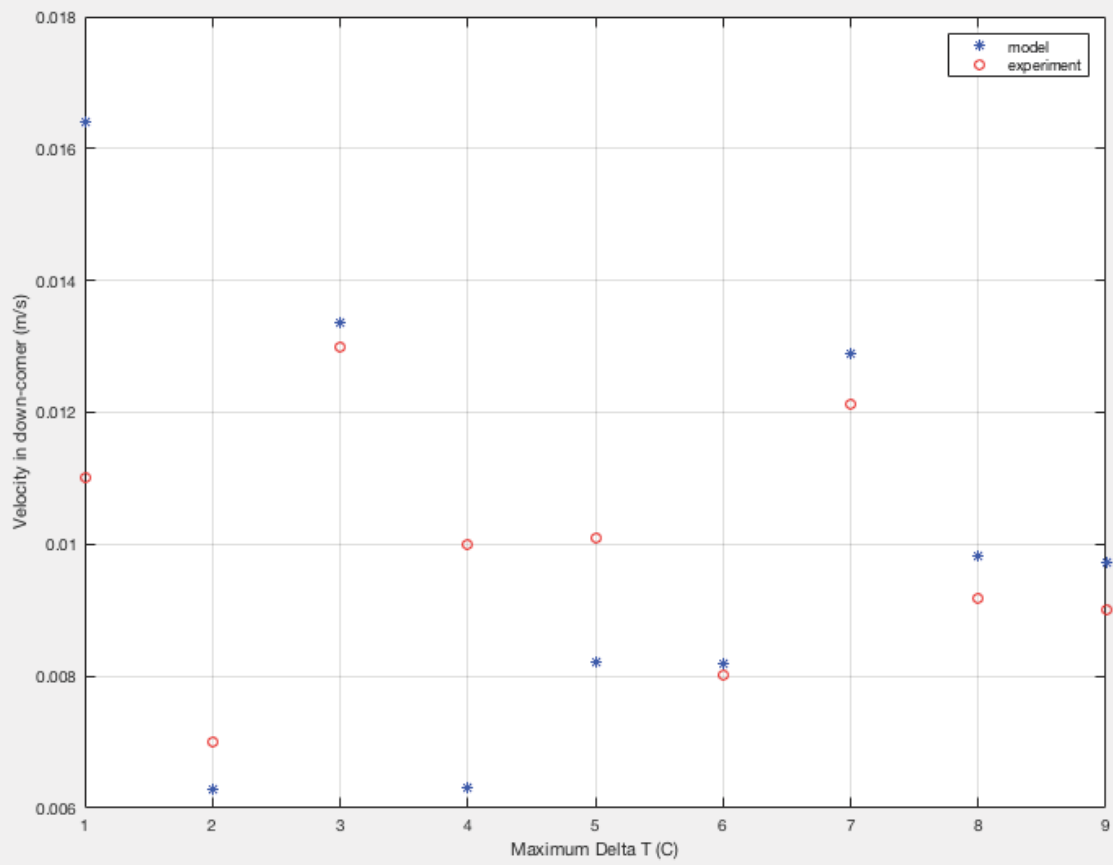
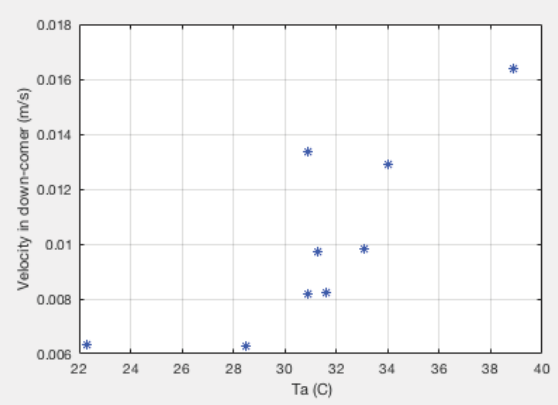
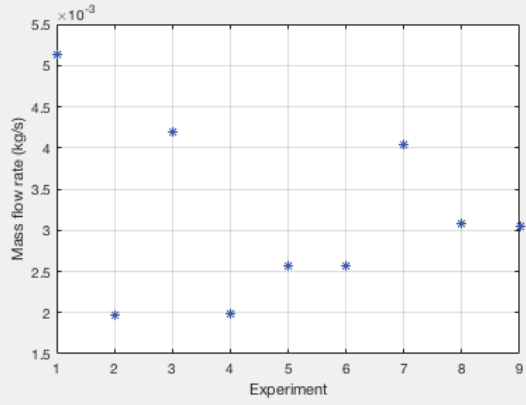
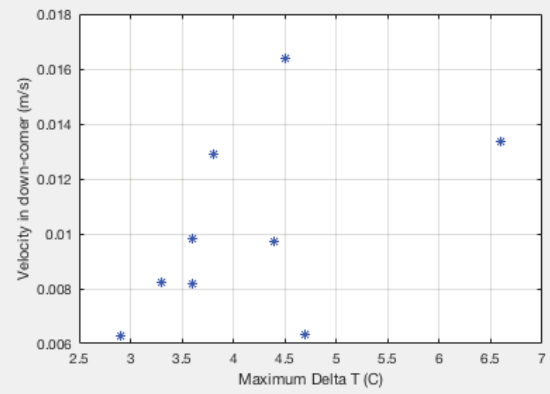
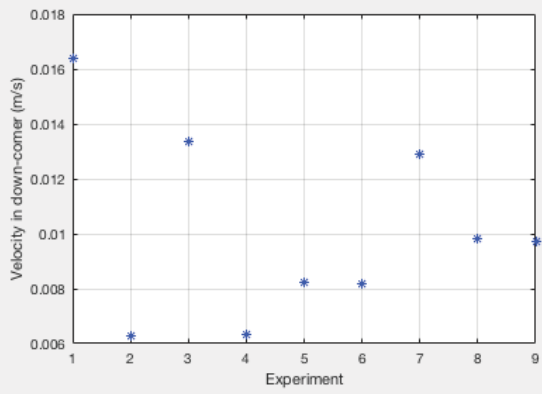
Set DeltaT Ta Mass flow rate Velocity Re  
8 3.6 33.1 0.00308 0.00982 262  
As  $Re < 1300$  the flow is laminar and the assumption is correct

Set DeltaT Ta Mass flow rate Velocity Re  
9 4.4 31.3 0.00305 0.00972 249  
As  $Re < 1300$  the flow is laminar and the assumption is correct

0.0164 0.006285 0.013371 0.0063205 0.0082109 0.0081794 0.012891 0.0098176  
0.0097245

0.0051321 0.001972 0.0041956 0.0019864 0.0025743 0.002565 0.0040405 0.003077  
0.0030496

>>



## 6.3 Appendix C – appendices for CFD model

### 6.3.1 Computational Fluid Dynamics modelling methodology

The CFD passive fluid flow and heat transfer analysis within the thermosiphon PBR was performed using the commercial CFD package ANSYS Fluent, version 17.2 which is based on the finite volume method (Fluent, 2016). The geometry creation was the first step and a simplified 2D model from the 3D cylindrical domain has been considered here using the DesignModeler software as shown in Figure 66(A) and (B). In essence, this approach minimizes the computational cost by enabling the CFD model to easily predict the experimental scenario within a shorter time. The computational domain had a height of 0.65 m corresponding to the dynamic liquid level observed in experiments with the physical model. The mesh generation within the computational domain was attained with the Mesher of FLUENT, shown in Figure 66(C) and (D). The mesh was composed of 49,566 fine element sizes with their quality is reported in Table 19. This mesh was not uniform throughout the computational domain as boundary layer inflation (5 rows of mesh with size of 0.1 mm and growth factor of 1.2 (Alizadehdakhel et al., 2010)) was used to ensure sufficient resolution of detail in the near wall regions with significant thermal and momentum gradients.

Table 19: Mesh quality details

Mesh Metric	Minimum value	Maximum value	Average value
Orthogonality	0.6291	1.0	0.99373
Skewness	1.3057e-010	0.58139	2.3036e-002
Aspect ration	1.0	10.003	2.289

This discretization enabled the governing equations (mass and energy balance equations) to be solved numerically by iteration at specific locations while assuming the flow to be laminar without viscous heating (Louisos et al., 2013), incompressible and non-reactive with constant physical properties (e.g.  $C_p$ ,  $k$ ,  $\rho$ ,  $\mu$ ) of water operating at 313.15 K in the formulation of the buoyancy term since as the bacteria cell dried weight and nutrient concentrations are very low compared to the volume of water within the reactor (Gandhi et al., 2011; Malik et al., 2013) as illustrated in Table 20. The boussinesq approximation was also incorporated into the model to account for buoyancy driven convection as the working fluid (mostly water) density changes induced by temperature field according to (equation (34)) (Gandhi et al., 2011; Malik et al., 2013).

$$\rho = \rho_{\infty}[1 - \beta(T_s - T_{\infty})] \quad (34)$$

Where  $\beta = 1/T_{\infty}$  ( $K^{-1}$ ) is the coefficient of thermal expansion (Louisos et al., 2013),  $\rho_{\infty}$  is the water density,  $T_{\infty}$  is the ambient temperature and  $T_s$  is the operating temperature.

Table 20: Thermophysical properties of water (Lide, 2003)

Properties	Units	Value
Specific heat capacity	$JKg^{-1}K^{-1}$	4178.5
Density	$Kgm^{-3}$	992.222
Thermal expansion coefficient	$K^{-1}$	0.003193358
Dynamic viscosity	$Kgm^{-1}s^{-1}$	0.000653
Thermal conductivity	$Wm^{-1}K^{-1}$	0.6305

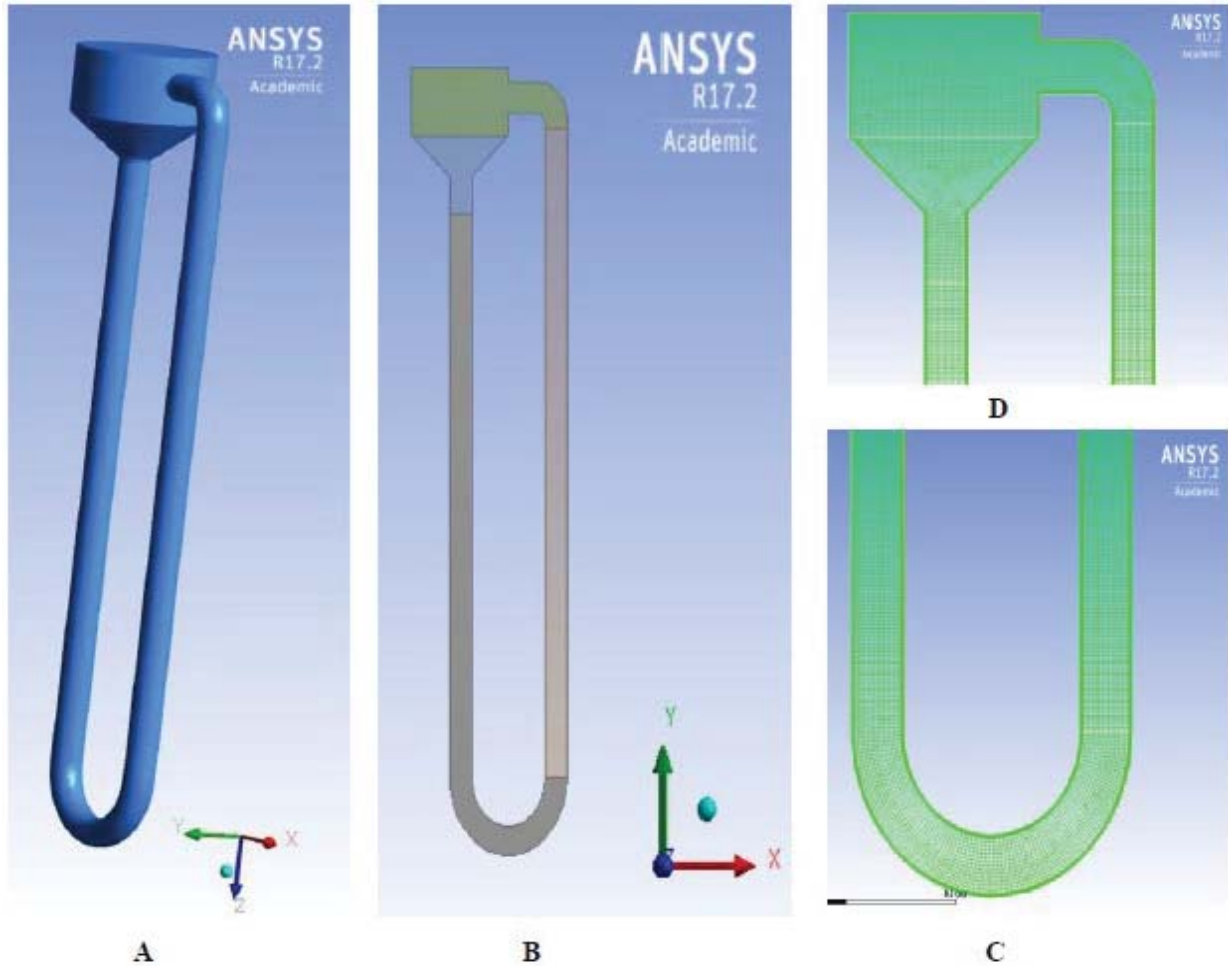


Figure 66: (A) and (B) are the 3D and 2D Thermosiphon PBR reactor geometries while (B) and (C) are the element meshing used at the top and bottom sections of the reactor respectively

### 6.3.1.1 Boundary conditions

A non-slip boundary condition is applied to all the walls except for the top water surface which was defined as a free surface with constant shear (free slip) at an atmospheric pressure of 1 atmosphere (101.325 KPa) from the reference pressure point (Gandhi et al., 2011; Louisos et al., 2013; Xu et al., 2014). In order to simulate light transmission and non-uniform sensible heat generation, a user defined function (UDF) from (equation (39)) is interpreted and hooked to the riser cell zone. A zero-heat flux was assigned to all the walls as adiabatic sections assuming no heat is gain or lost because they are thermally insulated except for the riser and cooling wall

sections where a convection heat transfer coefficients of  $1.46 \text{ J/s.K}$  and  $202.06 \text{ J/s.K}$  were defined as boundary conditions. A body force term of  $9.8 \text{ ms}^{-1}$  was used as the acceleration due to gravity while an experimentally observed operating temperature of  $303.15 \text{ K}$  was assigned.

### **6.3.1.2 Solution strategy and convergence criteria**

The numerical simulations were run on an i7-4510U CPU 2.00GHz 2.60GHz processor Intel(R) computer with 16 GB RAM and 64 bit operating system (Dell Inc., Stellenbosch, South Africa) using the pressure-density based solver and a combination of SIMPLE algorithm for pressure-velocity coupling and Second Order Upward Schemes for momentum and energy discretization (Basak et al., 2016; Louisos et al., 2013; Malik et al., 2013; Rek et al., 2012). An unsteady simulation with a step time of 0.01s and time step size of 5,000 was employed to model the dynamic behavior of the TPBR since it experiences a high temperature to velocity coupling to drive the buoyancy flow (Alizadehdakhel et al., 2010; Fadhl et al., 2013; Roldán et al., 2014). The under relaxation factors were 0.3 for pressure, 0.6 for momentum and 0.8 for energy and radiation as defined by (Rout et al., 2012). The pressure discretization used Body-force-weighted Schemes while the Green-Gauss scheme is used for spatial discretization (Louisos et al., 2013; Rout et al., 2012). The numerical computations in this study were considered converged when the scaled residuals for continuity, momentum and energy components had fallen below  $10^{-3}$  and  $10^{-6}$  respectively, as used by other researchers (Alizadehdakhel et al., 2010; Basak et al., 2016; Fadhl et al., 2013; Rek et al., 2012; Williamson and Wilson, 2009). Generally, it took 60.1s and 103,348 iterations for the simulation converged.

## 6.3.2 Experimental fluid dynamic studies

### 6.3.2.1 Experimental set-up

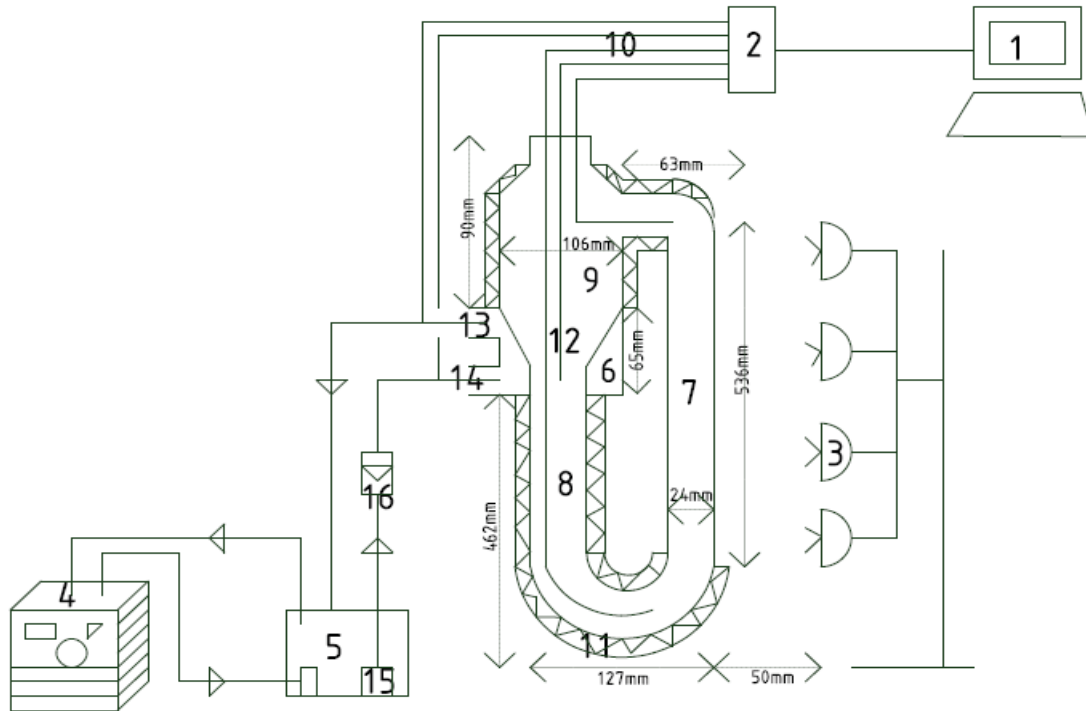


Figure 67: Schematic diagram of the experimental setup: (1) Computer, (2) Data acquisition unit, (3) Halogen lamps, (4) Water Chiller, (5) Reservoir, (6) Cooling water jacket, (7) Riser, (8) Down comer, (9) Storage tank, (10) Thermocouples, (11) Thermal insulation, (12) Cooling section, (13) Cooling water outlet, (14) Cooling water inlet, 15. Submersible water pump

The experimental rig and a schematic view of the experiment setup are shown in Figure 67. The thermosiphon PBR was constructed with glass using the measurements given in section 3.2.1 and fixed on a framework to ensure vertical orientation. To minimize thermal heat losses to the surrounds, a layer of cotton wool and aluminium foil were used for thermal insulation by wrapping the storage tank, down-comer and up-riser excluding the cooling section to enable visibility of flow. The fluid temperatures were used as an indicator of system performance and the temperature distribution along the thermosiphon PBR were monitored with thermocouples (RTD, PT100, Simplex, Class A) with a 3 wire Nickel Sheath (SS316) of 3 mm diameter were placed and connected to a 4 channels data-acquisition unit (WIKA Instruments REB(TR40), South Africa) with a data sampling rate of 60 seconds which are then transferred to a Dell PC (64-bit, Intel(R) Core (TM) i7-4510U CPU) for further processing. Three of the thermocouples labeled  $T_1$ ,  $T_2$  and  $T_3$  were used to monitor the storage tank, down comer and up riser temperatures while two others labeled  $T_{w,in}$  and  $T_{w,out}$  were used measure the inlet and outlet temperatures of the cooling sections, and the accuracy of the thermocouples was within  $\pm 1^\circ\text{C}$ . During experiments,

the cooling water circuit supplies water at predefined conditions (constant temperature and flow rate of 17°C and 0.5 L/min respectively) to the inlet through an 8 mm ID flexible silicon tubing while the waste heat from the outlet water was removed in a secondary reservoir with a temperature controlled water chiller (HAILEA HS-28A, China) before being recirculated into the system from the secondary reservoir using a submersible water pump (Waterhouse WH360, South Africa). An inline water flow meter (SEAL Water Tech Rotameter 0.1-1.4LPM G1/2", South Africa) was incorporated into the cooling water circuted which was used to control and measure the inlet volumetric flow rate into the cooling sections. Heating on the riser was provided by the luminance of 4 halogen floodlights fixed on a metal frame enabling the panel to be shifted forward and backward so as to either increase or decreasing the luminance reaching the riser.

**6.3.2.2 Fluid flow, heat and light transfer in the TPBR**

As shown on the design in Figure 67, the increase and decrease of the working fluid’s temperature is brought about by the external one-sided illumination on the riser section and circulation of cooled water through the cooler (tube-in-tube cooling water jacket tube with the water flowing through the annulus) respectively. These are continuously responsible for density differential accounting for thermosiphoning within the TPBR (Gandhi et al., 2011; Louisos et al., 2013). A radiant energy balance around the irradiated area (the riser section) characterizes the light absorption as sensible heat flowing into the system. This is illustrated in Figure 68.

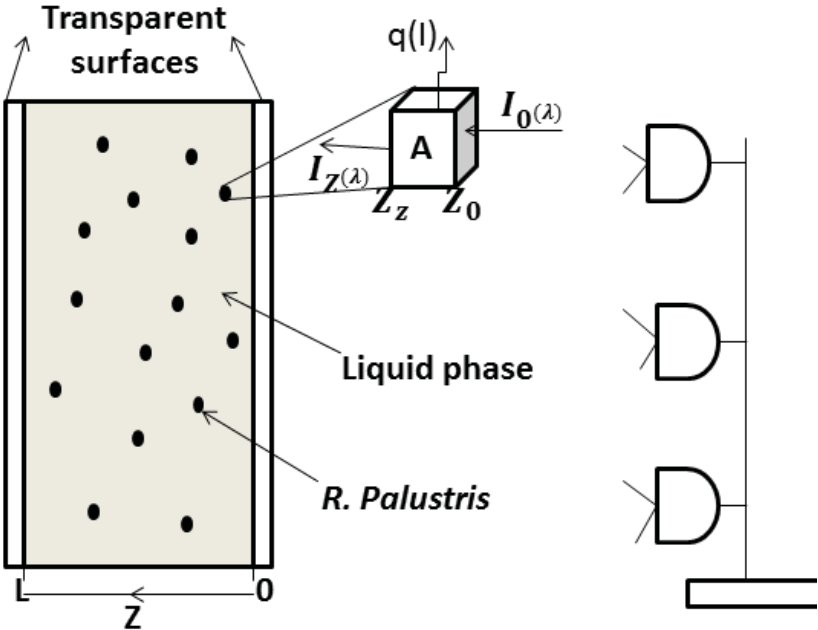


Figure 68: Schematic view of light radiating the TBPR front the front surface  $z=0$ , to the rear surface  $z=l$ , with  $A$ ,  $I_0(\lambda)$ ,  $I_z(\lambda)$ , and  $q(l)$  being the irradiated area, incident radiant illumination, radiant illumination at any point  $z$ , and volumetric sensible heat generated at that point  $z$  within the riser respectively.

### 6.3.2.2.1 Model assumptions:

1. The irradiance at any point within the riser ( $I_{z(\lambda)}$ ) is a function of the total surface irradiation at the riser ( $I_{0(\lambda)}$ ), the optical properties of the culture (bacterial cell spectral mass extinction coefficient,  $K_b$ , the concentration and morphology of the microbial cells,  $X$ ), and the radial distance from that cell centroid/point ( $z$ ) to the illuminated surface which is mathematically govern by the Beer-Lambert Law (Acién et al., 1998; Acién Fernández et al., 1999; Benson and Rusch, 2006; Luo and Al-Dahhan, 2004; Ogbonna et al., 1995).
2. The light transfer is unidirectional since it is symmetric to the plane of the PBR (Murphy and Berberoğlu, 2011), and set to be perpendicular to the y-axis therefore the radiant illumination ( $I_{0(\lambda)}$ ) is to be constant in that direction and the light transmitted to any cell centroid/point ( $z$ ), was determined only in the x-axis (Berberoglu et al., 2007; Murphy and Berberoğlu, 2011; Sato et al., 2010).
3. The phases (liquid and microbial cells) are well-mixed and randomly oriented, cold, only absorbing and non-scattering in the photosynthetic active region (PAR) of the light spectrum, at very low biomass concentration ( $< 1Kg/m^3$ ) (Berberoglu et al., 2007; Murphy and Berberoğlu, 2011).
4. The riser's top and bottom surfaces are non-reflecting (Berberoglu et al., 2007; Jacobi et al., 2012).
5. Steady state radiation transfer prevails (Berberoglu et al., 2007) yielding (equation (35))

$$I_{0(\lambda)}A - I_{z(\lambda)}A - q_{(I)}A(z_z - z_0) = 0 \quad (35)$$

$$I_{0(\lambda)}A - I_{z(\lambda)}A - q_{(I)}A(z_z - z_0) = 0 \quad (36)$$

$$q_{(I)} = \frac{I_{0(\lambda)} - I_{z(\lambda)}}{Z_z - Z_0} \equiv \frac{\Delta I_{(\lambda)}}{\Delta Z} \equiv \frac{dI_{(\lambda)}}{dZ} \quad (37)$$

According to the Beer-Lambert law (equation 39), where  $K_0$  is the overall spectral attenuation coefficient, and  $K_0 = K_b X$ , where  $K_b$  is the spectral mass extinction coefficient accounting for shelf shading effects between the bacterial cells at a biomass concentrations,  $X$  (Benson and Rusch, 2006; Luo and Al-dahhan, 2004; Murphy and Berberoğlu, 2011).

Solving for the volumetric heat source term in (equation (37)) by substituting (equation (36)) results to the general (equation (38)) considered as volumetric heat-source due to the light attenuation by bacterial absorption.

$$\therefore q_{(I)}(W/m^3) = \frac{dI_{(\lambda)}}{dZ} \equiv -K_0 I_{0(\lambda)} e^{-K_0 Z} \quad (38)$$

However, the halogen lights produce a complete electromagnetic spectrum while the photosynthetic bacteria absorb only in the visible and infrared regions. Therefore, (equation (38)) was modified to generate volumetric heating only in the regions where the bacterial absorption occurs, leading to (equation (39)) which is implemented by a user-defined function (UDF).

$$q_{(l)}(W/m^3) = \int_{400}^{900} \frac{dI(\lambda)}{dZ} d\lambda = \int_{400}^{900} -K_{0,\lambda} I_{0(\lambda)} e^{-K_{0,\lambda} Z} d\lambda \quad (39)$$

$K_b$  for *Rhodospseudomonas palustris* was experimentally estimated using the UV/VIS spectrophotometer (Model AE-S60-4U, A&E lab (UK) Co., Ltd) for normal-normal transmittance measurement of five samples with known biomass concentration over the spectral range of 400 and 900 nm with (equation (40)).

$$K_b = \left[ \frac{\text{slope of } Ab \text{ vs } [Biomass]}{Z_{cuvette}(m)} \right]_{400}^{900} \quad (40)$$

On the other hand, the heat sink removes the sensible heat generated by (equation (39)) because of heat release through convection heat transfer from the walls of the cooling section to the circulating cooled water as per the experimental apparatus Figure 69. This entire process is fully captured by an energy balance of the system (equation (41)) operating under continuous heating and cooling but reaches steady state when ( $\dot{Q}_{lights} = \dot{Q}_{lost}$ ), enabling the radiant energy from the illuminating lights to be turnoff for ambient water cooling which is governed by the newton's law of cooling (equation (42)). The heat transfer coefficient of the cooling walls was theoretically determined with the Newton's law of cooling by curve fitting (equation (43)) with experimental data as illustrated in Figure 70.

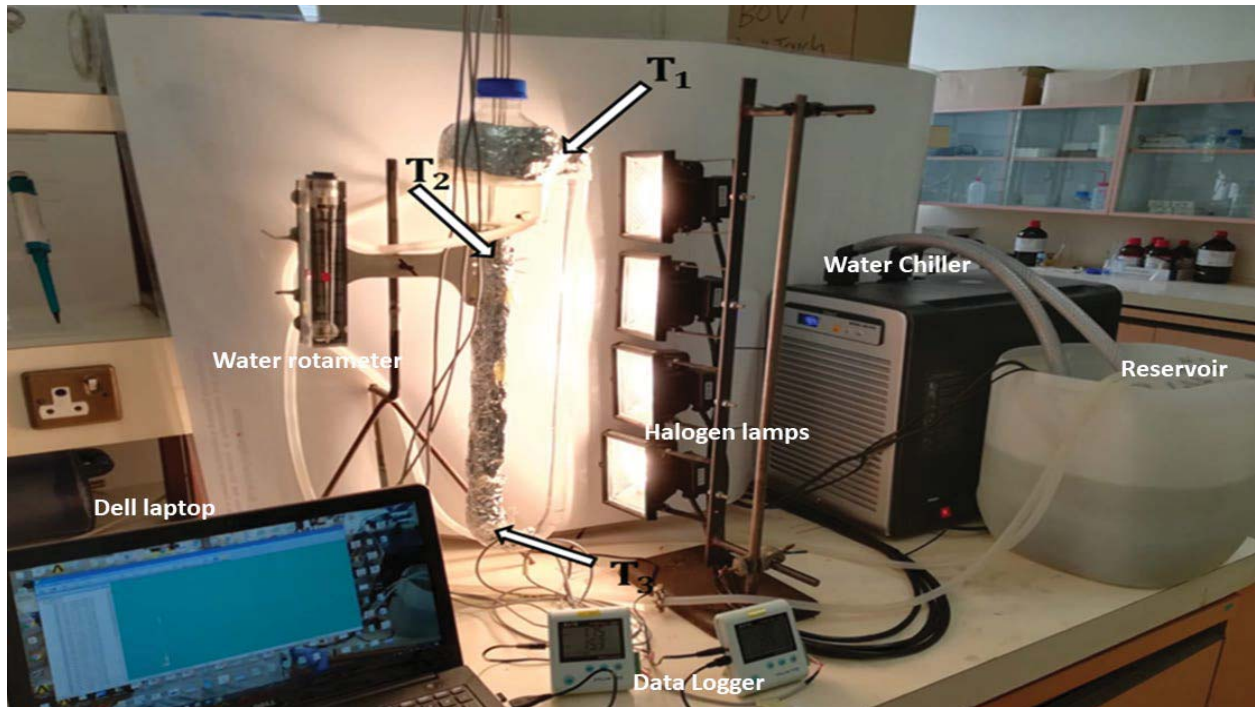


Figure 69: Photograph of the thermosiphon PBR in full operation for heat transfer analysis with indicated the indicated positions of measuring position.

$$MC_p \frac{dT}{dt} = \dot{Q}_{lights} - \dot{Q}_{lost} \quad (41)$$

$$MC_p \frac{dT}{dt} = -\dot{Q}_{lost} \quad (42)$$

$$T(t) = (T_{stab} - T_{w,out})e^{\left(-\frac{th_c A_c}{\rho V C_p}\right)} + T_{w,out} \quad (43)$$

Where  $M$ ,  $\rho$ ,  $V$  and  $C_p$  are the mass (kg), density ( $Kg/m^3$ ), volume ( $m^3$ ), and specific heat capacity ( $J/Kg.K$ ) of water respectively,  $\dot{Q}_{lights}$  and  $\dot{Q}_{lost}$  are the rate of heating (J/s) by halogen lamps and rate of losing heat (J/s) by convection respectively,  $t$  is time (s),  $h_c$  is the heat transfer coefficient of cooling section ( $J/s.K$ ),  $T_{stab}$  and  $T_{w,out}$  are the stabilization and outlet sub cooling water temperatures (K) respectively.

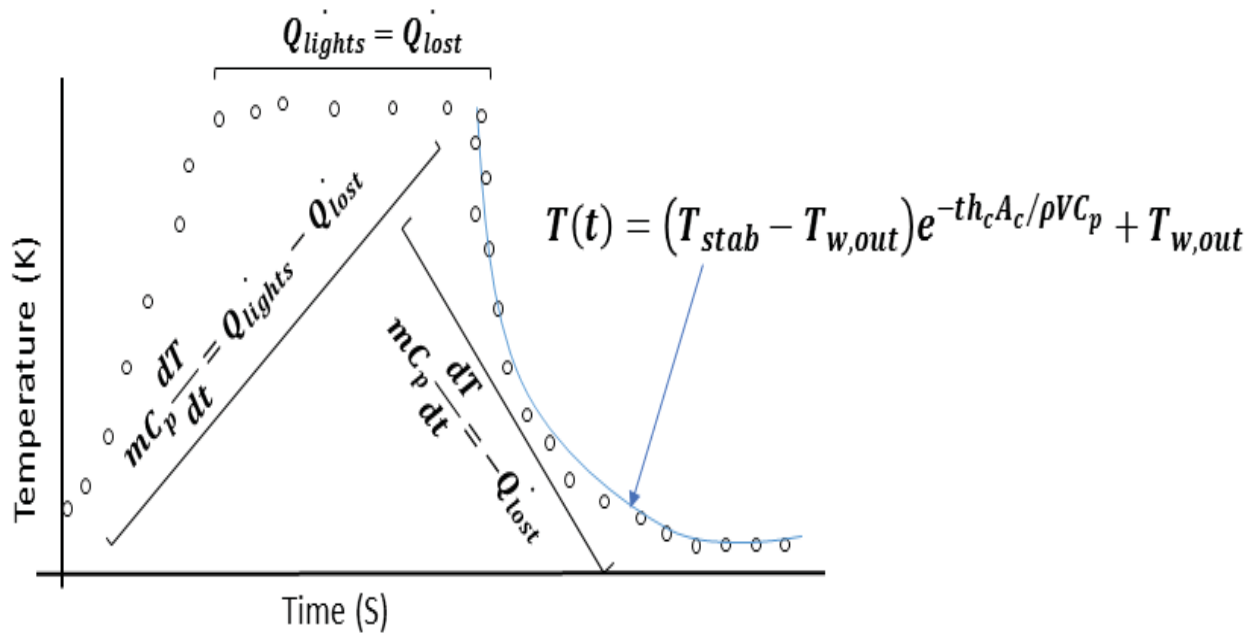


Figure 70: Schematic of the thermosiphon PBR's heating and cooling curve illustrating all the various sections where the heat transfer equations are applied

The riser wall's heat transfer coefficient was estimated with the newton's law cooling by curve fitting (equation (44)) to experimental data obtain from hot water cooling down to ambient in the thermosiphon PBR as illustrated in Figure 71.

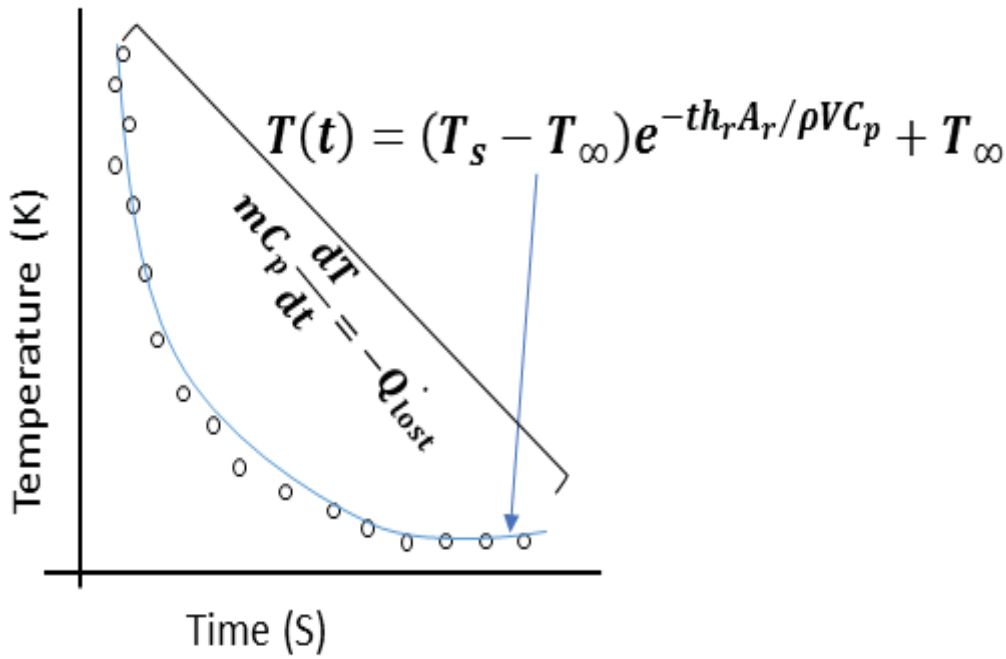


Figure 71: Schematic of thermosiphon PBR's cooling curve illustrating the application of Newton's law of cooling for modeling the riser's heat transfer coefficient

$$T(t) = (T_s - T_\infty)e^{\left(-\frac{th_r A_r}{\rho V C_p}\right)} + T_\infty \quad (44)$$

Where  $h_r$  and  $A_r$  are the heat transfer coefficient ( $J/s.K$ ) and area ( $m^2$ ) of the riser section respectively,  $T_s$  and  $T_\infty$  represent the hot water and ambient temperature (K) respectively.

### 6.3.2.3 Lamp radiation model

Using the blackbody radiation spectrum of halogen lamps at a color temperature of 2900 K and numerically computing the thermosiphon PBR's available radiant flux density ( $W/m^2$ ) with equation (44) results to an overestimate of the radiant flux density, not practically available for bacterial absorption and attenuation. This is mainly because only a small fraction of the emitted lamp's intensity is in the visible and infrared wavelengths where the photosynthetic bacteria absorb. Therefore, focusing only on the photosynthetically active region (PAR) of the lamp's emission curve (350 to 950), illustrated in Figure 72, and numerically computing the area under that portion,  $A(T_{PAR})$  (equation (45)) will estimate a more appropriate amount of radiant flux density available for bacterial absorption and attenuation.

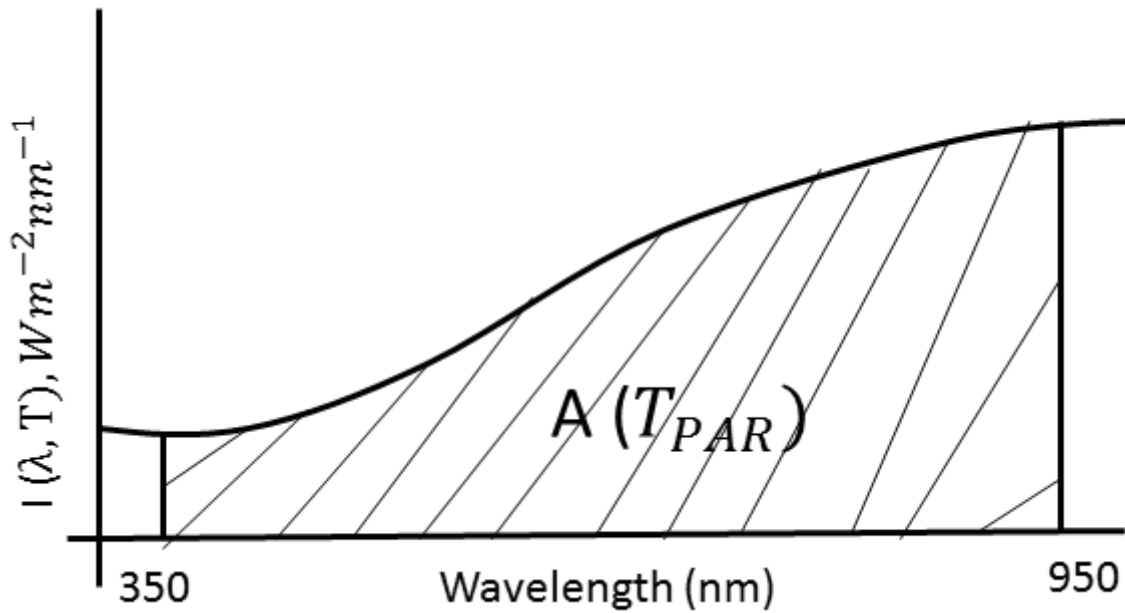


Figure 72: Schematic diagram of the halogen lamp's emission spectral in the photosynthetically active region with the shaded area showing the region for numerical computation of the radiant flux density

$$A(T_{PAR}) = \int_{350}^{950} I(\lambda, T) d\lambda \quad (45)$$

However, the emission spectral of halogen lamps only starts at 380 nm as per the manufacturer's specification meanwhile the photosynthetic bacteria absorb in the wavelength range of (400 to 950 nm). Therefore, the box model method (Berberoglu et al., 2007) was employed to accurately estimate the weighted average radiant flux density ( $W/m^2$ ) for bacterial absorption at centered wavelength  $\lambda_c$  (400, 500, 600, 700, 800 and 900 nm) assigned as midpoint of each box, using 6 boxes of wavelength intervals (350 to 450, 450 to 550, 550 to 650, 650 to 750, 750 to 850, and 850 to 950 nm) such that the area under the original spectrum equals the are under the box (Berberoglu et al., 2007) Figure 73 with (equation (46)).

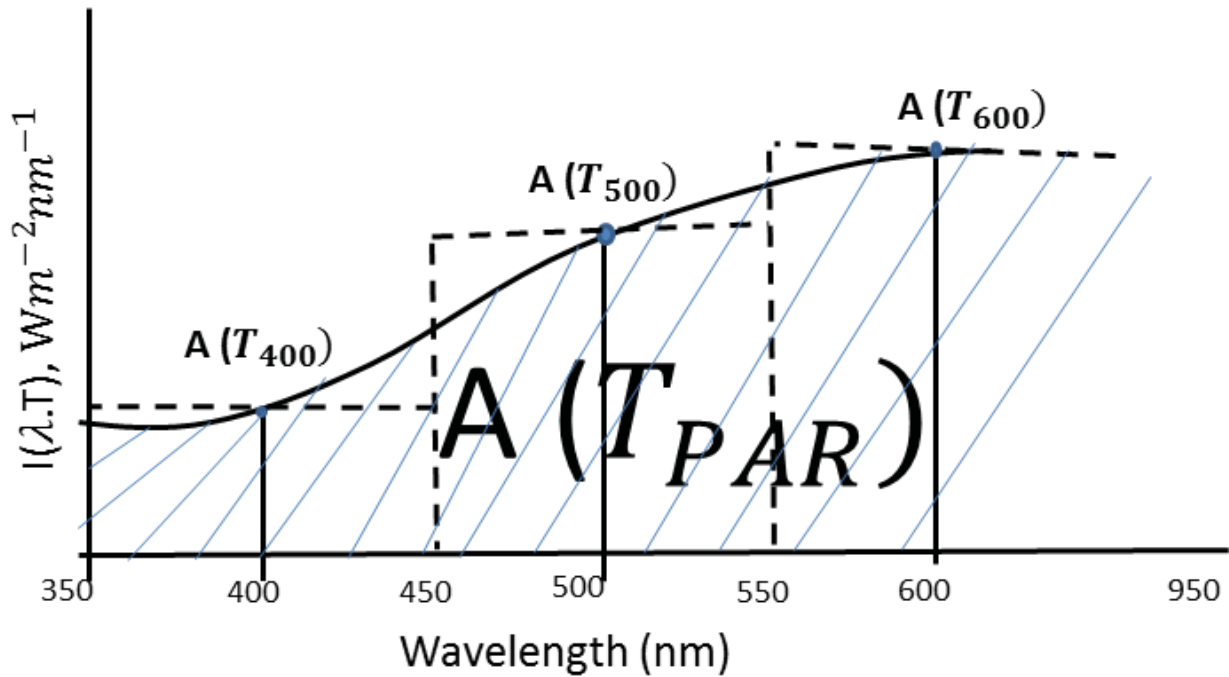


Figure 73: Schematic diagram of the box model applied to the photosynthetically active region of the halogen lamp spectrum

$$A(T_{400}) = \frac{\int_{350}^{450} I(\lambda, T) d\lambda}{10} \quad (46)$$

#### 6.3.2.4 Rate of heating from light transfer

The *Rhodospseudomonas palustris* within the thermosiphon PBR are living cells, purple in color which absorbs light in the visible and near far infrared wavelengths for their photosynthetic and metabolic heat generation purposes bringing about the thermal effect which induces a temperature differential when the thermosiphon PBR is circulated. That thermal effect has been reported to be a function of the optical properties of the culture (bacterial cell spectral mass extinction coefficient,  $K_b$ , the concentration and morphology of the microbial cells,  $X$ ) and by holding these parameters constant, one can investigate the metabolic heat contributions to the overall thermal effect by experimenting with fresh (active) and dead (inactive) bacterial cells at known biomass concentrations within the thermosiphon PBR. That metabolic heat contribution may enhance the thermosiphon PBR's natural convection flow power thereby maintaining more bacterial cells in free suspension, improving mass transfer, and eliminating the light and nutrient gradients through enhanced mixing thereby increasing to increase biomass productivity. The inactivation process of this active bacterial cells (see Figure 75) without tampering on their cell morphology as well pigment color was achieved by heating the fresh bacterial culture to an inactivation temperature of 70 °C while holding that temperature for 60 minutes.

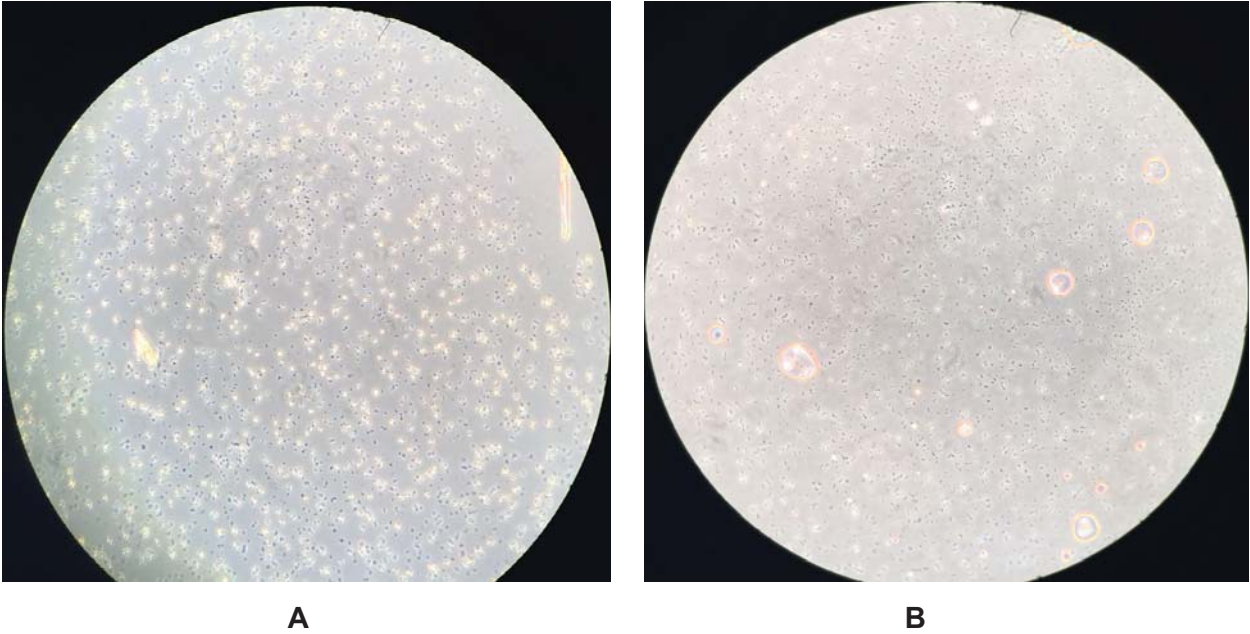


Figure 74: Photograph of (A) active and (B) inactivated *Rhodospseudomonas palustris* under a light microscope with a magnification of 40×

When the thermosiphon PBR is set up for experimental measurement of the rate of heat transfer from the solar simulators as describe in, the energy balance of the system operating at steady state equation ( $\dot{Q}_{lights} = \dot{Q}_{lost}$ ) is modified with equation (equation (47)) to calculated the rate of heat gain by the system from the solar simulators (equation (48))

$$\dot{Q}_{lost} = hA(T_{stab} - T_{w,out}) \quad (47)$$

$\dot{Q}_{lost}$  is the rate of heat loss (J/s) by the thermosiphon PBR to the circulating cooling water,  $h$  is the heat transfer coefficient of previously estimated (J/s.K),  $T_{stab}$  and  $T_{w,out}$  are the stabilization and outlet cooling water temperatures (K) respectively.

$$\dot{Q}_{lights} = hA(T_{stab} - T_{w,out}) \quad (48)$$

### 6.3.2.5 Bacterial culture for experimental testing in prototype TPBR

*Rhodospseudomonas palustris* strain NCIMB 11774 was the photosynthetic bacteria strain selected for use in this study. It was grown in a synthetic medium containing: Glycerol (50 mM), Na- glutamate (10 mM), yeast extract (0.73 M),  $K_2HPO_4$ (0.98 M),  $KH_2PO_4$  (1.3 M),  $NaS_2O_3 \cdot 5H_2O$  (1 M), PABA (15 mM),  $MgSO_4 \cdot 7H_2O$  (0.81 M),  $CaCl_2 \cdot 2H_2O$  (0.34 M), NaCl (6.8 M),  $FeC_6H_5O_7$  (20 mM), ZnCl (0.51 mM),  $MnCl_2 \cdot 4H_2O$  (0.51 mM),  $H_3BO_3$  (0.97 mM),  $CoCl_2 \cdot 6H_2O$  (0.84 mM),  $CuSO_4 \cdot 2H_2O$  (0.12 mM),  $NiCl_2 \cdot 6H_2O$  (84 $\mu$ M),  $Na_2MoO_4 \cdot 2H_2O$  (0.17 mM), Vitamin B12 (0.73 $\mu$ M), Thiamine (0.45 mM) and  $H_2O$  (0.98 mL) with the pH at about  $7.3 \pm$  as shown in (Appendix A). The media was kept sterile by autoclaving at 120°C for 15 mins. Bacterial colonies cultured on algar were picked and resuspended into an airtight 1,000 mL Schott bottle containing the growth

medium, and placed into an incubator set at 35°C with about 2500 lux external illumination from a 100 W tungsten lamp. The bacterial inoculum was allowed to grow for 5 days until it reached mid-logarithmic phase with an optical density of around 1.0, and then used for experimental testing in the Thermosiphon PBR.

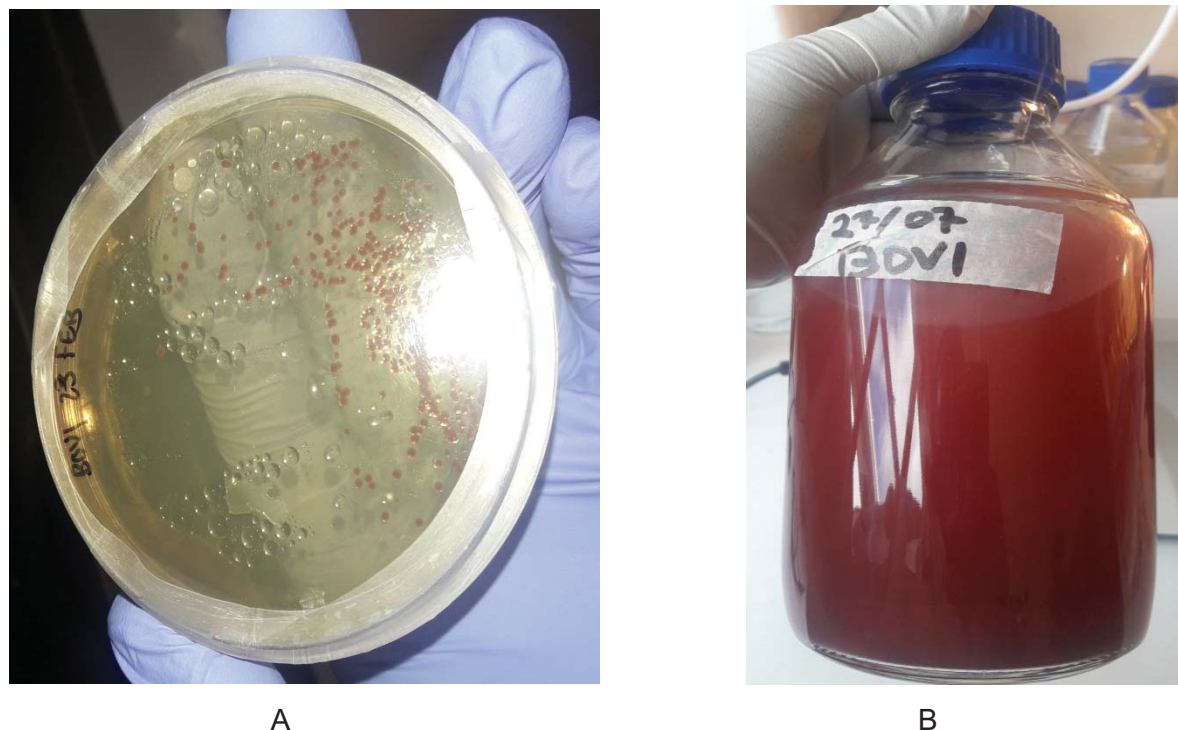


Figure 75: Photographs of (A) *Rhodospseudomonas palustris* incubated on agar and (B) planktonic *Rhodospseudomonas palustris* biomass used for all experimental testing

### 6.3.2.6 Fluid flow visualization

The hydrodynamics due to mixing in the TPBR were characterized quantitatively through the marker image tracking method (Joshi et al., 2009) and qualitatively by comparing the local velocity fluid flow profile to that of the numerical CFD simulation at the selected riser section. This entailed the drop wise addition of a 3.5 M *NaOH* solution through one of the holes on the septum-sealed port at the cap of the TBPR into the working fluid composing of 5 mL Bromothymol Blue indicator (0.4 mM), buffer solution (10 ml each of  $KH_2PO_4$  (0.12M) and  $K_2HPO_4$  (98mM)) and  $0.5\text{ kg/m}^3$  *Rhodospseudomonas palustris* (fresh and dead). The visualization of color change (yellow to blue color) for both experiments containing fresh and dead *Rhodospseudomonas palustris* was focused on the riser section. The propagated color change through the buoyancy flow field of the riser's bottom (point A) to the top (point B) with respect to time ( $T_{AB}$ ) was recorded with a digital camera (SAMSUNG RF8JA1C8BRN, Taiwan). Quantitative analysis was carried out by calculating the riser's flow velocity with (equation (49)) and compared to that predicted by

the CFD simulations. At the same time, the recorded flow video was intercepted at 15s intervals to produce photos which were then qualitatively compared to the CFD simulations flow mixing.

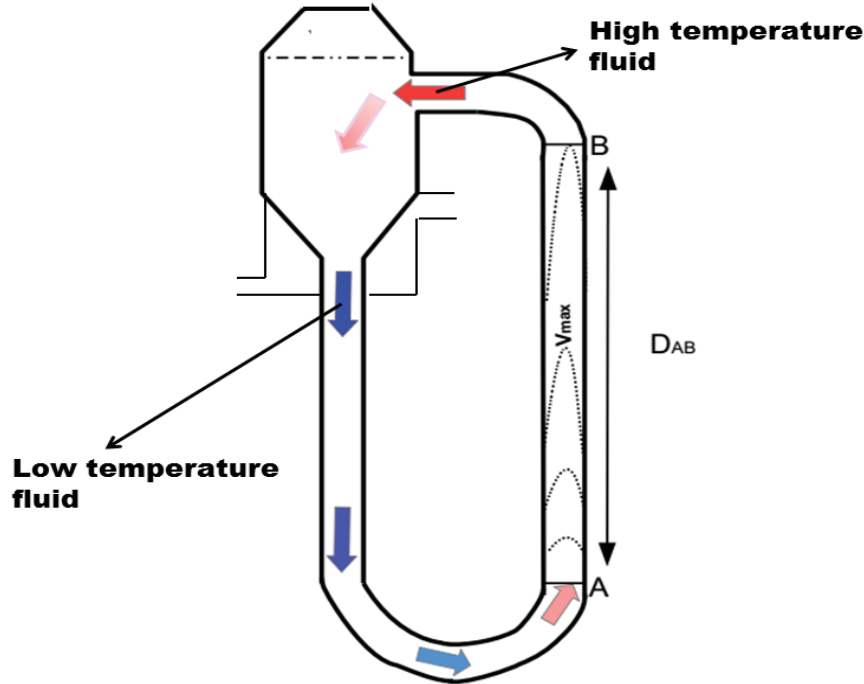


Figure 76: Schematic diagram for the estimation of local flow velocity through the riser section

$$V_{AB} = \frac{D_{AB}}{T_{AB}} \quad (49)$$

### 6.3.2.7 Sedimentation experimentation

The rate of cell circulation and settling in the thermosiphon PBR was investigated by monitoring the biomass concentration in the storage tank over time for the fresh and dead bacterial cells. This entailed collecting 5 mL samples at 60 minutes intervals with a syringe through one of the holes on the septum-sealed port at the cap of the thermosiphon BPR and calculating its cell dry weight from absorbance measurement with UV/VIS spectrophotometer (Model AE-S60-4U, A&E lab (UK) Co., Ltd) at 660 nm using a calibration curve. The rate of cell settling ( $X_{S_t}$ ) was calculated by deducting the bacterial cell concentration in free suspension ( $X_t$ ) from the known initial biomass concentration ( $X_0$ ) as per (equation (50)) and illustrated on Figure 77.

$$X_{S_t} = X_0 - X_t \quad (50)$$

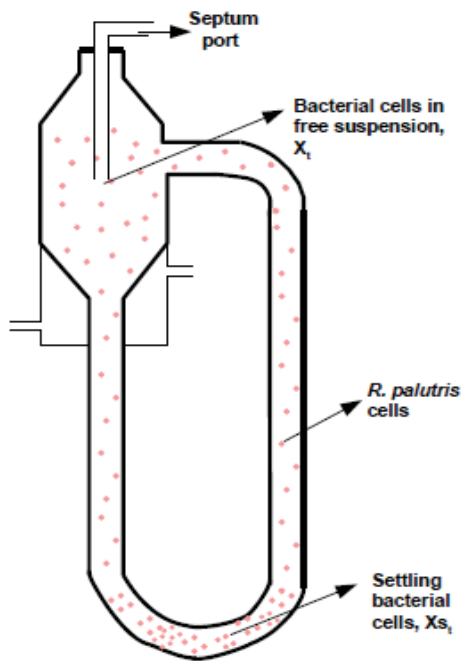


Figure 77: Schematic diagram for the estimation of biomass settling rate

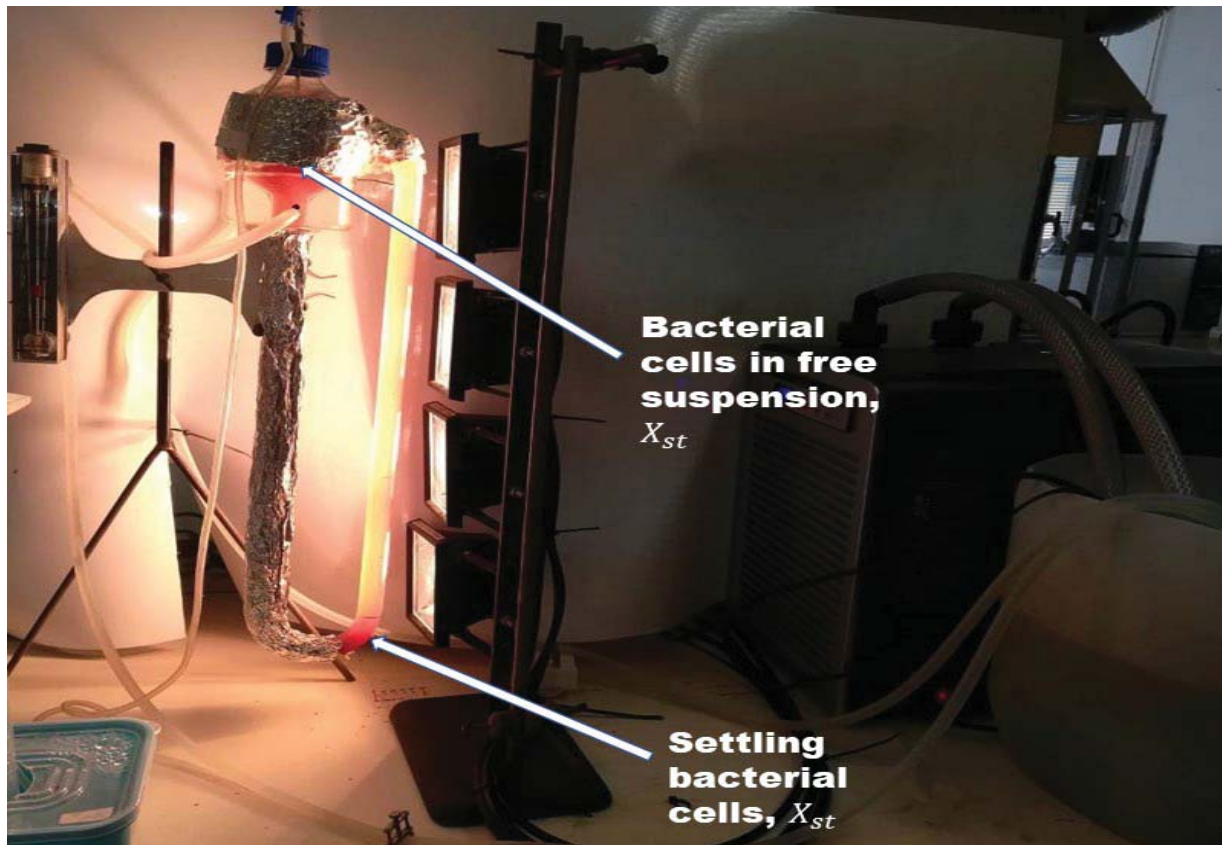


Figure 78: Photograph of the experimental setup illustrating the estimation of biomass settling

### 6.3.3 UDF source code

User define function for the implementation of non-uniform volumetric heat generation term

```
/*heat_source udf for non-uniform volumetric heat generation due to light penetration*/
#include "udf.h"
#define I_o1 1.42916235e+03 /*radiant intensity for 350-450 nm (W/m^2)*/
#define I_o2 5.254294537e+03 /*radiant intensity for 450-550 nm (W/m^2)*/
#define I_o3 1.105942157e+04 /*radiant intensity for 550-650 nm (W/m^2)*/
#define I_o4 1.694148845e+04 /*radiant intensity for 650-750 nm (W/m^2)*/
#define I_o5 2.145313883e+04 /*radiant intensity for 750-850 nm (W/m^2)*/
#define I_o6 2.411873212e+04 /*radiant intensity for 850-950 nm (W/m^2)*/
#define Kb_o1 2.2042e+02 /*350-450 nm bacterial mass absorption coefficient (m^2/Kg) */
#define Kb_o2 2.2344e+02 /*450-550 nm bacterial mass absorption coefficient (m^2/Kg) */
#define Kb_o3 1.7231e+02 /*550-650 nm bacterial mass absorption coefficient (m^2/Kg) */
#define Kb_o4 1.2378e+02 /*650-750 nm bacterial mass absorption coefficient (m^2/Kg) */
#define Kb_o5 1.7758e+02 /*750-850 nm bacterial mass absorption coefficient (m^2/Kg) */
#define Kb_o6 1.2465e+02 /*850-950 nm bacterial mass absorption coefficient (m^2/Kg) */
#define X 0.5 /*bacterial biomass concentration (kg/m^3)*/
#define X_1 1.934554e-01 /* light entering point (m) */
/*All dimensions are in SI units*/

DEFINE_SOURCE(heat_source, c, t, dS, eqn)
{
    real xc[ND_ND]; /*position vector */
    real Z, K_o1, K_o2, K_o3, K_o4, K_o5, K_o6, source;
    K_o1=Kb_o1*X, K_o2=Kb_o2*X, K_o3=Kb_o3*X, K_o4=Kb_o4*X, K_o5=Kb_o5*X,
    K_o6=Kb_o6*X; /*overall spectral attenuation coefficients (m^-1)*/
    C_CENTROID(xc,c,t); /*acquire the cell centeriod*/
    Z= X_1 - xc[0]; /*determine the distance from the light entering point */
    source = - 1.0*((K_o1*I_o1*exp(-K_o1*Z))+ (K_o2*I_o2*exp(-K_o2*Z))+ (K_o3*I_o3*exp(-
    K_o3*Z))+ (K_o4*I_o4*exp(-K_o4*Z))+ (K_o5*I_o5*exp(-K_o5*Z))+ (K_o6*I_o6*exp(-K_o6*Z)));
    /*spectral energy source term (W/m^3)*/
}
```

```
printf("Z is %e source is %e\n", Z, source); /* display on screen for inspection */  
dS[eqn]=0.0;  
return (-1*source); /* (-1) accounts for the opposition orientation of physical riser position */
```

